Politecnico di Milano

Department of Aerospace Science and Technology

Doctoral Program in Aerospace Engineering

Hybrid Rocket Propulsion for Active Removal of Large Abandoned Objects

Doctoral Dissertation of:
Pietro Tadini

Supervisor:
Prof. Luigi T. DeLuca

The Chair of the Doctoral Program:
Prof. Luigi Vigevano

2014 - XXVI

ABSTRACT

During the last 40 years, the mass of orbiting artificial objects increased quite steadily at the rate of about 145 metric tons annually, leading to a total of approximately 7000 metric tons. Now, most of the cross-sectional area and mass (97% in Low Earth Orbit (LEO)) are concentrated in about 4500 intact objects, i.e. abandoned spacecraft and rocket bodies, plus a further 1000 operational spacecraft. According to the most recent NASA results, the active yearly removal of approximately 5 large abandoned intact objects would be sufficient to stabilize the debris growth in LEO, together with the worldwide application of mitigation measures. However, besides legal and political issues, remediation measures are strongly hampered by high costs involved. In fact, the adoption of active debris removal freaks the space community out due to a so big expense, which does not provide any kind of direct earning and no possibility to be amortized. Recent simulations and cost analysis have shown that the active removal of only large historical abandoned objects will provide a reduction of long-term costs with respect to a no-remediation scenario. Several removal solutions have been proposed, such as different tether approaches, drag augmentation systems and the use of electrical engines or chemical rockets. The latter represent the preferred way for the controlled reentry of the removed target and, in the perspective of cost reduction, hybrid rocket technology is considered a valuable option, due to significant lower costs if compared with the actually used bi-propellant liquid systems. The possibility to use non-toxic propellants, besides their lower prices, reduces the complexity of handling, storability and load operations, decreasing the connected costs and avoiding the need of a special staff. Hybrid rockets can also be implemented for Post Mission Disposal (PMD) missions, by designing small, compact and cheap on-board propulsion systems for new satellites.

Very important is the propellant selection: hybrid propulsion is characterized by fuel and oxidizer in different state of matter. Typically, polymeric or paraffin materials are used as solid fuel, burned with non-toxic liquid or gaseous oxidizers. In case of long mission duration or ground storage, the selected propellants must keep their physical properties to guarantee the engine operations when required. Hydroxyl-Terminated Polybutadiene (HTPB) R45 is one of the most used materials in the space propulsion field, in particular as solid fuel in hybrid propulsion. It is characterized by high mechanical properties, resulting very suitable for combustion applications, despite its not great ballistics performance. In this respect, a simulated aging study was carried out, by means of thermal treatments defined considering the Arrhenius equation and the relative empirical *van't Hoff rule*. Storage modulus, Loss modulus and the dumping coefficient tanδ were measured at aging checkpoints by means of Dynamic Mechanical Analyzer (DMA). The HTPB R45 supplied by AVIO revealed a strong longevity, with quite low mechanical properties reduction over the simulated time.

Despite several advantages, hybrid rocket technology is still characterized by a relatively low Technology Readiness Level (TRL), missing of an in-space demonstrative

mission, as well as poor combustion efficiency, O/F shifting and low fuel regression rates (r_f). An internal ballistics combustion analysis was performed at laboratory scale level. A swirling oxidizer flow was used to improve the convective heat exchange between the flame and the regressing surface together with a HTPB-based fuel formulation loaded with 10% of an aluminum activated micron-sized powder. Besides the regression rate enhancements provided by their separately application, the r_f increase achieved by the techniques combination results similar to that achieved with metallized HTPB in standard injection. However, the combined approach revealed the possibility of limiting the performance shift of burning hybrid systems by means of swirl injection, which seems able to limit the convection heat transfer reduction during the combustion.

Hybrid propulsion could represent a key choice for all space debris applications to be performed in the next future. A design tool, based on quasi-one-dimensional Euler equations combined with chemical equilibrium, for hybrid rocket internal ballistics analysis and preliminary sizing was implemented following the approach suggested by Funami and Shimada. The regression rate is estimated for the couple $HTPB + H_2O_2$ by means of Marxman's model. H_2O_2 catalytic decomposition can be used both for the engine ignition and Reaction Control System (RCS), spilling from the same tank (90% concentration H_2O_2). The preliminary design of a HPM is performed for two targets: Cosmos-3M 2nd stage (1.4 t) and Envisat (7.8 t), both at the same altitude. The first represents a very good candidate for a demonstrative mission and technology validation, whereas the second is the target with the highest priority level, since in case of accidental collision a large number of new debris might be generated. A ΔV of 220 m/s is required for a controlled reentry. Each object is removed by a De-orbiting Kit (DeoKit) powered by a Hybrid Propulsion Module (HPM) (also able to perform a mid-range rendezvous of 20 m/s ΔV) and equipped with a Active Debris Removal (ADR) platform and two RCS systems, one for close-proximity operations and one for attitude control. A Cosmos-3M can be de-orbited using a single boost maneuver by an HPM of 258 kg (DeoKit 566.8 kg), with a length of 2.14 m and a width 90 cm. Vega can load 2 DeoKits, while Soyuz up to 6 allowing for multi-removal scenario. For Envisat a two-burns disposal is preferred to reduce the HPM mass, size and combustion time. The HPM results of 1260 kg (DeoKit 1771 kg), with a length of 3.76 m and a width 1.55 m. The latter can be put on orbit only by a heavy launcher such as Soyuz, which can load up to 2 DeoKits for the removal of Envisat-like objects.

ACKNOWLEDGMENTS

The author wish to acknowledge Prof. Luigi T. DeLuca for the research opportunities given during the PhD course and the staff of *Space Propulsion Laboratory* (SPLab) for the help and constant support.

A great acknowledgement to Prof. Toru Shimada, Dr. Koki Kitagawa and all members of Shimada-Laboratory, that work within the *Hybrid Rocket Research Working Group* (HRrWG) at the *Institute of Space and Astronautical Science* (ISAS) in Japan. A special acknowledgement to Dr. Yuki Funami for his important help and support in numerical code implementation.

In the frame of the project collaboration about ADR with hybrid propulsion, an acknowledgement to Prof. Michele Grassi (*University of Naples "Federico II"*), Dr. Urbano Tancredi (*University of Naples "Parthenope"*), Dr. Luciano Anselmo and Dr. Carmen Pardini (*National Research Council*), for the important cooperation experience and support in the research activities.

Last but not the least, a special acknowledgement to author's family and Diana, for the continuous and precious sustainment during the years of PhD course.

CONTENTS

LIST OF FIGURES

LIST OF TABLES

- A: cross-sectional area, m^2
- a_s: speed of sound, m/s
- B: blowing parameter, $\rho_f r_f/(GC_f/2)$
- b_k: kilogram-atoms of element k per kilogram of mixture, $kg\text{-}atom/kg$
- b_k°: assigned kilogram-atoms of element k per kilogram of total reactants, $kg\text{-}atom/kg$
- c_p: specific heat at constant pressure, $J/(kg \cdot K)$
- $c_{p,eq}$: equilibrium specific heat at constant pressure, $J/(kg \cdot K)$
- $c_{p,fr}$: frozen specific heat at constant pressure, $J/(kg \cdot K)$
- $c_{p,re}$: reaction specific heat at constant pressure, $J/(kg \cdot K)$
- c_s: fuel specific heat, $J/(kg \cdot K)$
- c_{T_F}: thrust coefficient
- $c_{v,eq}$: equilibrium specific heat at constant volume, $J/(kg \cdot K)$
- c^*: characteristic velocity, m/s
- C: constant in Wilke equation
- C_f: skin-friction coefficient
- $C_{p,j}^\circ$: molar heat capacity at constant pressure for standard-state for species j, $J/(kmole \cdot K)$
- $C_{v,j}^\circ$: molar heat capacity at constant volume for standard-state for species j, $J/(kmole \cdot K)$
- D: diameter, m
- e: specific internal energy, J/kg
- e_t: specific total energy, J/kg
- E': Storage modulus, Pa
- E'': Loss modulus, Pa
- E_a: activation energy, J
- E_t: total energy (ρe_t), J/m^3

- E_j°: molar standard-state internal energy for species j, $J/kmole$
- f_{safe}: safety factor
- f_{spl}: splitting function in AUSMDV
- f^*: zero-transpiration friction factor
- F: reaction rate change factor
- F_{DB}: flux of debris
- $\hat{f}$: Helmholtz energy of mixture, J/kg
- $\hat{F}$: Helmholtz energy of mixture with constraints, J/kg
- g_0: gravitational acceleration, $9.807\ m/s^2$
- $\hat{g}$: Gibbs energy of mixture, J/kg
- G: local bulk mass flux, $kg/(m^2 \cdot s)$
- $\hat{G}$: Gibbs energy of mixture with constraints, J/kg
- h: specific enthalpy, J/kg or convective heat transfer coefficient, $W/(m^2 \cdot K)$
- h_{dc}: decay mean altitude, km
- h^*: zero-transpiration convective heat transfer coefficient, $W/(m^2 \cdot K)$
- H_j°: molar standard-state enthalpy for species j, $J/kmole$
- H: total enthalpy, J/kg
- $\Delta H_{v,eff}$: effective heat of gasification, J/kg
- ΔH_{vap}: heat of vaporization, J/kg
- ΔH_s: net surface heat of reaction, J/kg
- ΔH°: standard enthalpy of formation, J/kg
- i: inclination, deg
- I_s: specific impulse, s
- $I_{s,tot}$: total specific impulse, $N \cdot s$
- I_v: volumetric specific impulse, $(kg \cdot s)/m^3$
- ΔI_s: relative difference between ideal and corrected performance
- k_i: reaction rate coefficient Arrhenius equation, J/mol

- k_s: soot absorption coefficient
- K: constant parameter in AUSMDV
- L: characteristic fragment length, m
- Le: Lewis number
- l_p: cross-section perimeter, m
- $\dot{m}$: mass flow rate, kg/s
- M: mass, kg
- N_{cc}: cumulative number of catastrophic collision
- N_s: number of chemical species
- N_t: number of time steps
- N_x: number of x steps
- O/F: oxidizer to fuel mass ratio
- p: pressure, Pa
- P_i: physical property at the aging time t_i
- Pr: Prandtl number
- Q: heat flux, W/m^2
- r_f: fuel regression rate, m/s
- $\dot{s}_t$: throat erosion rate, m/s
- R: radius, m or orbit object rank
- Re: Reynolds number
- R°: universal gas constant, 8.3144 $J/(mol \cdot K)$
- S_j°: molar standard-state entropy for species j, $J/kmole$
- S_p: scaling parameter as a function of temperature
- St: Stanton number, $Nu/(Pr \cdot Re)$
- T: temperature, K
- T_F: thrust, N
- t: time, s or thickness, m

- u: axial velocity, m/s
- v: generic velocity, m/s
- V: volume, m^3
- w: molecular weight, $kg/kmol$ or atomic weight, $kg/kg\text{-}atom$
- W: weight, N
- x: axial location, m or number of carbon atoms
- y: number of hydrogen atoms
- Y: mass fraction

Greek Letters

- α: absorptivity
- α_{conv}: convergent semi-aperture angle
- α_{div}: divergent semi-aperture angle
- β: parameter for numerical flux calculation
- γ: specific heat ratio
- γ_s: isentropic exponent
- δ: phase lag between stress and strain, rad
- ϵ_{noz}: nozzle expansion area-ratio
- ϵ_x: discretization function parameter
- ε: emissivity or strain, m
- ζ: surface roughness, μm
- η: performance multidimensional losses or efficiency coefficient
- κ: gas thermal conductivity and MUSCL accuracy parameter
- λ: Lagrangian multiplier
- μ: gas viscosity, $N \cdot s/m^2$
- ν_j: chemical potential of species j, $J/kmole$
- ξ: mixture fraction
- ρ: density, kg/m^3

- ρ_f: fuel density, kg/m^3
- σ: Stefan-Boltzman constant or stress, Pa
- ϕ_{corr}: performance correction factor
- Φ: equivalence ratio, F/O
- ψ_{p_c}: pressure factor
- ψ_{eta_c}: combustion efficiency factor
- ψ_{wrad}: wall radiation factor
- Ω: right ascension of ascending node, deg

Subscripts

- a: ambient conditions
- b: burn
- c: convective and combustion chamber
- cc: catastrophic collision
- C: carbon
- $cata$: catalyst
- $cbed$: catalytic bed
- DB: debris
- dc: decay
- e: boundary layer edge and nozzle outlet section
- eff: effective
- f: fuel
- fl: flame
- H: hydrogen
- $h-p$: head-plate
- i: initial or chemical species index
- j: index of chemical species
- k: index of chemical element

- L: left side
- L, noz: nozzle length
- m: max speed of sound
- mix: gas mixture
- noz: nozzle
- p: propellant or port
- pipe: feed pipes
- pres: pressurant
- o: no blowing presence
- O: oxygen
- ox: oxidizer
- rad: radiant
- ref: reference
- R: right side
- RCS: RCS system
- s: isentropic or specific or soot
- spl: splitting
- str: structural
- t: throat
- tank: tank
- tot: total
- tu: tensile ultimate
- v: volumetric
- z: general index
- w: wall
- 0: total reactants, zeroth iteration
- 1/2: interface

Superscripts

- bray: Bray approximation correction
- buta: butadiene correction
- ideal: ideal state or performance
- corr: corrected performance
- real: real performance
- wet: propellant loaded configuration
- dry: no-propellant-loaded configuration
- 90%: 90% of HTP concentration
- 98%: 98% of HTP concentration
- ○: standard state or assigned condition

ACRONYMS

ADR	Active Debris Removal
AUSM	Advection Upwind Splitting Method
AUSMDV	Advection Upwind Splitting Method flux-Difference-Vector-splitting
cc	combustion chamber
CEA	Chemical Equilibrium for Applications
CFL	Courant-Friedrichs-Lewy
CIS	Commonwealth of Independent States
CSSI	Center for Space Standards & Innovation
CTRZ	Central Toroidal Recirculation Zone
DeoKit	De-orbiting Kit
DMA	Dynamic Mechanical Analyzer
EDMSWG	European Debris Mitigation Standards Working Group
EDT	Electrodynamic Tether
EEW	Electrical Explosion of Wire
EPDM	Ethylene Propylene Dimethyl Monomer
FPA	Flight Path Angle
GOX	Gaseous Oxygen
GEO	Geostationary Earth Orbit
GNSS	Global Navigation Satellite System
JSpOC	Joint Space Operation Center
HDPE	High Density Polyethylene
HPM	Hybrid Propulsion Module
HRE	Hybrid Rocket Engine
HRMs	Hybrid Rocket Motors
HTP	High Tested Peroxide
HTPB	Hydroxyl-Terminated Polybutadiene

IADC	Inter-Agency Space Debris Coordination Committee
ISS	International Space Station
LEO	Low Earth Orbit
LOX	Liquid Oxygen
LRMs	Liquid Rocket Motors
LT	Low Melting Temperature Thermoplastic
MEO	Middle Earth Orbit
MMH	Monomethyl-hydrazine
MTT	Momentum Transfer Tether
MUSCL	Monotone Upstream-centered Schemes for Conservation Laws
PB	Polybutadiene
PE	Polyethylene
PIV	Particle Image Velocimetry
PMD	Post Mission Disposal
PMM	Polymethylmethacrylate
PP	Polypropylene
Q1D	Quasi-One-Dimensional
RCS	Reaction Control System
R/Bs	Rocket Bodies
S/C	Spacecraft
SSN	U.S. Space Surveillance Network
SSO	Sun-Syncronous Orbit
SRMs	Solid Rocket Motors
TRL	Technology Readiness Level
UDMH	Unsymmetrical dimethyl-hydrazine
VFP	Vortex Flow Pancake

1 INTRODUCTION

Nowadays, the near-Earth orbit space, especially the Low Earth Orbit (LEO), is affected by the presence of a significantly amount of orbital debris, whose number is in constant growth [1, 2]. All of them are the byproduct human space activities during the last 40 years. In a so crowded environment, the probability of catastrophic collisions between large abandoned objects, Spacecraft (S/C) and Rocket Bodies (R/Bs), is not negligible and, when it happens, the number of new orbital fragments drastically grows, becoming always more a menace for operative satellites and for the International Space Station (ISS). In order to keep under control the debris environment, an international committee, Inter-Agency Space Debris Coordination Committee (IADC), was established to facilitate the information exchange between space agencies, promoting cooperation on space debris research activities [3]. In recent years, some guidelines were defined to limit the generation of new debris by new space launches and satellite activities. However, long-term simulations [2, 4] suggest that without the direct removal from orbital space of large abandoned objects the probability of catastrophic collisions will significantly grow in the next future, increasing the risk of "Kessler Syndrome" outbreak [5], a collisional cascade able to hamper all the future human activity in LEO.

Nevertheless, among the international community there are some doubts about the active debris removal, concerning the high costs of both the technological development and Active Debris Removal (ADR) mission, as well as the implications of the near-Earth space management by the different nations. First of all, great cost is the main obstacle to active removal implementation. As the launch of a new satellite is characterized by a certain cost level, the amount for an ADR mission would be equal or larger, for something which will not produce any direct gain, in term of research or business, to the mission owner, both private and governmental; rather the effective advantage of ADR would be perceived by the entire space community only in a long-term scenario. At this early stage, it is not so easy to understand the correct cost entity and its evolution in the next future. In fact, many technologies proposed for active removal present a low Technology Readiness Level (TRL), especially concerning the capture of non-cooperative objects. In such situation, a significant contribute could be provided by a demonstrative ADR mission, realized in the frame of an international cooperation, which might define a standard solution able to drive the future development of different, and even more complex, missions for active removal of large abandoned objects [6]. A recent study [7], performed by DLR (German Space Agency), deals with a preliminary estimate of the cumulative ADR costs in the next 200 years. Three cost models are considered: hardware costs, launch costs and operational costs. The latter include even the personnel costs for an estimate duration of

the ADR mission. The hardware costs include the de-orbiting kit components and the propulsion system, whose cost amount is related to the required velocity increment ΔV for the reentry maneuver. An average value of 140 million of dollars (U.S. dollar of fiscal year 2012) for the removal mission of one object is estimated [7]. The DLR's costs predictions, highlight that, in a long-term perspective, the removal of 5 large objects per year will be theoretically cheaper than the application of just mitigation measures (90% PMD), the latter characterized by higher long-term damage costs due to catastrophic collisions. Nevertheless, a so high economic expense could not be sustained permanently and just the removal of a fixed number of high priority abandoned objects would be largely preferred, as long as all the new S/C and R/Bs will be equipped with devices for maneuver capability and post mission disposal [7].

The implementation of this complex project needs the effort of each nation, endowed with space access, in a world wide agreement in the management of future debris environment, especially in LEO. In fact, there is not a clear regulation about consequences and liability in case of damage provoked by space debris; the Convention on International Liability for Damage Caused by Space Objects, ratified in 1972, does not provide any guideline for space debris problem, as well as for their definition in a global unique manner [6]. Currently, only the owner of an intact object can proceed with its removal from orbit, otherwise he should give his permission to a private customer or governmental space agency. Even more, the ADR technology could be used for military or non-peaceful purpose, firing up the global doubts on its effective implementation [6]. Therefore, active debris removal is a strong challenge, not only concerning the technology development and realization costs, but even for the political issues related to the equilibrium between the most powerful nations. In the near future, a global international cooperation could overcome the current situation and, meanwhile, the research activity should find a technological solution for the active removal of large abandoned objects.

In recent years, several concept solutions were proposed for ADR; the research activity about this topic yearly grows with the design of new technological approaches, especially for what concern the de-tumbling and the capture of a non-cooperative object. The latter, actually, is the greatest technological challenge imposed by ADR. With regards to the object final disposal there is a quite large agreement about a de-orbiting with controlled atmospheric reentry, driving the target toward a uninhabited region (South Pacific or Atlantic Oceans) [8, 3, 9]. Such kind of mission can be easily performed by means of chemical propulsion systems, since the use of other approaches, such ad tethers, drag augmentation systems or electric propulsion is more suitable for a slow target disposal on a decay orbit of 25 years of lifetime. On the contrary, a chemical propulsion unit, if attached to the abandoned object, is able to provide a fast and more safe de-orbiting, allowing for the selection of the impact location and fragments footprint. Within the group of chemical systems, hybrid propulsion seems to be a very promising solution. The use of a Hybrid Propulsion Module (HPM) for Active Debris Removal (ADR) was first proposed in the frame of a cooperation work between six italian institutions: *Politecnico di Milano*, *University of Naples "Federico II"*,

Institute of Science and Technology of the Information (ISTI/CNR), *University of Naples "Parthenope"*, *University of Padua* and *Politecnico di Torino*. The group was assembled and coordinated by Politecnico di Milano [10]. Hybrid rocket technology exhibits several characteristics very suitable for this kind of missions, especially for the possibility of cost reduction with respect to conventional bi-propellant liquid rockets.

This work aims to evaluate the hybrid technology as possible propulsion solution for in-space operations related to the active removal of large abandoned objects. The implementing of active removal systems represent a great challenge and the development of new and cheap technologies is required. Hybrid propulsion, despite its low TRL, offers several interesting advantages in this field. The preliminary design of hybrid propulsion motors for active debris removal missions is carried out. For this purpose a design tool for internal ballistics analysis and performance evaluation was implemented following the same approach used by Funami and Shimada [11, 12] and considering a specific propellant combination. The oxidizer and fuel selection has an important impact on the overall mission and engine configuration. In this respect, an aging study about Hydroxyl-Terminated Polybutadiene (HTPB) was performed, with the aims to evaluate its possible use for long-time space missions, especially in the case of small hybrid motors equipped on new satellites for Post Mission Disposal (PMD) operations. Moreover, since hybrid combustion is characterized by low fuel regression rates, the possibility of its enhancement with HTPB-based fuel was investigated at laboratory scale level by means of non-conventional oxidizer injection and addition of metal additives to the solid fuel.

Plan of Presentation

The work is presented according to the following scheme:

- Chapter 2: an introduction to the space debris problem, debris growth rate, long-term debris environment simulations, targets selection and proposed technology solutions.
- Chapter 3: hybrid propulsion applied to active debris removal, technology development and state of the art, propellant selection, ADR mission concept and requirements.
- Chapter 4: fundamentals of hybrid rocket combustion, state of the art of research and advanced solutions for regression rate enhancement.
- Chapter 5: experimental study on the internal ballistics of a lab-scale hybrid burner and HTPB aging with DMA analysis.
- Chapter 6: numerical study based on the development of a HRE code for overall internal ballistics analysis.
- Chapter 7: implementation of a performance evaluation tool within the HRE code.

- Chapter 8: preliminary design of HPMs for active removal of two selected targets.
- Chapter 9: conclusions with some suggestions for future works and code implementations.

2 SPACE DEBRIS REMOVAL

2.1 OVERVIEW ON SPACE DEBRIS PROBLEM

2.1.1 Space Debris Growth Rate

From the beginning of the *space run*, the human society concentrated a significant effort in the development of satellites for various activities, such as telecommunications, military surveillance, as well as research on both Earth and space environment. However, after fifty years of space activity a a great number of debris have been left behind. In Figure 1, one can see the annual growth of the orbital objects, catalogued by U.S. Space Surveillance Network (SSN), through January 2012 [1, 2]; the total amount is dominated by fragmentation debris. A significant contribute is due to the explosion of upper-stage rockets after the completion of their mission. This tendency was reduced after 1980s, when new approaches in propulsion design avoided their typical final outbreaks [13].

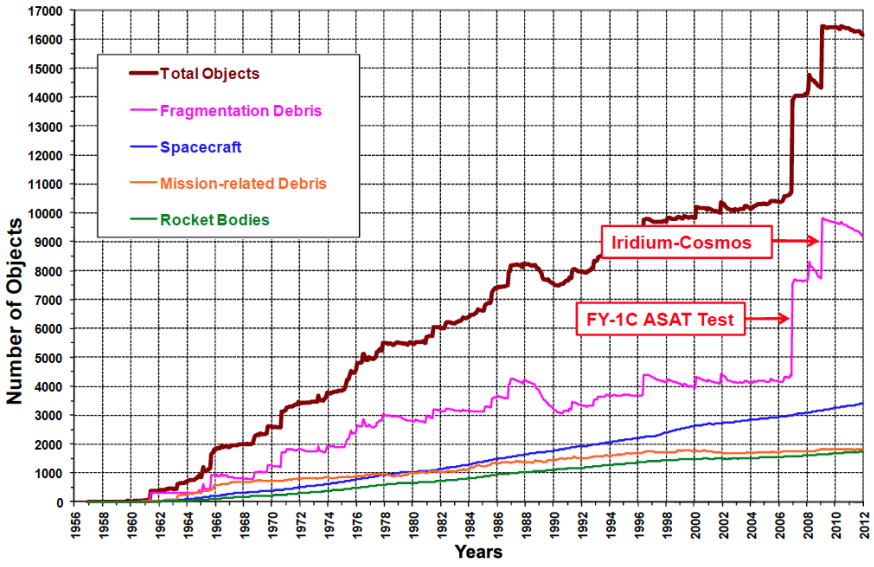

Figure 1.: Historical SSN cataloged objects growth through January 2012 [2].

The two big jumps visible in Figure 1 correspond to the Fengyun-1C destruction due to an anti-satellite test, performed by China in 2007, and the unexpected accidental collision between Cosmos-2251 (Russian military satellite) and Iridium-33 (U.S. communication satellite) in 2009. While the Iridium was still operational at the time of the incident, the Cosmos was out of service from 1995, being an abandoned ob-

ject. The two catastrophic events generated a significant large amount of fragmented debris, more than 1500 for Cosmos-Iridium and up to 3000 for Fengyun-1C, still in orbit [13, 14]. Because of this, the orbital environment below 1000 km of altitude was strongly altered, since the number of fragments raised of about 117% [4]. In 2013, January 22, according to Center for Space Standards & Innovation (CSSI), a small Russian satellite (BLITS) collided with an orbital fragment produced by Fengyun-1C destruction [15]. As of 14 May 2013, around 16,952 objects were catalogued, of which about 11,249 are fragmented debris [2, 14, 16]; only 1050 are operational satellites and approximately 4650 are intact abandoned objects in the circumterrestrial space; among the abandoned group, 2688 are S/C while 1965 are R/Bs [16, 17]. The fragmented group is referred to orbital debris with a minimum size of 10 cm, but additional data provided by more precise radars have shown approximately a total amount of 500,000 pieces of 1 cm size, while a population of hundreds millions is estimated for debris of 1-mm level [1, 14]. The highest debris density is registered in LEO, below 2000 km, where 1939 S/C and 813 R/Bs are present. In this altitude range, just 502 spacecraft are operative, hence about 2250 are abandoned [16, 17]. In term of mass, a relatively steady increase from the beginning of space age [2, 1, 4] of about 145 metric tons per year was estimated [14]. As of 14 May 2013, the total mass in orbit is about 6670 metric tons, ISS included (420 metric tons). This large amount is dominated by spacecraft (53.3%) and rocket bodies (42.5%), while just 2.5% corresponds to mission related objects and 1.7% to orbital fragments [16, 1, 17, 4]. Focusing on LEO, the total mass is approximately 2650 metric tons (ISS excluded) and the 97% of which is concentrated in S/C and R/Bs [16, 17, 4]. Overall, the average spacecraft mass is 950 kg, if the ISS is included, otherwise results about 838 kg, while an average mass of 1442 kg is for rocket bodies. The average mass of intact S/C and R/Bs in LEO is 934 kg (ISS excluded); the latter raises to 1046 kg for the overall abandoned objects. The 89.5% of catalogued objects are due to the space activity of Commonwealth of Independent States (CIS) (URSS,Ukraine, Russia), United States and China, with respectively 37.4%, 29.7% and 22.4%. Therefore, the near-Earth space environment is characterized by a complex orbital situation, which produces considerable consequences on the actual and future space activities of human society. The so large number of orbital fragments involves the risk of collision for operational spacecraft, with possibility of mission failure, as well as for the abandoned intact objects, that represent possible sources of new debris. Every day about 30 conjunction warnings for operational spacecrafts are issued by the U.S. department of Defense's Joint Space Operation Center (JSpOC) [1]. According to these alert notifications, in 2010 over 100 collision avoidance maneuvers were executed by the satellite operators to reduce the impact probability with the catalogued objects. Even the ISS, between 1999 and 2011, had to perform 13 avoidance maneuvers [1] and this allows to understand the hazard level connected to the space debris and their constant growing. When a collision is predicted for two abandoned objects, with no propulsion or communication abilities, it will become a source of new debris of different sizes, as happened for Cosmos-Iridium crash. The random collision between catalogued debris, together with the generation of new fragments, could evolve into a collisional cascade, known as "Kessler Syndrome" [5], which consists in

the exponential growing of orbital debris [13]. This concept was introduced for the first time in 1978 by D. J. Kessler and G. Cour-Palais [13]; they analyzed the processes involved in the generation of asteroid belts around planets making a parallel with the debris population around the Earth, concluding that the collisional breakup of orbital objects would become a significant new source of debris in the near future (around year 2000) [13]. Nevertheless, in more recent studies, Kessler little doubts that the "Kessler Syndrome" (so-called by J. Gobbard from NORAD [5]) will quickly become the principal source of new small debris, since the trend observed from 1978 till now is less steep than initially predicted and new operational procedures have little slowed the orbital fragment growing [5, 4]. Despite this, although later than predicted by Kessler, random collisions will gradually go to control the orbital debris environment in the next future [1, 2, 4, 5, 18].

In any case, the growth of space debris is still far to be stabilized or stopped [1, 4, 19, 18, 20] and already now all the space activities are influenced by such orbital environment. In fact, the new spacecraft have to add protection shields, increasing the cost of the satellite as well as of the launch, due to the increase of payload mass. For example, some modules of the ISS are equipped with protections able to sustain impacts with debris below 14 mm, while typical spacecraft can be significantly damaged by fragments of 5 mm size, because of their hypervelocity [1, 4]. The active collision avoidance must be improved by the optimization of tracking and position prediction, being useful when the involved spacecraft has maneuvering capability. Moreover, in order to avoid collisions during the orbit injection of new satellites, according to JSpOC warnings, the countdown "holds" before the launch could increase, involving significant greater operational costs [14].

2.1.2 Long-Term Predictions

In order to understand the possible future evolutions of the circumterrestrial orbital environment, in terms of debris population growth, long-term prediction models have been developed [21, 22, 23, 24, 25, 26]. Among these, the Critical Density Model [24] defined by Kessler, was based on the balance between fragments production (source) and debris natural removal by the atmospheric drag (sink), applied to the orbital environment of year 1999. The results of this study highlight that, for a defined altitude, the fragments population depends only on the amount of intact objects and a practical limit exists in their number in-orbit to prevent the increase of small debris population. The most critical situations were identified between 600 and 1700 km (LEO range) where the number of S/C and R/Bs is well above a defined unstable threshold [4, 13, 24]. The most advanced model for long-term debris environment study is LEGEND, developed at the NASA Orbital Debris Program Office by Liou [26, 27]. This program consists of a three-dimensional model for long-term orbital debris evolution analysis. Several hundreds of years can be simulated, considering objects with a minimum size of 10 cm (catalogued by SSN). A Monte Carlo approach together with a pair-wise collision probability evaluation algorithm are used to predict

future collision activities (each run predicts a different future situation). The LEGEND accounts for atmospheric drag and solar flux models as well as orbital propagators for altitude ranges up to 40,000 km. Moreover, for the fragments simulation after a collision, the NASA Standard Satellite Breakup Model [28], based on well-observed explosions in orbit and laboratory experiments, is assumed [26, 27]. For purpose of evolutionary simulations, the collisions are classified in two main groups [5]:

- *Non-catastrophic*: collision between an intact object and a fragment with a generation of debris of about 100 times the mass of the fragment. This situation can contribute to the short-term environment, since just few fragments will be larger enough to be tracked, and to the hazard of operational spacecraft.
- *Catastrophic*: this is the worst case in which small and large fragments are generated, going to have both short-term and long-term effects. The largest debris produced can be the cause of new catastrophic impacts with other intact abandoned objects, thus promoting a cascading effect on the long-term.

A further case is defined: *negligible non-catastrophic*, which is represented by the collision between a very small fragment and an intact object, resulting in a negligible debris generation, theoretically unable to affect both the short-term and long-term environment [5]. By means of the NASA Breakup Model [28], LEGEND predicts that the majority of collisions between catalogued objects will be *non-catastrophic* (55%) and only the 45% will be *catastrophic*.

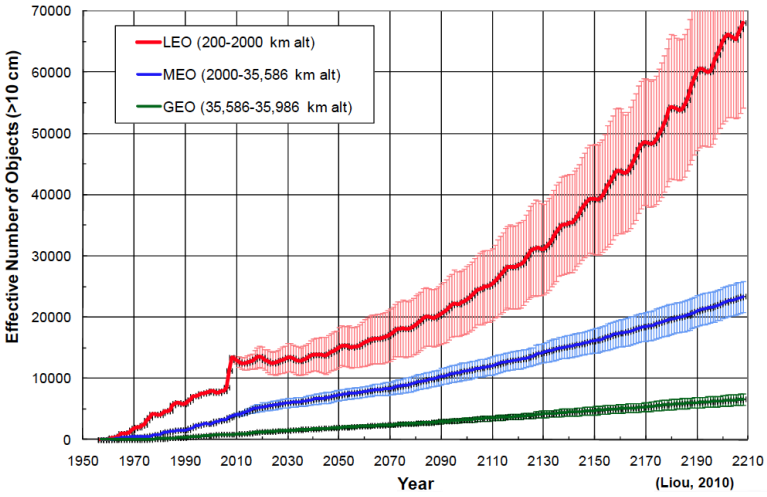

Figure 2.: Orbital debris number future projection with regular launches and no mitigation. Each curve is the average of 100 runs with LEGEND [4].

In Figure 2, one can see the near-Earth debris environment evolution simulated with LEGEND, by assuming regular launch activity and non-mitigation for the next 200 years. The three curves are referred to different orbital ranges: Low Earth Orbit (LEO), Geostationary Earth Orbit (GEO), between 35,586 and 35,986 km of altitude, and Middle Earth Orbit (MEO), that is the region between LEO and GEO. Each curve

represents the average value of 100 Monte Carlo simulations, with the corresponding 1-σ error bars [1, 2, 4, 24]. These results describes the worst possible scenario (under the assumption made), in which the number of debris in LEO are characterized by a steep non-linear increase. This prediction agrees with the one performed by the Critical Density Model [24], for what concern the overcoming of the unstable threshold of the current orbital situation in LEO [5]. On the contrary, the evolution trend in MEO and GEO appears relatively moderate, on the simulated time interval, characterized only by few accidental collisions. Therefore, the attention and the action priority is focused on the LEO range, the most used and most populated for a great number of human activities. Even if all launches were stopped from year 2006, the collisions would not stop, going to raise up in any case the number of debris larger than 10 cm, although with a much lower rate of grow [1, 2, 4]. These results suggest that the debris population in LEO has already reached an unstable condition which, even in the best scenario, will increase the effective number of orbital fragments below 2000 km. Ascertained the current orbital situation, a direct action seems to be strongly required. The Inter-Agency Space Debris Coordination Committee (IADC) was established for the worldwide coordination of all activities related to the presence of space debris in LEO environment. The task of this committee is to facilitate the information exchange between space agencies, promoting cooperation on space debris research activities [3]. In 2009 an official program called *Stability of the Future LEO Environment* was started to improve the studies and the data comparisons in the research community [2]. Over the years two different approaches were defined: mitigation and remediation, both characterized by advantages and disadvantages, but, as asserted by many researchers, both necessary for the future stabilization of the debris growth in LEO.

2.1.3 Mitigation and Remediation scenario

The solutions applied or suggested for the reduction the space debris growth rate can be divided in two groups [14]:

- *Mitigation*: this approach aims to reduce the generation of new debris, by combining different measures, such as new S/C design and manufacture processes, R/Bs passivation at the end of mission, that is the emptying of the residual propellant, and Post Mission Disposal (PMD) strategies.
- *Remediation*: this is a concept method that aims to remove large abandoned intact object, characterized by high risk of collision, from LEO. This solution requires the definition of a complex and specific mission type, never attempted since the beginning of the space run.

From the beginning of 1990s, the enhanced sensitivity to the space debris problem and the results achieved by the earlier prediction models, promoted the voluntary adoption of mitigation measures by single space agencies [29]. However, the main effort toward mitigation solutions was made in the frame of IADC and in 2002 the first version of a space debris mitigation guidelines was approved by IADC Steering Group

[3, 30]. In 2004, this set of guidelines was included into the code of conduct defined for space debris mitigation by the European Debris Mitigation Standards Working Group (EDMSWG) [3, 31]. Then, in 2008, the United Nations promoted a set of mitigation guidelines mainly derived from the IADC work [3, 32]. The mitigation guidelines propose several approaches to reduce or totally cancel the production of new debris during space missions. For example, more resistant materials to space environment and protection shields against small hypervelocity fragments could save the spacecraft from critical damages, able to create new fragments or lose the control of the satellite; little changes in the operational procedures to limit the production of debris larger than 1 mm during the flight mission for the in-orbit injection of new payloads [14]; new spacecraft must be equipped with propulsion systems [33] for avoidance maneuvers according to space surveillance, so increasing the overall collision avoidance capability. However, the most effective proposed measure is the post mission disposal, after the mission completion of the S/C or R/B [14, 29, 30, 31, 32]:

- the object must be transferred to a protected region on a decay orbit of 25 year lifetime;
- if possible the object must be directly de-orbit with a controlled reentry or re-orbit above 2000 km altitude;
- geosynchronous objects must be re-orbit to a long-term graveyard orbit with a minimum altitude of 200 km more than GEO;
- Global Navigation Satellite System (GNSS) satellites in MEO must be removed from their constellation altitude and place in a graveyard region which does not interfere with other constellations.

The post mission disposal, as well as the collision avoidance, requires the installation of a propulsion device on the spacecraft, in order to lower its orbit, or re-orbit, to a graveyard protected region. It is easy to gather that any of these mitigation measures involves an increase of costs on the overall space mission. For this reason, not all space agencies or private customers are always inclined to apply these solutions. In Figure 3, one can see the long-term simulation in LEO, performed by LEGEND [26, 27], based on different level of PMD application (25-years rule [29]). The red curve is the same of Figure 2, representing the case of non-mitigation while the green one refers to a case in which the 95% of new space missions follows the mitigation guidelines by performing the suggested PMD after the mission completion [2]. These results suggest that a massive implementation of mitigation measures would significantly reduce the growth rate of orbital debris over the next 200 years. Nevertheless, being the current environment already above the critical density [13, 4, 24], the increase of space fragments could not be stopped, going on to represent an hazard for future space missions and human activities in LEO. Even by exploiting the maximum collision avoidance capability together with the 90% of successful PMD is not possible to contrast the growth of debris environment; in fact, despite the 80% of the active

spacecraft in LEO have maneuver capability, their total mass is just the 9% on the mass in LEO [4].

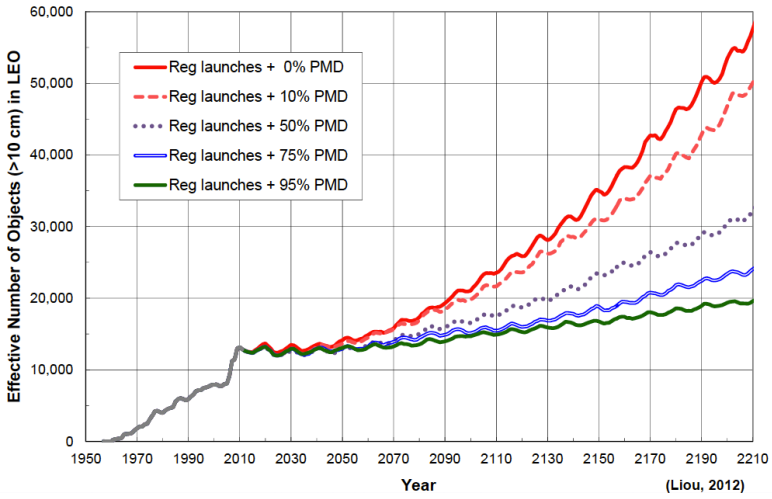

Figure 3.: Orbital debris number in LEO, future projection with different levels of applied PMD [2].

Different future scenario were tested by several long-term evolution models providing similar results [2], therefore the space debris community agrees on the conclusion that the only application of mitigation measures would not be sufficient to prevent the increase of debris environment, precluding the use of LEO region for future applications [1, 2, 13, 4, 16, 17, 24, 25, 3].

In the light of these considerations, the international community is discussing the possibility and the feasibility of the remediation approaches, that is the active removal of existing debris, in particular the abandoned intact objects, that, more than others, in case of collision, represent a potential source of new space debris. Spacecraft and rocket bodies in LEO environment are mainly distributed between 600 and 1000 km altitudes and high orbit inclinations ($> 65°$). At this altitude their lifetime on orbit is very high, even more than hundreds years. Debris at altitudes below 600 km do not represent a high risk since their lifetime is significantly small due to the stronger effect of atmospheric drag. Recently, Liou performed some long-term simulations, by means of LEGEND, considering future scenario in which both mitigation and remediation are applied [1, 2, 4, 13]. He assumed an active removal of 2 or 5 objects per year, beginning from year 2020. Nevertheless, this assumption was too optimistic since the space community would not be ready for such kind of effort, due to the complexity and high cost of ADR. Hence, a more realistic assumption considers the beginning of remediation activity in 2060 and in Figure 4 the predicted evolution of LEO environment with a yearly removal of 5 objects, as well as regular launch activity, is presented. Each curve is the average value of 50 LEGEND Monte Carlo runs. In term of mass, the removal of five large objects per year means to extract from LEO an average mass of 6.8 tons every year [4].

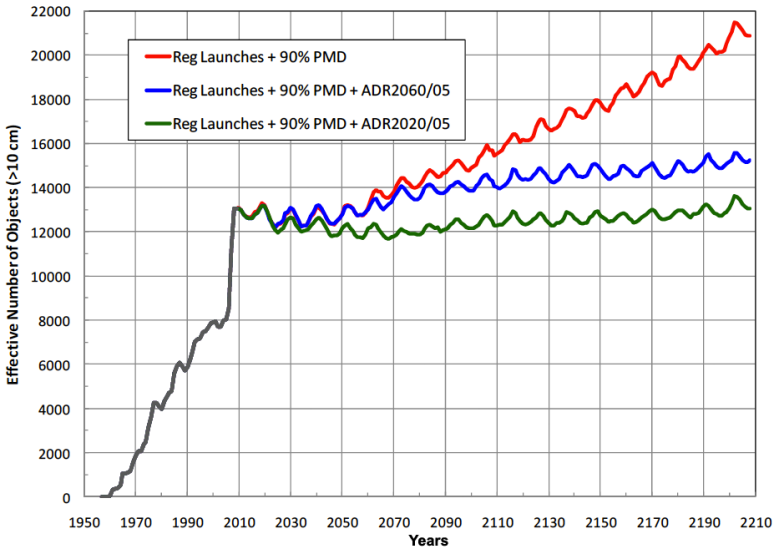

Figure 4.: Orbital debris number in LEO, future projection with 90% PMD and 5 large intact objects yearly removed since years 2060 and 2020 [4]. Average curves obtained with 50 LEGEND Monte Carlo runs.

The results in Figure 4 show that the active removal of 5 abandoned S/C or R/Bs could be able to stabilize the increase of debris in the next 200 years; the best scenario would require the begin of ADR missions in 2020, but this option is quite far to be realistic. According to Liou's simulations the implementation of ADR will reduce the average number of catastrophic collisions predicted in the next future, in fact, in the worst case (no PMD, no ADR) about 47 collisions are expected, while in the other cases, presented in Figure 4, this number decreases to 32 for ADR begun in 2060 and 25 for ADR begun in 2020 [1, 4]. In conclusion, the results of long-term simulations on the evolution of debris number in LEO environment provide a quite dramatic situation for the near future. Mitigation measures can be applied, obtaining an important and positive effect on the reduction of debris growth rate. However, even a 90% of effective mitigation won't be sufficient to stop the fragments generation due to collisions between on-orbit objects and the need of active removal of at least 5 large intact objects per year seems to be the only way for the future stabilization of space debris growth [1, 2, 13, 14, 4, 17, 3].

2.1.4 Large Abandoned Objects Ranking

The remediation approach, to be effective and really useful, must focus the attention on abandoned objects characterized by highest collision probabilities. Moreover, as much large is the object as great is the potential amount of fragments that it can

produce in case of collision. In the perspective of ADR, these types of targets can be ranked as

$$R \propto P_{cc} \times M^{0.75} \tag{2.1}$$

where P_{cc} is the probability of catastrophic collision while M is the sum of the target mass and impacting debris mass. However, since the mass of the latter is averagely of 3 orders of magnitude slower [16], the value of M is very close to the mass of the considered target. The power exponent, in accordance with NASA Standard Breakup Model, reproduces the trend of the cumulative number of fragments, larger than a defined characteristic length L, due to a catastrophic collision [28, 16]. The probability of catastrophic collision, which is $P_{cc} << 1$, is proportional to the average flux F_{DB} of debris leading to catastrophic breakup and after few mathematical passages [16], the rank can be expressed as

$$R \propto F_{DB}(h_{dc}, i, M)\ M^{1.75} \tag{2.2}$$

where the flux F_{DB}, for quasi-circular orbits in LEO, is a function of the slowly decaying mean altitude h_{dc} and of orbit inclination i, as well as the mass M. The rank R, according with 2.2, significantly depends on the target mass, due to the high power exponent. From the point of view of long-term debris evolution, this result means that the removal of a large massive object in a densely populated LEO region is more advantageous than the removal of abandoned objects with average mass values (~ 900 kg).

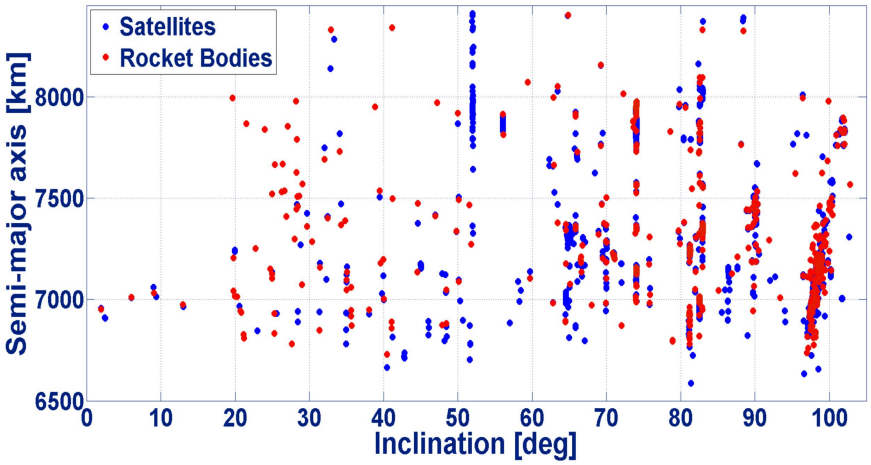

Figure 5.: Distribution of intact S/Cs and R/Bs in LEO as a function of semi-major axis and inclination [17]. The Earth equatorial radius is about 6378 km.

In Figure 5, one can see the distribution of intact objects in LEO as a function of semi-major axis and inclination. In recent years, about the 20% of new launches are headed to Sun-Syncronous Orbit (SSO) [16], with an orbital inclination of about 98°, see Figure 5. Considering this inclination band and the same mean altitude the Eq. 2.2, accordingly with ESA's MASTER-2009 model [16, 34], allows to understand that

the removal of one abandoned object with a mass of 9000 kg is equivalent to the removal of about 30 smaller average-mass targets [16]. The available informations, collected in [16], highlight the presence of 25 abandoned objects having masses larger than 4000 kg, orbiting on quasi-circular orbits altitudes between 700 and 1100 km. They represent about the 10% of mass in LEO (ISS exclude) but approximately the 1.1% of S/C and R/Bs. These objects are described in Table 1 and only one of them is a spacecraft: Envisat, lost by ESA on 8 April 2012 for a critical failure [16, 35]. The latter, two Zenit second stages (Russian) and four CZ-2C second stages (Chinese) occupy SSOs, while eighteen Zenit second stages orbit the Earth with an approximately inclination of 71°. All these targets are characterized by a very high lifetime, above 100 years. Since each of them represents a significant source of new fragments, in case of collision, their rank R results very high, classifying them as the best candidates for active removal in LEO. In fact, in case of catastrophic impact, up to about 4700 new fragments larger than 10 cm could be generated, as estimated in [16]. In Table 1 the characteristics of this group of target are described.

Object	**No.**	**Dry Mass [kg]**	**Mean Altitude [km]**	**Inclination [deg]**	**Mass of Critical Impactor [kg]**	**Removal Relative Ranking**
CZ-2C 2^{nd} stg	3	4000	727-827	98.1-98.3	1.6	5.6
CZ-2C 2^{nd} stg	1	6000	817	98.3	2.5	10.4
Envisat	1	7800	767	98.4	2.8	24.6
Zenit 2^{nd} stg	18	8900	829-851	71.0	3.6	17.6
Zenit 2^{nd} stg	2	8900	808-996	98.3-99.1	3.6	16.5

Table 1.: Largest S/C and R/Bs in LEO between 700-1100 km altitudes and relative ranking for ADR in comparison with average-target of 934 kg (R = 1) placed in the same Envisat's orbit [16].

The mass of critical impactor, shown in Table 1, is the minimum fragment mass required to fully destroy the considered intact object. Descriptions about the critical mass estimation are provided in [16, 36]. The data and analysis described suggest that the existence on orbit of such large abandoned objects represents a very high hazard concerning the potential increase of debris environment. In fact, it was estimated [16] that a catastrophic destruction of a Zenit stage or Envisat would be able to increase the number of debris larger than 10 cm in LEO of 40%, especially in the region below 1000 km, currently densely populated by both active and abandoned S/C and R/Bs. In particular, Envisat has a ranking nearly equal to the removal of 25 average-targets with similar orbit, being the highest priority large abandoned object.

Besides the highest priority group, a great number of smaller S/C and R/Bs are present in LEO. Most of these are abandoned upper stages, such as the Cosmos-3M second stage, having a mass of about 1400 kg, diameter of 2.4 m and a length of 6.5 m. Approximately 300 R/Bs of this type are still on orbit, mainly concentrated in four altitude-inclination bands [17, 3]: 850-1050 km - $i = 83°$, 900-1050 km - $i = 66°$, 900-1000 km - $i = 74°$, 650-850 km - $i = 74°$. Despite their lower priority ranking,

Cosmos-3M 2nd stages represent an interesting candidate for ADR missions; in fact, for any given inclination an average number of about two objects would be found in each 5° bin of right ascension of the ascending node Ω, showing more favorable concentrations around specific orbit planes [17]. Such distribution would favor multiple rendezvous with a single mission, involving a lower propellant consumption for the ADR system. Moreover, these stages could be captured by using the same technology and procedure and the reentry risk assessment. In fact, the fragmentation analysis for a disposal with atmospheric reentry should be performed just for one object-type, resulting representative of the entire class. Therefore, due to their high number and orbital distribution, the Cosmos-3M second stage seems to be a very good candidate for demonstrative missions and multiple removals with a single launch. R/Bs theoretically appear more easy targets than S/C and, considering the challenge represented by active removal, they could be selected for the practical development of procedures, technologies and on-orbit tests.

2.2 ACTIVE DEBRIS REMOVAL

2.2.1 ADR Mission Concept

The yearly removal of at least five large objects from LEO is considered a significant challenge for actual technology level. An ADR mission is strongly multidisciplinary and all aspects must be deeply investigated, since some of them have never been applied. Several studies were carried out in recent years, promoted by international space community, with the aim to define and analyze possible ADR scenario [1, 16, 17, 3, 8, 9, 37, 38, 39, 40, 41, 42, 43, 44]. Nowadays, it does not exist a standard approach, because of the presence of different target typologies located in correspondence of several altitudes and inclinations. Overall, the ADR mission envisages a far-rendezvous phase, during which the ADR vehicle intercepts the target, followed by a close-rendezvous phase used for the near approach necessary to allow close-proximity operations, such as a fly-around for debris inspection and then its capture. The target capture is the most critical point, since it has been never verified the docking possibility with a large non-cooperative object [16, 8, 9]. Once the target is captured, the final step consists in the debris disposal. Different solutions were proposed:

- the perigee of the target's orbit is decreased enough to allow the natural atmospheric reentry in max 25 years (25-years rule);
- controlled atmospheric reentry, by driving the target toward a non-inhabited region (South Pacific or Atlantic Ocean). It can be performed by one or multiple burns by means of a dedicated propulsion device;
- transfer of the target to an higher orbit, outside the LEO region.

Among them, the 25-years rule does not allow any safe direct control of the impact footprint during the reentry phase, as well as the impact location could remain

unknown, representing a potential hazard for inhabited regions if large target are involved. On the contrary, the controlled reentry, being more safe due to the control of impact footprint and location, provides a fast disposal, significantly reducing the possibility of collision which affects the target transfer on a long-term decay orbit. Therefore, a controlled reentry approach is preferred [16, 17, 8]. Depending of the solutions selected for an ADR mission, such as the the removal of one or multiple objects, the ADR vehicle can be conceived in different ways:

- single vehicle able to perform the rendezvous, the capture and the removal of one target [16];
- a mother ship vehicle able to carry multiple de-orbiting kits. Each kit can be released on target's orbit plane and it performs the rendezvous, the capture and the disposal [8]; otherwise the mother ship performs the rendezvous with the target and its capture, then a de-orbiting kit is attached to the captured object [17, 3, 9];
- a family of single de-orbiting kits carried out by the space launcher upper stage, as primary or secondary payload, and released by the latter on the orbital plane of the selected targets.

The design and development of the ADR vehicle strongly depends on the technologies considered for the removal mission. Currently, different conceptual proposals are under investigation.

Propulsion

Several propulsion solutions are proposed for ADR: chemical propulsion for direct controlled reentry [16, 17, 8] or, in order to save the mass of required propellant, transfer to a decay orbit of 25 years (uncontrolled reentry) by low thrust impulse or by using electrical propulsion [8, 41, 45]. A cost analysis for the de-orbiting of a 1.2 metric ton IRS-1C satellite was presented for different propulsion options, suggesting that chemical rockets can be a viable solution [46]. Chemical propulsion takes advantage of Solid Rocket Motors (SRMs), Liquid Rocket Motors (LRMs) and Hybrid Rocket Motors (HRMs). Solid rocket technology is suggested both for mitigation and remediation [40] (with specific impulses I_s of about 200-250 s) but, even if it seems a good solution for the PMD of new small satellites its application to active removal may show some difficulties, since the thrust level generated is usually high and multiple burns are not possible. A controlled reentry can be performed with one or more impulses of thrust; however the multiple approach would allow for a better control of the disposal and final impact location, as well as the fragmentation footprint [8]. On the other hands the bi-propellant liquid technology ($I_s \sim$ 350-500 s), typically used for space operations and upper stages, provides both disposal possibilities to the detriment of significant higher costs with respect to SRMs. A recent study in Politecnico di Milano considers the chemical propulsion for a contact-less de-orbiting system [47]. Electric propulsion is characterized by very high specific impulse level ($I_s > 1000$ s) but, at the

same time, extremely low thrusts, requiring a continuos engine functioning for very long time, allowing to save the higher propellant consumption of chemical systems, but using large solar arrays or large batteries [8, 48]. This kind of system could be used only for apply the 25-years rule and, since they do not allow for an elliptic transfer orbit but multiple quasi-circulars [8, 49], the velocity requirement would be higher if compared with chemical propulsion one. Moreover, electric propulsion is still a quite expensive technology. In [41, 45], electric rockets are proposed for contactless removal approach. The propulsion solution can be even used for the re-orbiting of the target above the LEO region, instead of the object de-orbiting.

Tether Systems

Currently, several studies propose the use of tether systems for large debris removal [8, 39, 42, 43, 44]. For example, the Electrodynamic Tether (EDT) solution exploits the Lorentz force due to the interaction between the Earth magnetic field and the conductive tether, in which a electric current flows. If the tether, in relative motion with respect to magnetic field lines, is surrounded by ionosphere plasma, a current flow will be induced in the wire, generating a force used to modify the target orbit [8]. Another possibility offered by EDT is to generate the current in the wire by means of the de-orbiting kit equipped with power supply system, contrasting the electromotive force induced by the magnetic field. In such mode, the force is used to lower the target orbit (25-years rule) and even to raise the de-orbiting kit altitude, which can reach a new target. The second option is more complex and requires an autonomous spacecraft, but it allows for higher thrust level than the first option. However, the latter could be designed in small simple kits, attached to each target by a mother ship. Note that the tether length required for de-orbiting purpose is very large ($\sim$ 10 km) [8]. Another use proposed is the Momentum Transfer Tether (MTT), which exploits the two bodies motion with respect of the center of gravity between the target and the de-orbiting kit connected by a tether. When the wire is cut both bodies are boosted into elliptical orbits: with a higher perigee for the de-orbiting kit and a lower perigee for the target (25-years rule). This system, if precisely designed, might allow for multiple debris removal. Even in this case the tether length required is large and, generally, tether solution do not permit controlled reentry [8, 39].

Drag Augmentation Systems

A easy way to force the natural orbit decay due to the atmospheric drag is the attaching of an inflatable system to the target [8, 3]. This system can be design to increase the debris cross-sectional area enough to reduce its orbital lifetime to 25 years. The size of the inflatable de-orbiting kit depends on orbit altitude, as well as the atmospheric drag level and on the solar flux activity. The inflatable system could be attached on the target by means of a mother ship, loaded with multiple kits. However, even this solution does not allow for a controlled reentry [8].

2.2.2 Docking with Non-Cooperative Objects

The control acquisition of a non-cooperative target is the main challenge of the active removal mission. Typically, despite the effect of gravity-gradient stabilization, an abandoned object is subjected to tumbling (rotation about the short axis). This motion can be provoked by different causes: a collision with small debris, attitude control system failures, in case of R/Bs a little "kick" received during the release of payload or the passivation procedure, etc. Therefore, in order to achieve the control of the target it is necessary to know its motion conditions and to develop a strategy and a technology able to reduce the relative motion between the de-orbiting kit (or mother ship) and the abandoned object. Only by this way it might be possible to capture the debris and then attach a disposal system. The target capture strategy could be divided in two consecutive phases. The first contact, or soft docking, is necessary to reduce the relative attitude motion with respect to the debris; the second step consists in the creation of a robust structural connection between the target and the de-orbiting kit [16, 17]. Concerning R/Bs, a good connection point is the gas dynamic nozzle, designed to sustain strong thermal, fluid dynamics and structural stresses, while the payload cone could be considered as right point for S/C, but even for R/Bs. Several systems are proposed for soft docking phase such as electro-adhesive system [50, 51], robotic arms [9, 37], but also a contact-less method by means of dedicated micro-thrusters device, actually under study at Politecnico di Milano. Concerning the hard docking many different solutions are considered such as foam gluing, clamp or claw mechanisms [38, 52], harpoon and corkscrew mechanisms for connection inside the nozzle [38, 16, 17]. On the other hand, some studies theorize the possibility of target capturing by means of a tethered-net device [38, 42, 53]. The tethered-net can be launched from a certain distance from the debris, reducing the collision risks and the difficulty of a near approach (i.e. soft docking + hard docking).

3 ACTIVE DEBRIS REMOVAL BY HYBRID PROPULSION MODULE

3.1 HYBRID PROPULSION MODULE

3.1.1 Hybrid Rocket Technology for ADR

The target size, the disposal strategy and the propulsion technology are important aspects with a strong impact on mass budget, system volume, and cost of the propulsion unit. Considering a large object, the capability of throttling and re-ignition may represent a stringent requirement for the adequate control of the rendezvous and disposal maneuvers, whereas compact design is important for easier docking to the target and for dynamic stability of the final assembly. Compact volume may request a higher average propellant density but may collide with ΔV requirements for a controlled atmospheric reentry, needed for highest altitude of LEO range. Thrust level should stem from a trade-off choice about the risk of debris fragmentation, especially for large S/C, and long mission duration (correlated to propellant storability and collision risk during maneuver). Several innovative proposals are under development nowadays with varying time frames of realization; however, most of them need in-orbit demonstration of reliability and applicability for a real mission. Among this pool of technologies, solid propellants represent a simple, reliable, and proven technology but feature low specific impulse, limited flexibility and not suitability for multi-burn missions, while liquid bi-propellants fill the gaps left by the solid propellants, but larger volumes and higher degree of complexity are requested. In fact, the walls of combustion chamber and nozzle require a sophisticated cooling system to sustain the aggressive combustion environment with which they are in direct contact and high resistance material are required; even the injection system need a complex design and all these features involve a quite high level of costs for liquid bi-propellant technology. Furthermore, storability of the propellant must be carefully considered, as well as the high toxicity of typical liquid substances used for space applications (NTO, MMH, UDMH, etc.). Thus, hybrid rocket technology for de-orbiting applications is considered a valuable option due to the high specific impulse achievable, intrinsic safety, possibility of green propellant use, low cost technology and, especially, re-ignition and thrust throttleability. The latter may be a key aspect to avoid the risk of fragmentation for the most fragile components of a large abandoned satellite, during the de-orbiting maneuver, by manage the oxidizer mass flow rate, after the ignition, to gradually reach the required level of thrust. A Hybrid Rocket Engine (HRE) typically features the oxidizer in the liquid or gaseous state, while the fuel is in the solid state. Its safety is guaranteed by no-contact between fuel and oxidizer, except during the combustion phase. A hybrid rocket can also be built with particular geometries, using a tangentially ox-

idizer injection, resulting very compact and highly efficient [54, 55]. This particular kind of engine results very small in size. Such characteristics can be the right solution for space debris mitigation, by supplementing with this engine-type new satellites that will reach space in the future. This technology seems very promising even in the field of space debris remediation, making possible the active removal in LEO of large intact objects (several metric tons), both spacecraft and rocket bodies, by using a vehicle equipped with a HPM for the controlled reentry maneuver and several micro thrusters, for the attitude control, spilling the HPM liquid oxidizer and burning it as a monopropellant (dual-mode use) [56, 3]. Overall, a hybrid propulsion module represents a solution that mediates benefits and drawbacks from both liquid and solid rocket technology. On one side, it is bestowed the throttleability and reignition capability typical of liquids, specific impulse levels that fall in between the performance of solid and liquid propulsion ($I_s \sim$ 250-350 s), and a higher mean propellant density due to the use of a solid fuel. Nevertheless, a technological gap exists due to late development, so lower TRL, and lack of in-orbit demonstration. In the simplest possible configuration, a hybrid rocket is made by a center-perforated solid fuel placed in the combustion chamber where an injector blows in a liquid or gaseous oxidizer. This grain configuration shows a quite high volumetric efficiency for fuel amounts below 800 kg, with length-to-diameter L/D smaller than 20 [48]. Otherwise, a multi-perforation geometry is preferred. For ADR missions, the fuel mass required is relatively small, thus it is possible to reach volumetric efficiencies of about 80%. Low regression rate, together with poor combustion efficiency and oxidizer-to-fuel ratio shifting are the main drawbacks of hybrid technology, but different means are considered, especially for the enhancement of mass burning rate spanning from the use of advanced additives to different injection approaches (swirling oxidizer and vortex combustion) [54, 55, 57, 58]. Moreover, special innovative designs of the combustion chamber, such as vortex pancake, provides high combustion efficiency, low performance variation during combustion, and, in the case of solid metal additives, reduced emission of condensed combustion products thanks to the vortex effect [54]. The vortex pancake configuration may represent a very interesting solution for PMD missions [33, 59, 60]: this small and compact hybrid rocket could be easily integrated in the design of new satellites, providing both the maneuver capability, by using the oxidizer as monopropellant, and the final disposal to a decay orbit of 25-years lifetime or a direct atmospheric reentry. The development of active debris removal, besides legal and political issues, is strongly hampered by high costs involved. Therefore, cheap technological solution may allow for a more easy approach to ADR by the international space community. The hybrid propulsion could help in this direction. Once this technology has reached its complete maturity, the costs of hybrid propulsion modules might become very low, due to the cheap propellants (see 3.1.3) and structural materials required. For example, aluminum can be used for the combustion chamber, which does not need a cooling system for walls, since they are protected by the solid fuel, which is itself an insulating material. The exhaust nozzle can be realized without cooling system too, if the burn times are small (60-100 s) [48]. Moreover, the injection system does not need a complex design, as well as the tanks and feed sys-

tem, depending on the oxidizer selected. The ignition, if allowed by the oxidizer, can be performed by catalyst reaction avoiding the need of a pyrotechnic igniter (instead required for SRMs). Overall, this so reduced complexity could provide an important decrease in design and built costs, making the HRMs more suitable for controlled reentry than LRMs in perspective of ADR missions.

3.1.2 HRE Development State of the Art

On 17 August 1933 Korolev and Tickhoravov performed the first test flight of a hybrid rocket engine. Their HRE, known as GIRD-09, used Liquid Oxygen (LOX) as oxidizer and gasoline gel as fuel [55]. Meanwhile, at I.G. Farben Laboratories in in Germany some motor tests with 10 kN thrust for 120 s of combustion, based on the Andrussow concept proposal, were carried out by Noggerath and Lutz. The oxidizer was nitrous oxide (N_2O) while the fuel was solid carbon [55, 61]. These tests were characterized by low regression rate of the solid fuel because of the high gasification enthalpy required by carbon. During 1940s several tests were conducted by California Pacific Rocket Society in USA. They developed a rocket with rubber material as fuel and LOX as oxidizer which flown up to 9 km of altitude in 1951. Despite this research activity did not provide publications with detailed ballistics analysis, it revealed the nature of the diffusive flame that, in the HRE combustion, does not allow the born of instabilities due to cracks in the solid grain since, as asserted in that research, in a hybrid engine the chamber pressure is proportional to the oxidizer flow and not to the internal surface that is subjected to the flame [55]. Later, during 1950s, the research activity on HREs was continued by Moore and Berman at General Electric (polyethylene as fuel and hydrogen peroxide with concentration of 90% as oxidizer) and Avery, at Applied Physics Laboratory, who studied the reverse hybrid configuration by testing ammonium nitrate as solid oxidizer and JP as liquid fuel. Also Thiokol and UTC1 performed studies about reverse hybrid in the mid-1960, by using hydrazine-based liquid fuels and different solid oxidizers, such as ammonium perchlorate (AP), hydrazinium diperchlorate, and nitronium perchlorate, pressed with binder made by non-reactive fluorocarbon. However, the poor combustion behavior and low performance improvement shown were not sufficient to justify technological difficulties involved by the reverse hybrid configuration; therefore the focus of research remained of classic configuration: liquid/gaseous oxidizer and solid fuel. Contemporary, Marxman and co-workers developed the convective diffusion-limited model for classic hybrid combustion. This model is still used nowadays for hybrid combustion analysis [62, 63, 64, 65]. Always during sixties, in Europe some programs were carried out by ONERA (with SEP and SNECMA) in France and by Volvo Flygmotor in Sweden. In the frame of ONERA, the LEX program was based on a hypergolic propellant formulation based on red fuming nitric acid as oxidizer and an amine fuel consisting of nylon-metatoluene-diamine. The HRM was able to produce a thrust of 10 kN with throttle capability over a 5:1 range to optimize the thrust during the flight. The propellant mass fraction was of about 74%, with 52 kg of propellant, 5 kg

of payload and a gross mass of 75 kg. During this project, eight flights took place starting from 1964; they reached an altitude above 100 km. A larger rocket version, LEX-04, was developed for only ground tests (12 successful firing tests). On the other hand, Volvo Flygmotor program, begun in 1962, studied the hypergolic combination made by nitric acid and polybutadiene with an aromatic amine. During the test campaign the mechanical properties of the solid fuel grain resulted a limiting factor for system operating capability. This fact promoted the development of a fuel material with better mechanical properties by increasing the softening point of the solid phase. Using Sagaform A, two sounding rocket were realized: SR-1 with a launch mass of 361 kg, 264 kg of propellant and 25 kg of payload; SR-2 was designed with capability four times larger than SR-1. However, about this project there are just some technical reports and no confirmation about flight tests for SR-1 and SR-2 [55]. In United States UTC and Beech Aircraft conducted tests with hybrid sounding rockets in the frame of a design program for target drones. In 1967 UTC developed a very high thrust HRE, 180 kN, characterized by nitrogen tetraoxide (N_2O_4) as oxidizer and PB rubber loaded with 45% of aluminum as fuel. Instead of classic single centrally perforated grain configuration, UTC used a wagon wheel section shape in order to compensate the effect of low regression rate on the achieved thrust. In Figure 6, one can see the wagon wheel configuration, which became the base for solid grain design in following years by other research groups and companies.

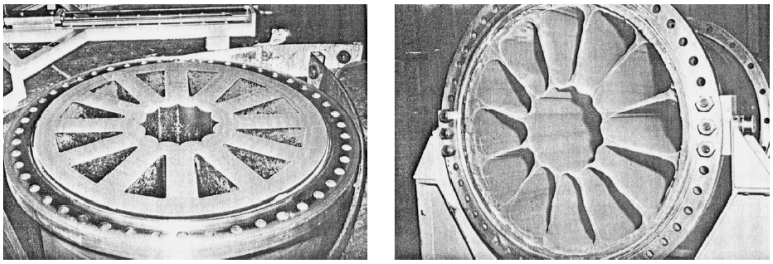

Figure 6.: UTC wagon wheel solid fuel grain before (left) and after firing test (right) [55].

More recently, in late 1980s, several sub-scale HRMs were realized and tests by AMROC [48, 55]. Among them, the H-500, designed for the propellant couple LOX/HTPB, could generate 312 kN of thrust for about 70 s, see Figure 7, while the H-250 was a larger scale version of the H-500, able to produce up to 1.1 MN of thrust thanks to a wagon wheel solid grain configuration with 15 ports (the central port was inert and closed at the head-end) with an overall diameter of 1.8 m. Later, always in USA, a new program called HPDP was carried out by an industrial team composed by NASA, Rocketdyne, DARPA, Lockheed Martin, Thiokol and CSD. They designed a hybrid motor with a modified HTPB fuel, made by seven ports plus a central not inert port, with a total web thickness larger than AMROC one of 50%. This design solution resulted more efficient and the reduced burning surface are, due to a lower number of ports, was compensated by a greater oxidizer mass flux; the thrust level generated was the same of AMROC motor.

Figure 7.: AMROC H-500 motor firing test, propellant couple LOX/HTPB [55].

A very significant milestones in the hybrid propulsion development is represented by the successful flight of SpaceShipOne at Ansari X-Prize in 2004, a competition oriented to promote technological advance in the field of free access to space [55, 61]. The SpaceShipOne was a sub-orbital spacecraft produced by Scaled Composites. The mission profile consists of three different phases:

1. the sub-orbital spacecraft is carried at altitude of 15 km by the White Knight, a mother aircraft;
2. once separated the sub-orbital spacecraft flies up to 100 km altitude, powered by a HRE;
3. a glide flight allows for the atmospheric reentry of the spacecraft.

The propulsion system of SpaceShipOne, designed by SpaceDev which kept the heritage of AMROC project, used HTPB as fuel with a four ports grain configuration and N_2O as oxidizer. The thrust generated was about 74 kN with a burning time of 87 s. The great success of this experience highlighted the high safety and low costs of hybrid propulsion technology and a new large and challenging project began, in the frame of a collaboration between the Virgin Group and Scaled Composite, with the aim to develop the first private spaceport dedicated to space tourism. The project, named SpaceShipTwo, consists in a more sophisticated scale-up of the previous concept, which is able to transport two pilots and six passengers. As of January 2014, 31 flight boost tests were successfully conducted, see Figure 8, and the company aims to begin the commercial flight within the end of 2014 [66].

In recent years, the interest on hybrid propulsion technology has grown up, inducing different research groups, in USA and Europe, toward significant efforts in this field. The team held by Kuo, at the Pennsylvania State University, carried out a detailed investigation on hybrid combustion phenomena, mainly focused on HTPB-based fuels loaded with metal additives [55]. On the other side of Atlantic Ocean, the ORPHEE program (European FP7) promoted an extensive experimental investigation,

Figure 8.: SpaceShipTwo during the boost phase after separation from mother-aircraft [67].

exploiting the cooperation of universities, industries and research centers, to identify solid fuel formulations able to provide significant regression rate enhancement [68]. HTPB-based and paraffin-based solid fuel were considered and the second one appeared as a very attractive material due to the greater regression rate enhancement provided, thanks to the entrainment melted fuel droplet, a phenomenon largely investigated by Karabeyoglu and co-workers at the Stanford Univerisity [55]. In 2010 a new FP7 allowed the born of SPARTAN project, which aims to study and evaluate possible future applications of hybrid propulsion, in particular the use of HTPB fuel for the soft-landing on Mars surface [69]. Currently, research projects on hybrid rocket are diffused in all over the world, for example, in Japan, the Hybrid Rocket ResearchWorking Group (HRrWG) of Institute of Space and Astronautical Science (JAXA) focuses the attention on the use of swirling flow oxidizer for the regression rate enhancement [55, 57, 70, 71, 72, 11]. Also Italy is involved in research activities on hybrid propulsion, such as the team of Russo Sorge, which began to work during 1970s at the University of Naples [55, 73, 74, 75], the University of Padua [76, 77], the Politecnico di Torino [78, 79, 80] and the Space Propulsion Laboratory (SPLab) of Politecnico di Milano. The latter implemented several experimental facilities for the study and the diagnostics of hybrid combustion phenomena, as well as the characterization of solid fuel with metal additives [81, 82, 83, 84, 85, 86, 87, 88].

3.1.3 Propellant Selection

A great advantage of hybrid propulsion is the use of non-toxic propellants, that are also significantly cheaper than common substances used in solid and liquid propulsion. Typical hybrid propellants almost do not reveal explosion hazards since the oxidizer and the fuel remain separated during all manufacture, storage and transport operations. This level of safety, together with their non-toxicity, reduces the overall costs of all ground operations before the mission. Different solid materials are considered as solid fuel, especially within the family of hydrocarbon [55]. During the years, the attention of research studies was mainly focused on carbon-based poly-

mers and paraffin wax materials, depending on their costs, mechanical properties and combustion performances. In the polymers group, typical fuels are, Polyethylene (PE), Polymethylmethacrylate (PMM) and Polybutadiene (PB) with hydroxyl on carboxyl ion as chain terminators. This materials are quite cheap [48], if compared with liquid propellants, making the hybrid solution more interesting from the point of view of costs minimization for active removal. The Hydroxyl-Terminated Polybutadiene (HTPB) is the most popular and well known solid fuel for hybrid propulsion, also due to its large use in solid propulsion as binder. It is a rubber compound very safe to handle, allowing to be easily powered with metal additives, maintaining very good mechanical properties. HTPB shows an isotropic behavior during the combustion [86], resulting very suitable for multiple burns mission, since the fuel grain perforations will keep the shape after the firing, see Figure 6. Although the regression rates provided are not so high (below 2.0 mm/s), HTPB is quite energetic and very safe material, since if soaked in liquid oxygen is not explosive [48]. Metal additives allow to reach greater regression rate levels, also providing a little increase in fuel density, which, for pure cured rubber, is about 915 kg/m^3 [88]. The HTPB preparation and curing process are described in Appendix G. With respect to HTPB, PE and PMM are cheaper, but the latter, for large grains, can be subjected to cracks due to heat loads during combustion process [48], introducing the hazard of nozzle throat obstruction. For example, the HTPB can cost about 10 $ per kilogram [89] depending on the amount purchased. This indicative price is referred to the not cured high viscous polymer. Considering that for ADR mission a relatively small quantity of fuel is required, due to low velocity increments involved, hence a solid grain charge would not have a big impact on overall mission costs. On the other hand, paraffin wax are recently acquiring large interest and use in the research community, due to the higher regression rate provided, up to two or three times that of HTPB [86]. These materials are characterized by very low melting temperatures, that involve the generating of a liquid layer above the fuel surface during the combustion; such layer is made unstable by the turbulence flow, so releasing small burning fuel droplets in the main stream. This process is known as *entrainment*. Nevertheless, paraffin fuels display anisotropic combustion and poor mechanical properties, the latter requiring the addition of polymeric additives in order to increase the elastic modulus and avoid the risk of cracks due to the combustion thermal and fluid dynamic stresses [86, 55]. In the frame of a multi-burn mission the anisotropic behavior may represent a significant drawback, since the shape of the fuel perforation after the firing would not be easily predictable (regards to oxidizer mass flux estimation for the following burn). In the light of these considerations, HTPB seems to be the most suitable choice for ADR applications, being a well known and safe material, tested in different operating conditions, able to provide quite high performance, with specific impulses close to that of paraffin wax [3]. However, paraffin materials, if fitted out with additives for mechanical properties increase, in the case of single-burn mission could represent an interesting solution, especially for small PMD on-board engines.

The most interesting oxidizers are Gaseous Oxygen (GOX) or Liquid Oxygen (LOX), nitrous oxide (N_2O) and hydrogen peroxide (H_2O_2) at high concentration, also known as High Tested Peroxide (HTP) [48, 55, 90, 33, 54]. Their performance, in term of ideal vacuum specific impulse $I_{s,vac}$, are compared in Figure 9, estimated using Chemical Equilibrium for Applications (CEA) software [91, 92], assuming 3.0 MPa of chamber pressure, an area-ratio of 50 and shifting nozzle expansion. HTPB is considered as solid fuel and introduced in the software by means of an empirical chemical formula evaluated in SPLab.

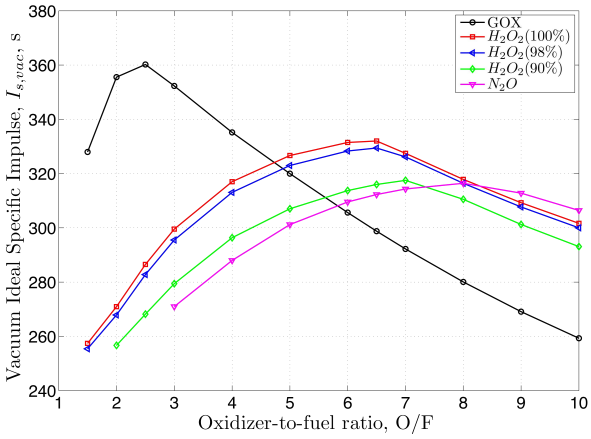

Figure 9.: Ideal vacuum specific impulse (chamber pressure 3.0 MPa and nozzle expansion area-ratio 50) for HTPB with different oxidizers.

All these oxidizers provide theoretical $I_{s,vac}$ above 300 s in correspondence of their optimal oxidizer-to-fuel ratio O/F, representing a valid option for rocket applications. Concerning in-space activity, as ADR is, liquid oxidizers are preferred, due to their higher density, hence a large storability amount. However, before enter in contact with the fuel port, the oxidizer must be properly vaporized, in order to limit combustion inefficiencies, not regular usage at the head section of the solid grain and the annihilation of the tangential velocity component in case of swirling injection [48, 71]. In case of LOX a separated gas generator should be used to provide hot gases in a pre-combustion chamber to vaporize the liquid oxygen. In Figure 10, the storability and feed systems complexity are compared for HTP and LOX. Liquid oxygen is cryogenic substance, therefore a more complex and expensive system is necessary for its conservation. Furthermore, the need of vaporization requires the gas generator. These features also entail a significant addition of mass on the overall propulsion system. On the contrary, the hydrogen peroxide can be easily vaporized by means of a catalytic decomposition, so injecting in the combustion chamber gaseous O_2 and H_2O at high temperatures, up to 1000 K depending of the concentration and reaction efficiency.

In case of HTP the costs and complexity are strongly reduced, just requiring a catalyst system for the oxidizer injection. Moreover, the hot gases produced are enough for the HTPB ignition ($\sim$ 800 K) [3], avoiding the need of a complex igniter. Hydro-

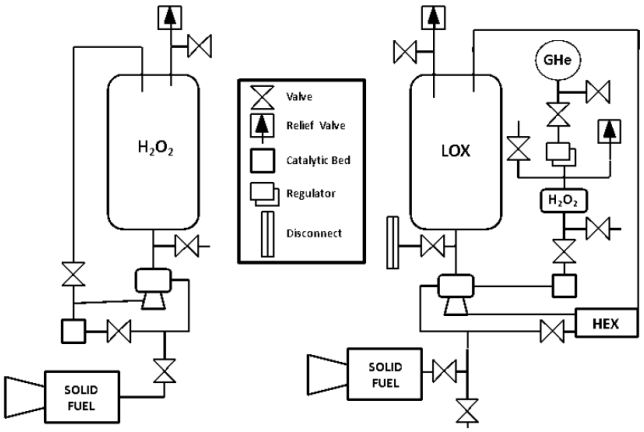

Figure 10.: Comparison between HTP (left) and LOX (right) storability and feed systems [55].

gen peroxide is a well known substance used for different applications in commercial, aerospace and defense industries during the last 100 years. Large amounts of H_2O_2 have been consumed by the paper and pulp business, while from 1930s, its decomposition reaction was exploited to develop the first monopropellant systems [93, 56, 90]. A very low vapor pressure characterizes the hydrogen peroxide, making it more easy to handle with respect to other liquid oxidizers or monopropellants, such as LOX and the toxic group made by nitrogen tetroxide (N_2O_4) or NTO, Monomethyl-hydrazine (MMH) and Unsymmetrical dimethyl-hydrazine (UDMH). A toxic propellant involves higher costs, especially for handling and ground operations: specialized staff and plants are required for the safe management of toxic substances and their cost is subjected to environmental laws that generally will become more strict in the next future (with consequent costs growth). In fact, by way of example, the average price of MMH and UDMH during 1990s was respectively about 17 $ and 24 $ per kilogram, but later, due to the upgrade of environmental regulation, the price of MMH jumped to 170 $/kg [94, 95]. The non-toxicity of hydrogen peroxide together with its easy handling, as well as its large diffusion, reduced the average price of HTP at 90-95% down to about 1 $ per kilogram, during 1990s. A so large difference in costs and handling make the hydrogen peroxide a very suitable option for ADR missions, by reducing the overall costs of the propulsion system. For rocket applications this high concentration of H_2O_2 are blended with water; typically at 90%, the most common grade, but even up to 98%. The latter provides higher mixture gas temperatures and better performance, but its cost becomes greater and the significant change in the adiabatic decomposition temperature involves a more complex design of the catalyst bed and more particular materials, with respect to typical systems used for HTP(90%) [56]. Because of the relatively low temperatures, the catalyst system (chamber, pipes, etc.) can be implemented with stainless steel, thus keeping low costs, while the catalyst bed is generally made by silver. The oxidizer density is about 1390 kg/m^3 for HTP(90%) and 1430 kg/m^3 for HTP(98%). The change in concentration entails the change of other properties, such as the freezing point which, for a percentage of 90%, is about

261.77 K (−11.5°C) [93]. Therefore, speaking of missions in space environment, a thermal system for the control of the oxidizer temperature must be considered. Despite this, hydrogen peroxide would represent a key choice for a propulsion system design for ADR, also because the dual-use capability. The latter consists in the possibility to use HTP as oxidizer for the primary hybrid propulsion engine and as monopropellant for the secondary propulsion system, made by several micro-thrusters for attitude control, spilling the oxidizer directly from the main tank [17, 3, 56]. Historically, the hydrogen peroxide became famous as an hazardous substance due to some incidents mainly happened between 1930s and 1960s, when the industrial practices for handling and rocket development were still immature and characterized by incidents even with other substances. In more recent years, two notable incidents, described and discussed in [96], enhanced the negative opinion about hydrogen peroxide, but they were provoked by the use of incompatible materials and system-design failure. Despite this, the H_2O_2 is enough stable both for what concern the typical industrial use and the space missions, as demonstrated by COMSAT spacecraft with a stored time of 17 years in vented tanks [97]. Modern industrial techniques are able to produce high hydrogen peroxide quality, with very low impurities percentage, making it more safe both for handling and for storing. Research studies have been carried out with the aim to improve the propellant properties especially for space applications; for example, the natural decomposition rate of hydrogen peroxide can be significantly reduced if stored in tanks made by specific materials, thus improving its long-term stability [96].

3.2 ADR MISSION CONCEPT AND REQUIREMENTS

With the aim of preliminary design of a hybrid propulsion rocket the mission requirements of an active debris removal must be defined. For this purpose, it is supposed a single De-orbiting Kit (DeoKit) which could be released by the launcher upper stage on the same orbital plane of the selected target. After a far-mid rendezvous, the close-range operations could be performed: the soft docking and hard docking phases. The near object operations could be remotely controlled by human operator. Once the object is captured and the DeoKit is structurally connected to it, it is possible to perform the final disposal by means of a controlled atmospheric reentry. The DeoKit is equipped with two different propulsion systems:

- *primary propulsion*: a hybrid propulsion module using HTPB as solid fuel and HTP with 90% of concentration as oxidizer. The ignition system is made by catalysts for the hydrogen peroxide decomposition, which provides hot-gases temperatures able to ignite the solid fuel;
- *secondary propulsion*: two different Reaction Control System (RCS) are equipped on thte DeoKit. The first provides relatively high thrust impulses, up to 50 N, used for attitude control during the far-mid rendezvous and disposal maneuvers; the second, able to generate low thrust impulses, up to 5 N, is used for

the DeoKit control during close-proximity operations. Both systems exploit the catalytic decomposition of hydrogen peroxide, spilled from the main oxidizer tank, working as monopropellant micro-thrusters.

The payload of HPM, besides the target mass, includes all the instrumentation for the flight control and tracking, communications, close-range measurements, object capture and mating, batteries and thermal control. A so conceived DeoKit would be able to perform the removal of a single pre-selected target, thus a certain number of DeoKits could be carried out by the launcher upper stage, which should release each one on specific orbital planes, multi-removal by a single launch. Three space launchers are available from ESA, with their respective upper stages:

- *Vega*: it can carry about 1500 kg to a SSO orbit of 700 km altitude, with a payload fairing 2.6 m wide and 7.88 m long. The upper stage of Vega (AVUM) is able to perform up to 5 controlled different burns [98].
- *Soyuz*: it can carry about 4500 kg to a SSO orbit of 660 km altitude, with a payload fairing 4.11 m wide and 11.433 m long. The upper stage of Soyuz (Fregat) is able to perform up to 22 controlled different burns [99].
- *Ariane V*: it can carry several metric tons (~ 20 t) in LEO, with a payload fairing 5.4 m wide and 17.0 m long. The upper stage Ariane V (ESC-A) is the most sophisticated and expensive, mainly used for large massive spacecraft or mission to GEO [100].

In order to transport multiple kits with one launcher, allowing for a multi-removal scenario, the mass of HPM must be minimized, according to the required velocity increment and the propellant couple selected. Moreover, the encumbrances optimization may favor the clustering of multiple DeoKit in the payload fairing. Certainly, the cheapest solution would imply the use of Vega launcher for a multi-removal mission [17]. For the HPM design the main size parameter is the velocity increment required for the target disposal. The considered strategy consists in a direct controlled reentry, the preferred option for the removal of large abandoned objects. By this approach the target can be rapidly removed, reducing significantly the risk of collision that characterizes the 25-years rule or slower un-controlled reentry options [8, 16, 17], and driven toward a non-inhabited area on the Earth surface. In Figure 11, one can see the required ΔV to move from initial orbit to an elliptical transfer orbit with perigee of 0 km (sea level). The disposal maneuver can be performed by one single apogee burns or multiple burns to gradually lower the orbit perigee altitude. While SRMs allow for just single burn strategy, the hybrid propulsion offers both the possibilities. In this respect, the main drawback of solid rocket use is the difficulty to control high thrust levels and once the combustion is ignited it cannot be stopped until the total propellant consumption (or nozzle break up to provoke high pressure drop). From high altitudes the use of two or three burns would provide a better control of the conditions for the final atmospheric reentry and impact footprint [8, 3]. However, this

option increases the time required for the overall disposal, as well as the need of propellant for a more complex attitude control, and below 300 km the torque induced by the enhanced atmospheric drag can significantly affect the control of the maneuvers.

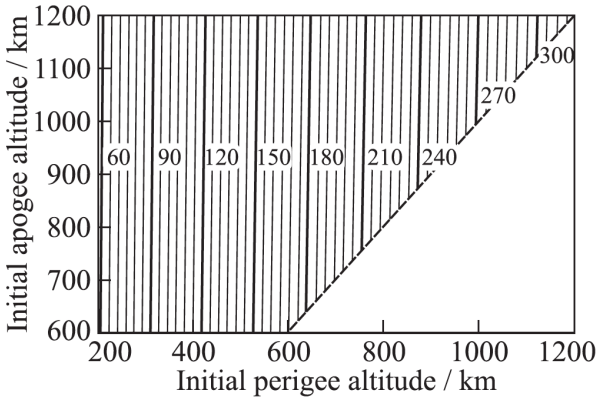

Figure 11.: Velocity increments required to remove a target from most crowded LEO altitudes [8].

Therefore, the disposal strategy must be defined accordingly with many factors. In this study, two targets are considered: a Cosmos-3M second stage [3, 17] and a Envisat-like object [16], whose data are shown in Table 2.

Target	**Dry Mass [kg]**	**Mean Altitude [km]**	**Inclination [deg]**	**ΔV Required [m/s]**
Cosmos-3M 22676	1400	767	74.0	200
Envisat	7800	767	98.4	200

Table 2.: Target selected for HPM preliminary sizing; the ΔV is referred to a transfer orbit with a perigee below 60 km [16, 17].

Both targets have an altitude of about 767 km, therefore the velocity increment for their removal is the same. The thrust level required will depends on the target mass. The Cosmos-3M is an upper stage rocket, so designed with a configuration able to sustain the mechanical stresses due to high thrust. On the contrary an abandoned spacecraft, like Envisat, has a less resistant overall structure, also presenting several appendages, such as solar panels, antennas, etc., that could be broken by the acceleration imposed to the structure by an impulse of thrust. Differently from solid propulsion, the throttleability of hybrid rockets should allow for a more softly acceleration during the initial phase of disposal maneuver, in order to avoid the generation of new potential debris. In this work, for the purpose of an overall HPM mass budget a single burn disposal is assumed, accordingly with [16, 17], for an immediate reentry of the large size target. The DeoKit-Debris mated system is steered to an elliptical transfer orbit with a perigee below 60 km and Flight Path Angle (FPA) $< -1.5°$ at an interface of 120 km altitude. A so steep FPA is necessary to reduce the ground impact area of the fragments that will survive to the atmospheric reentry.

4 HYBRID ROCKET PROPULSION STATE OF THE ART

This chapter deals with the fundamentals of hybrid rocket combustion, providing an overview of the classic theory developed Marxman and co-workers [62, 63, 64, 65] for the regression rate estimation. Typical methods for regression rate enhancement are then introduced.

4.1 HYBRID ROCKET COMBUSTION FUNDAMENTALS

In a hybrid rocket the gaseous or atomized liquid oxidizer reacts near the surface of the solid fuel. During the combustion the solid fuel is gasified by the heat feedback from the flame to the regressing surface, new gaseous fuel is introduced in the boundary layer going to sustain the process. The rate of heat transfer to the solid surface and the heat of decomposition of the solid fuel are the main controlling factors in hybrid combustion [62, 48]. The latter is characterized by a turbulent diffusion flame, which is established within the boundary layer developed on the fuel surface (see Fig. 12). In a real phenomena, the flame is thickened with continuos gradients. However, according to the Marxman's theory, the flame is assumed as a point of discontinuity, which occurs where the approximate stoichiometric ratio, between the gaseous oxidizer and vaporized fuel, is reached.

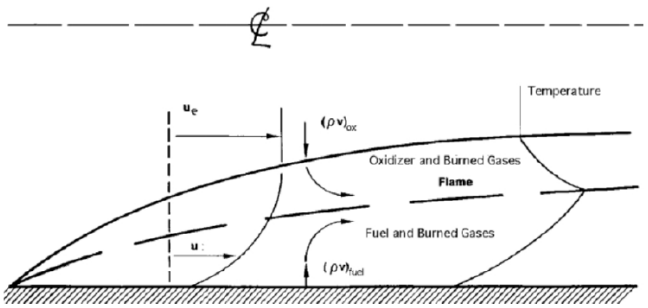

Figure 12.: Reacting boundary layer in a hybrid combustion process [62].

The boundary layer over the surface is divided in two regions by the flame sheet: an oxidizer rich zone above the flame, where the temperature and velocity gradients are in the opposite direction, and a fuel rich zone below the flame, where the gradients are in the same direction. Assuming that the main mechanism which drives the hybrid combustion is the heat transfer from the flame to the fuel surface, in order to evaluate

the fuel regression rate, under quasi-steady conditions, one can apply a simplified energy flux balance at the fuel surface [62, 55]

$$Q_{tot} = \rho_f r_f \Delta H_{v,eff} \tag{4.1}$$

where Q_{tot} is the heat transfer per unit of area to the fuel surface, ρ_f is the solid fuel density, r_f is the regression rate and $\Delta H_{v,eff}$ is the effective heat of gasification of the solid fuel. The latter includes the heat of vaporization ΔH_{vap}, the heat to warm the solid fuel from initial temperature T_i to the surface temperature T_w and the heat of depolymerization. In case of complex polymeric materials, the heat of depolymerization can be combined with the warming heat [48]. Hence, the effective heat of gasification can be evaluated as

$$\Delta H_{v,eff} = \Delta H_{vap} + \int_{T_i}^{T_w} c_s \, dT \tag{4.2}$$

where ΔH_{vap} is estimated by pyrolysis experiments and c_s is the specific heat of the solid fuel. Marxman et al. considered PMM, assuming that the solid material decomposes in its constituent monomer. The total heat transfer Q_{tot} generally includes the convection and radiation heat components.

During 1960s, Marxman et al. developed their diffusion-limited model, based on the following assumptions [62, 55]:

1. the boundary-layer flow over the fuel flat plate (slab configuration) is turbulent, due to the effects of fuel injection from the surface;

2. Reynolds analogy is valid in the boundary-layer (not necessarily in the flame sheet) and the Lewis (*Le*) and Prandtl (*Pr*) numbers equal to unity;

3. in the boundary layer, the velocity profile is slightly affected by combustion and wall blowing, allowing to keep the standard friction coefficient for turbulent boundary-layer.

Within this model Q_{tot} corresponds to a pure convective regime Q_c, by neglecting the radiative component. Q_c can be expressed as the convective heat flux at the regressing surface

$$Q_c = h \cdot (T_{fl} - T_w) = \kappa \frac{\partial T}{\partial y}|_{y=0} \tag{4.3}$$

The mass addition from the solid surface, *blowing*, induces a reduction of the convective heat transfer coefficient. This effect, called *blockage*, limits the heat feedback from the flame to the surface being the main responsible of the low regression rate of hybrid rockets. The Stanton number ratio St/St_o concerns to the blockage effect and can assume values between $0 < St/St_o \leqslant 1$, involving $r_f = 0$ when equal to unity. According to Reynolds analogy, the Stanton number ratio is equal to the local friction coefficient with and without fuel mass injection, C_f/C_{f_o}, where $C_{f_o} = 0.058 Re_x^{-0.2}$.

As described in [63, 48], the St/St_o can be expressed as a function of the blowing number B with the empirical expression developed by Maxman

$$\frac{St}{St_o} = \frac{C_f}{C_{f_o}} = \left[\frac{\ln(1+B)}{B}\right]^{0.8} \left[\frac{1+1.3B+0.364B^2}{\left(1+\frac{B}{2}\right)^2(1+B)}\right]^{0.2} \tag{4.4}$$

which can be represented by a simple formula (refitted by Altman [48, 55]) in the range $5 < B < 20$, typical values for hybrid systems

$$\frac{St}{St_o} = B^{-0.68} \tag{4.5}$$

The blowing number

$$B = \frac{\rho v|_w}{\rho_e u_e (C_f/2)} \tag{4.6}$$

is a thermodynamic parameter which describes the enthalpy driving force between the flame and the surface that causes the regression, but even a similarity parameter for a boundary layer with fuel suction [63, 55]. By substituting the Eq. 4.5 and 4.6 in the Eq. 6.11, one can obtain a simplified expression for hybrid combustion with no radiant heat transfer

$$\rho_f r_f = 0.03 G^{0.8} B^{0.32} \left(\frac{x}{\mu}\right)^{-0.2} \tag{4.7}$$

where G is the local specific mass flux (including oxidizer and fuel addition), μ is the gas-phase viscosity, x is the axial location. To be noted that B is fixed for a defined oxidizer/fuel combination and, since it is raised to a small power, only minor changes will be produced by large variations of $\Delta H_{v,eff}$ and Δh. As shown by Eq. 4.7, the fuel regression rate depends primarily on the total specific mass flux. During the combustion, as much as the port area increases G decreases, causing the reduction of r_f and the consequently oxidizer-to-fuel shifting (O/F growth). Furthermore, there is a negative dependence on axial location $x^{-0.2}$, which accounts for the effects of boundary layer growth on heat transfer. The increase of boundary layer along x-direction involves a decrease of the boundary layer temperature and the velocity gradients normal to the flat plate and consequently the decrease of convective heat flux. According to Marxman analysis, the fuel regression rate generally decreases with time and axial position along the fuel [63, 64, 55].

4.1.1 Thermal Radiation Contribute

The equation 4.7 results valid in a pure convective regime, since, as asserted by Marxman et al., for polymeric fuel formulations without metal additives the radiative component does not affect significantly the regression rate. In metal-loaded fuels, radiation is not directly affected by blockage (even though it can be increased by greater

blowing caused by radiation), representing a large energy contribute [62, 55, 61]. However, due to the presence of soot and fuel fragments, radiation can play an important role also in non-loaded fuel formulation [55]. Marxman defines a correction expression for the regression rate that includes the radiative contribute of the gas-phase [63, 55]

$$\rho_f r_f = [Q_c exp(-Q_{rad}/Q_c) + Q_{rad}]/\Delta H_{v,eff} \tag{4.8}$$

with

$$Q_c = 0.03 G^{0.8} (x/\mu)^{-0.2} B^{0.32} \Delta H_{v,eff} \tag{4.9}$$

$$Q_{rad} = \sigma \varepsilon_w (\varepsilon_g T_{fl}^4 - \alpha_g T_w^4) \tag{4.10}$$

where ε_w is the surface emissivity, ε_g and α_g the gas-phase emissivity and absorptivity respectively, while σ is the Stefan-Boltzman constant. In this analysis Q_{rad} is due to the gas-phase radiation, which does not provide significant increments in the net regression rate (below 10%) with respect to non-radiative case. The weight of radiation on regression rate was investigated by several authors, such as Estey et al., Strand et al. and Chiaverini et al. [55]. The work of Estey was focused on the identification of a scaling-law for HRE performance evaluation under different operating conditions and geometry parameters [101]. He estimates the radiative heat flux with an expression derived from Eq. 4.10, in which T_w is neglected (largely smaller than T_{fl}) and the gas-phase emissivity is estimated by an empirical expression defined using data from different motor scales. This correlation resulted better for metal-loaded fuels, while for non-loaded formulations Eq. 4.10 resulted the best. By means of a lab-scale slab motor, whose setup allows to measure pressure, average r_f and average oxidizer-to-fuel ratio, as well as optical observation of the reacting boundary layer and exhaust plume, Strand analyzed the influence of radiation, distinguishing between the contribute of principal gaseous products (CO,CO_2,H_2O), evaluated with Estey's approach, and soot particles [102]. The heat flux $Q_{rad,s}$ induced by the latter is

$$Q_{rad,s} = \sigma\, T_g^4 (1 - exp(a_p N_p)) \tag{4.11}$$

where N_p is the particle number density and a_p is a constant, that are evaluated by the expression 4.12 as a function of the weight fraction α_p and O/F

$$a_p N_p = 0.134\, [\alpha_p p/(1 + O/F - \alpha_p)] \tag{4.12}$$

assuming for soot particles the same temperature of the flame. Soot particles should have a size lower than 0.1 μm, therefore the temperature equilibrium with the surrounding environment should be quickly reached, making the previous one a reasonable assumption. The analysis performed by Strand highlighted that, under the investigated conditions, the radiative heat contribute can account for the 50% of the total heat flux [102, 55]. In more recent years, at the Pennsylvania State University,

Chiaverini performed a semi-empirical study about the radiative effects on a slab motor. In this setup, the regression rate was determined by X-ray radiography and ultrasound techniques [55, 103, 104]. Starting from the data of Strand, Chiaverini represents the experimental results by Eq. 4.13, in which the soot temperature is assumed as the 95% of the equilibrium flame temperature:

$$Q_{rad,s} = \sigma \, T_g^4 (1 - e^{k_s}) \tag{4.13}$$

where k_s is the absorption coefficient, which strongly depends on the O/F with a linear fashion, $k_s = 0.51 - 0.113O/F$, for a range between 1.5 and 3.5 [55]. Based on these results, Chiaverini proposed the following semi-empirical correlation, derived from Marxman's model

$$\rho_f r_f = a \; St \; B \; G\theta^b \left\{ c \left(\frac{Q_{rad}}{Q_c} \right)^d + exp \left[-c \left(\frac{Q_{rad}}{Q_c} \right)^d \right] \right\} \tag{4.14}$$

where a, b, c, d are empirical parameters, achieved by combustion data correlation. The parameters c, d are equal to unity in Marxman's theory, while the data fitting, by means of least mean squares, made by Chiaverini yielded $a = 0.524$, $b = 0.6$, $c = 1.3$ and $d = 0.75$. In Figure 13, one can see the weight of radiative heat flux during a combustion test (HTPB + GOX) performed by Chiaverini. The convective contribute results significantly greater at the beginning of combustion, but quickly decreasing to a heat flux level close to that of soot particles. The latter represents a large segment of the total heat flux, while the gas-phase contribute is almost negligible.

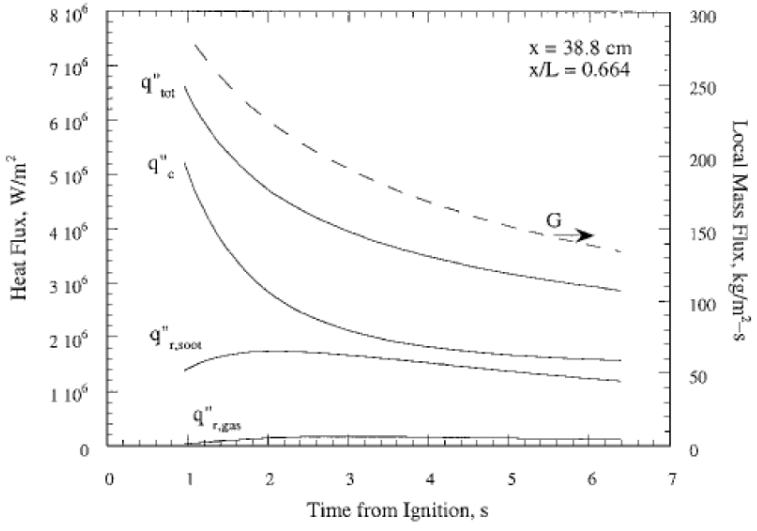

Figure 13.: Comparison between convective and radiative heat flux. HTPB+GOX in slab configuration [55].

4.1.2 Effect of Pressure

In the regression rate expression 4.7 developed by Marxman et al. the main parameter is the mass flux G, with no any explicit relation with the combustion pressure p_c. However, a regression rate dependence from pressure was observed in different studies. In some of them, the increase of pressure promotes the regression rate enhancement till a threshold value, after which the pressure effect becomes negligible, while, in others, the r_f is reduced by pressure increase [105]. George et al. provides an overview of the pressure effects on regression rate for polymeric fuels with several oxidizers [106]. An important work was conducted by Smooth and Price, that considered butyl rubber and poly-urethane as fuels and fluorine or a the mixture fluorine/oxygen as oxidizers [107, 108, 109]. In their tests, up to 1.2 MPa of chamber pressure and a G_{ox} range of 10-120 $kg/(m^2 \cdot s)$ were assumed. Smoot and Price observed that for mass fluxes below 25 $kg/(m^2 \cdot s)$ the regression rate was dependent from G_{ox} and not sensitive to p_c, while for mass fluxes above 70 $kg/(m^2 \cdot s)$, the r_f showed the opposite behavior. In the range between this two G_{ox} values, the regression rate was dependent by both terms. The dependence to pressure at high mass flux values was associated with the rate limiting chemical kinetic processes and to possible heterogeneous reaction in correspondence of fuel surface. Because of this, the classical turbulent boundary layer regression rate model developed on the base of convective heat transfer mechanism was improved to take into account the effects of condensed phase surface reactions.

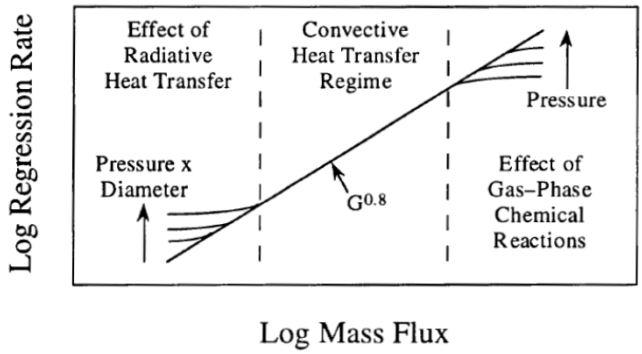

Figure 14.: Influence of pressure on regression rate for non-metallized fuels [55].

A diffusion-limited model, similar to that of Marxman et al., was derived for the low G_{ox} region, while for the intermediate zone the following expression was proposed

$$r_f = \frac{a\ G^{0.8} b\ p_c^n}{a\ G^{0.8} + b\ p_c^n} \tag{4.15}$$

but about the exponent n no details are provided. For the high G_{ox} region an expression very similar to Vielle law (typical of SRMs) is defined as

$$r_f = a\ p_c^m \tag{4.16}$$

Figure 14, summarizes the recent investigation results about the pressure influence of regression rate. For low G_{ox} the r_f tendency appears more related to the radiation effects, while at high G_{ox} the kinetic limited regime promotes the regression rate enhancement as the chamber pressure increases.

4.2 METHODS FOR REGRESSION RATE ENHANCEMENT

Despite hybrid propulsion is characterized by significant advantages, with respect to SRMs and LRMs, the main drawback of this technology is the low regression rate. Over the years, several methods for the regression rate enhancement have been proposed. Among them, non-classical injection techniques, also together with special fuel geometries, that exploit the fluid dynamic of the oxidizer, or, focusing on the fuel composition, energetic additives and paraffin-based fuels [55].

4.2.1 Non-Conventional Injection and Geometries

Non-classical flow injection and fuel grain geometry are diffused solution for the regression rate enhancement. Several studies have been conducted focusing the attention on the flow-type or fuel grain geometry or both combined. Shin et al. used metal wires radially embedded in the fuel grain to increase the turbulence when the rod emerged from the regressing surface [110]. A second possible positive effect of the wire was the heat conduction in depth of the solid grain. Nevertheless, this method do not provide significant regression rate enhancement (below 3-4%).

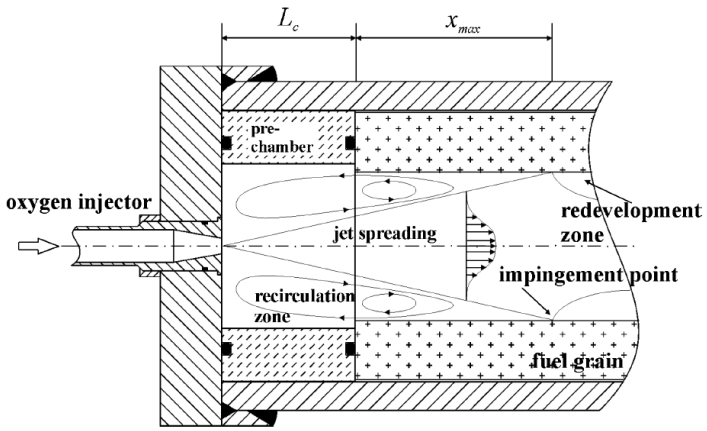

Figure 15.: Conical converging nozzle for axial head-end injection. Flowfield pattern generated [74].

On the other hand, the effects of a head-end injector strongly affect the motor behavior and the regression rate along the entire port length as observed by Carmicino and Russo Sorge [73, 74]. They performed several firings, at laboratory scale, for the couple PE/GOX using an axial converging nozzle (see Figure 15). The oxidizer

jet, so injected, produces three distinct flow regions in the fuel port, see Figure 15. A recirculation zone outer of the jet boundary, developed between the pre-chamber and the head-end of the fuel grain; an impingement zone where the oxidizer impacts against the fuel surface and, downstream from this point, a region of developing turbulent boundary layer. The regression rate profile obtained with such flow pattern significantly differs from that described by the classic theory [63], demonstrating the great importance of the geometry in the hybrid combustion process. Moreover, the time- and space-averaged power law approximation showed a lower dependence from the mass flux, with an exponent of 0.37 against the 0.8 of the Marxman's theory. The highest r_f was achieved in correspondence of the impingement region, up to 2.5 times higher, with a not so uniform profile along the longitudinal direction. Also a radial injector was tested, but obtaining little lower regression rates and larger pressure oscillations with respect to axial case. Under the investigated conditions, the use of head-end conical nozzle provided an increase of space-averaged r_f with the decrease of mass flux, testified by the decrease of O/F over combustion time. Such feature, together with a quite high combustion efficiency, may represent an attractive solution for small hybrid motors.

Another largely diffused approach is the swirling oxidizer flow, obtained by two or more pipes tangentially oriented with respect to the fuel port section (classic cylinder grain shape). The swirling flow induces the reduction of the boundary layer thickness in central perforated grains, due to the presence of a strong tangential velocity component, thus promoting the convective heat transfer enhancement [111, 112]. Moreover, a higher combustion efficiency can be achieved by swirling flow because of the increased residence time of hot gases inside the combustion chamber. Swirling head-end injection was investigated by Yuasa et al. burning PMM/GOX. The measured regression rate resulted 2.7 times higher than that of standard-flow hybrids, under similar operating conditions [70, 57, 55]. Swirling injection even provides a stable combustion and an easy and reliable ignition [113], favored by the increased convective heat exchange, feature which may allow easy reignition in vacuum environment for multi-burn missions.

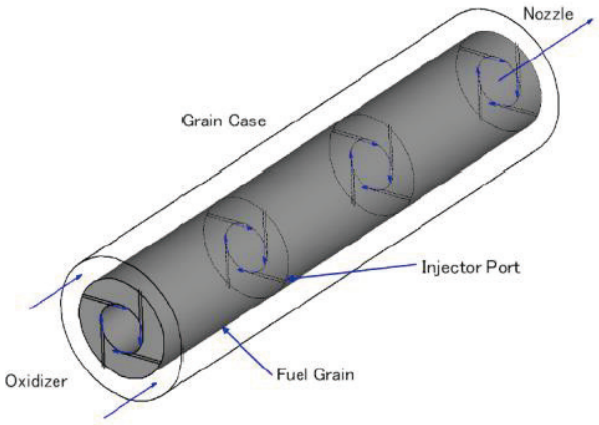

Figure 16.: Multi-section swirl injection method, fuel grain schematic [114].

Unfortunately, the swirl intensity quickly decays after few diameters from the injection section [111], due to wall friction, viscous dissipation and no any contribute to the tangential velocity component, thus completely losing the regression rate enhancement in the aft part of the fuel grain. In order to limit the decay of swirl, fuel grains with helical-shaped central port were tested by Lee et al., obtaining up to 80% with respect to standard-flow combustions [115], thanks to the enlarged fuel surface. However, the helical geometry is consumed during the combustion. Recently, Aso et al. proposed the use of multiple swirl injection sections along the solid grain with the aim to limit the swirl decay [114], see Figure 16. Paraffin-based and High Density Polyethylene (HDPE) fuels were considered with different grain configurations (i.e. the number of injection pipes, clockwise or counterclockwise flow, the number of injection sections). The combination of clockwise and counterclockwise sections revealed better performance than other cases and high regression rates.

Differently from Yuasa et al., during 1990s, Knuth et al. designed and realized a vortex hybrid motor in which the swirling oxidizer is injected from the aft part of the combustion chamber [55]. Due to the particular design scheme, a pair of coaxial bidirectional vortexes are generated in the central fuel port. This motor, tested with different fuel formulations, was able to generate up to 3560 N. By testing the couple HTPB/GOX a regression rate increase of about 400% was achieved at 100 $kg/(m^2 \cdot s)$ of mass flux, with respect to standard-injection motors. The exploiting of swirling oxidizer with non-conventional solid fuel geometries was even investigated by Gibbon and Haag at the Surrey Satellite Technology Ltd [54, 60]. They designed and tested the so called Vortex Flow Pancake (VFP), a hybrid motor with two flat and large solid fuel disks and with tangential injection sandwiched between them. Both fuel grains had a central perforation, which allows the hot gases course toward and throughout the nozzle. The combustion chamber was made by the gap between the two flat disks and, after the ignition, an intense combustion vortex was created by the tangential injection pipes, inducing the regressing of both fuel surfaces. This system revealed a very high combustion efficiency and a regression rate of one order of magnitude greater than classical hybrid configuration [54]. The vortex combustion promotes a larger time of residence in the combustion chamber, limiting the ejection of unburned agglomerates or fuel fragments that impact to the engine internal wall with no possibility to reach the central nozzle.

4.2.2 Energetic Additives

High-energetic materials, such as powders of metals and hydrides, can be mixed into the fuel grain with the aim to increase the regression rate, as well as the fuel density, the specific impulse, the attenuation of acoustic modes and even to limit the throat erosion caused by the oxidizer-rich exhaust flow [61, 55, 116]. This approach allows to keep a relatively inert material, guaranteeing the safety nature of HREs. Concerning the boundary layer combustion, the main advantage provided by the addition of energetic additives is the augmented heat release in the zone close to the regressing

surface, thus increasing the heat feedback to the solid fuel, hence the regression rate. During the last 60 years, a great interest has been given to metal additives, founding application both in solid and hybrid propulsion. The effects of micro-sized aluminum on different polymer-based fuels were examined by Lips [117]. In his experiments he used a mixture of 40% Fluorine and 60% Oxygen as oxidizer and various additive mass fractions in a polyurethane binder: the highest r_f was achieved by solid fuel loaded with 60% μAl and 10% carbon. Lips obtained similar performance using magnesium-coated aluminum $AlMg$ with 50% of magnesium mass fractions. Strand et al. performed tests using HTPB-based fuel loaded with 40% μAl and 30% coal [118]. The regression rate enhancement achieved with the addition of micro-sized powders was mainly due to the increase of the radiative heat flux from the flame region to the fuel surface, which opacity was greater because of the addition of coal. Just a small contribution was provided by the flame temperature rise due to the aluminum combustion. Such behavior can be associated with common micro-sized aluminum powders, whose particles are covered by a thin shell of alumina, characterized by a very high melting temperature ($\sim$ 2000 K) which must be reached for the ignition. Materials with lower ignition temperature, such as magnesium, show different behavior in hybrid combustion, providing different performance [61]. A very attractive metal is boron, characterized by the greatest volumetric oxidation heat of metal additives, but difficult to be ignited and reason of poor combustion efficiency [55, 119, 120]. The hard ignition of boron is probably due to its covered layer of boron oxide, which, despite its low melting temperature, the high viscosity of its liquid phase can hinder the diffusion of oxygen toward the boron core [120]. The boron ignition problem could be limited by doping with other metals such as Ti, Mg or fluorine-containing polymers. In more recent years, the advancements in the field of nano-technologies attracted the attention on nano-sized powders and their possible use in propulsion applications. Nano-particles are characterized by large specific surface that means a higher chemical reactivity with respect to micro-sized particles [61]. Because of this, nano-sized additives easily react, releasing their energy closer to the regressing surface during the combustion and providing higher regression rates if compared with micro-sized metals. Nano-aluminum, with typical size up to 100 nm, is an interesting candidate, due to its cost and availability. It can be produced with various methods and the most famous is ALEX, obtained by means of Electrical Explosion of Wire (EEW) [121]. The ignition of nAl occurs at temperatures very close to the aluminum melting point ($\sim$ 943 K) [122]. Nevertheless, the effective particles dispersion into the fuel matrix is very difficult, representing the main drawback of this solution [123, 124]. In Figure 17, one can see the comparison in term of regression rate for different solid fuel formulations, data achieved by the Penn State University. The HTPB loaded with 13% of Viton-A coated ALEX provides an r_f increase of about 130%, at $G_{ox} = 112\ kg/(m^2 \cdot s)$, with respect to the baseline case [55]. Besides metal additives, also the addition of hydrides in the solid fuel promotes large performance enhancements, but these materials are characterized by a high chemical reactivity with polymers, thus exhibiting a poor chemical compatibility with commonly used solid fuel, such as HTPB. Despite this drawback, hydrides are very attractive due to their large content of hydrogen, which

can provide higher specific impulses than standard solid fuel/propellant formulations [61]. Several studies have been performed about hydrides thermochemical properties and performance, described in [125, 126, 127, 128, 129]. Among them $LiAlH_4$ and AlH_3 have been mainly considered, but both exhibit chemical compatibility problems and, moreover, the second one is not available at commercial level [124].

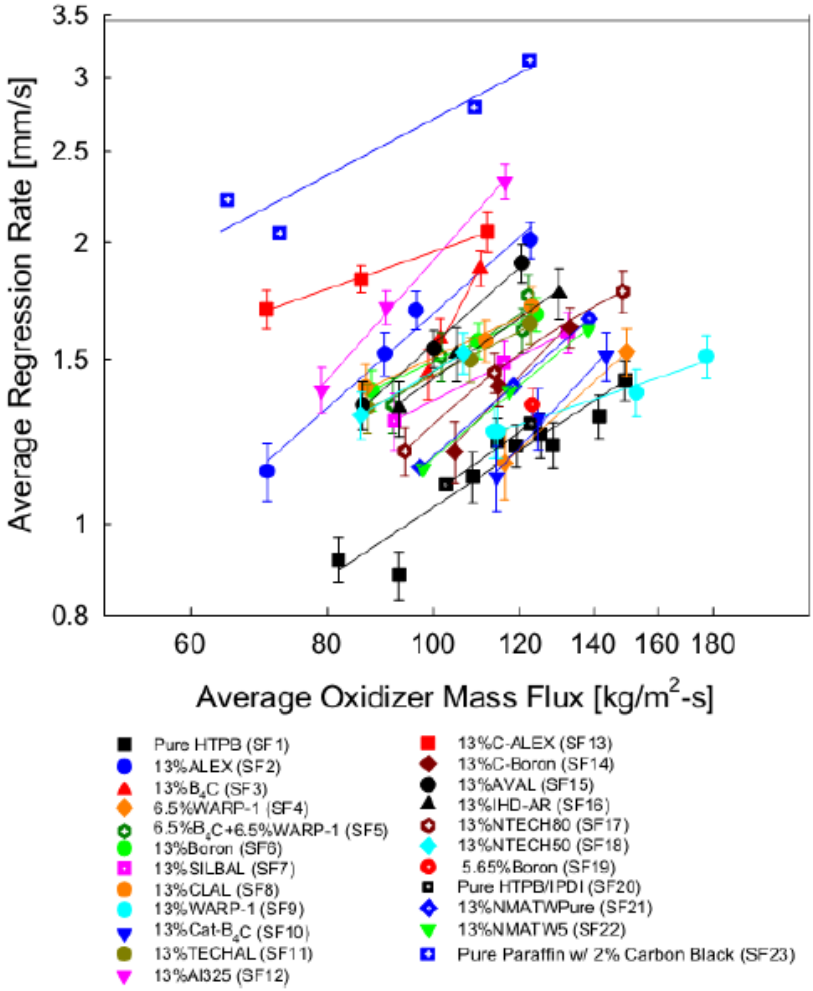

Figure 17.: Regression rate comparison for HTPB-based formulation loaded with different additives [55].

4.2.3 Entrainment

Research studies conducted during the second half of 1990s at Stanford University by Karabeyoglu et al. revealed the possibility to achieve high regression rate by using paraffin wax materials [130, 131] and other alkanes [132]. These type of materials allow to reach up to 400% of r_f increase with respect to conventional polymers used in hybrid propulsion. In Figure 17, pure paraffin provides the highest r_f values even if

compared with HTPB loaded with nano-metal additives. These so high ballistics performance are due to the entrainment of melted solid fuel droplets. Paraffin materials are characterized by low melting temperatures and the heat-feedback from the flame zone to the solid surface involves the generation of a thin fuel liquid layer over the grain surface. Then, the oxidizer flow destabilizes the liquid layer due to its low viscosity and low surface tension, thus releasing melted droplets that burn in the main stream [133]. This phenomenon, called entrainment, needs just the heat of liquefaction that is smaller than the heat of gasification, required by polymeric fuels, and the presence of the liquid layer reduces the blockage effect.

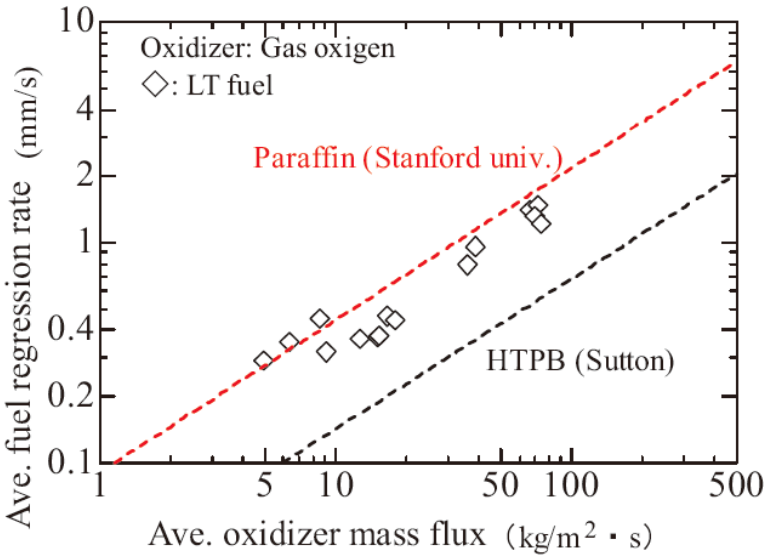

Figure 18.: Regression rate comparison for LT, paraffin and HTPB fuels [134].

Paraffin-based fuel represents a very attractive solution for future hybrid rocket applications. Nevertheless, these materials are characterized by poor mechanical properties, thus for real applications they must be mixed with special additives in order to increase their mechanical reliability. In Japan, a new Low Melting Temperature Thermoplastic (LT) material, currently under investigation, promises both regression rates of the same level of paraffin-based fuel and excellent mechanical properties like commonly employed polymers [134]. In Figure 18, the regression rate provided by LT fuel is compared with that of paraffin and HTPB.

5 EXPERIMENTAL STUDY

The experimental activity was focused on two main arguments of interest for the study of hybrid propulsion applied to ADR missions. Different regression rate enhancement techniques were analyzed and an aging study on HTPB was performed.

5.1 REGRESSION RATE ENHANCEMENT

5.1.1 Introduction

Concerning hybrid propulsion, a great research effort is focused on the development of techniques for regression rate enhancement. An overview on the different solutions proposed is provided in Chapter 4. In a hybrid motor with standard flow oxidizer injection the r_f of non-metallized fuel formulations mainly depends on the convective heat transfer from the flame to the regressing surface [55]. The flame zone is established in the boundary layer developed by the oxidizer flow over the solid fuel surface. A greater regression rate can be obtained by reducing the boundary layer thickness [57], thus increasing the convective heat transfer [112]. The latter could be performed by swirling oxidizer, characterized by a significant tangential velocity component able to lower the boundary layer in the central port [112]. Moreover, a higher combustion efficiency can be achieved by swirling flow thanks to the increased residence time of hot gases inside the combustion chamber. The regression rate enhancement achievable by this approach is quite significant as demonstrated by several authors [70, 57, 71, 115, 55] Another approach for the increase of regression rate consists to load the solid fuel with energetic additives, such as metal powders or hydrides, see Chapter 4. Metal additives with particle dimension in the micron-size range provide r_f enhancement mainly due to the augmented radiation heat flux from the flame to the fuel surface. This because of the low reactivity of conventional micron-sized metal additives. The particle reactivity can be enhanced by resorting to innovative micron-sized additives [135, 136] or nano-sized materials [55, 137, 135]. Because of their high reactivity [138], nano-sized particles can release energy closer to the regressing surface, providing significant r_f growth [55, 139]. On the other hand, nano-sized particles are easily subjected to cold cohesion/clustering requiring proper dispersion techniques during manufacturing [140]. Moreover, due to their reactivity level, nanoparticles can exhibit a high sensitivity to aging processes [141]. The **SPLab!** (**SPLab!**) developed a time-resolved technique for r_f data reduction. This exploratory study aims at investigating the combination of two different techniques for regression rate

enhancement: a swirling oxidizer flow injector and the solid fuel loading with an innovative micron-sized metal additive.

5.1.2 2D-Radial Micro Burner

In SPLab a non-intrusive optical technique is actually used for fuel regression rate measurement and ballistics analysis. To allow for optical access into the combustion chamber a special test rig concept was designed. With this setup, during the combustion, it is possible to observe the frontal section of a cylindrical strand, inserted in the injector head placed inside a stainless steel case. Such system concept, originally designed by Bosisio and Raina [84, 142], was then developed by Paravan [82, 86] and finally modified by Duranti, Sossi and Paravan [81, 124]. This kind of facility is used for the ballistic characterization of different solid fuel formulations from the point of view of regression rate. The schematic of the 2D-Radial micro burner is shown in Figure 19.

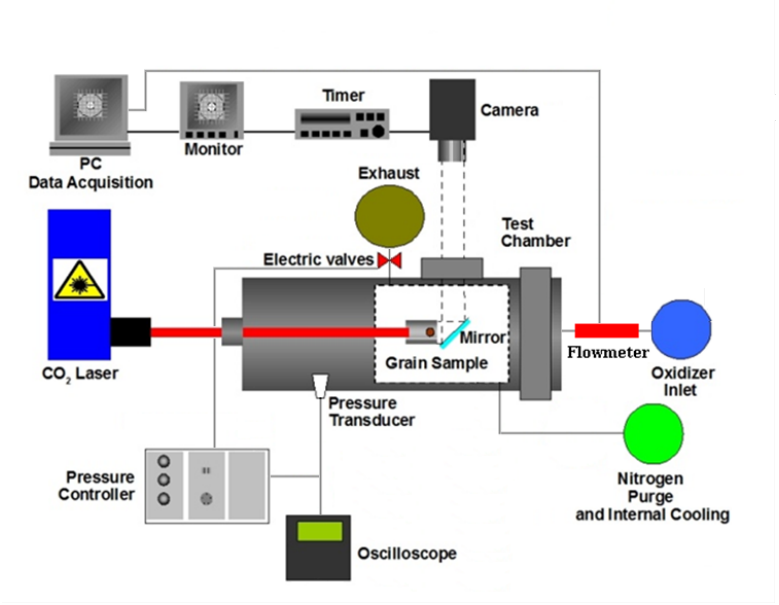

Figure 19.: 2D-Radial micro burner test rig schematic.

The combustion chamber is a cylinder, made by stainless steel AISI 316, housing the injector system and the optical accesses (quartz windows) for strand visualization. During the combustion, the head-end section of the fuel strand is fully visible thanks to a proper combination of lateral windows and a 45° mirror placed behind the injector, inside the combustion chamber. Two quartz windows are located in correspondence of the brass flanges, see Figure 20, in line with the central axis of the injector. The oxidizer is fed by cylinders and it is injected toward the tested strand through 8 channels (with diameter of 5.6 mm) realized in the internal width of the injector-head (see Figure 23). The cross-section of these channels can be changed by acting on regulation stems, thus allowing standard/swirled oxidizer injection. In or-

der to provide an homogenous oxidizer flow to the injection channels, a pre-injection chamber is located between them and the oxidizer inlet pipe, see Figure 20.

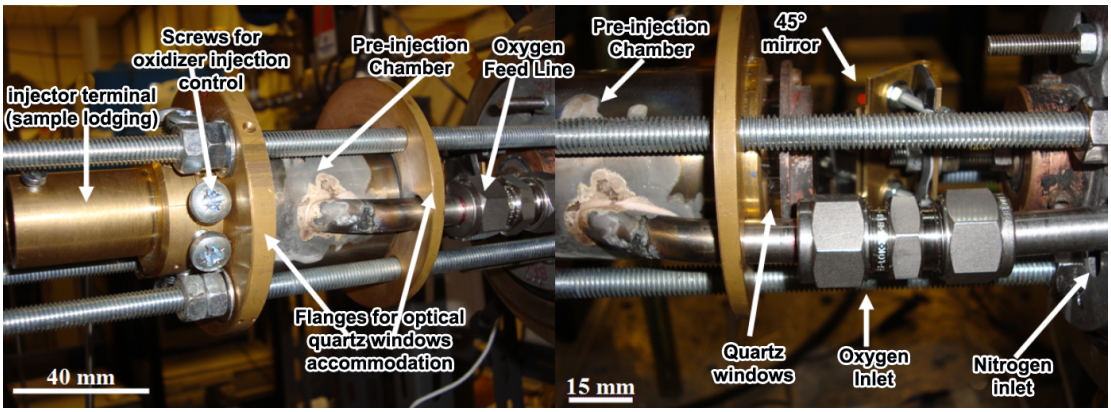

Figure 20.: 2D-Radial micro burner: injector details.

The solid fuel strands have a cylindrical shape, with a single central port perforation. The initial strand diameter (D_0) is 4 mm, with a web thickness of 7 mm and a grain length of 30 mm. The samples are connected to the injector by a brass cylinder, directly inserted into the injector-head. A great advantage of this setup is the possibility for independent regulation of the oxidizer mass flow rate and the chamber pressure, thus allowing the easily exploration of different test conditions. The oxidizer flow is measured by a digital mass flow-meter, Bronkhorst EL-FLOW SELECT (max flow rate of 250 $nlpm$), and regulated by a needle valve. During the combustion test the oxidizer mass flow rate is kept constant. When the combustion chamber is closed, the injector is totally included in and a nitrogen cold flow is injected in the outer region, during the test, to cool the injector and to keep clean the optical accesses from soot. The combustion chamber is connected by two pipes to six electro-valves that grant a constant pressure level during the firing. The electro-valves are driven by a pressure controller in a closed-loop: the instant chamber pressure, measured by a Kulite CT-190 pressure transducer, is compared with the threshold value set by the operator. The maximum pressure sustainable by the combustion chamber is 3.0 MPa but, because of the presence of optical accesses, the operating pressure must be limited below 2.0 MPa.

Sample ignition is achieved by pyrotechnic primer charge. The latter is inserted in the central perforation of the solid fuel grain and it is, in turn, ignited by a CO_2 laser beam impinging on it. The overall combustion process is recorded by a high speed camera Photron Ultima APX, which can operate at different speeds, up to 1000 fps, depending on the combustion duration and operating conditions. In some cases, when Photron is not available, the combustion recording is performed by a Xybion SVC-09. The video signal, is digitalized by a computer where all raw data are collected and stored. A more detailed description of the 2D-Radial micro burner is available in [124].

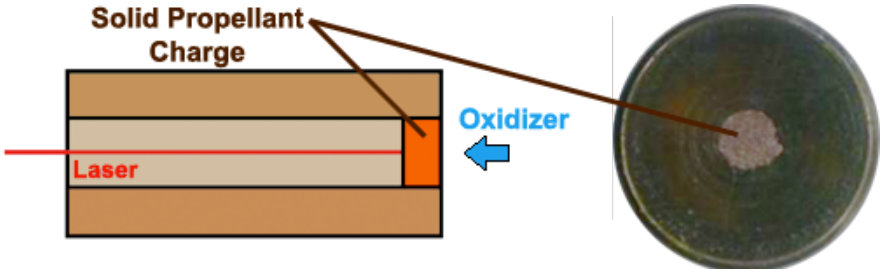

Figure 21.: 2D-Radial micro burner: laser ignition of solid propellant charge located in correspondence of the visualized section. Side view schematic (left) and frontal strand section with primer charge (right) [143].

5.1.3 Optical Time-Resolved Technique

An optical time-resolved technique for regression rate data reduction was implemented at the SPLab [124, 135, 144]. This non-intrusive technique is based on strand central port diameter sampling from the recorded combustion video, see Figure 22. During the test the head-end cross section is completely visible and the central perforation diameter is sampled along different radial directions (depending on combustion uniformity). Before the combustion test, the visible area is calibrated by a graduated paper, so that during the post-processing the distance between pixel can be related with the central port real size, see Figure 22.

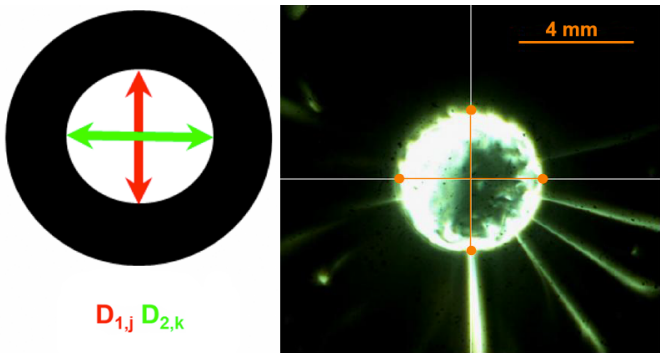

Figure 22.: Time-resolved optical technique: diameter sampling scheme (left) [124] and combustion visualization of the solid fuel head-end section (right)

The diameter sampling begins at the instant in which the flame is visible and completely distributed over the central port perforation, due to primer charge ignition. Depending on local grain head-end visualization quality [144], the sampling frequencies falls between 1 and 10 Hz. Usually two differently oriented local diameters are considered (e.g. vertical and horizontal), see Figure 22. For each local diameter three measures are achieved. The single local diameters $D_{j,k}(t_i)$, that are sampled at time t_i, are evaluated by observing the different brightness between the flame zone and

the regressing surface. Starting from the local measured diameters, the space-average mean diameter at $t_i(\overline{D}_i)$ can be defined as

$$\overline{D}_i = \frac{\sum_{j=1}^{2}\sum_{k=1}^{3} D_{j,k}(t_i)}{6} \tag{5.1}$$

The discrete D_i sequence is then fitted to achieve a continuos history of the space-average diameter evolution in time

$$\overline{D}(t) - D_0 = a_D \cdot (t - t_0)^{n_D}, \quad t \geqslant t_{ign} > t_0 \tag{5.2}$$

where the t_{ign} is ad hoc defined as the time which allows for the maximization of data fitting of Eq. 5.2. The definition of t_{ign} detailed discussed in [124]. Due to the fuel consumption, the central port diameter increases during combustion under steady operating conditions. The solid fuel ballistics can be completely defined starting from Eq. 5.2, as deeply described in [124, 135, 144, 145]. The histories of the r_f and of the oxidizer mass flux G_{ox} are defined as

$$r_f\left(t \geqslant t_{ign}\right) = \frac{1}{2}\frac{d\left[\overline{D}(t) - D_0\right]}{dt} = \frac{1}{2}a_D n_D (t - t_0)^{n_D - 1} \tag{5.3}$$

$$G_{ox}\left(t \geqslant t_{ign}\right) = \frac{\dot{m}_{ox}(t)}{\pi\frac{\overline{D}(t)^2}{4}} = \frac{\dot{m}_{ox}(t)}{\pi\frac{\left[D_0 + a_D (t-t_0)^{n_D}\right]^2}{4}} \tag{5.4}$$

The Eq. 5.3 is obtained by the time derivative of Eq. 5.2. The fuel mass flow rate and the oxidizer-to-fuel ratio can be obtained by substituting Eqs. 5.3, 5.4 into their relative expressions [124]. The results achieved by the time-resolved technique are checked by comparing them to the corresponding TOT data, in order to gain informations on data consistency between different reduction techniques, see Eqs. 5.5, 5.6, 5.7.

$$r_f(t_{ign}) = \frac{1}{2}a_D n_D (t_{ign} - t_0)^{n_D - 1} = \frac{n_D}{2} \cdot \frac{\overline{D}(t_{ign}) - D_0}{t_{ign} - t_0} \tag{5.5}$$

$$\langle r_f(t_{fin})\rangle = \frac{1}{t_{fin} - t_{ign}}\int_{t_{ign}}^{t_{fin}} r_f(t)\, dt = \frac{\overline{D}(t_{fin}) - \overline{D}(t_{ign})}{t_{fin} - t_{ign}} \tag{5.6}$$

$$\langle G_{ox}(t_{fin})\rangle = \frac{1}{t_{fin} - t_{ign}}\int_{t_{ign}}^{t_{fin}} G_{ox}(t)\, dt = \frac{\dot{m}_{ox}}{\frac{\pi}{4}\left\{\left[\overline{D}(t_{fin}) + \overline{D}(t_{ign})\right]/2\right\}^2} \tag{5.7}$$

The values obtained by TOT (right member in Eqs. 5.5, 5.6, 5.7) are compared with the analytical values (left member in Eqs. 5.5, 5.6, 5.7), defining an acceptable tolerance on their differences (below 1% for Eq. 5.5, 5% for Eq. 5.6, 5% for Eq. 5.7). In the developed time-resolved technique, Eq. 5.2 is defined for each of the performed tests. In order to summarize the achieved results, under the same operating conditions for a given fuel, various D_t are collapsed into an ensemble average curve. The latter is defined by a power-law interpolation of the time-trends identified by application

of Eq. 5.2 to the performed tests. The ensemble curve allows for the definition of proper error bars for D_t and $r_f(G_{ox})$. These are evaluated over the time (or G_{ox}) range, where at least two of the performed single runs are defined. Over this range, the error bars consist of confidence intervals centered on the average value resulting from the single test diameters at a given time, for Eq. 5.2, or regression rates at a given G_{ox}, for Eqs. 5.3 and 5.4. Confidence intervals are evaluated with 95% accuracy, more details in [124]. In order to compare the achieved results with literature data, a power-law approximation of analytical r_f vs. G_{ox} is proposed for each test and for ensemble curves, as

$$r_f(G_{ox}) = a_r \cdot G_{ox}(t)^{n_r}, \quad t \geqslant t_{ign} \tag{5.8}$$

5.1.4 Swirling Oxidizer

The 2D-Radial burner injector enables the control of the nature of the oxidizer flow. The standard injection configuration, with no swirling flow, involves all 8 channels left open, while in order to generate swirling flow it is possible to close some channels, as shown in Figure 23. Several preliminary tests were performed in order to evaluate the effective possibility of swirl flow in the 2-Radial micro burner; smoke was used to identify the swirl during initial cold flow visualizations. Finally, a quite well defined clockwise swirl was obtained by the intersection of four jets. In Figure 24, one can see the distribution of flame over the central perforation port during the combustion of a HTPB sample. It is easy to observe the presence of swirl, which does not appear symmetric with respect to the port diameter. This is due to the implemented injector configuration: the presence of only one oxidizer inlet into the pre-injection chamber may be the cause of such flow asymmetry.

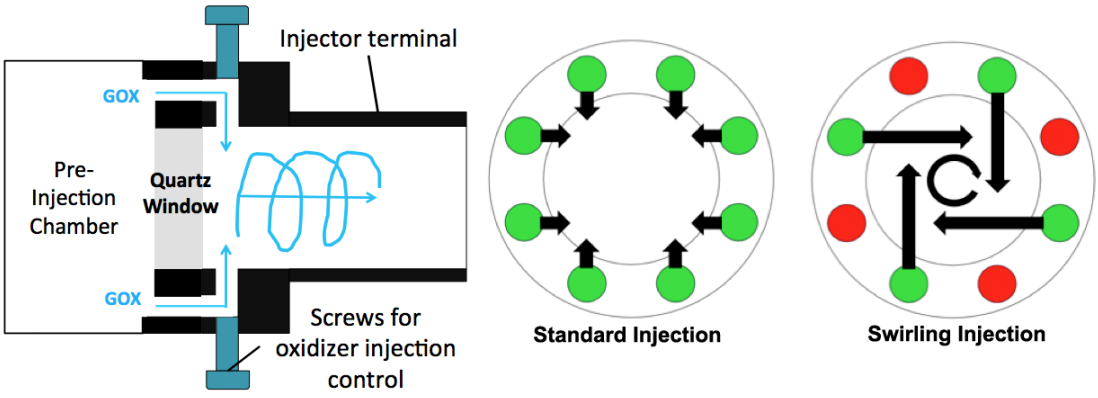

Figure 23.: Injector internal schematic (left), with reference to Figure 20. The 8 screws are configured to obtain standard injection flow (center) or swirling injection flow (right). The closed pipes are indicated in red [146].

Furthermore, the use of crossing jets instead of perfect tangential injection pipes involves the development of swirl in a restricted central zone of the main injector

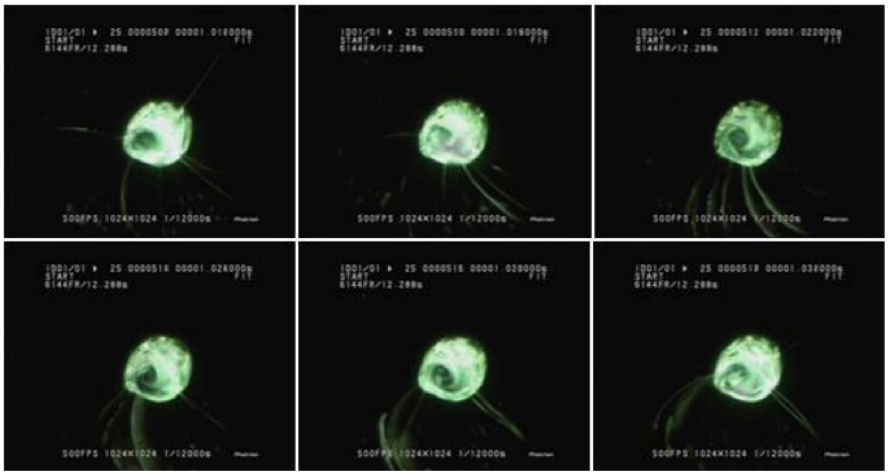

Figure 24.: Swirling combustion of HTPB: view of the head-end sample section (due to visualization by 45° mirror, high speed camera captures counterclockwise motion).

duct delimited by the jet directions. In the outer region it is reasonable to suppose the presence of recirculation. The small size of the injector and the experimental setup configuration do not allow for a direct measurement of the flow velocity components by anemometry neither by the use of more sophisticated techniques, such as Particle Image Velocimetry (PIV). Hence, in order to estimate the swirl intensity, it was used the approach suggested by Chang and Dhir [111, 112]. According to this method the ratio of the momentum flux through the injection pipes and the total momentum flux through the main duct section is correlated to the swirl intensity by an geometrical law

$$\frac{M_t}{M_T} = \frac{\dot{m}_t^2}{\dot{m}_T^2}\frac{A}{A_j} \tag{5.9}$$

where $\dot{m}_T$ and $\dot{m}_t$ are the total mass flow rates through the main duct and the injection channels, A is the cross-sectional area of the main injection duct, while A_j is the sum of the cross-sectional areas of all injection pipes. As in [111, 112], the injector geometry allows only for tangential inlet, hence the ratio between mass flow rates is equal to unity. Chang and Dhir provide an experimental law for local swirl intensity estimation

$$S = 1.48\left(\frac{M_t}{M_T}\right)^{0.93} \exp\left[-\tau\left(\frac{x}{D}\right)^{0.7}\right], \quad x/D \geqslant 2 \tag{5.10}$$

where

$$\tau = 0.113\left(\frac{M_t}{M_T}\right)^{0.35} \tag{5.11}$$

The swirl intensity S and its decay are evaluated as a function of the dimensionless axial distance from the injection section (x/D). Pursuant to Chang and Dhir investigation, the swirl decay rate is quite low at small distances from the injection section,

while it follows an exponential decrease moving downstream. The low decay rate can be associated with the presence of reverse flow and vortex breakdown observed very close to the injection location ($x/D \leqslant 2$) [111].

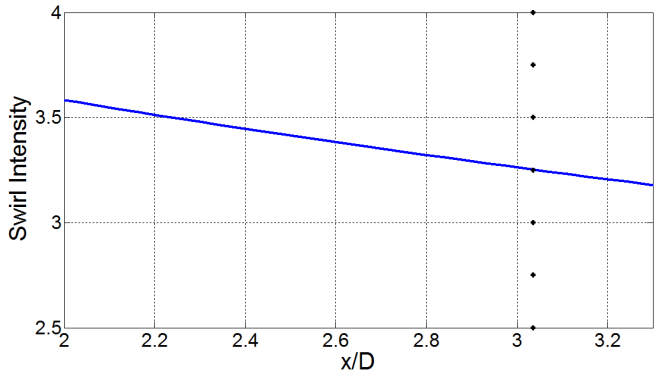

Figure 25.: Swirl intensity decay inside the 2D-Radial micro burner injector main duct. The black dots represent the axial position of the tested strand frontal section

In Figure 25, one can see the estimated values of swirl intensity and decay rate along the main injection duct, which connects the injection channels section with the frontal section of the tested strand. The Eq. 5.10 does not consider section changes in the swirl flow path. Thus the part of the curve beyond the dotted line reported in Figure 25 does not represent the swirl intensity inside the central perforation of the tested strand. The swirl intensity generated by the 2D-Radial micro burner injector is below 3.5, since the injection channels are not perfectly tangential to the main duct and the swirling flow is obtained by transversal crossing jets. This achieved S very small if compared with swirl intensities generated for hybrid combustion tests available in the open literature [70, 57, 147, 71, 55]. The swirl decay, during combustion into the solid fuel port, is influenced by different phenomena. The gaseous fuel released by the regressing surface initially travels normal to the surface, so that no additional angular momentum is introduced and the mass addition goes to reduce the mean tangential velocity component, thus the swirl intensity. Moreover, the heat addition into the boundary layer promotes a large temperature rise, which produces a large volume change. The latter involves an increase of the axial velocity component with the axial distance, with no any increase of tangential component [148]. Nevertheless, during combustion the wall surface roughness can be assumed negligible due to the barrier between swirling gases and the wall surface, produced by surface blowing. The latter consists in a lower impact in the swirl decay with respect to the swirl flow in a cold pipe.

New Swirl Injector

A new swirl injector was developed and tested in SPLab. Originally used to validate a fuel-embedded discrete resistive sensor based on the wire-cut technique [83], it was then evaluated as possible replacement for the injector of the 2D-Radial micro

burner. Also this new system burns cylindrical strands with a initial port diameter (D_0) of 6.0 mm, a web thickness of 12.0 mm and a fuel length of 70 mm. It was tested with no pressurization system and outside from a combustion chamber, thus each burn occurred at atmospheric conditions. The injector is designed to contain an interchangeable finned disk able to generate the desired swirl intensity. The disk used for the preliminary investigation was made by several winglets, see Figure 26, oriented to drive tangentially the oxidizer flow coming from the pre-injection chamber. Such disk produces a swirl intensity S of about 2.8 at the inlet section, according to Eq. 5.9. A smooth disk, without any winglets or channels is designed for tests with standard flow.

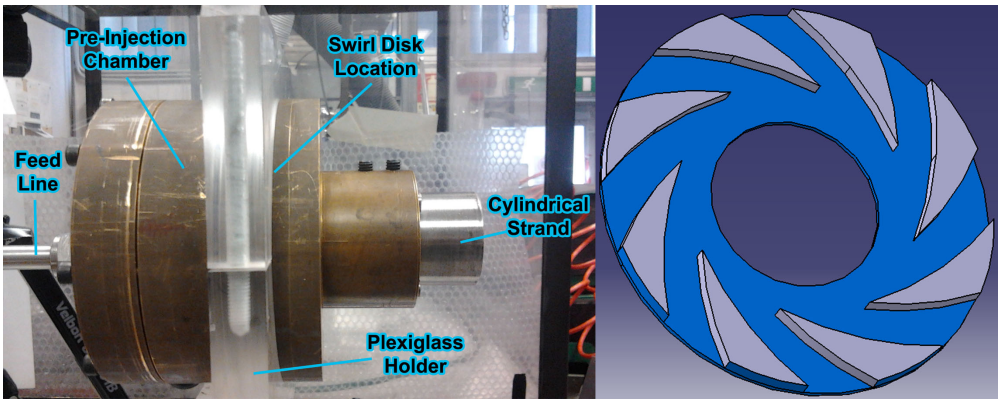

Figure 26.: New swirl injector schematic (left) and thinned swirl disk geometry (right).

The feed system is composed by two lines: the first with gaseous oxygen, used as oxidizer, while the second with gaseous nitrogen, injected for combustion interruption and system cooling after a burn completion. The oxidizer flow rate is regulated by a needle valve which allows for three fixed values: 140 nlpm, 210 nlpm and 340 nlpm. The optical acquisitions are performed by High Speed Cameras, by catching the strand side or throughout a quartz window placed behind the injector to see the combustion of the frontal strand section.

Figure 27.: Visualization of HTPB-based fuel combustion with swirling oxidizer (frontal strand section) with a frame rate of 50 fps.

In Figure 27, the swirling combustion visualization of a HTPB-based fuel sample is displayed. Although the injector disk includes 8 flow channels, just six inlets can be observed during the burn test (combustion of the frontal sample surface). This inconvenient is probably due to the presence of two elbow pipes for the oxidizer feeding into the pre-injection chamber; these two pipes will be replaced by two symmetric radially oriented inlets with respect to the injector central axis.

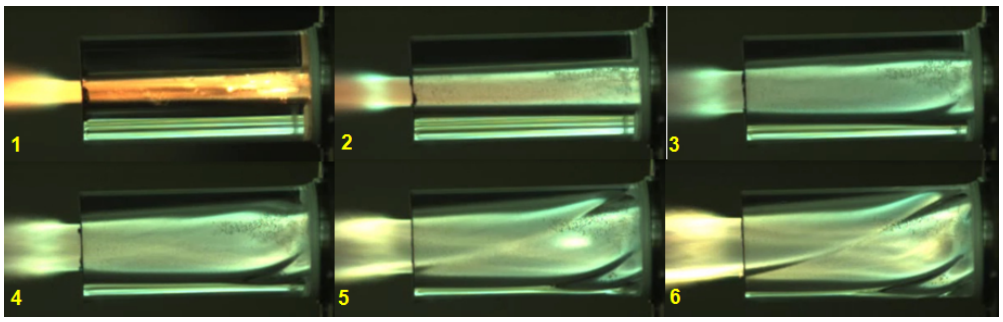

Figure 28.: Visualization of PMM fuel combustion with swirling oxidizer (side view).

In order to verify the presence of a marked swirling flow inside the fuel central perforation, few burn tests with PMM samples were performed. Thanks to its material properties and its high transparency grade, PMM allows for the combustion visualization along the fuel port. From Figure 28, one can see the port erosion, which results more intense at head-end of the cylindrical sample and decaying with the axial distance. The swelling region that one can see near the strand head-end is associated with the recirculation zone known as Central Toroidal Recirculation Zone (CTRZ), which occurs for swirling flows with $S > 0.6$ [149]. Similarly, it was observed by Yuasa et al. [150], by testing PMM and Polypropylene (PP) with swirling GOX, although more marked because of the significantly higher S generated.

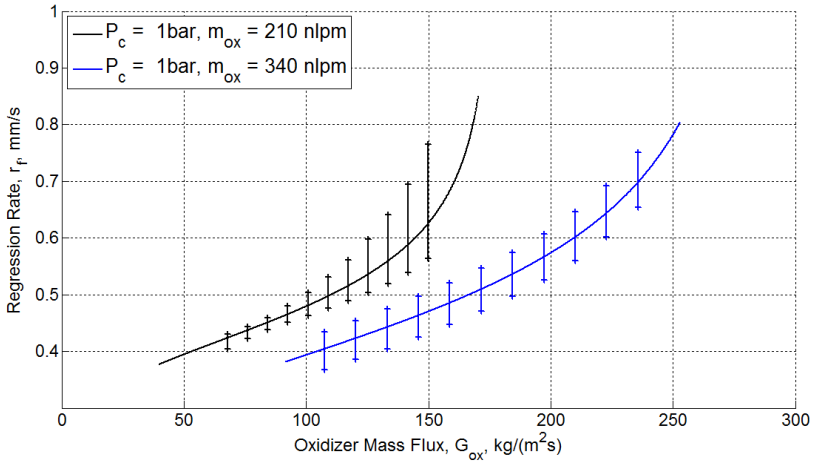

Figure 29.: Ballistic characterization of HTPB at ambient pressure conditions and swirling oxidizer for two different constant mass flow rates. Instantaneous regression rate ensembles achieved with optical time-resolved technique.

In Figure 29 one can see the ensemble curves, evaluated by means of the optical time-resolved technique, referred to HTPB combustions for two different constant mass flow rates $\dot{m}_{ox}$. In details, to an imposed $\dot{m}_{ox}$ of 340 nlpm corresponds an initial G_{ox} of 286 $kg/(m^2 \cdot s)$, with 6 mm of initial sample diameter, whereas to a $\dot{m}_{ox}$ of 210 nlpm an initial G_{ox} of 176 $kg/(m^2 \cdot s)$. Against the expectations, the fuel samples burned at lower mass flow rate constant value (i.e. at a lower initial G_{ox}) provided a higher regression rate than that achieved at 340 nlpm. Such behavior might be associated with the low pressure environment, in which the increased importance of surface kinetic [63] already provides a reduction of regression rate. Without any constraint (discharge nozzle), the combustion occurs at ambient conditions, quickly wasting in the outer environment the heat released by the hot gases. In this situation, the larger imposed oxidizer mass flow rate (blue curve in Figure 29) might produce a cooling effect on the diffusive flame, subtracting a part of the convective heat flux to the surface, hence limiting the regression rate. In support of this, in the recorded videos it was possible to observe, in some regions of the port, a melted fuel layer, destabilized by the turbulence flow during the combustion (no pictures are presented since on a single frame it is difficult to distinguish the melted from the solid phase). This might indicate that the eventually reduced heat flux transferred to the surface was not enough for the fuel gasification. The new injector could be better exploited by replacing the old one (see Figure 20) in the 2D-Radial micro burner. A more detailed ballistics characterization could be performed, considering different swirl intensities (different disk geometries).

HTPB with Swirling Oxidizer Flow

Combustion tests at a p_c of 1.0 MPa were performed for HTPB with swirling flow conditions. In this section, with the aim to provide an overview of the time-resolved technique operating steps, a representative history of $\overline{D}(t) - D_0$ is shown in Figure 30, while in Figure 31 the resulting $r_f(G_{ox})$ is presented. In Figure 30, one can see the space-averaged diameter history, which presents the typical behavior for the burning tests: a monotonic diameter increase for $t \geqslant t_{ign}$ due to solid fuel regression. According to Eq. 5.4, increasing $\overline{D}(t)$ yields a monotonically decreasing $G_{ox}(t)$. Consequently, the $G_{ox}(t)$ drop yields to the $r_f(G_{ox})$ decreasing behavior for increasing time observed in Figure 31. During combustion the r_f undergoes a monotonic decrease from its initial value. The initial value of the r_f exerts a limited influence on the final time-averaged regression rate, as shown by the $\langle r_f \rangle$ trend reported in Figure 31. The latter results in agreement with the overall TOT data characterizing the test. For the considered run, the power law approximation of Eq. 5.8 provides $n_r = (0.986 \pm 0.003)$. This value results relatively higher than the 0.8 identified by Marxman et al. [62, 63] for diffusion-limited turbulent combustion in standard flow conditions, highlighting a strong sensitivity to the mass flux under the investigated conditions. For swirling injection Yuasa et al. observed that the nature of the heat convective transfer is not modified [55], so obtaining power exponents close to that of standard conditions.

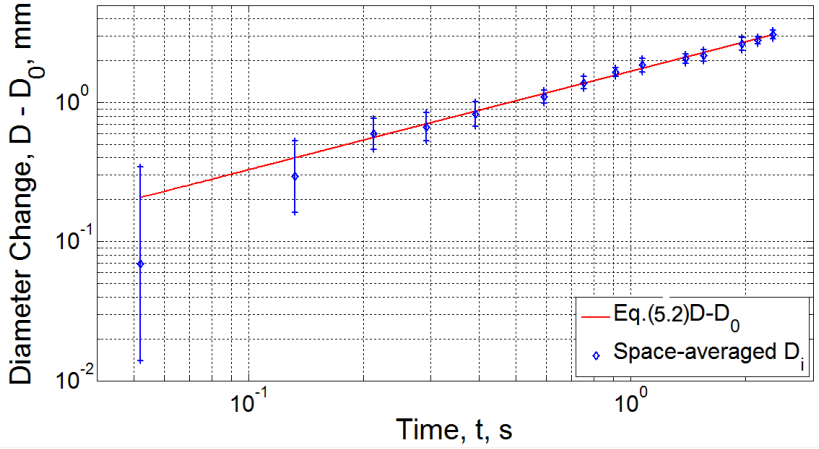

Figure 30.: $\overline{D}_i$ and history of space-averaged diameter in time for Test No. 03 (see Tables 3-4)

The high exponent obtained might be related to the strongly irregular swirling flow, generated by crossing jets, which may emphasize possible transient phenomena associated with the reacting boundary layer stabilization [124]. Moreover, the particular geometry of the injector, designed to allow for an optical access (see Figure 23) to visualize the frontal fuel section, presents a net cross-sectional change across the injection main duct and the fuel central perforation. The so imposed flow contraction and the recirculation, probably developed against the frontal fuel surface around the port inlet, might influence the flow pattern, as well as the boundary layer developing in the head-end region. In addition, a further small increase in the power exponent is due to the approximation of $r_f(G_{ox})$ by a power law (Eq. 5.8) with equi-spaced G_{ox} values instead of the fitting of measured data. Despite the poor data fitting, such choice provides a better power law approximation equally extended to the entire G_{ox} range. A complete and detailed description of the data reduction process and power law approximation is available in [124]. In spite of this difference in the single run exponent value, the ensemble average power law approximation of $r_f(G_{ox})$ with swirling flow results similar to the one with standard injection. However, in both cases, the achieved results are close to the value identified in [62, 63].

Test No.	$\mathbf{a_D}$ $\mathbf{mm/(s^{n_D})}$	$\mathbf{n_D}$	$\mathbf{R^2}$ Eq. 5.2
01	1.758 ± 0.019	0.718 ± 0.019	0.99
02	1.789 ± 0.024	0.715 ± 0.012	0.99
03	1.672 ± 0.026	0.707 ± 0.016	0.99
04	1.935 ± 0.013	0.685 ± 0.007	0.99
Ensemble	1.789 ± 0.001	0.713 ± 0.001	0.98

Table 3.: Power law fitting of $D(t)$, relevant parameters of Eq. 5.2.

Table 3 presents the diameters sampled in single runs; a high data fitting resulted for the Eq. 5.2 due to the ad hoc definition of t_{ign}. The identified $\overline{D}(t)$ trends yield

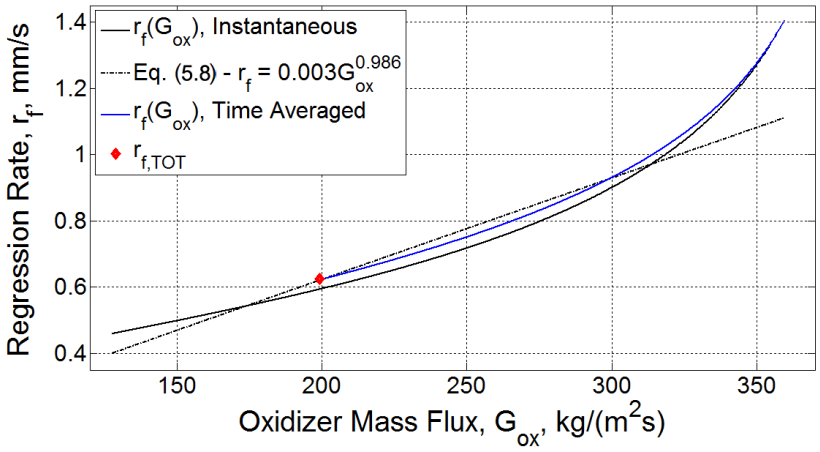

Figure 31.: Instantaneous and time-averaged $r_f(G_{ox})$ for Test No. 03. The power-law approximation of instantaneous data does not capture initial r_f.

Test No.	Eq. 5.5	Eq. 5.6	Eq. 5.7
01	1.2	0.2	0.8
02	0.6	2.6	0.9
03	1.8	0.9	0.4
04	1.4	−3.4	1.8

Table 4.: Consistency checks for single tests of HTPB in swirling flow, expressed as percent values evaluated with respect to the TOT data.

to a high consistency between time-resolved and TOT data, see Table 4. In Figure 32, one can see the ballistic characterization of the HTPB with swirling flow with respect to the baseline in standard flow, while in Table 5 are reported the relevant parameters of the Eq. 5.8 at the considered operative pressures. Because of the marked initial r_f is not captured by the power law approximation the data fitting applied to the achieved $r_f(G_{ox})$ is relatively low.

p_c MPa	a_r $(mm/s)/(G_{ox}^{n_r})$	n_r	R^2 Eq. 5.8
1.0	0.006 ± 0.001	0.894 ± 0.008	0.92
Baseline[a]	0.007 ± 0.001	0.856 ± 0.003	0.89

Table 5.: Power law approximation of $r_f(G_{ox})$, relevant parameters of Eq. 5.8 for HTPB ensemble with swirling flow ([a]Baseline with standard flow, see [144]).

In Table 6, the regression rate percent enhancement obtained by swirling flow injection is reported. The generated swirling flow provides r_f enhancements over 10% for $G_{ox} \geqslant 250$ kg/(m$^2 \cdot$ s) values. In particular, for $G_{ox} = 350$ kg/(m$^2 \cdot$ s), the regression rate enhancement with respect to the baseline is 28%. The quite low r_f increase observed seems in agreement with the estimated low swirl intensity, in turn yielding only a minor heat transfer enhancement with respect to the standard flow conditions.

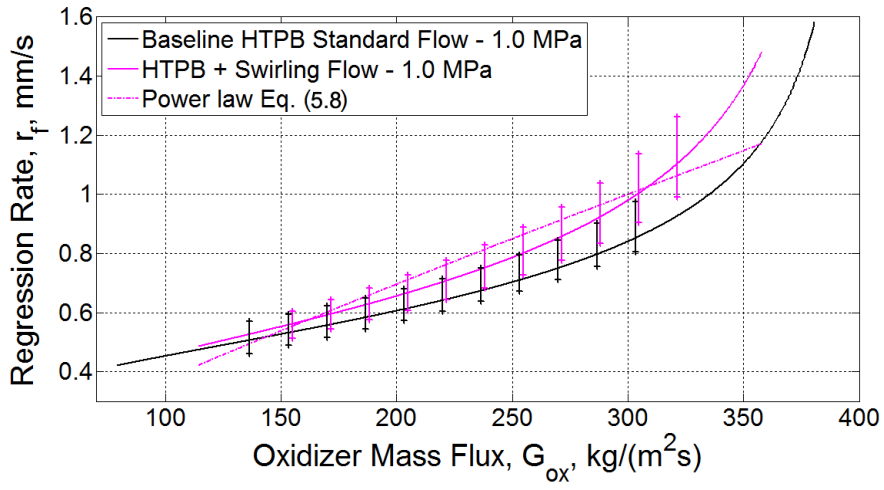

Figure 32.: Ballistic characterization of HTPB with swirling injection at 1.0 MPa. Baseline data from [144].

HTPB Swirl vs. Baseline[a]	**G_{ox} kg/(m² · s)**				
	350	**300**	**250**	**200**	**150**
1.0 MPa	28.1	17.4	10.9	5.8	1.1

Table 6.: HTPB + Swirling flow percent r_f enhancement with respect to baseline at 1.0 MPa([a]Baseline with standard flow, see [144]).

Furthermore, the swirl generated by crossing jets results less uniform and more conditioned by lateral recirculation zones if compared to a swirl generated by perfect tangential injection pipes.

5.1.5 Metal Additives

Fuel Formulation and Selected Additive

Besides the pure HTPB, a fuel formulation with 10% activated micro-sized aluminum powder (A-Al1) is considered. Details of the HTPB binder formulation are reported in Appendix G, while the A-Al1 characteristics are presented in Table 7. A curing level (-NCO/-OH) of 1.04 is chosen for HTPB binder. For the latter, dibutyltin diacetate is used as curing catalyst: it is added in excess to the formulation as 0.005% of the (HTPB+IPDI) mass. The solid fuel manufacturing is performed at controlled conditions and under vacuum. All the ingredients are mechanically mixed by an impeller (100 rpm). The complete description of the manufacture process is available in Appendix G. The A-Al1 powder was supplied to SPLab by FOI (Swedish Defence Research Agency) in the frame of the HISP (High Performance Solid Propellants for In-Space Propulsion) FP7 program.

Powder Characteriscs	A-Al1	Valimet H-3
Active Al Content, Al^0, %	93.2 ± 0.9	98.3 ± 0.7
Mass Average Diameter D_{43}, µm	5.5	5.1
Span	1.66	1.78
Specific Surface Area S_{sp}, m^2/g	2.6	1.2

Table 7.: Comparison between A-Al1 and starting conventional Al powder (Valimet H-3). Details are discussed in [151, 152].

The powder was produced starting from spherical 5.1 µm Valimet H-3 (batch 07-8002) by an activation process. No details are given about the latter, while a detailed characterization of the powder is reported in [151, 152]. The A-Al1 has a mass mean diameter of 5.5 µm (see Table 7). The active Al content is evaluated by hydrogen evolution from $Al + H_2O$ reaction, which yields a lower result for A-Al1 than for standard Valimet H-3. The higher specific surface area (S_{sp}) of A-Al1 powder should provide an enhanced reactivity with respect to micron-sized Valimet H-3, producing higher ballistics performance [151, 152].

HTPB + A-Al1 with Standard Oxidizer Flow

These combustion tests, as well as the techniques combination approach, were performed in collaboration with C. Paravan, at SPLab. In Figure 33, one can see the ballistic characterization of HTPB + A-Al1 with standard flow at 1.0 MPa, whose data are reported in Tables 8 and 9. Four combustion tests are used to evaluate the ensemble.

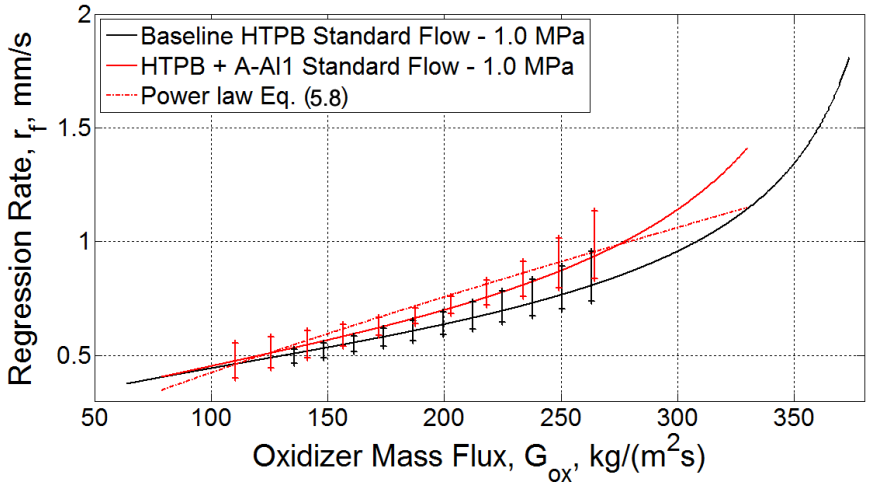

Figure 33.: Ballistic characterization of HTPB with standard injection at 1.0 MPa. Baseline data from [140].

For these tests, the presented baseline exhibits minor differences with respect to the one discussed in the previous section, due to minor changes to the injector standard configuration [140]. In spite of slight differences in r_f absolute value, the data collected with the same setup configurations enable the investigated fuel/injection technique relative grading with respect to the corresponding baseline fuel. The relative grading of the metallized fuel with respect to the baseline, burning under the same operating conditions and injector implementation, shows regression rate enhancements similar to those achieved burning HTPB with swirl injection (see Table 6 and Table 9).

p_c **MPa**	a_r $(mm/s)/(G_{ox}^{n_r})$	n_r	R^2 Eq. 5.8
1.0	0.009 ± 0.001	0.835 ± 0.002	0.94
Baseline[a]	0.012 ± 0.001	0.778 ± 0.003	0.89

Table 8.: Power law approximation of $r_f(G_{ox})$, relevant parameters of Eq. 5.8 for HTPB + A-Al1ensemble with standard flow ([b]Baseline with standard flow, see [140]).

The ballistic response of HTPB + A-Al1 shows a percent r_f increase of 19% with respect to baseline at 300 $kg/(m^2 \cdot s)$. The performance enhancement monotonically decreases as G_{ox} decreases. Only a faint 2.2% increase is achieved at 100 $kg/(m^2 \cdot s)$. Fuels loaded with conventional micron-sized Al powders usually exhibits a different behavior, with minor r_f enhancements for high G_{ox} values (due to the high thermal inertia of particles) and augmented performance for lower oxidizer mass fluxes due to the radiation heat transfer contribution [55, 140]. As shown by the n_r value reported in Table 8, under the investigated conditions HTPB + A-Al1 presents a G_{ox} sensitivity close to the one of the baseline.

HTPB + A-Al1 vs. Baseline[b]	G_{ox} $kg/(m^2 \cdot s)$				
	300	**250**	**200**	**150**	**100**
1.0 MPa	19.1	13.9	9.8	6.1	2.2

Table 9.: HTPB + A-Al1 percent r_f standard flow: percentage r_f enhancement with respect to baseline at 1.0 MPa([b]Baseline with standard flow, see [140]).

The different behavior of A-Al1 loaded fuel is related to the characteristics of the activated powder which shows a significant larger specific surface area S_{sp}, becoming more reactive with respect to common micron-sized aluminum powder. Similar behavior was observed for nano-sized powders (ALEX) [124] characterized by even higher S_{sp} values and consequently stronger reactivity. In the early phase of combustion, under high convective heat feedback, the regression rate is enhanced by the high reactive nano-sized additive while, once the heat feedback is reduced, in correspondence of low G_{ox} the powder seemed to behave as a thermal sink. By considering the achieved results for the micron-sized A-Al1, under the tested conditions, the significant lower r_f increase measured at lower G_{ox} could be similarly attributed to a

thermal sink behavior of the powder, probably favored by agglomeration phenomena, typically observed for micron-sized metals, together with a low Al content with respect to non-activated aluminum powder.

5.1.6 Techniques Combination - Results and Discussion

The final step consists in the combination of two regression rate enhancement techniques: a swirling oxidizer flow with a metallized HTPB fuel formulation, with the aim to exploit the higher heat exchange promoted by swirl to achieve a better and complete combustion of the metal additives. In Figure 34, one can see the ballistic characterization of HTPB + A-Al1 with swirling flow at 1.0 MPa; it is compared with the same formulation at the same chamber pressure but with standard flow. The ensemble curve is composed by the data of three performed runs. Table 10 reports the relevant parameters of power law approximation for the metal loaded formulation burned with swirling flow at 1.0 and 1.9 MPa. The combustion with swirling flow exhibits a quite low r_f enhancement with respect to the same fuel formulation in standard flow. As it is possible to see from Table 11, the regression rate percent increase at different G_{ox} remains below 10% and almost zero for $G_{ox} \geqslant kg/(m^2 \cdot s)$. Furthermore, in Figure 34, the error bars of the two ensembles are quite completely overlapped, meaning that the difference between the measured regression rates is very small.

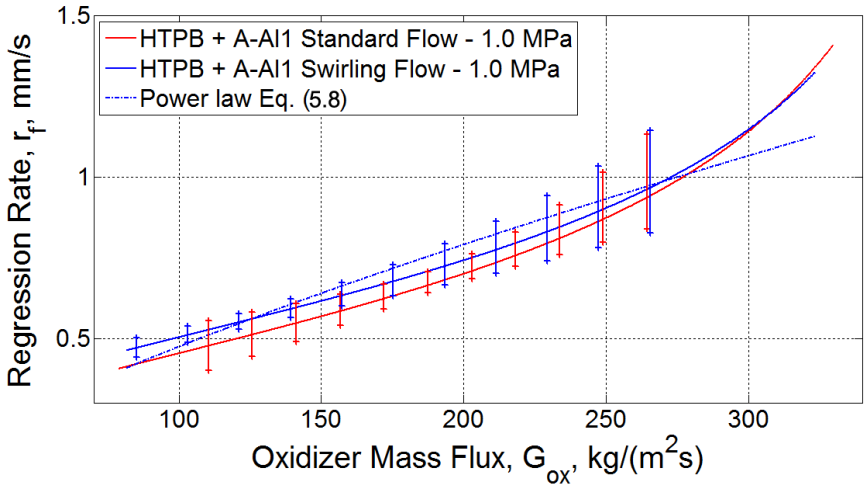

Figure 34.: Ballistic characterization of HTPB with standard injection and swirling injection at 1.0 MPa.

In Table 12, the r_f percent enhancement of HTPB + A-Al1 with swirling combustion between 1.0 and 1.9 MPa is compared to the one of the baseline burning in the same p_c range, but with standard injection. The higher chamber pressure seems to promote a higher regression rate in swirling conditions as shown by the r_f percent increases evaluated at different G_{ox}. Nevertheless, by comparing the increase of the swirl case with that of baseline under standard flow conditions, it is easy to observe a variance

p_c MPa	a_r $(mm/s)/(G_{ox}^{n_r})$	n_r	R^2 Eq. 5.8
1.0	0.016 ± 0.001	0.737 ± 0.005	0.95
1.9	0.019 ± 0.001	0.722 ± 0.005	0.95

Table 10.: Relevant parameters of Eq. 5.8 for HTPB + A-Al1 with swirling flow.

of the same order. Under the investigated conditions, the swirling combustion with metal additives is faintly influenced by p_c changes. A detailed discussion of p_c effects on solid fuel observed in the 2D-Radial micro burner is reported in [140, 144]. The use of swirling flow for HTPB with micron-sized A-Al1 does not seem to provide significant regression rate enhancements. This behavior could be mainly associated with the low intensity and the low uniformity of the generated swirl by the injector system of 2D-Radial micro burner. Under the investigated conditions the swirl intensity does not induce significant enhancement of the heat transfer coefficient.

HTPB + A-Al1 Swirl vs. Standard Flow	G_{ox} $kg/(m^2 \cdot s)$				
	300	**250**	**200**	**150**	**100**
1.0 MPa	0.5	3.5	6.0	8.4	11.0

Table 11.: HTPB + A-Al1 swirling flow percent r_f enhancement with respect to the standard flow injection at 1.0 MPa.

This yields limited r_f enhancement with respect to the standard flow injection for both baseline and A-Al1 loaded fuels. For the metallized fuel formulations, standard flow and swirl injection produce similar regression rate increases with respect to the baseline, under the investigated operating conditions. These are mainly related to the enhanced reactivity of A-Al1 which provides greater r_f for $G_{ox} > 200$ $kg/(m^2 \cdot s)$ with respect to the baseline. The swirl flow does not promote further r_f increase or improvements in the overall quality of the combustion process. This is testified by the presence of condensed combustion products (CCPs) detaching from the solid fuel grain during the combustion (see Figure 35). Though no quantitative evaluation of CCPs sizes was performed, no significant qualitative differences exist between the standard and the swirl injections in the observed burning behavior of HTPB + A-Al1.

1.9 MPa vs. 1.0 MPa	G_{ox} $kg/(m^2 \cdot s)$				
	300	**250**	**200**	**150**	**100**
HTPB + A − Al1 Swirl	17.5	13.8	12.8	11.1	9.1
Baseline[b]	21.3	17.4	14.3	11.4	8.4

Table 12.: Baseline and HTPB + A-Al1 r_f increases for p_c of 1.0 and 1.9 MPa. For the metallized fuel a swirling injection is considered, while baseline data refer to standard flow.

In conclusion, under the tested operating conditions, for $G_{ox} = 350\ kg/(m^2 \cdot s)$ a percent r_f enhancement of 28% with respect to standard flow injection was achieved. This performance enhancement decreases as combustion proceeds, and nearly disappears for $G_{ox} = 100\ kg/(m^2 \cdot s)$. A HTPB-based fuel formulation loaded with micron-sized A-Al1 was burned with standard and swirling oxidizer flow injections.

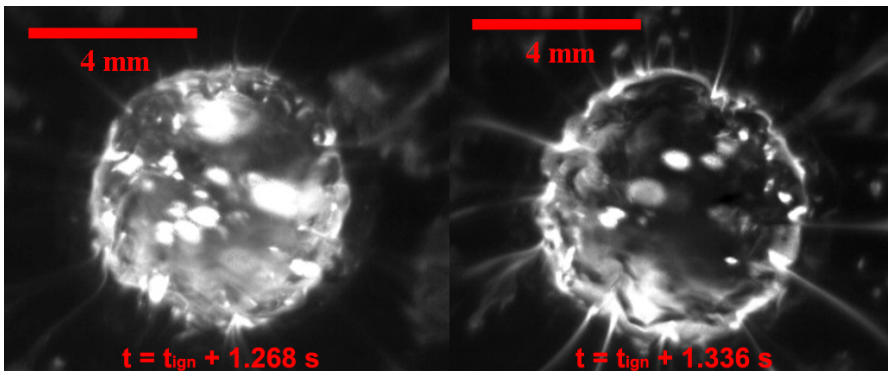

Figure 35.: Overall combustion quality of HTPB + A-Al1 results low for both standard flow injection (left) and swirling flow (right) [152].

Under the investigated conditions, the use of standard oxidizer flow for the combustion of HTPB provides a regression rate enhancement of 19% for $G_{ox} = 300\ kg/(m^2 \cdot s)$, with respect to the baseline. The combustion of HTPB + A-Al1 with swirl injection provides percent r_f increases similar to those achieved by the same fuel formulation burning with standard flow, though swirl provides better performance as G_{ox} decreases (Table 11). For $G_{ox} < 150\ kg/(m^2 \cdot s)$ the generated low intensity swirl limits the convective heat transfer reduction providing a combustion less sensitive to G_{ox} changes. Though further analysis are required, this result suggests the possibility of limiting the performance shift of burning hybrid systems by means of swirl injection. Under the investigated conditions, the performance of HTPB + A-Al1 highlighted the effectiveness of the powder activation process to enhance the reactivity of micron-sized additives. The A-Al1 shows the possibility to tailor the additive characteristics yielding a micron-sized powder (it does not require dedicated dispersion procedures) with enhanced reactivity. Further investigations would consider higher swirl intensities, to promote larger convective heat exchanges, and different additives type, such as nano-sized aluminum powders. In term of swirl, the actual potential of the 2D-Radial injection system is quite limited and the obtained swirling flow is weak and characterized by poor efficiency. In the next future, the 2D-Radial micro burner will be equipped with a new swirl injector (described in Section 5.1.4), which will allow for a better swirl quality and a more precise selection of its intensity, for several investigation purposes.

5.2 SOLID FUEL AGING

5.2.1 Introduction

The propellant selection for a space mission, besides the obtainable performance, must take into account both the mechanical properties and long-term storability. Considering solid material (fuel or propellant binder), its resistance to strong thermal and fluid dynamic stresses is fundamental for a safety motor firing. In fact, a weak material could crack generating large fragments able to close the nozzle throat, with the risk of engine explosion. Because of this, high mechanical properties are required and the material quality must be preserved as long as possible during the storage. Concerning the space debris problem, new satellites must be equipped with small engines able to perform their de-orbiting after the mission completion. Satellite missions in LEO can be long, even several years, therefore the selected propellants must conserve their characteristics for the required time. The use of hybrid rockets for Post Mission Disposal (PMD) seems a cheap and advantageous solution and, in this case, HTPB offers high mechanical properties with a safe and quite easy manufacturing process. Nowadays, despite its large use in space propulsion field, the aging behavior of HTPB-based material is not so well understood. In this respect, the open literature offers only few available investigations, in which the dynamic testing is used to study the aging process of such elastomer [153]. The elastomers are materials whose mechanical properties depend on their manufacturing process, as well as their ingredients composition. These materials are able to sustain large deformations without any permanent change, recovering easily the original shape [154, 155]. Generally the plastic material used in the industrial field are not made of pure elastomers, but by a mix of monomers or basic polymers, linked each others in order to create chains and networks. Moreover, chemical agents (fillers: active charge or inert) are introduced into the mix, to reinforce the final material. The active charges (to reinforce) increase the mechanical properties, such as hardness and ultimate strength, much more than inert charges. Plastic materials are divided in two categories:

- *Thermoplastic Polymers:* this kind of material is characterized, at chemical level, by linear chains that flow one each others after heating. When this material is kept heating at a precise temperature its consistency allows the manufacture, then, by decreasing the temperature, it is possible to freeze the material with the desired shape. This process can be performed many times before reaching a significant level of material decay. All thermoplastic polymers are characterized by a high level of elasticity;
- *Thermosetting Polymers:* this kind of material is characterized by a tridimensional polymeric structure (after cross-linking process), which provides higher hardness respect to linear polymers and not solubility to solvents, such as Toluene. The cross-linking process is accelerated by the increase of curing temperature and by the addiction of chemical catalysts. The hardening process is not reversible, hence it is not possible to mold the material more times than one.

In the field of space propulsion the typical materials used as solid fuels are both thermoplastic polymers, such as PMM and PE, and thermosetting polymers, such as HTPB. This one is abundantly used in SPLab as binder for solid propellant and solid fuel for hybrid combustion. The pure HTPB is presented as a liquid with the viscosity of honey. The mixing step occurs at sub-atmospheric pressure, in order to extract all the air bubbles that may remain trapped due to polymer viscosity. The presence of air bubbles in the cross-linked material would undermine the mechanical characteristics and the ballistic properties of combustion. During the mixing a small percentage of energetic additives can be added, such as micro or nano powders, in order to increase the ballistic performance. The obtained mixture is then poured directly inside the engine case, equipped with suitable molds, necessary to impart the desired shape to the solid grain. Once cast into the case, the HTPB is still in a liquid state. Therefore it is necessary to subject it to heat treatment to get a complete cross-linking. At this point the mold can be removed and, after a period of storage, the material is ready to be used. The mechanical characteristics of the final product must be able to withstand the engine ignition, which in few instants pressurizes the combustion chamber by subjecting the solid fuel to compression and high thermal and fluid dynamic stresses, caused by the combustion process itself. The solid fuel must be able to sustain such efforts without fragmentation, which could cause the clogging of the nozzle throat, with the risk of engine explosion. However, unlike solid propellants, in hybrid rockets the presence of cracks in the solid fuel is not a source of dangerous combustion instability, due to the nature of the diffusive flame, and this is a big advantage in terms of safety and simplicity in the manufacture of material.

5.2.2 Aging Behavior

HTPB is an hygroscopic material, very sensitive to the presence of humidity. In order to keep unchanged its properties, the storage in an anhydrous environment is required. The conservation process is essential for the maintaining of design features over time, until 10/20 years. For example, the ingredients of HTPB-based propellants or solid fuels can interact with the atmosphere or each to another, involving irreversible changes, especially in term of mechanical properties. These deterioration may be a critical factor during the combustion phase at high pressures, causing possible decreases of ballistics performance or material fragmentation. The aging of HTPB-based material is a consequence of several processes:

- Mechanical processes as vibration, thermal slump, thermally induced stresses during temperature changes;
- *Chemical* processes as oxidative cross-linking, chain scission by hydrolysis and consecutive reactions following oxidative attack, antioxidant depletion, binder oxidation;

- *Physical* processes as plasticizer depletion and migration, humidity, presence of liquid burn catalyst (depletion by migration), phase transition, dewetting.

Chemical and physical aging can typically be promoted by hydrolytic, oxidative or thermal reactions and diffusion phenomena governed by kinetic processes. Swelling, hardening, softening and discoloration was observed [153]. However, for hybrid propulsion, HTPB is used as solid fuel, without addition of oxidizer ingredients, thus the impact on aging caused by chemical reactions may be less predominant, with respect to thermal and hydrolytic reactions. The aging of a polymeric material can be simulated by accelerated-aging tests, consisting in a prolonged thermal curing. This procedure is able to modify the material characteristics in the similar way of a natural aging of several years. The material is aged at a range of temperatures and, during the aging period, the samples are tested by Dynamic Mechanical Analyzer (DMA), in order to measure mechanical properties such as the Storage and Loss Modulus or tensile strength. Thus the material characteristics change-rate can be evaluated for each test temperature. Assuming that the storage temperatures activate an identical aging mechanism [153, 156, 157], using the Arrhenius equation one can estimate the aging rate constant:

$$k_i = A \cdot exp\left(-\frac{E_a}{R^\circ T_i}\right) \tag{5.12}$$

where A is the pre-exponential, R° is the ideal gas constant and T is the temperature. Starting from Eq. 5.12 it is possible to find out an expression to relate the in-service time aging with the accelerated aging test time, thus the time-temperature profile. It is important to consider that high temperatures might activate mechanisms that, under typical storage conditions, are not present. Because of this, the accelerated-aging tests are performed at low temperature ranges, usually up to 70°-80°. The Layton model is a good approach to analyze the aging processes [153]; it describes the relative change of mechanical properties, such as strain, Young's modulus, maximum stress and hardness. By the integration of the following empirical relation

$$\left(\frac{dP(t,T)}{dt}\right)\Bigg|_T = \frac{S_p(T)}{t} \tag{5.13}$$

one can obtain

$$P(t,T) = P_0(t_0) + S_p(T) \cdot c \cdot \log\left(\frac{t}{t_0}\right) \tag{5.14}$$

where P_i is the physical property at aging time t_i (t_0 is referred to the start time), T is the aging temperature, S_p is the scaling parameter and c is a constant equal to $\ln(10)$. Eq.5.14 describes the material behavior and predicts the change of P after long aging time. Now, by considering the hypothesis of identical aging both for accelerated and natural aging, hence

$$P(t_a, T_a) = P(t_n, T_n) \quad \text{and} \quad P_0(t_0, T_a) = P_0(t_0, T_n) \tag{5.15}$$

the Eq. 5.14 is rewritten as

$$t_n(T_n) = t_0 \cdot \left(\frac{t_a(T_a)}{t_0} \right)^{\frac{S_p(T_a)}{S_p(T_n)}} \tag{5.16}$$

where the index n is referred to the natural aging, while index a referred to accelerated aging. Eq.5.16 is known as Layton model, used to predict the polymer behavior after aging, correlating the accelerated and natural aging. The combination of Layton model with the Arrhenius law (for aging acceleration factor estimate) provides a satisfying description of the polyurethane behavior. However, the mathematically description of energetic material degradation by kinetic models is very complex, due to the competition of several reactions with different kinetic orders and autocatalyst.

5.2.3 Accelerated Aging

In this research project the Storage modulus, the Loss modulus and the damping efficiency (tanδ) of HTPB have been measured by DMA and analyzed according to Arrhenius methodology. Hexahedral samples of 35x15x5 mm (see Figure 136, Appendix G) have been realized using HTPB R45 (45 is the number of monomers) supplied by AVIO Space; in Appendix G HTPB composition and manufacturing are detailed described. The time-temperature profile was established considering the empirical formula known as *van't Hoff rule* [157], or *RGTrule*, for four different temperatures: 60°, 70°, 80°, 90°C. The accelerated aging is the only way to investigate the aging characteristics of a material in a short experimental time. By the increasing of its in-service temperature, chemical and physical aging processes can be accelerated. To predict the in-service time of HTPB-based material one can use the Arrhenius equation, see paragraph 5.2.2, which states the proportionality between the equivalent use time, at any accelerating temperature, and the activation energy E_a, for the physico-chemical process considered. The main hypothesis in support of the Arrhenius approach is that the chemical processes occurring at the accelerating temperature exposures and those that occur under the natural aging are identical [156]. Nevertheless, this assumption is not always true, hence the data results may not be the same observed during a natural aging. The long-term behavior evaluation under HTPB storage conditions requires thermal treatment at different temperatures, in a range between 30°-90°. A high test temperature means a shorter time under thermal load stress. However, in correspondence of 80°-90° it is necessary to take into account the possible activation of mechanisms that do not belong to typical operative in-service conditions.

Time-Temperature Profiles

In order to design a time-temperature profile program it is possible to find out an expression suitable for chemically aging processes, starting from the Arrhenius equation. Therefore, considering the aging constant k for two temperatures

$$k_1 = A \cdot exp\left(-\frac{E_a}{R^\circ T_1}\right) \quad and \quad k_2 = A \cdot exp\left(-\frac{E_a}{R^\circ T_2}\right)$$

stating the logarithm

$$lnk_1 = lnA - \frac{E_a}{R^\circ T_1} \quad and \quad lnk_2 = lnA - \frac{E_a}{R^\circ T_2}$$

and deducting the two equations

$$lnk_2 - lnk_1 = -\frac{E_a}{R^\circ}\left(\frac{1}{T_2} - \frac{1}{T_1}\right)$$

one can obtain, considering the inverse ratio between the time t_i and the reaction rate constant k_i

$$t_i \propto \frac{1}{k_i} \tag{5.17}$$

$$\frac{k_2}{k_1} = exp\left(-\frac{E_a}{R^\circ}\left(\frac{1}{T_2} - \frac{1}{T_1}\right)\right) = \frac{t_1}{t_2}$$

Now, the scaling can be done from t_T and T_T, time and temperature at test conditions, to the looked for data t_E or T_E (temperatures are in K), hence one can write

$$t_E = t_T \cdot exp\left(\frac{E_a}{R^\circ}\left(\frac{1}{T_E} - \frac{1}{T_T}\right)\right). \tag{5.18}$$

Eq. 5.18 allows the scaling of test time t_T to the target time t_E, considering the temperatures T_E and T_T in the Arrhenius equation.

Empirical Formula - van't Hoff rule

Considering an aging process caused by chemical reactions and assuming low activation energy in a two steps mechanism [157], the aging process can be quite reasonable described with the *van't Hoff rule*:

$$t_E\,[y] = t_T\,[d]\,F^{\left(\frac{T_T - T_E}{\Delta T_F}\right)} \cdot \frac{1}{365.25d} \tag{5.19}$$

where t_E is the time in years at temperature T_E while t_T is the test time in days at temperature T_T, F is the reaction rate change factor, or simply scaling factor, per the temperature interval ΔT_F. The two temperatures are referred to Celsius scale. Eq. 5.19 is an empirical formula, suitable with activation energy values from 80 to 120 kJ/mol and temperatures between 20°-90°C. The scaling factor F assumes a value around 3 or 4 per 10°C of temperature change interval ΔT_F [156, 157].

5.2.4 HTPB-based Fuel Aging Program

In hybrid propulsion the HTPB polyurethane resin is used as fuel, without addition of oxidizer substances. The activation energy E_a of polyurethane resin is about 82 to 150 kJ/mol [158], while the temperature interval considered for the accelerated aging is between 60°C and 90°C; these values are suitable for the application of the *van't Hoff rule*, obtaining a scale factor F of about 3.8 per 10°C of ΔT_F. However, in order to design the aging plan in a conservative way, a scale factor of 2.5 was chosen, performing a longer thermal treatment than that corresponding to higher scaling factors (between 3-4). Four temperatures have been taken into account to simulate 10 years of aging: 60°C, 70°C, 80°C, 90°C. One can see that the temperature range is quite large. First of all because the available period for this research was short, secondly the furnaces availability in our laboratories depends on the need of several other researches. Therefore, to perform the aging at temperatures below 60°C would take too much time, making not possible to proceed with this work. The highest temperature allows to complete the accelerated aging in a very short time, less than one month. Nevertheless, a different trend has been found for the mechanical properties, probably due to chemical or thermal reactions that attend only for high temperatures. Considering the formula 5.19, in table 13, one can see the amount of days required to simulate 10 years of aging, for the considered temperature range:

Temperature	**2years**	**4years**	**7years**	**10years**
60°C	27	59	104	148
70°C	12	24	42	59
80°C	5	10	17	24
90°C	2	4	7	10

Table 13.: Number of accelerated aging days to simulate 10 years of natural aging

These values have been evaluated considering a scale factor of 2.5 per 10°C of temperature change interval.

Sample Casting and Setting

A set of 12 HTPB samples has been made for each temperature considered. This choice because of the repeatability of DMA measure instrument: it is usually necessary at least a couple of samples to be sure that the performed measure is acceptable. For this purpose, 3 samples were tested for each simulated year. Four castings were realized using Resodyn® Acoustic Mixer:

- 1° *Casting - 14/05/2012*: 4 samples has been prepared with the aim to test the performance of the acoustic mixer and to refine the manufacture procedure. Only 2 of these have shown a quality suitable for DMA measures, with no bubbles and regular sample shape; $\rho_{HTPB}{}^{(1)} = 917.16\ kg/m^3$
- 2° *Casting - 16/05/2012*: 12 samples prepared and all of them suitable for DMA measures. $\rho_{HTPB}{}^{(2)} = 921.6\ kg/m^3$;

- 3° *Casting - 18/05/2012*: 12 samples prepared and all of them suitable for DMA measures; $\rho_{HTPB}{}^{(3)} = 918.7\ kg/m^3$
- 4° *Casting - 24/05/2012*: 12 samples prepared and all of them suitable for DMA measures; $\rho_{HTPB}{}^{(4)} = 916.13\ kg/m^3$;
- 5° *Casting - 11/10/2012*: 12 samples prepared and all of them suitable for DMA measures; $\rho_{HTPB}{}^{(5)} = 915.92\ kg/m^3$;
- 6° *Casting - 17/11/2012*: 4 samples, for the *No Aging Baseline*, prepared and all of them suitable for DMA measures; $\rho_{HTPB}{}^{(6)} = 915.63\ kg/m^3$.

Note that two of four samples prepared with the first casting, have not reached a quality level equivalent to the others. However, one of them remained, protected by a thin layer of cellophane, on a table in the laboratory for 145 days. Then, it was processed with DMA, obtaining an estimate of HTPB mechanical properties after natural aging. This unique measure was considered just for comparison with simulated aging, during the post-processing. This particular sample is classified as *T*145. Table 14 shows all the details about temperatures, samples, begin and end date of each aging treatment performed.

Temperature	**Start Date**	**End Date**	**Casting (samples)**
60°C	29/05/2012	25/10/2012	3°(12)
70°C	28/05/2012	27/07/2012	1°(2), 2°(10)
80°C	13/10/2012	05/11/2012	5°(12)
90°C	30/05/2012	08/05/2012	4°(12)
T145	15/05/2012	07/10/2012	1°(1)
Baseline	/	/	6°(4)

Table 14.: List of thermal accelerated-aging treatments

Note that for the aging at 70°C the 2 samples, produced during the first casting, were used together with 10 samples from the second casting. In order to classify each sample and made them easy to be recognized and tested, in table 15 one can see three examples of sample classification code.

Example	**Temperature**	**Letter**	**Year Step**	**Casting**
T60-A-2y-185	60°C	A	2 years	18/05/2012
T70-L-10y-165	70°C	L	10 years	16/05/2012
T00-A	Baseline	A	No Aging	17/11/2012

Table 15.: Samples Cataloging

Twelve letters of the italian alphabet (A, B, C, D, E, F, G, H, I, L, M, N) have been used to mark a complete group of samples for every temperature. The code T00 is referred to the *No Aging Baseline* samples, prepared and tested with DMA after the curing process.

Storage Setting

This research on HTPB behavior was focused on the simulated aging in dry conditions. The presence of a certain level of humidity in the in-service condition is not taken into account. The aging behavior of polymer is very complex, it depends on different mechanisms that can operate at the same time. Humidity can have a strong influence on the material aging, making difficult a well comprehension of thermal treatment effects. With the aim to preserve the samples from humidity, they were put on plastic support over a layer of salts, in a closed box, see Figure 36. The box was inserted in a furnace equipped with air ventilation. Approximately every 2 weeks the box were extracted and the cover was opened to refresh the air inside it. A further step would consider a thermal treatment in vacuum conditions, to simulate the in-service situation of a hybrid engine equipped on an operative satellite. Nevertheless, the dry conditions offered by the used furnaces can be assumed, in first approximation, similar to vacuum environment from the point of view of humidity.

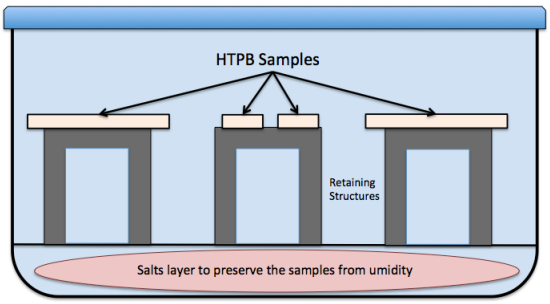

Figure 36.: Storage box for thermal treatment.

5.2.5 DMA Measures

A polymer is a viscoelastic material and its complex behavior is caused by the combination of two mechanisms. The first is the elastic model, described by the Hooke law, in which, during stress application, the energy is absorbed by the material and completely released when the force is removed. The second one is the viscous model, described originally by Newton, which considers the deformation of a flow subject to stress application; this deformation increases proportionally over time. In such a way, the flow dissipates the energy introduced, which is not given back but converted into heat [154]. Viscoelastic materials can be analyzed with DMA. It allows to evaluate the complex modulus, knowing the sample geometry, by applying stresses on the material and measuring the corresponding strains or vice versa. The variation of complex modulus can be measured varying the frequency of the stress or the temperature of the sample. The measured stress is dismantled in the overlapping of a signal in phase with the elastic component (deformation), which provides the value of Storage modulus E' and in a signal with $\pi/2$ of phase different, which provides the Loss modulus

E''. The ratio between Storage and Loss modulus results in the loss tangent $\tan\delta$, as shown below

$$E' = \frac{\sigma_0}{\varepsilon_0}\cos\delta \qquad \text{and} \qquad E'' = \frac{\sigma_0}{\varepsilon_0}\sin\delta \tag{5.20}$$

where σ and ε, are respectively the stress and the strain, while δ is the phase lag between them and $\tan\delta = E''/E'$. The complex modulus results from the storage and loss modulus as $E = E' + iE''$. For the purpose of this research, aged samples have been tested in *Multi-Frequency Sweep* mode, with the aim to measure the change of Storage and Loss modulus over different stress intensities for the fourth levels of simulated aging. DMA results are very sensitive to the measure of sample geometry. An error on the latter is propagated cubically to E' and E'' evaluated [154].

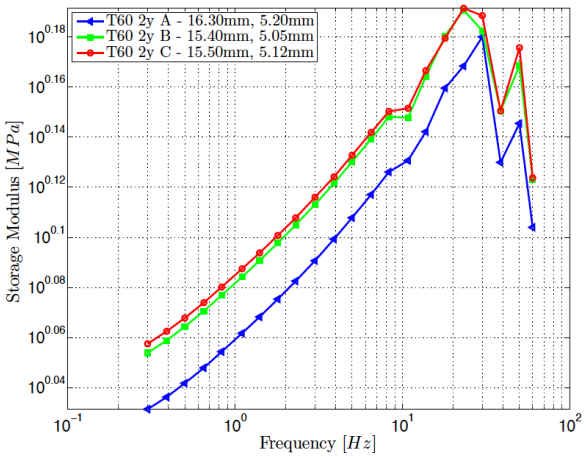

Figure 37.: Storage modulus vs. stress frequency - Simulated aging of 2 years at 60°C of temperature.

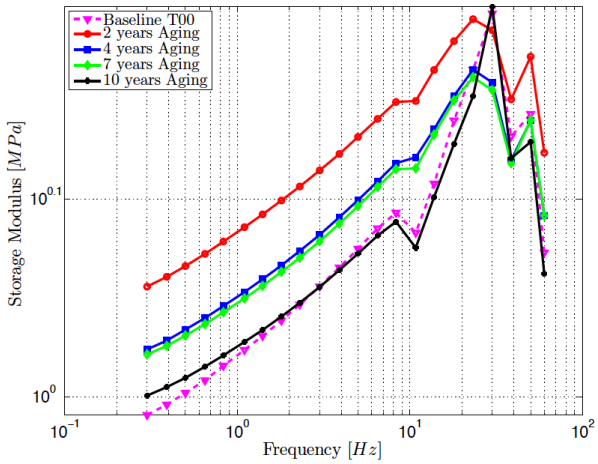

Figure 38.: Ensemble Comparison - T60 - Storage modulus vs. stress frequency.

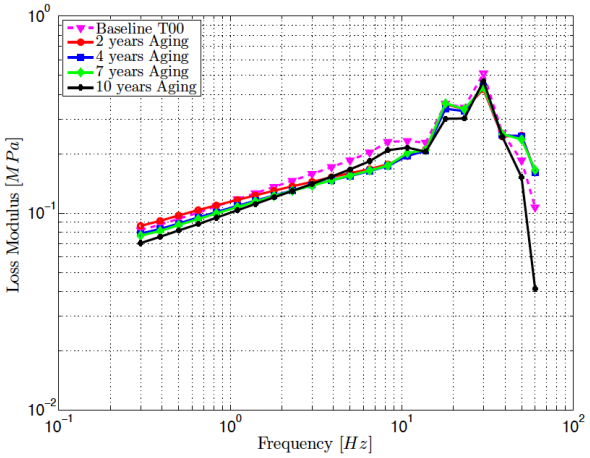

Figure 39.: Ensemble Comparison - T60 - Loss modulus vs. stress frequency.

All the measurements were performed at a constant room temperature of 30°C (the minimum value for the instrument testing chamber), with an imposed oscillation amplitude of 15 µm for a frequency range between 0.3 and 60 Hz. The rectangular samples were set with a Dual Cantilever clamp. The Storage modulus measures, for samples treated with a temperature of 60°C, are shown in Figure 37. The latter is referred to a simulated aging of 2 years. Three samples were tested for each case: 2 years (2y), 4 years (4y), 7 years (7y) and 10 years(10y) of simulated aging. Figure 37 quotes the width and the thickness of samples. One can see that curves B and C coincide, while curve A shows lower E′ values. This is a significant example of the instrument sensitivity to the sample size, manually measured before the test; in fact, sample A is wider and the thickness is larger, while sample B and C are quite similar, providing a repeatable measure. The trend of the Storage modulus is quite linear till a frequency value of about 10 Hz, after which the sample goes in resonance. The ensemble curve is evaluated considering the average E′ value for a considered frequency of the total range. The error bars, see [159], are referred to the corresponding standard deviation.

Therefore, for each frequency the average and standard deviation of the dependent variable is calculated, obtaining the ensemble curve. This calculation does not take into account data from the abnormal curve, which is out of a reasonable interval of repeatability. The same is done for the other reference years, thus obtaining the comparison between all simulated agings, for a selected temperature, and the *baseline ensemble T*00; the latter achieved with three repeatable measures performed on no-aged samples. The Storage modulus comparison 60°C is reported in Figure 38; the baseline trend coincides with the 10y trend, while the others curves reach higher E′ values. With regard to Loss modulus ensemble comparison, see Figure 39, no large differences are observed between all curves, but all seem to be lower than the baseline. Even the tanδ ensembles, see Figure 39, do not show significant differences between years, resulting lower than the baseline. A similar behavior is observed for the others

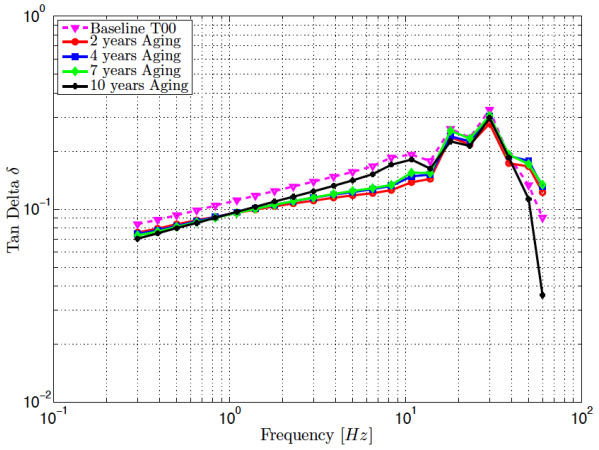

Figure 40.: Ensemble Comparison - T60 - Tanδ vs. stress frequency.

test temperature cases. The latter ensemble graphs and relative comments can be found in [159].

5.2.6 Results and Discussion

In this Section the most significant results are presented, while for a more detailed analysis with all the performed measurements the read of [159] is recommended. Two aging mechanisms seem to be active, one at 60°C and 70°C different from what happens at 80°C and 90°C. The frequency range assumed acceptable is that characterized by a quasi-linear change, before the resonance, of the variables of interest: between 0.3 and 8.3 Hz. The Storage modulus over simulated time, for each test temperature, is displayed in Figure 41, and it is referred to a single value of stress frequency (1.8 Hz).

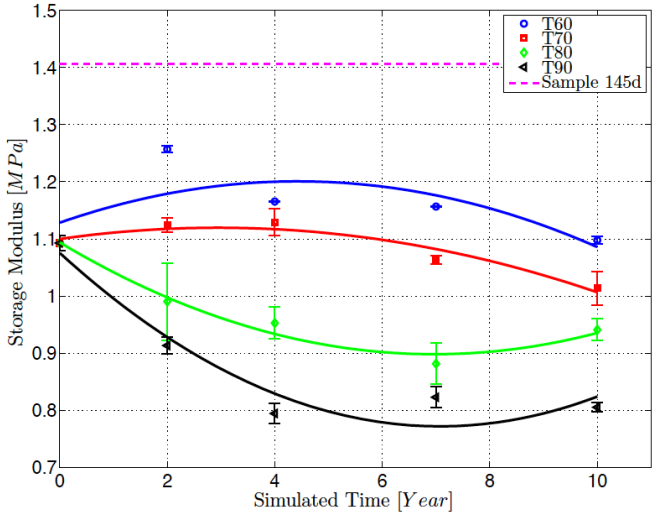

Figure 41.: Storage modulus vs. simulated time at frequency of 1.8 Hz

The experimental points (at 2y, 4y, 7y, 10y) are interpolated with a second order polynomial function evaluated by least mean squares method. The dotted line represents the the single value measured for sample T145 at the fixed frequency. The trend at T60 and T70 is similar and, contemporary, significantly different with respect to T80 and T90. The same difference is observed for the damping coefficient $\tan\delta$, while the trend of Loss modulus resulted quite similar for all temperature cases [159]. Considering Figure 41, the trend of T60 and T70 initially increases, reaching a maximum, after which, one can see a decrease back to initial value, in the case of T60, or to a lower value in the case of T70. On the contrary, T80 and T90 initially decrease till a minimum value, after which the curves increase reaching a lower value respect to initial one. The minimum values of T80 and T90 are shifted forward respect to the maximum values of T60 and T70. The largest error bars are for T80 data while T60 presents the data 2y quite dispersed with respect to the others at the same temperature. The latter value has been measured again without obtaining a better result. Note that all data are very far from the T145 value, not subjected by thermal treatment. Natural aging results in a hardening of the material, probably because of humidity presence. However, sample T145, as of the end of 2013, still appeared very flexible, without the development of any scare on its surface, as usually observed on HTPB sample left at ambient not protected condition for a long time. Probably, this high longevity is provided by the *unknown antioxidant* inserted by AVIO after the polymerization process, see Appendix G. In Figures 42, the Storage modulus over the thermal treatment temperature is presented. Each curve is referred to one step of simulated aging, from 2 to 10 years.

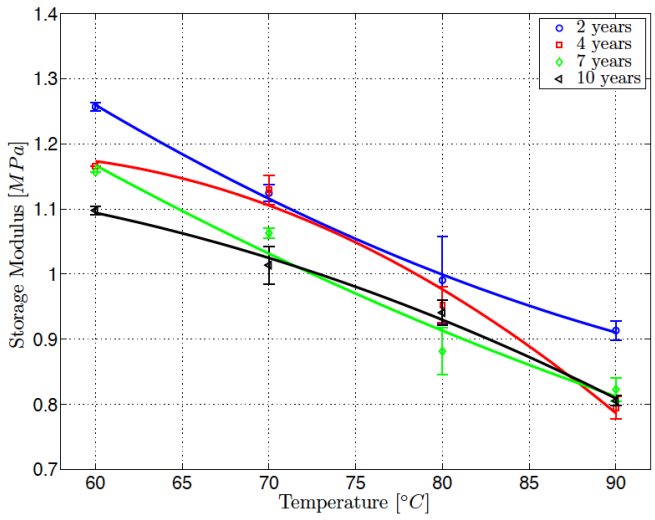

Figure 42.: Storage modulus vs. accelerated aging temperature at frequency of 1.8 Hz

The Storage modulus quite decreases with the temperature, this means that different thermal treatments with different temperatures cause different aging effects. Such difference is very large, about 27% at interval extremes, while the decrease between 60°C and 70°C is only about 6.4%. A so big lack between aging performed at 60°C

and that performed at 90°C can be explained as a consequence of the activation of further reactions (chemical or thermal) beyond 80°C of temperature. In the light of this, just low temperatures, not over 70°C, should be considered for aging simulation, both for measures repeatability and for aging mechanisms that are active in the operational conditions of the considered material. For what concern the Loss modulus, a certain data dispersion is observed, but the trend can be accepted as quite constant with the treatment temperature. The slope of the damping coefficient $\tan\delta$ increases with temperature, accordingly with its mathematical definition [159]. The behavior highlighted by the Storage modulus variations over simulated time and accelerated-aging temperature seems to be caused by the break of cross-links between polymer chains. This conclusion can be confirmed by the test defined by the Flory-Huggins theory. A polymer, after cross-linking process, drowned in a solvent, tends to delate, increasing its volume. The absorption of solvent by the polymer is possible because the cross-links are elastic, having a certain degree of motion. The swelling level is proportional to the amount of absorbed solvent, this phenomena is very prominent and generates a tridimensional deformation of the sample. The diffusion of the solvent inside the polymeric reticulum causes the enlargement of the molecular structure that is counteracted by the tendency of the same to be distributed according to a smaller volume. The balance between the internal force, which tends to expand, and the external one, which tends to retain, defines the amount of liquid absorbed by the polymer and thus the degree of the swelling. The swelling degree depends on the average length of the cross-links between polymer chains. HTPB polyurethane resin can be tested with toluene, in order to confirm that its aging behavior is caused by the break of cross-links. In case of aged material it is reasonable to obtain an high degree of swelling, because the broken cross-links leave space for a higher absorption of solvent, much more than the quantity absorbed by a not aged sample.

Type	1° **Step** *Weight [g]*	2° **Step** *Weight [g]* | *Percent*	3° **Step** *Weight [g]* | *Percent*
T00-0**y**	0.0012	0.0054 | 450%	0.0009 | 75%
T145	0.0009	0.0045 | 500%	0.0007 | 78%
T60-10**y**	0.0029	0.0151 | 520%	0.0025 | 89%
T70-10**y**	0.0018	0.0092 | 511%	0.0014 | 78%
T80-10**y**	0.0031	0.0162 | 522%	0.0024 | 77%
T90-10**y**	0.0092	0.0524 | 570%	0.0069 | 75%

Table 16.: Flory-Huggins test - Weight measures and incremental percentages results.

The Flory-Hugging test consists in the bath of a HTPB sample, a small piece cut very thin, inside toluene for 24 hours. The sample weight must be measured before (Step 1) and after (Step 2) the bath, in order to evaluate the percentage increase of weight. A third weight measure (Step 3) is taken after the complete evaporation of toluene from the polymer sample. This kind of test has been performed considering one sample for each aging temperature. Except for the baseline and for the sample T145, the samples selected were those referred to 10 years simulated aging. In table

16, one can see the three weight measures and the relative percentage increment. As expected, the weight increase observed for the aged samples is significant, confirming that the aging of HTPB is caused by the break of cross-links between polymer chains. Note that the highest increment has been for the sample treated at a temperature of 90°C. This value can be reasonably due to the high temperature, which activates further chemical o thermal mechanisms, in agreement with what is suggested in the literature to simulate the aging of a polymer which has to be preserved for a long time. High temperatures, over about 80°C, involve the activation of mechanisms that during the natural aging are not present [157]. Therefore, low treating temperatures are preferred for HTPB aging investigations. The aging behavior observed in this work seems to disagree with that described in the literature, which reveals an hardening of the material over the simulated aging time. Probably, these differences can be caused by the presence of the *unknown antioxidant* in the HTPB, inserted by AVIO to preserve the material properties of the polyurethane resin, see Appendix G. In fact, an antioxidant substance tends to react before the polymer chain components, preserving it from oxidation. Moreover, a strange distribution of tridimensional hotspots has been observed within the thickness of rectangular samples. They appear like darkener regions in which the aging seems more advanced [159]. This pigmentation might be associated with the reaction of extinguished tin, activated by the thermal treatment or by the light. In fact, the hotspots were not found on baseline samples, stored in low humidity conditions without light exposition. In the technical report [159], more data analysis are provided, also concerning the mass losses during the thermal treatment and a set of SEM analysis on the aged samples. This study produced a baseline database about the AVIO HTPB R45 actually used in SPLab, useful for further investigations, especially to observe the aging with the addition of metal additives. The implementation of an ad hoc law which relates the simulated aging of a selected mechanical property with the real aging time (as described by the Layton Model) would be necessary, to provide a more complete analysis. Furthermore, the evaluation of the aging rate constant, obtained from the Storage modulus E' and the damping coefficient $\tan\delta$, can be performed in order to make a comparison with the Arrhenius behavior. With the aim to verify the importance of the antioxidant effects on the aging of HTPB, a new accelerated aging campaign with pure HTPB R45, without any antioxidant substance, should be implemented.

6 COMPUTATIONAL STUDY

This chapter deals with the numerical approaches used for the preliminary design of propulsion systems for active removal missions. Initially, at a early stage, a very essential zero-dimensional code, based on an empirical regression rate expression, was considered. Then, a more complex Quasi-One-Dimensional (Q1D) code has been developed during the trainee at the *Institute of Space and Astronautical Science (JAXA)*, in order to overcome the significant limitations imposed by the previous code and to estimate the regression rate of the propellant combination $HTPB + H_2O_2$, of which it is hard to find available data in the literature survey.

6.1 ZERO-DIMENSIONAL SEMI-EMPIRICAL APPROACH

Since this study is mainly focused on the Q1D code, a briefly description of the zero-dimensional semi-empirical approach is provided. By this approach, the fuel mass flow rate $\dot{m}_f$ is estimated by using an experimental simplified regression rate expression, valid for quasi-steady conditions in the diffusion-limited theory developed by Marxman et al. (see Chapter 4). In the frame of preliminary analysis, the empirical power law from Sutton [160, 55], valid for the propellant couple $HTPB + GOX$, was considered

$$r_f = 0.03 G_{ox}^{0.68} \tag{6.1}$$

Eq. 6.1 was obtained for an oxidizer mass flux range of about 35-280 $kg/(m^2 \cdot s)$. The fuel grain is cylindrical with a single central circular perforation. At each time instant t the regression rate is calculated, by knowing the port area and the oxidizer mass flow rate $\dot{m}_{ox}$, and applied to the total fuel length L_f. Then, the fuel mass flow rate is calculated as

$$\dot{m}_f(t) = \rho_f r_f(t) L_f D_p(t) \tag{6.2}$$

where ρ_f is the fuel density and D_p the port diameter. Thus, once obtained the propellant mass flow rate $\dot{m}_p(t) = \dot{m}_{ox} + \dot{m}_f(t)$ and the oxidizer-to-fuel ratio $O/F(t) = \dot{m}_{ox}/\dot{m}_f(t)$, the pressure in the combustion chamber p_c is obtained as

$$p_c(t) = \frac{c^*(t)}{A_t} \dot{m}_p(t) \tag{6.3}$$

where A_t is the nozzle throat area, defined by the user, while c^* is the characteristic velocity evaluated with NASA CEA software [91, 92]. The latter is used for the calculation of thermochemical properties and performance parameters of the gas

products mixture throughout a de Laval[1] nozzle. By means of CEA software the most significant performance parameters, such as c^*, the thrust coefficient c_s, the specific impulse I_s, in correspondence of both the throat and exit nozzle sections, as well as the other thermochemical parameters, are collected in data tables as function of chamber pressure and O/F in the interested operative ranges. All the considered performance parameters are described in Chapter 7. For the hot gases nozzle expansion a Bray approximation [162, 163] is applied: chemical equilibrium conditions (*shifting*) are assumed from combustion chamber up to the throat section; from the latter to the exit section no chemical reactions occur anymore (*frozen*) and an isentropic expansion is assumed. For the final performance calculation, the two-dimensional losses in the nozzle divergent and the positive contribute to the thrust, due to vacuum conditions at the exit section, are considered. Finally, for the comparison with mission requirements, the velocity increment is calculated for a linear accelerated motion, under the hypothesis of equilibrium between centripetal and centrifugal forces, with no atmospheric and solar radiation drag. The iterative process is carried on, by changing the fuel grain size, the oxidizer mass flow rate, the nozzle throat diameter and combustion time, as long as the required velocity increment is reached. This simple code, originally implemented in MATLAB®, was converted in a more user-friendly tool with Simulink®, by two students of Aerospace Engineering (P. Campi and A. Rivolta) in the frame of an educational laboratory project at SPLab.

The main weakness of the zero-dimensional code is the use of an empirical formula for the regression rate and fuel mass flow rate estimate; in fact, the experimental expression is based on a quite small mass flux range and, moreover, it is valid only for GOX oxidizer. However, in first approximation, the Eq. 6.1 was assumed even for HTPB combustion with hydrogen peroxide at 90% of concentration, because of the difficulty to find an experimental r_f expression with such oxidizer in the available literature. Since the regression rate of $HTPB + H_2O_2$ should be lower than $HTPB +$ GOX at the same operative conditions, due to the significant excess of water in the H_2O_2 decomposition products, during the initial phase of active removal mission design project, a safety margin of 25%-30% on the velocity increment ΔV was applied [3, 16, 164, 17, 165, 166]. In order to examine in depth the physical mechanisms that occur in the hybrid combustion and to numerically estimate the regression rate for propellant couple $HTPB + H_2O_2$, a more complex computational code has been developed.

6.2 QUASI-1D HYBRID ROCKET ENGINE CODE

A quasi-one-dimensional code lends for a more detailed analysis of the hybrid rocket internal ballistics, by using moderate complex models, so requiring relative low computational costs and allowing for long-time combustion simulations. The purpose of the *HRE Code* is to provide a numerical tool for the preliminary design, ballistics analy-

1 Convergent-divergent nozzle invented by Gustaf de Laval in 1888 [161].

sis and performance estimation of hybrid rocket motors. This code considers the fluid dynamics of the main stream, assuming a quasi-steady flame with very small characteristics times of combustion reaction and solving the energy-flux balance equation at the solid fuel surface for the regression rate estimation, following the same calculation approach developed by Funami et al. [11]. The *HRE Code* allows for testing of different regression rate calculation models, with different propellant combinations. In this study, HTPB is selected as solid fuel while, as oxidizer, GOX and H_2O_2 are considered. The main interest, for preliminary sizing, is the couple HTPB + H_2O_2, of which is quite difficult to find regression rate measurements on the open literature, thus preventing the use of the simple zero-dimensional code with enough precise way.

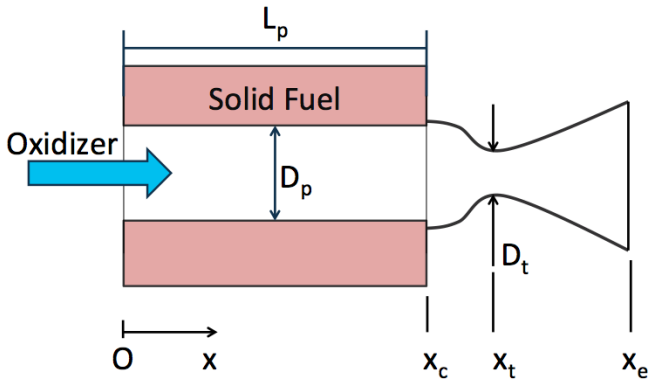

Figure 43.: Hybrid rocket engine configuration.

The calculation domain is composed by the combustion chamber and a de Laval nozzle [48, 160], see Fig. 43. A simple central circular perforation is assumed for the fuel grain, while the oxidizer is axially injected. It is assumed that the gasification of the cured HTPB produces gaseous butadiene (C_4H_6) which immediately reacts with the gaseous oxidizer. Furthermore, when hydrogen peroxide is used, it is assumed already decomposed, by catalytic reaction, into O_2 and H_2O before entering in the combustion chamber. The decomposition reaction of hydrogen peroxide is

$$H_2O_2 \rightarrow \frac{1}{2}O_2 + H_2O \tag{6.4}$$

and it is referred to pure hydrogen peroxide concentration, not diluted in water, able to generate hot gases with an ideal temperature of about 1200 K (catalyzer ideal efficiency).

6.2.1 Flowfield Basic Equations

The governing equations for the considered flowfield (Fig. 43) are the Quasi-One-Dimensional (Q1D) inviscid compressible Euler equations [167] with the addition of a conservation equation for the mixture fraction ξ [11, 168, 169].

$$\frac{\partial A\mathbf{Q}}{\partial t} + \frac{\partial A\mathbf{F}}{\partial x} = \mathbf{S}_{Q1D} + \mathbf{S}_{Mass} \tag{6.5}$$

$$\mathbf{Q} = \begin{pmatrix} \rho \\ \rho u \\ \rho e_t \\ \rho \xi \end{pmatrix}, \qquad \mathbf{F} = \begin{pmatrix} \rho u \\ \rho u^2 + p \\ (\rho e_t + p)u \\ \rho \xi u \end{pmatrix}$$

$$\mathbf{S}_{Q1D} = \begin{pmatrix} 0 \\ p\frac{dA}{dx} \\ 0 \\ 0 \end{pmatrix}, \qquad \mathbf{S}_{Mass} = \begin{pmatrix} l_p \dot{m}_f \\ 0 \\ l_p \dot{m}_f h_w \\ l_p \dot{m}_f \end{pmatrix}$$

where $\mathbf{Q}$ is the vector of conservative quantities, $\mathbf{F}$ is the flux vector, $\mathbf{S}_{Q1D}$ is the geometric source term for quasi-1D approximation, $\mathbf{S}_{Mass}$ is the source term due to the mass release by the fuel surface, A is the cross-sectional area, ρ is the density, u is the velocity along x-direction, e_t is the specific total energy of the gas mixture, p is the pressure, $\dot{m}_f$ is the mass addition from the solid fuel surface, l_p is the cross-section perimeter and h_w is the enthalpy of the fuel gas evaporated from the surface. The effects of the contour change of the rocket chamber and the nozzle over the axial coordinates are considered in the source term including dA/dx. Even the mass addition from the burning surface is a source term, resulting from the integration over the perimeter boundary of the solid fuel surface. The primitive values vector is

$$\mathbf{W} = [\rho, u, p, \xi]^T. \tag{6.6}$$

The specific total energy of the gas mixture is expressed as follow

$$e_t = e + \frac{u^2}{2} \tag{6.7}$$

$$e = \sum_{i=1}^{N_s} h_j Y_j - \frac{p}{\rho} \tag{6.8}$$

$$h_j = \Delta H_j^\circ + \int_{T_{ref}}^{T} c_{p,j}\, dT \tag{6.9}$$

where e is the specific internal energy of the gaseous mixture, h_j, Y_j and Δh_j° are, respectively, the specific enthalpy, the mass fraction and the standard formation enthalpy of the chemical species j. The specific heat at constant pressure $c_{p,j}$ is a

function of temperature T (T_{ref} is a reference temperature value). For each chemical species j, the specific heat at constant pressure can be obtained by fitting the JANAF's data [91]. The pressure p is calculated by the equation of state

$$p = \sum_{j=1}^{N_s} \frac{Y_j}{w_j} \rho R^{\circ} T \tag{6.10}$$

where R^0 is the universal gas constant and w_j is the molecular weight of the chemical species j (N_s species). The boundary conditions at the inflow are applied to the inner ghost cell: the oxidizer mass flow rate, hence the inlet velocity, is define by the user, the pressure is defined by a zeroth-order extrapolation from the numerical domain, the temperature depends on the initial conditions of the oxidizer chosen and the mixture fraction is equal to zero. In order to solve the Eq. 6.5 is necessary to know the mass released by the burning surface $\dot{m}_f$. The latter is estimated by solving the energy flux balance at the solid fuel surface.

6.2.2 Regression Rate Estimation

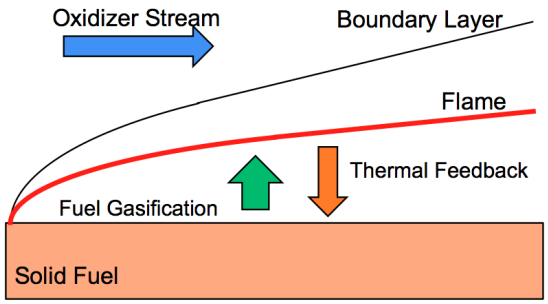

Figure 44.: Schematic of combustion zone above the solid fuel.

As described in Section 4.1, the regression rate under pure convective regime can be estimated by means of the diffusion-limited model developed by Marxman and co-workers [62, 63, 64, 65]. Starting from the energy flux balance at the fuel surface, Eq. 4.1, Marxman derives the following regression rate expression

$$\rho_f r_f = 0.03 G \left(\frac{G \cdot x}{\mu}\right)^{-0.2} \left(\frac{St}{St_o}\right) \left(\frac{u_e}{u_{fl}}\right) \frac{\Delta h}{\Delta H_{v,eff}} \tag{6.11}$$

where G is the local specific mass flux, μ is the gas-phase viscosity, x is the axial location, St/St_o is obtained by Eq. 4.4, u_e is the main stream velocity, u_{fl} is the velocity at the flame and Δh is the difference between the enthalpy at the flame h_{fl} temperature and the enthalpy at the wall of the gas phase h_w. $\Delta H_{v,eff}$ is expressed by Eq. 4.2, where, for HTPB fuel, ΔH_{vap} is evaluated as equal to 430 cal/g and c_s

as equal to 1632.85 $J/(kg \cdot K)$ according to [170]. When $Pr = 1$ and the radiation component is negligible [55], the blowing number, Eq. 4.6, can be approximated by

$$B = \frac{u_e}{u_{fl}} \frac{\Delta h}{\Delta H_{v,eff}} \tag{6.12}$$

depending on the velocity ratio u_e/u_{fl} calculated with

$$\frac{u_{fl}}{u_e} = \frac{O/F \cdot \frac{\Delta h}{\Delta H_{v,eff}}}{K_{ox_e} + (O/F + K_{ox_e}) \frac{\Delta h}{\Delta H_{v,eff}}} \tag{6.13}$$

where O/F is the local oxidizer-to-fuel mass ratio and K_{ox_e} is the mass fraction of oxidizer in the main stream. It is assumed that the local O/F and the ratio $\Delta h/\Delta H_{v,eff}$ are constants along the axial location, in a given chemical system [63]. Besides Marxman model, in the frame of this numerical work, the regression rate is also estimated with Greatrix model [171], with the aim to find the most simple and suitable model for the r_f calculation.

Greatrix Model

Starting from previous works on thin-layer, energy-film approach for estimation of the erosive burning in solid propellant rockets, Greatrix suggests a similar approach for the prediction of fuel regression rate in hybrid rockets [171]. He rewrites the energy-balance of Eq. 4.1 in an explicit way

$$\rho_f r_f [c_s(T_w - T_i) - \Delta H_s] = h(T_{fl} - T_w) \tag{6.14}$$

where h is the convective heat transfer coefficient, which includes the blowing effect due to the fuel mass release from the surface, while ΔH_s is a *net surface heat of reaction* absorbed by the solid phase. This term is positive if exothermic and negative if endothermic. By considering HTPB solid fuel, ΔH_s corresponds to the ΔH_{vap}, estimated by Lengellé [170], and, being absorbed by the fuel surface, it assumes a negative sign $\Delta H_s = -\Delta H_{vap}$, so that the term in square brackets of Eq. 6.14 becomes

$$c_s(T_w - T_i) - (-\Delta H_{vap}) = \Delta H_{v,eff} \tag{6.15}$$

Greatrix considers a one-dimensional energy conservation approach to describe the region between the regressing surface and the flame position, identifying an energy-zone thickness δ_{fl}, in which the following assumption are defined:

- absence of surface reactions that can affect the gas-phase;
- the combustion heat release is mainly toward the flame front position;
- homogeneous condensed phase;
- quasi-steady conditions.

As described in [171], once obtained the temperature profile expression inside δ_{fl}, by equating the heat input from the gas-phase with the heat released from the solid-phase in correspondence of the surface, one can obtain the energy-zone thickness

$$\delta_{fl} = \frac{\kappa}{\rho_f r_f c_p} \ln\left[1 + \frac{c_p(T_{fl} - T_w)}{c_s(T_w - T_i) - \Delta H_s}\right] \tag{6.16}$$

where κ is the gas thermal conductivity. Furthermore, it is possible to define the expression for the convective heat transfer coefficient at the gas-phase side, as

$$h = \kappa \frac{dT}{dy}|_{y=0}(T_{fl} - T_w)^{-1} = \frac{\rho_f r_f c_p}{\exp(\rho_f r_f c_p \delta_{fl}/\kappa) - 1} \tag{6.17}$$

and, in the case of no-transpiration (no blowing effect), the convective heat transfer coefficient can be reduced to $h^* = \kappa/\delta_{fl}$ and, by substituting it in Eq. 6.17, it is possible to rewrite h as a function of the no-transpiration convective heat transfer coefficient, obtaining a solution which results fairly accurate for subsonic transpired turbulent flows [171]. At this point, Greatrix introduces the Reynolds analogy in order to rewrite h^* as a function of the Darcy-Weisbach friction factor f^* for turbulent flows

$$h^* = \frac{\kappa^{2/3} c_p^{1/3} G \cdot f^*}{\mu^{2/3} \cdot 8} \tag{6.18}$$

The friction factor can be estimated with a Colebrook's semi-empirical formula, valid for fully developed turbulent flow in a pipe, as used by Greatrix to represent the central fuel cylindrical perforation. However, he also provides an explicit expression for flat-plate developing flow (valid for $\zeta/x > 2 \cdot 10^{-3}$ with $Re_x > 1 \cdot 10^6$; $\zeta/x > 2 \cdot 10^{-5}$ with $Re_x > 1 \cdot 10^8$; etc.)

$$f^* = 4\left[1.89 - 1.62\log_{10}\left(\frac{\zeta}{x}\right)\right]^{-2.5} - 7.04\left[1.89 - 1.62\log_{10}\left(\frac{\zeta}{x}\right)\right]^{-3.5} \tag{6.19}$$

which is in function of axial location x and the effective fuel surface roughness height ζ (assumed equal to 5 μm for HTPB solid fuel [171]). The friction factor calculated is valid for incompressible flows, hence a correction for compressible case must be applied (see [171]). Finally, by substituting the Eqs. 6.18 and $h^* = \kappa/\delta_{fl}$ in Eq. 6.16 one can obtain the fuel r_f expression

$$r_f = \frac{h^*}{\rho_f c_p} \ln\left[1 + \frac{c_p(T_{fl} - T_w)}{c_s(T_w - T_i) - \Delta H_s}\right] \tag{6.20}$$

The regression rate defined by Greatrix's semi-empirical model differs from the Marxman et al. model primarily for the use of the heat transfer convection coefficient as a function of an empirical formula for the friction factor instead of the Stanton number ratio and the blowing parameter, defined and used by Marxman and many other researchers. As asserted by Greatrix, the regression rates estimated with his pure convective model fairly match the experimental results obtained by different authors [171]. Moreover, the application of the Greatrix model to calculate the regression rate

from the diameter sampling achieved with the 2D-Radial micro burner, performed by Paravan [124] at SPLab, has shown a quite good agreement with the regression rate estimated by the time-resolved technique (see Chapter 5). Nevertheless, in this work the Greatrix model is tested within the *HRE Code* and the calculated r_f results quite far from that measured in the experimental tests of Shanks and Hudson [172], the selected case for code validation.

6.2.3 Combustion Model

Combustion is a complex process in which many chemical species are involved and several elementary reactions occurs at the same time. Typically, a combustion calculation deals with a reduced number of chemical species and reactions, focusing only on the most significants and representatives for the analyzed case. It is assumed that:

- all chemical species are ideal gas (no condensed species considered);
- oxidizer and fuel are mixed and react immediately in the control volume.

In this study, nine chemical species are considered: butadiene C_4H_6, molecular oxygen O_2, carbon dioxide CO_2, water H_2O, carbon monoxide CO, molecular hydrogen H_2, hydroxyl radical OH, atomic oxygen O, atomic hydrogen H. This set of species, preliminary selected and analyzed with NASA Chemical Equilibrium for Applications (CEA) software [91], provides nearly the same flame temperature obtainable with the complete number of species that are really involved in the combustion of the same propellant couple [11]. Temperature, pressure and chemical composition are evaluated with *chemical equilibrium* calculation (particular reactions are not considered). The latter consists in a free energy minimization by means of Lagrange's method of undetermined multipliers with specified constraints. In this work the minimization of Gibbs and Helmholtz free energies are implemented, complying with the guideline of NASA [91]. The application of one or the other depends on which variables are used to characterize the initial thermodynamic state.

MINIMIZATION OF GIBBS ENERGY The Gibbs energy [160, 91] per kilogram of mixture $\hat{g}$, for a mixture of N_s gaseous species, is defined as

$$\hat{g} = \sum_{j=1}^{N_s} \nu_j n_j \tag{6.21}$$

where ν_j is the chemical potential per kilogram-moles of species j and n is the number of kilogram-moles of species j per kilogram of mixture. The free energy minimization is subjected to the following constraints

$$b_k - b_k^\circ = 0 \quad k = 1, .., l \tag{6.22}$$

where b_k° is the assigned number of kilogram-atoms of element k per kilogram of total reactants, the index l is the number of chemical elements (in this work $l = 3$ due

to the reduced number of chemical species considered) while the number of kilogram-atoms of element k per kilogram of mixture (i.e. mixture of products) is

$$b_k = \sum_{j=1}^{N_s} a_{kj} n_j \quad k = 1, .., l \tag{6.23}$$

where a_{kj} are the stoichiometric coefficients, that is the number of kilogram-atoms of element k per kilogram-mole of species j. The applied constraint (Eq. 6.22) means that the mole number of elements of reactants must be conserved. By using the Lagrange's method, the minimized function $\hat{G}$ is defined as

$$\hat{G} = \hat{g} + \sum_{k=1}^{3} \lambda_k (b_k - b_k^\circ) \tag{6.24}$$

where λ_k are Lagrangian multipliers [91]. To calculate $\hat{g}$ is necessary to evaluate the chemical potential ν_j as a function of temperature, pressure and its value at standard state ν_j°. The latter, and in the same way the other thermodynamic terms in standard-state such as the molar specific heat at constant pressure $C_{p,j}^\circ$ and constant volume $C_{v,j}^\circ$, the molar enthalpy H_j°, the molar entropy S_j° and the molar internal energy E_j° of the species j (all terms are as a function of temperature), is estimated by fitting the JANAF's data [91]. The minimization of Gibbs energy permits the determination of equilibrium composition for a thermodynamic state defined by an assigned pressure p_0 and temperature T_0 [91]. Being a non linear problem, an iteration procedure, in which n is assumed as independent variable, is required to obtain the final composition. For this purpose, a descent Newton-Raphson method is used to correct, with a certain number of iterations, the initial estimate of composition n_j and temperature T. A complete and detailed description of the entire calculation method and conditions for solution convergence is provided by [91, 92].

MINIMIZATION OF HELMHOLTZ ENERGY The Helmholtz energy [160, 91] per kilogram of mixture $\hat{f}$, for a mixture of N_s species, is defined as

$$\hat{f} = \hat{g} - pV \tag{6.25}$$

and it is related the the Gibbs energy, in turn depending on chemical potential ν_j, which, for Helmholtz energy, is a function of temperature and volume, as well as the chemical potential in standard state ν_j°, still estimated by JANAF's data [91]. Also for Helmholtz minimization, the mass-balance constraint is applied, obtaining the minimized function

$$\hat{F} = \hat{f} + \sum_{k=1}^{3} \lambda_k (b_k - b_k^\circ) \tag{6.26}$$

where b_k° is the constraint on conservation of the mole number of elements of reactants. The equilibrium composition is obtained by specifying the thermodynamic

state with temperature T_0 and volume V_0, or, for a constant-pressure combustion process, the specific internal energy e_0 and the volume V_0 can be assigned for a constant-volume combustion [91]. As for Gibbs minimization, an iteration process is required to obtain the final composition, thus a descent Newton-Raphson method is used(see [91, 92]). Once evaluated the temperature and the composition of the mixture, it is possible to calculate the other necessary thermodynamic quantities. First of all, the specific heat at constant pressure of the equilibrium composition

$$c_{p,eq} = c_{p,re} + c_{p,fr} \tag{6.27}$$

which is the sum of a *reaction* contribution and a *frozen* contribution [91], respectively expressed as

$$c_{p,re} = \sum_{j=1}^{N_s} n_j \frac{H_j^\circ}{T} \left(\frac{\partial \ln n_j}{\partial \ln T} \right)_p \tag{6.28}$$

and

$$c_{p,fr} = \sum_{j=1}^{N_s} n_j C_{p,j}^\circ \tag{6.29}$$

where the term $(\partial \ln n_j / \partial \ln T)_p$ is obtained by differentiating the Eq. 6.10 with respect to temperature:

$$\left(\frac{\partial \ln V}{\partial \ln T} \right)_p = 1 + \left(\frac{\partial \ln n}{\partial \ln T} \right)_p \tag{6.30}$$

while, by differentiating with respect to pressure:

$$\left(\frac{\partial \ln V}{\partial \ln p} \right)_T = -1 + \left(\frac{\partial \ln n}{\partial \ln p} \right)_T \tag{6.31}$$

In order to calculate the $c_{p,eq}$, one needs to solve a non linear equations system by means of an iterative process (detailed described in [91]) necessary to obtain the derivative terms in the right side of the Eqs. 6.30 and 6.31. Finally, the specific heat at constant volume of the equilibrium mixture is

$$c_{v,eq} \equiv \left(\frac{\partial e}{\partial T} \right) = c_{p,eq} + \frac{\frac{pV}{T} \left(\frac{\partial \ln V}{\partial \ln T} \right)_p^2}{\left(\frac{\partial \ln V}{\partial \ln p} \right)_T} \tag{6.32}$$

then, with the specific heat ratio $\gamma = c_{p,eq}/c_{v,eq}$ one can evaluate the isentropic exponent

$$\gamma_s = -\frac{\gamma}{\left(\frac{\partial \ln V}{\partial \ln p} \right)_T} \tag{6.33}$$

used for calculation of the speed of sound

$$a_s = \sqrt{nR^\circ T\gamma_s} \tag{6.34}$$

where R° here is expressed in $J/(kmol \cdot K)$. The complete treatise of the entire chemical equilibrium calculation process is explained in [91]. In the HRE Code the minimization of Helmholtz energy is applied to obtain the thermodynamic state and composition of the main flux, the average quantities inside the combustion chamber and the de Laval nozzle; the initial state is estimated by the Q1D compressible Euler equations, that provide the density, the temperature, the total energy and the mixture fraction. On the other hand, the minimization of Gibbs energy is used to evaluate the thermodynamic state of the flame region, requiring, as inputs, the combustion chamber pressure, which is calculated with Eq. 6.10 once obtained the composition and temperature of the main flow, by means of Helmholtz energy. In Gibbs calculation the stoichiometric mixture fraction is considered. In the HRE code, the mixture fraction is the ring of connection between fluid dynamic calculation and thermochemical calculation [11].

Transport Properties

Once obtained the equilibrium composition and the temperature, it is necessary to evaluate the transport properties of the gas mixture. In NASA CEA manual [91, 92] a transport properties database is provided: for each chemical species one can estimate the viscosity and thermal conductivity as a function of temperature. For the estimation of gas mixture thermal conductivity κ_{mix} and viscosity μ_{mix} the Wilke approach [173] can be used, valid for low density gases. Wilke defined a coefficient $\phi_{z,j}$ which takes care of the viscosity interaction between the gases of the mixture. This interaction coefficient is given by

$$\phi_{z,j} = \frac{C}{\sqrt{8}}\left(1+\frac{w_z}{w_j}\right)^{-1/2}\left[1+\left(\frac{\mu_z}{\mu_j}\right)^{1/2}\left(\frac{w_j}{w_z}\right)^{1/4}\right]^2 \tag{6.35}$$

where C is a constant, typically 1 for estimation of μ_{mix} and 1.065 for estimation of κ_{mix} [173]. By knowing the interaction coefficient one can obtain

$$\mu_{mix} = \sum_{z=1}^{N_s} \frac{X_z\mu_z}{\left(\sum_{j=1}^{N_s} X_j\phi_{zj}\right)} \tag{6.36}$$

and

$$\kappa_{mix} = \sum_{z=1}^{N_s} \frac{X_z\kappa_z}{\left(\sum_{j=1}^{N_s} X_j\phi_{zj}\right)} \tag{6.37}$$

where X_z and X_j are the mole fraction of the species *zth* or *jth*, respectively [173]. The transport properties are required for the estimation of regression rate r_f, in particular, Marxman et al. model needs the mixture viscosity of the main stream, which

is calculated using temperature obtained by Helmholtz energy minimization, while Greatrix model needs both the mixture viscosity and mixture thermal conductivity in the energy-zone thickness δ_{fl}, both calculated using the flame temperature obtained by Gibbs energy minimization. The NASA database provides the viscosity and thermal conductivity for all the chemical species considered in this work, except for butadiene C_4H_6. However, by observing the results of chemical equilibrium calculation, in the range of interest for this study, one can see that the mass fraction of butadiene species is significantly smaller (some orders of magnitude) than mass fraction of the other eight species. This result suggests the possibility to neglect the viscosity and thermal conductivity of butadiene in the calculation of the transport properties of the gas mixture. Hence, for the purpose of this work, as assumption, the transport properties of gaseous butadiene are not considered in the Wilke approach.

6.2.4 Mixture Fraction

The mixture fraction is defined as [11, 168]

$$\xi \equiv \frac{b_C^\circ - b_C^{\circ(ox)}}{b_C^{\circ(f)} - b_C^{\circ(ox)}} \tag{6.38}$$

where b_C° represents the assigned kilogram-atoms of Carbon per kilogram of total reactants if no superscript specified, per kilogram of fuel if superscript is (f) and per kilogram of oxidizer when the superscript is (ox). As described in the previous section, to minimize the free energies of Gibbs and Helmholtz some constraints must be specified. For chemical equilibrium, the conservation of element mole number is assumed: b_C°, b_H° and b_O° must be assigned (the 9 species selected are composed only by these 3 elements). As one can see from Eq. 6.38, the term b_C° can be expressed as a function of the mixture fraction, previously estimated by flow field equations and, considering a generic hydrocarbon formula C_xH_y, one can write

$$b_C^\circ = \left(\frac{1 \cdot x}{12 \cdot x + 1 \cdot y} - 0\right)\xi - 0 = \frac{x}{12x + y}\xi \tag{6.39}$$

where x represents the number carbon atoms and y the number of hydrogen atoms, while 12 and 1 are the approximated atomic weight of carbon and hydrogen respectively, in kg/kmol. It is necessary to relate b_C° with b_H° and b_O°, thus providing a complete set of constraints to the chemical equilibrium algorithm. Once defined such relation it is possible to execute the chemical equilibrium algorithm with condition constraints imposed by solving the compressible Euler equations for the flowfield. In this work one fuel type and two oxidizer types are considered:

- **Fuel**: gaseous butadiene C_4H_6, defined by the generic alkynes[2] formula C_nH_{2n-2};
- **Oxidizer** 1: gaseous oxygen O_2;

2 Alkynes are unsaturated hydrocarbons with triple bonds between carbon atoms.

- **Oxidizer** 2: gaseous decomposition products of hydrogen peroxide H_2O_2.

Since the first assumption of the HRE Code consists in considering only gaseous species, the gasification of HTPB is represented by gaseous butadiene chains released by the fuel surface into the combustion chamber. This hypothesis agrees with Lagelle's experimental results about solid fuel pyrolysis: the experiments have shown that the pyrolysis gas produced by the degradation of HTPB consists mostly of C_4H_6 [170, 55]. Following the first assumption, the hydrogen peroxide can be used in HRE Code by considering its decomposition products, see Eq. 6.4. This solution provides a significant advantage in terms of chemical modeling, in fact, because H_2O_2 decomposes into O_2 and H_2O, it is not necessary to change the set species selected for the chemical equilibrium calculation. However, different propellant couples requires different relations between the element moles numbers (b°_C, b°_H and b°_O) as a function of the mixture ratio.

Propellant Couple: $C_4H_6 + O_2$

The relation between the element mole number is based on the following assumption:

All chemical species has the same velocity $\Rightarrow b^\circ_C : b^\circ_H = x : y$

so one can write

$$\begin{cases} b^\circ_H = \frac{y}{x} b^\circ_C \\ w_C b^\circ_C + w_H b^\circ_H + w_O b^\circ_O = 1 \end{cases} \tag{6.40}$$

where w_k is the weight per mole of element k ($w_C = 12$, $w_H = 1$ and $w_O = 16$). By substituting Eq. 6.39 in the Eqs. system 6.40 it is possible to obtain the relation between the element moles numbers, used as constraints for minimization of Gibbs and Helmholtz energies

$$\begin{cases} b^\circ_C = \frac{x}{12x+y}\xi \\ b^\circ_H = \frac{y}{12x+y}\xi \\ b^\circ_O = \frac{1}{16}(1-\xi) \end{cases} \tag{6.41}$$

The stoichiometric mixture fraction ξ_s is obtained by considering the generic reaction between a hydrocarbon and oxygen molecule

$$C_xH_y + \left(x + \frac{y}{4}\right) O_2 \rightarrow xCO_2 + \frac{y}{2}H_2O \tag{6.42}$$

and, being valid $b^\circ_{C,s} : b^\circ_{H,s} : b^\circ_{O,s} = x : y : (2x + y/2)$ [168], the stoichiometric element moles numbers are

$$\begin{cases} b^{\circ}_{C,s} = \frac{x}{12x+y}\xi_s \\ b^{\circ}_{H,s} = \frac{y}{12x+y}\xi_s \\ b^{\circ}_{O,s} = \frac{1}{16}(1-\xi_s) \end{cases} \tag{6.43}$$

and ξ_s can be estimated as

$$\xi_s = \frac{12x+y}{44x+9y} \tag{6.44}$$

where the approximated molecular weight values has been used (w_{H_2O} = 18 and $w_{CO_2} = 44$). The stoichiometric mixture fraction is used in the minimization of Gibbs energy, whose algorithm is applied to the flame region in order to estimate the flame temperature and flame composition. Because of this, ξ_s remains a constant parameter while, on the contrary, the mixture fraction depends on the average conditions in the combustion chamber and it is calculated by Eqs. 6.5, becoming a basic input of the algorithm for the minimization of Helmholtz energy. Moreover, still considering the chemical reaction of Eq. 6.42, it is possible to evaluate the local O/F, to be used in regression rate calculation by Marxman et al. model

$$O/F_{[C_4H_6+O_2]} = \frac{\left(x+\frac{y}{4}\right) w_{O_2}}{1 \cdot w_{C_xH_y}} = \frac{11 \cdot w_{O_2}}{2 \cdot w_{C_4H_6}} \quad . \tag{6.45}$$

Propellant Couple: $C_4H_6 + H_2O_2$

By proceeding in the same manner and considering the same assumption applied for the previous propellant couple, one can write

$$\begin{cases} b^{\circ}_{C} : b^{\circ}_{H,f} = x : y \\ b^{\circ}_{H,ox} : b^{\circ}_{O} = 2 : 2 \\ \\ with \\ b^{\circ}_{H} = b^{\circ}_{H,f} + b^{\circ}_{H,ox} \end{cases} \tag{6.46}$$

where b°_{H} is divided into the fuel component $b^{\circ}_{H,f}$ and the oxidizer component $b^{\circ}_{H,ox}$, being the hydrogen peroxide made by hydrogen besides oxygen. This procedure is based on an elements balance between fuel and oxidizer molecules; it is reasonable to assume that the elements balance between butadiene and hydrogen peroxide remains valid also considering the decomposition products of H_2O_2 as oxidizer. Now, with the same approach used before, the following system can be solved

$$\begin{cases} b^{\circ}_{H,f} = \frac{y}{x} b^{\circ}_{C} \\ b^{\circ}_{H,ox} = b^{\circ}_{O} \\ w_C b^{\circ}_{C} + w_H (b^{\circ}_{H,f} + b^{\circ}_{H,ox}) + w_O b^{\circ}_{O} = 1 \end{cases} \tag{6.47}$$

obtaining

$$\begin{cases} b_C^\circ = \frac{x}{12x+y}\xi \\ b_H^\circ = \frac{1}{17}\left(1+\frac{8}{9}\xi\right) \\ b_O^\circ = \frac{1}{17}(1-\xi) \end{cases} \tag{6.48}$$

that are the relation between the element moles numbers and the mixture fraction. The stoichiometric mixture fraction is obtained considering the generic reaction between a hydrocarbon and oxygen molecule

$$C_xH_y + \left(2x+\frac{y}{2}\right)H_2O_2 \rightarrow xCO_2 + (2x+y)H_2O \tag{6.49}$$

and, similarly as before, on can write

$$\begin{cases} b_C^\circ = \frac{x}{12x+y}\xi_s \\ b_H^\circ = \frac{1}{17}\left(1+\frac{8}{9}\xi_s\right) \\ b_O^\circ = \frac{1}{17}(1-\xi_s) \end{cases} \tag{6.50}$$

that are the element moles numbers as a function of the stoichiometric mixture fraction, which can be estimated as

$$\xi_s = \frac{12x+y}{80x+18y} \tag{6.51}$$

Finally, still considering the chemical reaction with hydrogen peroxide (Eq. 6.49), it is possible to evaluate the local O/F, to be used in regression rate calculation by Marxman et al. model

$$O/F_{[C_4H_6+H_2O_2]} = \frac{\left(2x+\frac{y}{2}\right)w_{H_2O_2}}{1\cdot w_{C_xH_y}} = \frac{11\cdot w_{H_2O_2}}{w_{C_4H_6}} \quad . \tag{6.52}$$

The described approach is valid for the propellant couple made by HTPB and pure hydrogen peroxide, not diluted in water. It is important to remember that the HRE Code considers only gaseous species, thus the gasified HTPB is approximated by gaseous butadiene C_4H_6 while the hydrogen peroxide is assumed, at the combustion chamber inlet, already decomposed into gaseous O_2 and H_2O, in their relative amount. Therefore, the oxidizer inlet conditions are expressed in term of mass fraction and thermochemical properties of a mixture made by the products of H_2O2 catalytic decomposition. The mass fraction Y_h of the species h is define as

$$Y_h = \frac{n_h w_h}{\sum_{j=1}^{N_s} n_j w_j} \tag{6.53}$$

where N_s is the number of species, in this case equal to 2. Thus, by considering the mass fraction definition and the Eq. 6.4 it is possible to calculate the amount of gaseous oxygen O_2 and water H_2O produced by hydrogen peroxide decomposition, hence defining the oxidizer inlet composition by means of mass fraction:

- $Y_{O_2} = 0.47$
- $Y_{H_2O} = 0.53$

This ratio corresponds to the relation between the element moles numbers and mixture fraction, previously developed. The simulation of combustion with high tested peroxide (i.e. hydrogen peroxide diluted in water), with typical percentages of 90%-98%, involves a change in the ratio between mass fractions at the inlet, as well as different relations between the element moles numbers and the mixture fraction, because the water species must be considered in the elements balance. In the frame of this study, for simplicity, the HRE Code considers only pure H_2O_2 and for the hybrid rocket design a correction on the performance will be applied to evaluate hydrogen peroxide diluted in water. A detailed description of this downstream-correction is provided in section 7.2.

6.2.5 HRE Code Algorithm

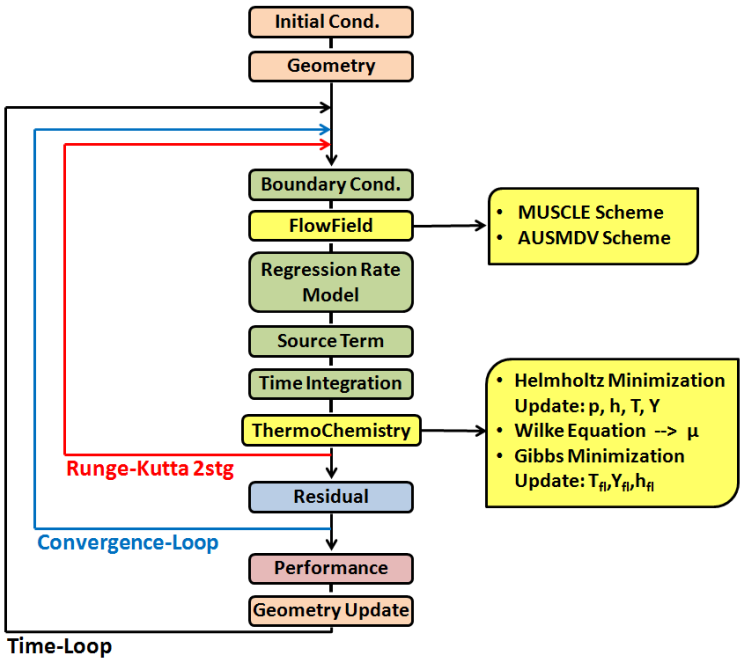

Figure 45.: HRE Code algorithm schematic.

In Figure 45 a schematic of the HRE Code algorithm is presented. Before loop phase, the initial conditions, the rocket geometry and boundary conditions, as well as some input specifications, are defined. For each t_n step of the time-loop the flowfield equations and the chemical equilibrium are solved in all cells of the Q1D domain,

obtaining a convergent solution and calculating the fuel regression rate r_f. Then, the solid fuel port diameter D_p is updated as

$$D_{p,i}^{n+1} = D_{p,i}^{n} + \left(2 \cdot r_{f,i}^{n} \cdot \Delta t\right), \quad i = 1, N_x \quad n = 1, N_t \tag{6.54}$$

thus it is possible to proceed with the calculation of a convergent solution for t_{n+1}, and so on. This calculation approach provides a quasi-static description of the regression rate during the combustion time; this means that transient phenomena cannot be considered. The code is made by several subroutines: the primitive variables, after the boundary condition update, are processed by the *FlowField subroutine*, which applies the second-order MUSCL scheme and AUSMDV scheme to calculate the numerical fluxes on each cell interface. Then, the regression rate is estimated, in order to evaluate the mass source term $\overline{\mathbf{S}}_{Mass,i}^{n}$, as well as the $\overline{\mathbf{S}}_{Q1D,i}^{n}$. The first Runge-Kutta stage is applied and the results of time integration are processed by *ThermoChemistry subroutine*, which performs the chemical equilibrium calculation, pressure update and transport properties estimation. This procedure is repeated for the second stage of the Runge-Kutta loop. The description of the discretization method, high accuracy and numerical fluxes schemes, as well as the integration of the governing equation, are collected in F.

Convergence Criteria

The convergence criteria is based on the residual calculation for the total energy E and the pressure p

$$R_E^n = \frac{\sqrt{\sum_{i=1}^{N_x} \left(E_{t,i}^{n} - E_{t,i}^{n-1}\right)^2}}{N_x - 1}, \quad i = 1, N_x \quad n = 1, N_t \tag{6.55}$$

$$R_p^n = \frac{\sqrt{\sum_{i=1}^{N_x} \left(p_i^{n} - p_i^{n-1}\right)^2}}{N_x - 1}, \quad i = 1, N_x \quad n = 1, N_t \tag{6.56}$$

The convergent solution is reached when both residual values are below a defined tolerance *tol*: $R_E^n \leqslant tol \wedge R_p^n \leqslant tol$. In Figure 46, one can see a typical residual trend of HRE Code simulation: third order accuracy in space ($\kappa = 1/3$, see Table 29) and *tol*$= 10^{-4}$.

The use of a two-stages Runge-Kutta method, despite its high accuracy, involves a quite high number of iteration (see Figure 46), requiring more computational time with respect to a more efficient scheme, such as Explicit Euler or implicit schemes.

Boundary Conditions

Being a one-dimensional code, boundary conditions are required at inlet and outlet flow (applied in correspondence of ghost cells).

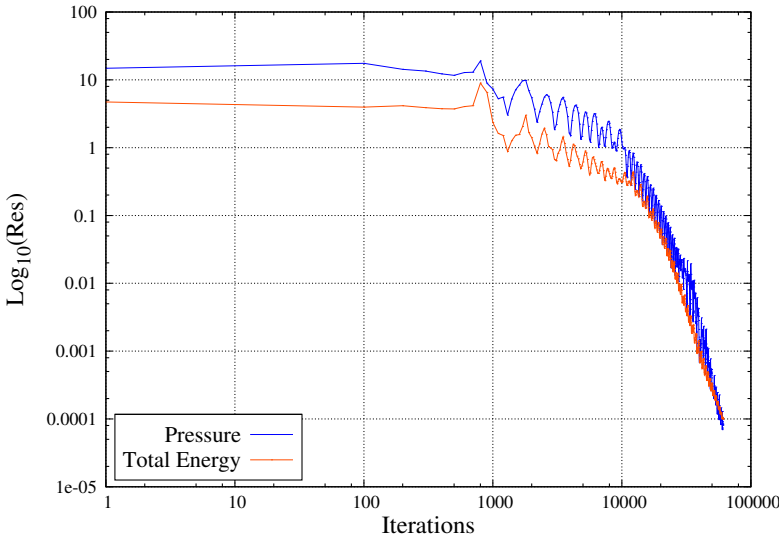

Figure 46.: Pressure and total energy residual of a typical HRE Code run vs. iterations number.

INLET FLOW At the inlet the oxidizer flow conditions are specified, in particular the gas composition in term of mass fraction Y_j, which is made only by O_2 species in case of GOX or by a O_2 and H_2O (in relative proportional amount) in case of hydrogen peroxide. Oxidizer temperature and mass flow rate are defined by the user. The pressure is extrapolated from the computational domain and the inlet density is calculated with Eq. 6.10. The other thermochemical quantities, e_i, e_t, h, c_p, c_v and γ are estimated by fitting the JANAF's data [91] and considering the initial oxidizer state. For simplicity and to reduce the computational cost, the specific heat at constant pressure and constant volume at the inlet are estimated considering only the *frozen* contribute (see Eq. 6.27). In the inlet ghost cell, the mixture fraction is equal to zero.

OUTLET FLOW The outlet conditions depend on the $Mach$ number of the exhaust flow, which can be subsonic or supersonic [167]. If $Mach < 1$ the flow in the nozzle divergent is *subsonic*: the velocity u, the density ρ and the mixture fraction ξ are extrapolated from the computational domain solution (zeroth-order extrapolation), while pressure p_a and temperature T_a are imposed at ambient conditions. The other thermochemical quantities are obtained with the same procedure described for inlet conditions. If $Mach > 1$ the flow in the nozzle divergent is *supersonic*: all the ghost cell outlet variables are extrapolated from the computational domain solution.

FUEL SURFACE TEMPERATURE The fuel surface temperature T_w corresponds to the temperature at which the fuel pyrolyzes and, considering HTPB, its value was observed to fall between 800-1000 K (HTPB pyrolysis is extensively discussed in [55, 170, 105]). For simplicity, in HRE Code the surface temperature is assumed as constant value, along the port length and during the combustion. A further development of

the computational model will include the application of the one-dimensional conduction law for the estimation of the fuel surface temperature.

OXIDIZER INLET TEMPERATURE When GOX is used as oxidizer the inlet temperature, T_{ox} is generally assumed equal to 300 K. On the other hand, when H_2O_2 is considered, a mixture of gaseous O_2 and H_2O, at high temperature, are assumed to enter in the combustion chamber. These hot gases are the products of hydrogen peroxide catalytic decomposition and, assuming an ideal catalytic reaction, the inlet temperature can raise to 1277 K. However, in the real applications, the H_2O_2 decomposition is not perfectly adiabatic and the catalyst efficiency depends on many factors, such as the material, the bed shape and its aging. In the HRE Code it is possible to modify the inlet oxidizer temperature for H_2O_2 by means of an efficiency parameter η_{cata} of the catalyst, which decreases the ideal inlet temperature of the decomposition products

$$T_{ox} = \eta_{cata} \cdot T_{ox}^{ideal} \quad . \tag{6.57}$$

Geometry

The computational domain consists of two parts: the combustion chamber (cc) and the de Laval nozzle [48, 160]. The combustion chamber is made by the solid fuel cylinder, which has a central circular perforation. The user defines the initial fuel perforation diameter D_p and the length L_f, see Figure 113. The convergent-divergent nozzle diameter $D_{noz}(x) = 2 \cdot r_{noz}(x)$, as a function of the x location, [169] is defined by

$$r_{noz}(x) = R_t - \frac{(R_c - R_t)}{(x_c - x_t)^4}(x - x_t)^4 + \frac{(R_c - R_t)}{(x_c - x_t)^2}(x - x_t)^2 \tag{6.58}$$

where R_c and R_t are, respectively, the inlet nozzle section radius and nozzle throat radius, while x_c and x_t are the respective locations of nozzle inlet and throat, see Figure 43. The Eq. 6.58 provides a symmetric nozzle, which is used for ballistics analysis in HRE Code, where rocket performance are not required.

For the purpose of preliminary design and mission analysis, a high expansion area-ratio nozzle ϵ_{noz} must be used, in order to optimize the performance attainable by the gas dynamic expansion. In this case the nozzle geometry is built by assembling the convergent part with the divergent part, each one obtained considering Eq. 6.58 but with different values assumed for R_c and x_c, that for the divergent are R_e and x_e

$$\begin{cases} R_e = R_t\sqrt{\epsilon_{noz}} \\ x_e = x_t + R_t\left(\frac{\sqrt{\epsilon_{noz}}-1}{tg\alpha_{div}}\right) \end{cases} \tag{6.59}$$

In Figure 47, one can see the comparison between the two nozzle types described: the simple symmetric nozzle provided by Eq. 6.58 and the assembled nozzle type obtained by the combination of two symmetric nozzles with different shapes, both

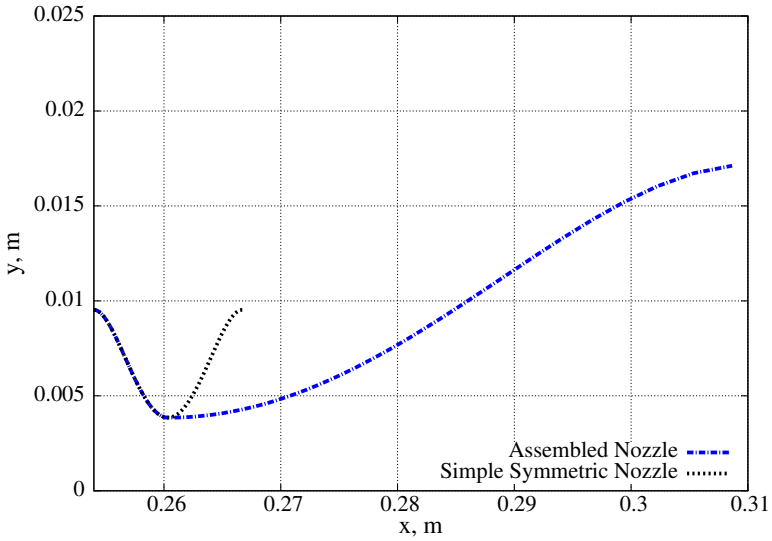

Figure 47.: Shape comparison between the symmetric nozzle, used for ballistics analysis, and the assembled nozzle, used for performance estimation and mission analysis. In this example the assembled nozzle is characterized by $\epsilon_{noz} = 20$.

defined by Eq. 6.58. The length of nozzle convergent is defined considering a semi-aperture angle α_{conv} of 40°-45°. In rocket motors the α_{conv} value does not show significant change in the nozzle performance [48, 160].

User Inputs

Several input data must be provided by the user within a *input subroutine*. First of all, engine geometry defined by the fuel length L_{fuel}, fuel central perforation diameter D_p, the nozzle throat diameter D_t and the type of nozzle, symmetric or with high values of ϵ_{noz}; the combustion conditions defined by the oxidizer mass flow rate $\dot{m}_{ox}$, the total combustion time t_b and the time intervals Δt, as well as the solid fuel surface temperature, assumed constant over fuel length during the combustion [170, 55]. Concerning the numerical flux calculation, the Courant-Friedrichs-Lewy (CFL) number [174], defined as

$$CFL = \frac{\Delta t \cdot |u + a_s|}{\Delta x} \tag{6.60}$$

must be selected, as well as the the desired accuracy order in spatial solution within MUSCLE scheme (respectively CFL = 0.3 and third-order spatial accuracy are used in this study). Other few parameters such as the convergence tolerance, max iteration number, etc. must be defined by the user. For the purpose of performance estimation and preliminary sizing, further inputs are provided as described in Chapter 7.

Tolerance and Time Interval Selection

The selection of the tolerance tol and time interval Δt values is based on a preliminary test simulation campaign. The same motor geometry and flow conditions were simulated with different tol for convergent solution and Δt for time integration. In Table 17, one can see the results of this analysis with respect to fuel regression rate (in mm/s) calculation.

$r_f[mm/s]$	$\Delta t[s]$ **0.5 vs. 0.3**	tol **10^{-2} vs. 10^{-4}**
Δr_f MAX [%]	0.74	0.042
Δr_f MIN [%]	0.27	0.002

Table 17.: Percentual difference in regression rate calculation for different Δt and tol, for a fixed motor geometry and flow conditions.

The percentage values in Table 17 are referred to regression rate results in mm/s; this means that:

- the increment of Δt from 0.3 to 0.5 s provides a change of the order of 10^{-3} on the regression rate value. Such variation is observed at the level of microns, hence, no significant changes are observed on the regression rate calculation when $\Delta t = 0.5$ s is used;
- the enlargement of the tolerance on residual from 10^{-4} to 10^{-2} involves a change on the regression rate value of the order of 10^{-4}. Even in this case no significant effects are observed on the regression rate with a larger tolerance for code convergence.

In the light of these results, the combination of a $\Delta t = 0.5$ s with a convergence tolerance of 10^{-2} allows for a significant reduction of computational time with no significant decrease in calculation precision. This results very useful in the frame of preliminary sizing, which requires many calculation runs and long-time combustion simulation.

6.3 APPLICATION AND VALIDATION

6.3.1 Time- and Space-Average Regression Rate

The HRE Code estimates the regression rate r_f along the fuel central perforation L_f. A typical r_f profile, with respect to axial location, at consecutive time-steps and obtained with Marxman model [63, 62, 64, 65, 55], is shown in Figure 48.

For the purpose of comparison with data from literature survey, the estimation of time- and space-averaged regression rate $\bar{\bar{r}}_f$ results more appropriate. The latter

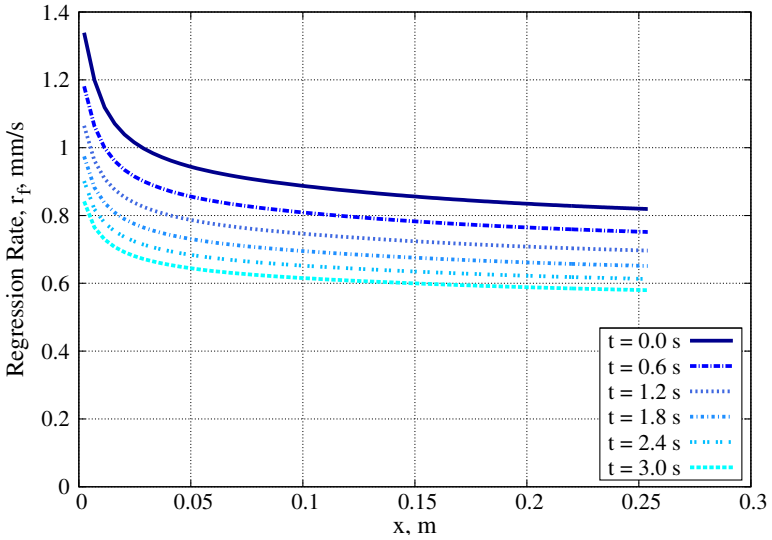

Figure 48.: Regression rate profile along the fuel port at different time steps (Marxman model).

is calculated by knowing the amount of fuel mass released during the combustion process

$$\Delta m_f = \rho_f \int_0^{L_f} \pi \left(r_{p,final}^2 - r_{p,initial}^2 \right) dx \tag{6.61}$$

where r_p is the port radius before and after combustion. The space-average final radius is obtained as

$$\bar{r}_{p,final} = \sqrt{r_{p,initial}^2 + \frac{\Delta m_f}{\pi \rho_f L_f}} \tag{6.62}$$

and the time-space-averaged regression rate results

$$\bar{\bar{r}}_f = \frac{\bar{r}_{p,final} - r_{p,initial}}{t_b} \tag{6.63}$$

where t_b is the combustion time. The fuel regression rate estimated with HRE Code, by means of Marxman et al. and Greatrix models, has been compared with some experimental cases. For an accurate comparison, it is necessary to know all the characteristics of the firing test, in terms of motor geometry, such as fuel length, fuel port and nozzle throat diameters, as well as the oxidizer mass flow rate and the combustion time. In the literature survey it is quite difficult to find works that provide so many details. Because of this, two cases are considered:

- HTPB + GOX - Shanks and Hudson [172]
- HTPB + H_2O_2 - Farbar, Louwers and Kaya [175]

A further experimental case is compared with HRE Code results: combustion tests performed with the SPLab experimental facilities, in particular the 2D-Radial micro burner.

6.3.2 Marxman Model vs. Greatrix Model

Both regression rate models, Marxman et al. and Greatrix, have been tested and compared with the selected experimental cases. For the regression rate calculation by Greatrix model very important is the choice of friction factor formula f^*, required for the the estimation of the zero-transpiration convective heat coefficient h^* in Eq. 6.18. Greatrix, in [171], for the central fuel cylindrical perforation suggests the use of an explicit form of the Colebrook's semi-empirical expression for f^* evaluation, valid for a fully developed turbulent single-phase flow in a rough pipe. In Figure 49, one can see the regression rate profile along the x-coordinate in the fuel port at $t = 0.0$ s, evaluated with Marxman et al. and Greatrix models at the same test conditions and fuel geometry. For the latter, three different friction factor explicit expressions were considered:

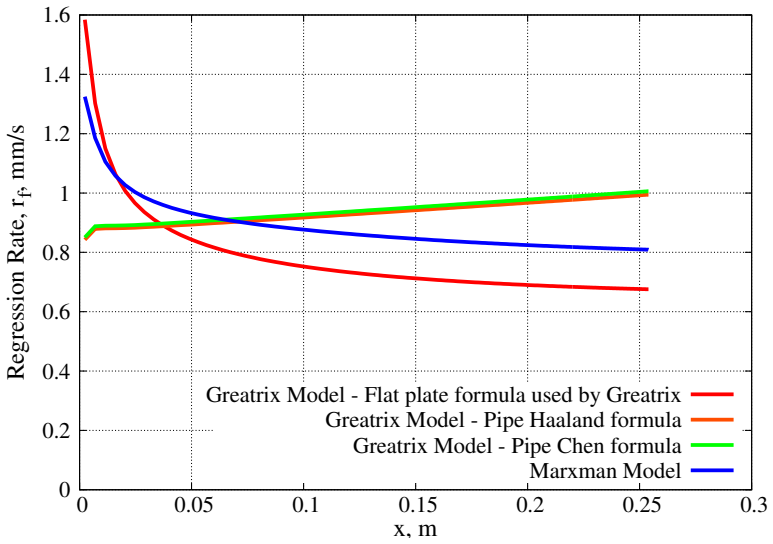

Figure 49.: Regression rate comparison with Marxman model and Greatrix model with different friction factor explicit formulas.

A. flat-plate formula (Eq. 6.19 used by Greatrix [171];

B. pipe flow Haaland formula [176, 177];

C. pipe flow Chen formula [176, 177].

Concerning the use of fully developed flow expressions, in which the velocity profile remains unchanged along the stream direction, the two explicit formulae of Haaland and Chen are respectively

$$\begin{cases} \frac{1}{\sqrt{f^*}} = -1.8 \log \left[\left(\frac{\zeta}{3.7 D_p} \right)^{1.11} + \frac{6.9}{Re_D} \right] \\ \\ 4000 \leqslant Re_D \leqslant 10^8 \quad \text{and} \quad 10^{-6} \leqslant \zeta / D_p \leqslant 0.05 \end{cases} \tag{6.64}$$

and

$$\begin{cases} \frac{1}{\sqrt{f^*}} = -2 \log \left[\frac{\zeta}{3.7065 D_p} - \frac{5.0452}{Re_D} \log \left(\frac{(\zeta / D_p)^{1.1098}}{2.8257} + \frac{5.8506}{Re_D^{0.8081}} \right) \right] \\ \\ 4000 \leqslant Re_D \leqslant 10^8 \quad \text{and} \quad 10^{-7} \leqslant \zeta / D_p \leqslant 0.05 \end{cases} \tag{6.65}$$

With the Greatrix model such formulae provide almost the same regression rate, characterized by a slight increase along the x distance. This behavior seems mainly due to the growth of the logarithm term of Eq. 6.20, which depends on the flame temperature and the specific heat at constant pressure within the energy-zone thickness [171]. The direct use of Eq. 6.64 or Eq. 6.65 means to consider a fully developed turbulent flow in the entire fuel port. This friction factor depends on the port diameter and probably it is not so appropriate for the evaluation of the local r_f along the axis, rather than for a space-averaged regression rate approximation, which assumes the grain length as a single finite element. The Marxman theory, developed for a flat-plate turbulent boundary layer, is compared with the Greatrix model assuming the friction factor formula for the flat-plate developing flow (Eq. 6.19). For both models, in Figure 49, it is observed a quite small decrease of the r_f along the fuel port except near the fuel head-end, where the steep trend is due to the initial growing of the boundary layer. In these zone its thickness is very small causing a higher heat transfer to the fuel surface. This effect appears more pronounced for the r_f obtained with Greatrix, due to the considered semi-empirical friction factor formula. Nevertheless, in practical applications such effect is not so pronounced [48] or even absence if we consider a cylindrical fuel geometry, since the injector configuration revealed to have a strong influence on the flow pattern inside the port diameter [73, 74], as well as on the local regression rate profile. In this sense, both models, based the convective energy-flux mass balance in the boundary layer, are far to be applicable in the same way to hybrid motors with different injector geometries and scale size. During the years, the Marxman theory was widely investigated and, in the case of uniform injection oxidizer flow and low radiation effects, it was demonstrated the strongly regression rate dependence on the mass flux ($r_f \propto G^{0.8}$) [63, 55]. Of course, this cannot be assumed valid for all motor geometries and scales; in fact, as reported in [73, 74], the spread jet obtained with a conical injector significantly modified the flowfield of the entire central fuel perforation postponing the boundary layer developing zone downstream in the port, after the impingement point where the oxidizer impacts to the grain surface (see Figure 15). In this motor, the r_f at the head-end resulted smaller than that measured in correspondence (the maximum value) and above of the impingement

point. Due to this so complex flowfield, the time- and space-averaged regression rate showed a lower dependence on mass flux ($r_f \propto G^{0.37}$) with respect to the classical theory. Therefore, the high complexity of the internal chamber flow prevents an easy definition of a unique law able to widely describe the hybrid rockets behavior. Nevertheless, being the aim of this work the development of a relatively simplified design tool for preliminary sizing of a hybrid motor for ADR missions, therefore a preliminary estimation of propellant consumption and available thrust, the Marxman et al. model, despite its limitations, at this level can be considered. The latter, widely investigated and supported by experimental results is preferred instead of Greatrix model, which, although similar, has been evaluated and compared just with literature source results. From now on, the Greatrix model, originally considered for its simplicity, will be use for comparison purpose, assuming the flat-plate expression for the friction factor.

6.3.3 HTPB + GOX | Shanks-Hudson Tests

The first case considered for HRE code testing and validation is the experimental campaign performed by Shanks and Hudson [172] for the propellant couple HTPB + GOX. They tested six HTPB grains, each one with multiple consecutive firings of 3 seconds. After every burn, the mass of fuel was measured in order to estimate the time- space-averaged regression rate $\bar{\bar{r}}_f$. For the comparison with HRE Code, only the first 3 grains were completely simulated, considering all firings, while, for *Grains 4,5* and *6*, just the first firing was computed.

	Test Conditions			*Exp. Results*	
Sample	**Run Number**	$\dot{m}_{ox}$ [kg/s]	t_b [s]	$\bar{\bar{G}}_{ox}$ [kg/(m² · s)]	$\bar{\bar{r}}_f$ [mm/s]
Grain 1	01	0.0735	3	205.1	1.03
Grain 1	02	0.0635	3	117.2	0.99
Grain 1	03	0.0544	3	78.9	0.73
Grain 1	04	0.0467	3	55.6	0.66
Grain 2	01	0.0798	3	225.4	0.99
Grain 2	02	0.0610	3	107.8	0.93
Grain 2	03	0.0540	3	70.7	0.58
Grain 2	04	0.0458	3	49.6	0.49
Grain 3	01	0.0780	3	219.2	1.02
Grain 3	02	0.0594	3	106.5	0.85
Grain 3	03	0.0526	3	70.3	0.61
Grain 3	04	0.0454	3	49.5	0.53
Grain 4	01	0.0510	3	147.8	0.88
Grain 5	01	0.0560	3	161.4	0.91
Grain 6	01	0.0520	3	147.6	0.98

Table 18.: Test conditions for HTPB + GOX case.

In Table 18, one can see the data resume of all firings considered for HRE Code simulation. Moreover, on the right side of Table 18 the experimental results [172] obtained by Shanks and Hudson are presented. All the six grains have the same dimensions: 25.4 cm of length and a central port diameter of 19.06 mm. The throat diameter D_t is not provided in [172], so it was deducted geometrically by the rocket motor schematics presented in the paper. A D_t of 7.7 mm has been estimated, which is able to provide a chamber pressure very close to the measurements carried out by Shanks and Hudson ($\sim$ 3.0 MPa). The simulation was performed using both Marxman et al. and Greatrix models. The oxidizer is gaseous oxygen ($Y_{O_2} = 1$) with an inlet temperature of 300 K. The surface temperature T_w of the fuel is assumed equal to 820 K [105], while the fuel density is 915 kg/m^3. A $\Delta t = 0.3$ s and a convergence tolerance of 10^{-4} are applied. For ballistics analysis a simple small symmetric nozzle, designed with Eq. 6.58, is used. In Figure 50, the time- and space-averaged regression rate comparison between experiments [172] and HRE Code is presented. The results are fitted with a power law in order to obtain the simplified regression rate expression [63, 55].

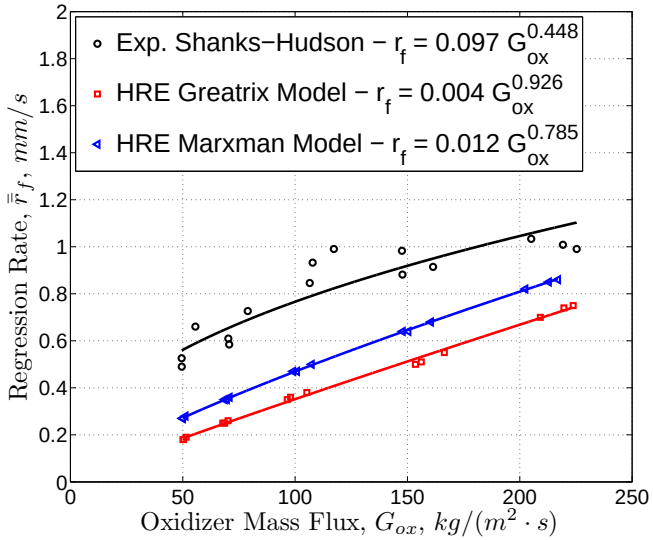

Figure 50.: Time- space-averaged regression rate comparison: experimental vs. numerical results. Simplified power law for *HTPB + GOX* case.

The coefficient a_p and the exponent n_p of the power laws are reported in the legend. The experimental curve shows a low power ($\sim$ 0.45) with respect to Marxman theory, for which a strong dependence of the regression rate on mass flux G is expected ($n_p \sim 0.8$). The power evaluated for Greatrix model results higher than 0.8, because in the semi-empirical r_f expression (see Eq. 6.20) the mass flux is raised to a power of 1.0. In Shanks and Hudson experiments the quite low n_p could reasonably due to oxidizer injection, as discussed in Sections 4.2.1 and 6.3.2. The injector of this motor is made by an injection pipe which leads the oxidizer to flow throughout a diffusion screen followed by a pre-chamber. This system quite differs from the conical nozzle used by

Carmicino and Russo Sorge [73, 74], whereas the power exponent of time- and space-averaged regression rate results relatively close, meaning that minor changes in the injection geometry strongly affects the motor behavior, hence the internal flowfield and the developing of a turbulent boundary layer. By observing the Figure 50, one can see that both models, Greatrix and Marxman, underestimate the regression rate. In Figure 51, a bars plot emphasizes the relative differences between experimental and numerical results. Each bar is referred to the mean value of $\bar{\bar{r}}_f$ and $\bar{\bar{G}}_{ox}$ at five different mass flux ranges, corresponding to different firings conditions for the same grain (see *Run Number* in Table 18). The relative percentage differences are estimated as

$$\Delta r^{\%}_{f,i} = \frac{r^{num}_{f,i} - r^{exp}_{f,i}}{r^{exp}_{f,i}} \cdot 100 \tag{6.66}$$

where the index i is referred to the firing number (see Table 18); Eq. 6.66 is used also for mass flux percentages. In Table 19 the average percentages, at the average G_{ox} ranges, are reported. For both models, the difference from the experimental values significantly increases as the mass flux decreases, becoming of 51% for Marxman and 67% for Greatrix. The lowest value is observed at high mass fluxes, 16.6% for Marxman and 27.8% for Greatrix. Concerning the G_{ox} values the lack from experimental results remains below 10% for both models. From this comparison one can see that both Marxman and Greatrix models do not match the experimental results of Shanks and Hudson [172]. The numerical O/F results higher than experimental case (see Figure 56), for which an average value between 1.5 and 4.5 was estimated [172], very close to stoichiometric value for HTPB and GOX.

Relative percentages					
G_{ox} [kg/(m^2 · s)]	217	152	111	73	52
Marxman et al. Model					
$\overline{\Delta r_f}^{\%}$	-16.6	-29.5	-48.0	-44.8	- 51.1
$\overline{\Delta G_{ox}}^{\%}$	-2.7	0.4	-7.3	-5.0	-2.4
Greatrix Model					
$\overline{\Delta r_f}^{\%}$	-27.8	-43.9	-60.6	-60.4	-67.2
$\overline{\Delta G_{ox}}^{\%}$	-0.4	4.3	-9.6	-6.0	-1.8

Table 19.: Relative percent differences in regression rate between experimental data and numerical results. HTPB + GOX case.

In the HRE Code the radiation contribute is not considered, see Section 4.1, and this could be one of the reasons for a so large distance between numerical solution and experiments. In fact, the radiant heat flux can account for more than 50% of the total heat flux [55]. Furthermore, while the numerical domain is made only by the central fuel port and a nozzle connected to the aft port section (see Figure 113), the experimental setup consists of a more complex geometry, involving an injector with diffusion screen, pre- and post- combustion chambers, that have an important

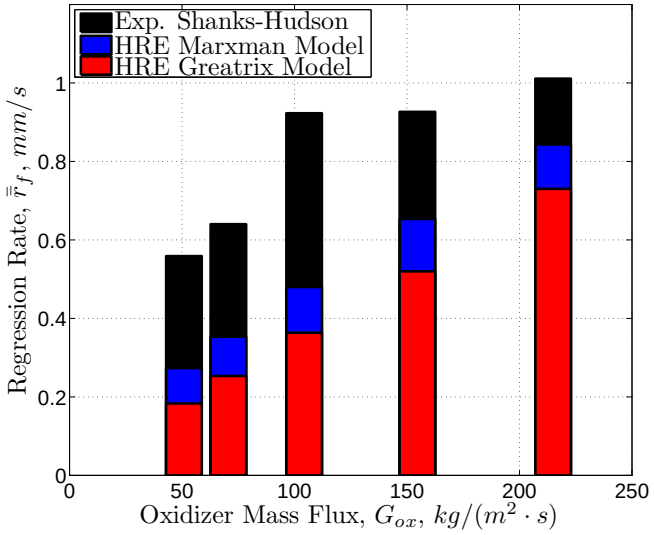

Figure 51.: Time- space-averaged regression rate comparison: experimental vs. numerical results. Bars plot for *HTPB + GOX* case.

role in the definition of the internal the flow pattern, as demonstrated in the literature. Therefore, besides the lack due to the missing of soot radiative contribute, the r_f trend could be mainly influenced by the particular injector geometry and the Marxman et al. model, for how it was defined, scarcely matches the experimental results, as verified by the growing discrepancy observed at low mass flux values, due to the high exponent of the power law.

6.3.4 HTPB + GOX | SPLab Tests

In this case, the HRE Code results are compared with experimental data achieved with the 2D-Radial micro burner built in SPLab. This facility, the acquisition procedure and the time-resolved technique for data reduction are described in Chapter 5. The instantaneous regression rate corresponds to a space-averaged value $\bar{r}_f$, since only the frontal fuel section can be observed by the optical instrumentation. Therefore, from this point of view, it is only possible to achieve an average measure of the port diameter for each time instant t^n. On the contrary, the HRE Code calculates the regression rate profile along the fuel port at each t^n, thus, for purpose of data comparison, the space-averaged regression rate is estimated, excluding the steep-slope region of r_f profile (see Figure 48), which cannot physically be measured by the optical technique (a defined number of cells are not included in the average calculation). The SPLab facility is quite smaller than the other cases considered for validation, the cylindrical solid fuel has a port diameter of 4.0 mm and a length of 30 mm; moreover, the hot gases are not accelerated by a gas dynamic nozzle but throughout a pipes system with electro-valves, that allow to maintain a constant chamber pressure during the firing.

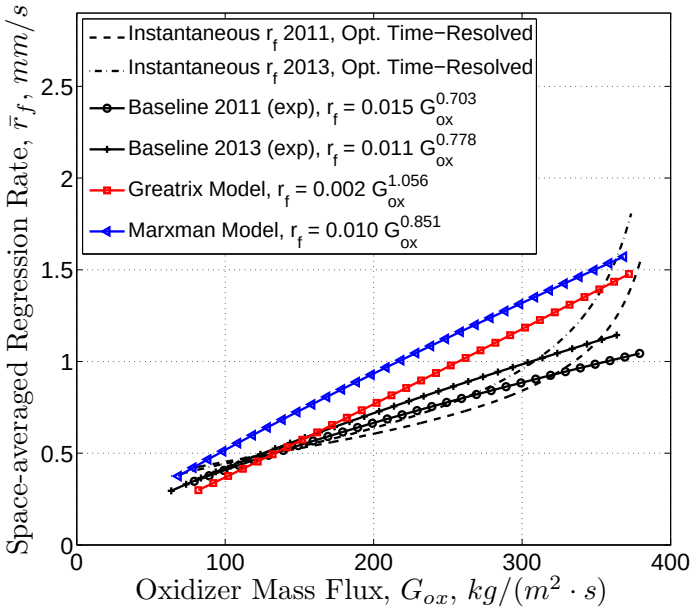

Figure 52.: Regression rate comparison between 2D-Radial micro burner (SPLab) experimental results and HRE Code estimation. For experimental case both instantaneous r_f and power law approximation are presented.

The HRE Code is not designed for a such kind of system, thus a nozzle throat of 3.0 mm was assumed in order to achieve an average pressure of 1.0 MPa during a combustion of 4.0 s (combustion time and pressure used in the experimental tests [152]). In Figure 52, the results from Marxman and Greatrix models are compared with the instantaneous regression rate curves and the respective power law approximations. The experimental curves considered are the baseline ensembles, 2011 and 2013 [124, 152], described in Chapter 5, and they are referred to a constant mass flow rate of about 0.005 kg/s.

Relative Percentages $\overline{\Delta r_f}^{\%}$	**G_{ox}** $\mathbf{kg/(m^2 \cdot s)}$					
Marxman et al. Model	**350**	**300**	**250**	**200**	**150**	**100**
Baseline 2011	52.4	49.0	45.1	40.4	34.5	26.7
Baseline 2013	35.4	34.0	32.2	30.0	27.3	23.6
Greatrix Model	**350**	**300**	**250**	**200**	**150**	**100**
Baseline 2011	40.4	33.0	24.7	15.2	4.1	-9.8
Baseline 2013	24.7	19.5	13.6	6.7	-1.5	-12.0

Table 20.: Relative percent differences in regression rate between experimental SPLab data and numerical results. HTPB + GOX case considering two experimental baselines [140, 152].

The numerical simulations, both for Marxman and Greatrix models, are performed at the same operative conditions, by using a time interval Δt of 0.2 s. Note that the power exponent of the numerical curves is a little bit higher than the power imposed in the relative analytical models; this is due to a re-fitting of the regression rate experimental ensembles by means of an equi-spaced G_{ox} range. From comparison results, one can see that, in contrast to the Shanks and Hudson case comparison, the numerical results are more close to the experiments. Also the O/F results of the same range of the experiments. The HRE code works at adiabatic conditions while, in the 2D-Radial micro burner, the HTPB sample is inserted in a bigger chamber, pressurized with nitrogen flow jet at ambient temperature, used to cool the injector walls and keep clean the optical windows. Such configuration does not allow for adiabatic conditions, involving reasonable lower combustion temperatures, as well as lower regression rate values. Furthermore, being the fuel strand largely smaller than the burn chamber (connected by exhaust pipes to the electro-valves), the hot gases, as well as soot, generated within the fuel port may quickly expand into the latter, residing for a relatively small time in the central perforation, without giving a significant radiative contribute to the fuel regressing process. Such behavior could justify the overestimation obtained with a pure convective model and, eventually, the better matching between numerical and experimental results previously obtained with Greatrix model [124]. Concerning the power law approximation, the experimental exponents resulted quite near to that expected by Marxman theory, thus showing a strong dependence from the mass flux. Probably the injection system of the 2D-Radial micro burner is able to provide a relatively uniform flow. However, further test comparisons would be necessary to better understand these results behavior.

6.3.5 HTPB + H_2O_2 | Farbar-Louwers-Kaya Tests

The last case considered for HRE code testing and validation is the experimental campaign performed by Farbar, Louwers and Kaya [175] for the propellant couple HTPB + H_2O_2(90%). They tested two HTPB grains, each one with a density of about 907 kg/m^3 and a combustion time of 7-8 s. After every burn, the mass of fuel was measured in order to estimate the time- space-averaged regression rate $\bar{\bar{r}}_f$. In Table 21, one can see the data resume of the two firings performed with HRE Code and, on the right side of the same table, the experimental results [175] obtained by Farbar et al. are presented.

	Test Conditions			*Exp. Results*		
Sample	**Run Number**	$\dot{m}_{ox}$ [kg/s]	t_b [s]	$\overline{P_c}$ [MPa]	$\bar{\bar{G}}_{ox}$ [kg/(m² · s)]	$\bar{\bar{r}}_f$ [mm/s]
Grain 1	01	0.10	8.08	3.69	150	0.67
Grain 2	01	0.12	6.99	3.54	93	0.37

Table 21.: Test conditions for HTPB + H_2O_2 case.

Note that the oxidizer mass flow rates $\dot{m}_{ox}$ declared by Farbar et al. for the two tested grains do not seem realistic. In fact, in [175] they assume injection mass flow rates of 0.00325 kg/s (*Grain 1*) and 0.00344 kg/s (*Grain 2*), that, considering the grain port diameters, provide an initial G_{ox} of 6 and 3 $kg/(m^2 \cdot s)$, respectively. These values are largely far from the average mass fluxes measured during the combustion tests, respectively 150 and 93 $kg/(m^2 \cdot s)$ (see Table 21). Furthermore, with such $\dot{m}_{ox}$ values the measured average chamber pressures, of about 3.5 MPa, is not reached. Therefore, it might be possible an error in the data definition during the paper writing. For purpose of data comparison, within HRE Code different mass flow rates have been assumed. Their values were defined by some consecutive attempts turned to obtain the same test conditions, in terms of average chamber pressure and average G_{ox}, for the defined motor geometry. The two grains have the same length of 39.15 cm, while the port diameter D_p is 25.4 mm for *Grain 1* and 38.1 mm for *Grain 2*. A throat diameter D_t of 8.0 mm is defined [175]. Farbar et al. consider hydrogen peroxide with a concentration of 90% in water; as discussed in Section 6.38, the HRE Code can simulate only pure hydrogen peroxide, with no water dilution. In Figure 53, one can see the comparison between numerical results and experimental data, while in Figure 54 the differences between simulation and experiment are emphasized by a bars diagram. The numerical simulation was performed considering only the Marxman model. Again, the HRE Code underestimates the regression rate, showing a maximum relative difference of 28.4% with respect to the *Grain 1* test, while a relative difference of 13.5% is obtained for *Grain 2*.

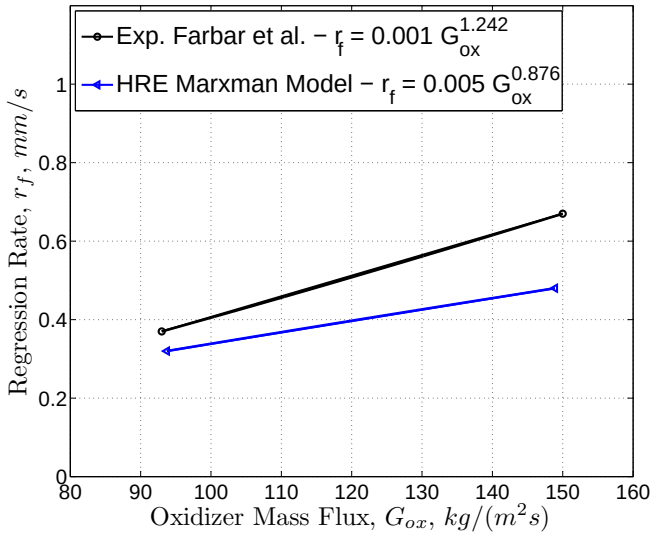

Figure 53.: Time- space-averaged regression rate comparison: experimental vs. numerical results. Simplified power law for *HTPB* + H_2O_2 case.

Concerning the mass flux, the distance from experimental values is below 1% for both the tested grains. In Table 22, the percentage differences between experiments and numerical solution are reported. Unfortunately, the available data in [175] consist of only two regression rate measures and, because of this, the comparison level is quite

poor. The simplified regression rate expressions, displayed in Figure 53, are obtained by fitting the $\bar{\bar{r}}_f$ data with a power law. The exponent n_p of the experimental curve results quite high (~ 1.2), because of a fitting made by only two points.

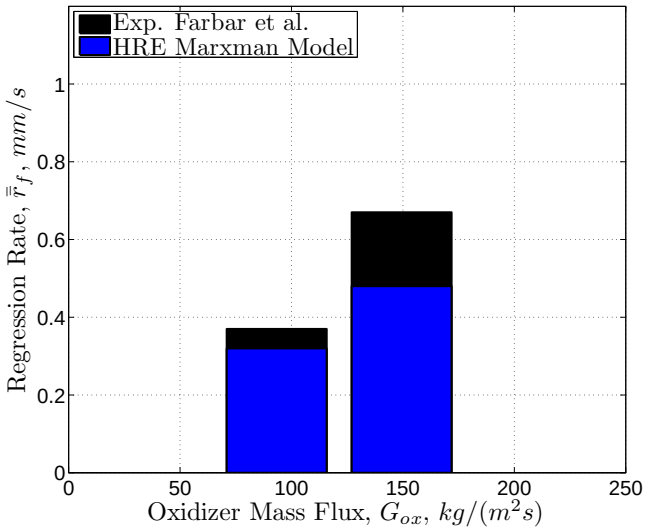

Figure 54.: Time- space-averaged regression rate comparison: experimental vs. numerical results. Bars plot for *HTPB* + H_2O_2 case.

Relative percentages		
G_{ox} [$kg/(m^2 \cdot s)$]	150	93
Marxman et al. Model		
$\overline{\Delta r_f}^{\%}$	-28.4	-13.5
$\overline{\Delta G_{ox}}^{\%}$	-0.7	0.8

Table 22.: Relative percent differences in regression rate between experimental data and numerical results. $HTPB + H_2O_2$ case.

Even the numerical curve shows a higher power due to the poor fitting, but still close to the value defined in Marxman theory, since in the regression rate expression the mass flux is raised to a power of 0.8 (see Eq. 4.7). Note that the HRE Code considers pure hydrogen peroxide for r_f calculation; this means that if the simulation is made with H_2O_2 diluted in water, the underestimate of regression rate would be larger. However, much more experimental data would be necessary for a better comparison and numerical analysis. The main remark is a general tendency to underestimate the regression rate by HRE Code, as already observed in the comparison with Shanks and Hudson experiments with similar motor scale [172]. As touched on before, a possible reason could be, besides the role of the injection geometry, the neglecting of radiation contribute, which, in the case of hydrogen peroxide, should be more intensive due to the presence of a higher concentration of H_2O in the gas products, with respect to the combustion with GOX.

6.3.6 Results and Discussion

In this study, a code for hybrid rocket ballistics analysis and preliminary design (HRE Code) was implemented. It is based on relatively simple physical models allowing for quite small computational costs. With the purpose of preliminary HPM sizing, the HRE Code leads to simulate different propellant couples and, in particular, the combination HTPB + H_2O_2, of which it is hard to find experimental data and regression rate power laws in the literature survey. For the regression rate estimate a pure convective mass balance at the fuel surface was applied, considering, and comparing, the Marxman et al. [62, 63, 64, 65, 55] and Greatrix [171] models. The HRE Code was here designed to work for two different propellant combinations: HTPB + GOX and HTPB + H_2O_2. In the frame of this research, the final objective is to get a flexible design tool for the preliminary design of a HPM for active removal missions in LEO. The code was tested with experimental data from literature survey and from combustion tests performed in SPLab. A general tendency to underestimate the regression rate was observed for both models: Marxman and Greatrix. The results obtained with Marxman r_f expression show a difference from the experimental regression rate of 16.6% at high mass flux and a maximum value of 51.1% at low mass flux, for the couple HTPB + GOX [172]; by considering the couple HTPB + H_2O_2, a maximum difference of 28.4% is observed at high mass flux while, at low mass flux, a difference of 13.5%. However, the latter comparison level is quite poor, because no many suitable data were found in the literature (only two available firings from [175]). In contrast, the comparison with SPLab experiments shows a little overestimate of the regression rate, higher with Marxman model, while Greatrix model resulted closer. However, the use of Greatrix model in the same test conditions of Shanks and Hudson [172] provides results even farther from the experiments: a minimum difference of 27.8% and a maximum of 67.2%. As discussed in Section 6.3.2, to compare Greatrix with Marxman, the estimation of skin friction was performed assuming a semi-empirical expression valid for developing flow on a flat-plate [171], instead of a diameter-dependent relation valid for fully developed turbulent flow in a pipe, as used by Greatrix. In spite of this comparison, the Marxman model is preferred for the purpose of preliminary sizing of the HPM. Focusing on the Shank and Hudson case [172, 175], the HRE Code underestimates the regression rate. This lack between numerical solution and experimental data could lay at the use of a pure convective energy flux balance at the fuel surface. In fact, the total heat flux Q_{tot} includes also the radiative heat flux Q_{rad}, made by gas-phase and soot particles contributes. Despite the gas-phase component can be assumed negligible, since it was observed to provide a regression rate increment below 10% for non-metallized fuels [63, 55], the soot component results very important in the combustion mechanism and regression of solid fuel: the total radiative heat flux was observed to account for more than 50% of the total heat flux [102, 55]. Nevertheless, as widely discussed in the literature, this lack between experimental and numerical solution might be mainly associated with the effect of injector geometry. The latter has a strong influence on the flow pattern in the combustion chamber, thus producing significant differences in the regression rate behavior with

respect to that described by the classic theory [73, 74]. In particular, the experimental time- and space-averaged r_f achieved by Shank and Hudson is characterized by a low power exponent (~ 0.45), showing a lower r_f dependence on the mass flux. Similar results have been obtained by Carmicino and Russo Sorge, that demonstrated the importance of the injection system in a hybrid motor, whose combustion behavior can be influenced along the entire grain length. Besides the missing of the soot radiative contribute, the Marxman theory does not take into account more complex flowfields than the turbulent boundary-layer and this could explain both the discrepancy between the regression rate curves (see Figure 50) and their different trends, in terms of power exponents.

Comparison results between the two considered propellant couples at the same combustion conditions ($\mathtt{Grain1}|_{\mathtt{Run1}}$ in Table 18) are presented, the fuel geometry is that of the Shank and Hudson case [172]. In Figures 55, 57 and 58 the regression rate and the mass fraction of each species along the x-location is shown, for both cases, GOX and H_2O_2, respectively. In the Appendix F, Figures 116, 117, 118 and 119 describes the primitive variables profiles along the fuel port: density ρ, velocity u, pressure p and the mixture fraction ξ, at two different time instants t^n are respectively shown, while in Figures 120 and 121 one can see, respectively, the average temperature and flame temperature profiles at two consecutive burn times. From Figure 58, it is immediate to observe the greater amount of H_2O than the GOX case (Figure 57); in fact, the hydrogen peroxide enters in the rocket chamber already decomposed into oxygen and water (see Eq. 6.4).

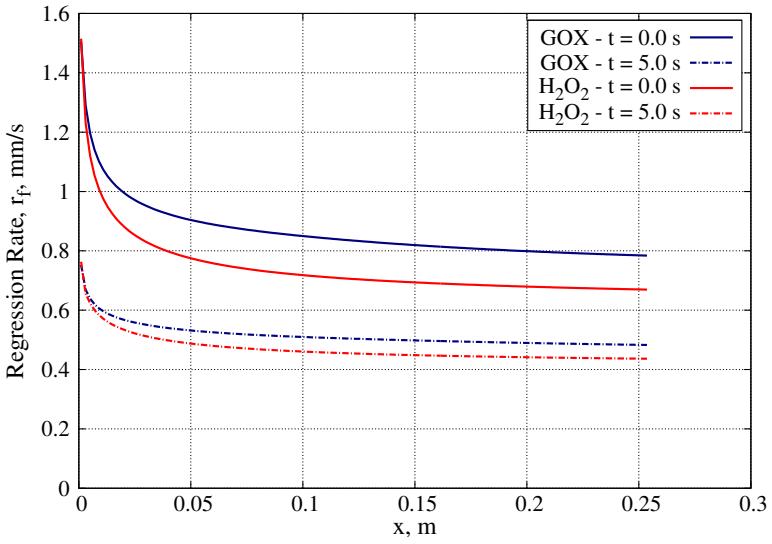

Figure 55.: Regression rate profile along x-location in the combustion chamber and de Laval nozzle. Comparison between two different propellant couples: HTPB + GOX (blue) and HTPB + H_2O_2 (red) at $t = 0.0$ s and $t = 5.0$ s.

Therefore, the combustion with H_2O_2 is characterized by a significant excess of H_2O, as well as lower densities of the gas products mixture, lower average and flame

temperatures. These characteristics provide benefits in terms of throat erosion, which is significantly reduced with respect to the GOX combustion [178]. As expected, a significant lower flame temperature for the combustion with hydrogen peroxide produces lower regression rates than combustion in pure oxygen oxidizer (see Figure 55). In Figure 56, the oxidizer-to-fuel ratio O/F for both propellant couples is compared over 5 seconds of combustion. As expected, the decrease of oxidizer mass flux, due to the increase of port cross-sectional area, yields a lower release of gasified mass from the fuel surface, therefore the O/F increase. In Figure 56, the O/F of H_2O_2 case is higher because, at the same oxidizer mass flow rate, the regression rate is lower than GOX case.

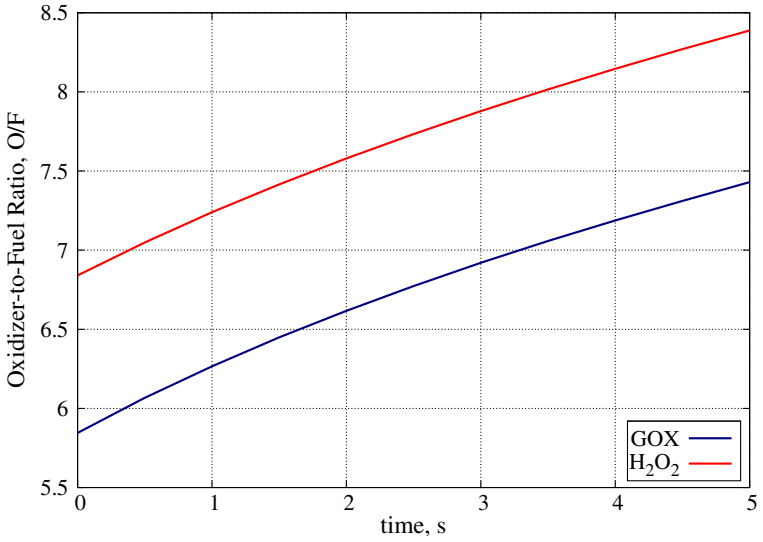

Figure 56.: Oxidizer-to-fuel ratio O/F over 5 seconds of combustion. Comparison between two different propellant couples: HTPB + GOX (blue) and HTPB + H_2O_2 (red).

For the time being, the calculation results obtained with the HRE Code, despite a certain underestimation in the regression rate and the relatively poor matching with the experimental case, can be considered acceptable for the preliminary design and propellant mass budget of a Hybrid Propulsion Module for active removal missions; in fact, the numerical approach provides regression rates of correct order of magnitude, which are useful for preliminary estimate of fuel and oxidizer consumption during a defined combustion time. For a more advanced design level and motor optimization a lumped parameters model based on direct experimental results, valid for a specific size scale range, would be more effective and preferred. However, if there is not the possibility of firing tests with a dedicated experimental facility the numerical approach becomes very useful, at least, as in this case, for preliminary investigations and design choices. In this sense, the HRE Code results a quite easy and flexible tool which allows to consider different propellant couples by modifying the list of chemical species involved in the chemical equilibrium. In this work, it has been used to estimate the regression rate produced by the combustion of HTPB with H_2O_2, of which in literature there were not available data. Moreover, the so structured code

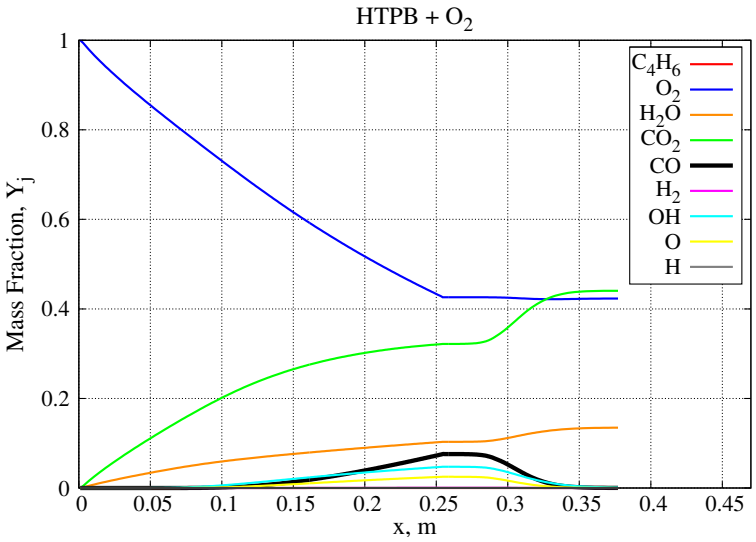

Figure 57.: Mass fraction profile of gaseous chemical species, involved in the combustion of HTPB + GOX, along x-location in the main stream: chamber and de Laval nozzle.

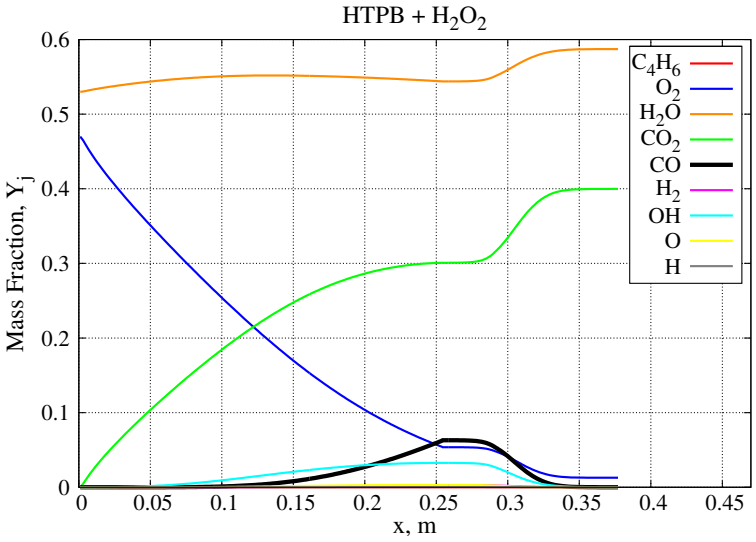

Figure 58.: Mass fraction profile of gaseous chemical species, involved in the combustion of HTPB + H_2O_2, along x-location in the main stream: chamber and de Laval nozzle.

is a valuable base platform for future implementations, test of different regression rate models and data reduction of experimental measures. For the purpose of this research, the underestimation of regression rate plays a *conservative* role in term of mission design, resulting in larger system size. Moreover, this technology, unlike the solid propulsion, besides the injection geometry [73, 74], is very sensitive to scale change, typically showing, from small to large dimensions, a decrease of regression rate [55]. The scale increase involves a reduction of the convective heat flux due to the significant growth of the flame zone height above the fuel surface, which produces less strong temperature gradient between the flame and the surface [55]. Even thermal radiation may become more significant in larger scale motors. The scale effects in hybrid rocket combustion, extensively discussed in [101, 55], were investigated by many researchers, aiming to find a scale correlation for regression rate prediction in a certain size ranges. Therefore, considering all these aspects and the fact that hybrid propulsion technology has not been tested in vacuum space conditions yet, a certain conservative approach in the preliminary design is required and the underestimation limits of HRE Code should not significantly affect the final results in HPM sizing and mass budget.

7 PERFORMANCE ESTIMATION

The HRE Code is used to estimate the regression rate for a selected propellant couple, thus the mass flow rate $\dot{m}_f$ released from the solid fuel surface at each time instant. Therefore, once obtained the propellant mass flow rate $\dot{m}_p = \dot{m}_{ox} + \dot{m}_f$, the rocket performance can be estimated. This chapter deals with the performance evaluation, considering the typical losses that affect chemical rockets, as well as the throat erosion effects, generally important for hybrid rockets due to their oxidizer-rich exhaust gases [160, 48, 178]. The preliminary rocket sizing aims to understand the propellant consumption, so the mass budget, necessary to satisfy the mission requirements.

7.1 PERFORMANCE ANALYSIS

7.1.1 Performance Parameters

In rocket propulsion the thrust generated T_F represents the most important quantity, expressed as

$$T_F = \dot{m}_p u_e + (p_e - p_a) A_e \tag{7.1}$$

where u_e, p_e and A_e are, respectively, the exit velocity, the exit pressure and cross-sectional area of the nozzle exit, while p_a is the ambient pressure. The second term on the right member of Eq. 7.1 is the static term, which accounts for over- or under-expansion exhaust conditions: the first case involves a negative contribute to the thrust (shockwaves occur downstream the nozzle exit), while in the second one, because of the further gas expansion outside the nozzle, the contribute to the thrust is positive [160, 48]. By knowing the thrust, it is easy to evaluate the specific impulse I_s, which assesses the force generated by the rocket with respect to the propellant mass flow rate:

$$I_s \equiv \frac{T_F}{g_0 \dot{m}_p} \tag{7.2}$$

where g_0 is the gravitational acceleration [160, 48]. The total specific impulse $I_{s,tot}$ can even be defined as

$$I_{s,tot} \equiv I_s \cdot W_{prop} = T_F \cdot t_b \tag{7.3}$$

where W_{prop} is the weight of the consumed propellant and t_b is the combustion time [160, 48]. Moreover, the volumetric specific impulse I_v, expressed as

$$I_v \equiv \overline{\rho}_{prop} \cdot I_s \tag{7.4}$$

assesses the generated thrust for unit of occupied volume, in fact $\overline{\rho}_{prop}$ is the average propellant density. Other useful parameters are the thrust coefficient c_{T_F} and the characteristic velocity c^*. The first is a non-dimensional parameter which assesses how much the nozzle divergent is able to increase the thrust with respect to the static value at the throat [160, 48]. Therefore, it is a quality indicator of the nozzle expansion and it is expressed as

$$c_{T_F} \equiv \frac{T_F}{p_c A_t} \tag{7.5}$$

where p_c is the chamber pressure and A_t is the throat cross-sectional area; typical c_{T_F} values between 1-2. On the other hand, the characteristic velocity assesses the efficiency of thermochemical conversion processes in the combustion chamber [160, 48]. This parameter is defined as

$$c^* \equiv \frac{p_c A_t}{\dot{m}_p} \tag{7.6}$$

and the specific impulse can be rewritten as

$$I_s = \frac{1}{g_0} \frac{T_F}{p_c A_t} \frac{p_c A_t}{\dot{m}_p} = \frac{1}{g_0} c_{T_F} c^* \quad . \tag{7.7}$$

In Figure 59 the I_s comparison between two propellant configurations is presented. The geometry and the combustion conditions are the same considered in Section 6.3.6: fuel geometry of Shanks and Hudson case [172] with constant mass flow rate of 0.0735 kg/s, see Table 18, a throat diameter of 7.7 mm and a nozzle expansion area-ratio of 50. In the Appendix F, Figures 122, 123, 124 and 125, the thrust, the thrust coefficient, the characteristic velocity and the chamber pressure are respectively shown. As it is possible to observe in Figure 56, in the previous Chapter (section 6.3.6), the oxidizer-to-fuel ratio falls, for both propellant couples, between 6 and 8. In this O/F range the couple HTPB + H_2O_2 provides higher performance than HTPB + GOX; the latter, as displayed in Figure 9 (see Chapter 3), provides the best performance, but for O/F values around 2.0-2.5. The geometry configuration considered for this comparison involves an O/F range more close to the optimum combustion conditions with hydrogen peroxide. Note that the comparison is referred to ideal performance in vacuum environment and assuming gaseous butadiene C_4H_6 to represent HTPB in HRE Code.

7.1.2 Performance Correction and Losses

The HRE Code applies the chemical equilibrium in the whole domain, therefore evaluating the ideal rocket performance. In order to obtain a more realistic simulation, the

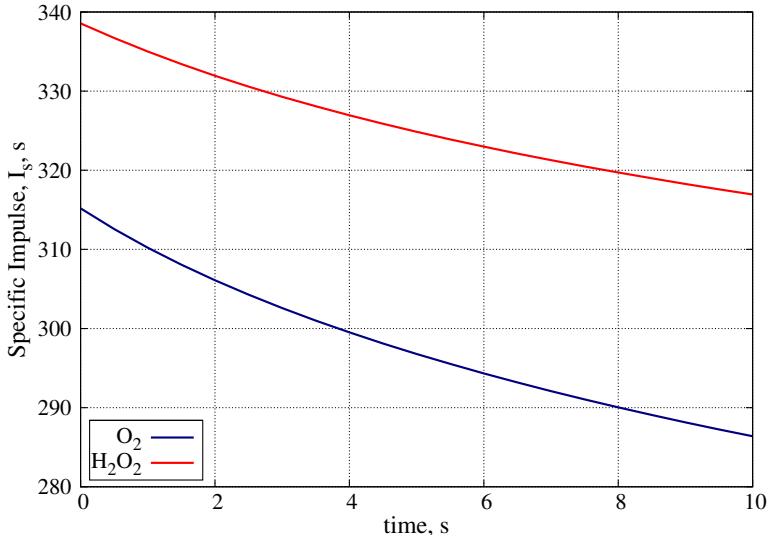

Figure 59.: Ideal specific impulse comparison between two different propellant couples: HTPB + GOX (blue) and HTPB + H_2O_2 (red); 10 seconds combustion time.

ideal results must be corrected. First of all, it is possible to consider a *Bray approximation* [162, 163] for the gas expansion in the de Laval nozzle, as well as the thrust losses due to the multi-dimensional characteristic of the exhaust flow. Moreover, the HRE Code works only with gaseous species and the HTPB is represented by gaseous butadiene C_4H_6 released into the combustion chamber from the fuel surface (see Chapter 6). This assumption produces little higher ideal performance. For simplicity, the Bray approximation and the butadiene correction are applied directly on the performance estimated by HRE Code for each convergence solution, with no any direct implementation inside the chemical equilibrium algorithm. The generic performance correction is evaluated in terms of difference between the ideal I_s^{ideal} and corrected I_s^{corr} specific impulse

$$\Delta I_s = \frac{I_s^{ideal} - I_s^{corr}}{I_s^{ideal}} \tag{7.8}$$

and the NASA CEA software [91, 92] is used to calculate I_s^{ideal} and I_s^{corr} as a function of oxidizer-to-fuel ratio O/F and chamber pressure p_c, assuming ideal combustion efficiency. Then, a generic correction factor ϕ_{corr} can be defined, starting from Eq. 7.8, as

$$\phi_{corr} = \frac{I_s^{corr}}{I_s^{ideal}} = 1 - \Delta I_s \tag{7.9}$$

and the ideal performance calculated with HRE Code can be corrected by

$$I_{s_{(HRE)}}^{corr} = I_{s_{(HRE)}}^{ideal} \cdot \phi_{corr} = \frac{T_{F_{(HRE)}}^{ideal}}{g_0 \dot{m}_p} \cdot \phi_{corr} = \frac{T_{F_{(HRE)}}^{corr}}{g_0 \dot{m}_p} \tag{7.10}$$

where $T^{corr}_{F_{(HRE)}}$ is the corrected thrust, with respect to the ideal one calculated by HRE Code, from which it is possible to estimate the corrected thrust coefficient $c^{corr}_{T_{F_{(HRE)}}}$ with Eq. 7.5. In order to directly apply the performance correction to HRE Code results, the $\phi_{corr}(O/F, p_c)$ are collected in database tables and fitted with approximation curves as function of O/F and p_c values. The operative ranges considered are:

- $2.0 < O/F < 15.0$;
- $0.5\ MPa < p_c < 8.0\ MPa$.

A more realistic specific impulse value I^{real}_s can be estimated as

$$I^{real}_{s_{(HRE)}} = \frac{1}{g_0} c^{corr}_{T_{F_{(HRE)}}} \cdot c^*_{(HRE)} \tag{7.11}$$

where $c^{corr}_{T_{F_{(HRE)}}}$ includes both the butadiene and Bray approximation correction applied to HRE Code results. Let's see in details the multi-dimensional loss coefficient η_{noz}, the butadiene ϕ^{buta}_{corr} and Bray ϕ^{bray}_{corr} correction factors.

Effects of Multi-dimensional Expansion

An important loss is due to the multidimensional behavior of the exhaust gases throughout the nozzle. This factor affects the thrust generated and it is multiplied to the first term of the second member of Eq. 7.1. For conical shape nozzle with axisymmetric flow, it is easily estimated as

$$\eta_{noz} = \frac{1}{2}(1 + \cos\alpha_{div}) \tag{7.12}$$

where α_{div} is the semi-open angle of the conical divergent. In case of bell shape the η_{noz} can be significantly reduced by the optimization of divergent shape, that even involves a decrease of divergent length with respect to conical nozzle [48, 160].

Butadiene Correction

The use of gaseous butadiene C_4H_6, to represent the HTPB fuel in the HRE Code, provides a little overestimation of the ideal performance. This is due to the different initial state of matter of HTPB, that is solid, and C_4H_6, as well as their different standard enthalpy of formation. In order to correct the performance estimated by HRE Code, a butadiene correction factor ϕ^{buta}_{corr} is evaluated by means of NASA CEA software [91, 92]. As previously described, ϕ^{buta}_{corr} is in function of O/F and p_c; a significant variation of this factor was observed only by changing the oxidizer-to-fuel ratio, whereas almost constant values are shown by varying the pressure. In Figure 60, one can see the ϕ^{buta}_{corr} with respect to O/F. Two different trends were observed about the achieved data: a certain slope for low oxidizer-to-fuel ratio values, while a quasi-constant value for larger O/F. These data has been fitted by a power law approximations, that, in the HRE Code at each time step, are used to estimate the

corrected performance by means of p_c and O/F calculated. The performance decrease falls between 2% and 6%, with an average value of 3%.

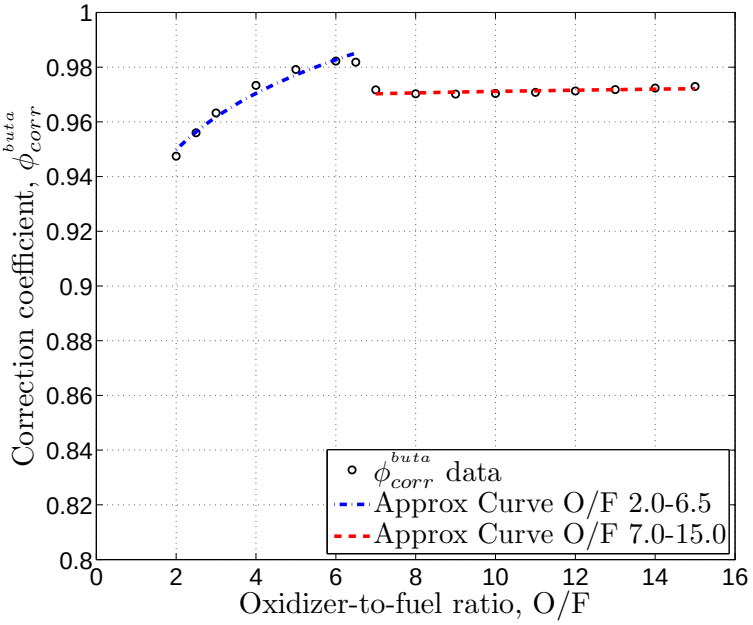

Figure 60.: Butadiene correction factor ϕ_{corr}^{buta} vs. oxidizer-to-fuel ratio. Two power law approximations are considered for two O/F ranges [HTPB + H_2O_2].

The data in Figure 60 are referred to the hydrogen peroxide case; the same approach is used for correction parameters in GOX case.

Bray Approximation

The Bray approximation is based on the identification of a point after which no chemical reactions occur anymore [162, 163]. After this point (Bray point) the flow is assumed frozen, the chemical composition remains unchanged. By analyzing the most significant recombination reactions (trimolecular and bimolecular) in the expansion flow, Bray identifies the frozen point approximatively in correspondence of the throat of the nozzle, in the initial region of the divergent. Therefore, considering a rocket engine, chemical equilibrium conditions (*shifting*) can be assumed both in the combustion chamber and the nozzle convergent, where lower flow velocity still allow for chemical reactions; instead, in the nozzle divergent, from the throat section, all chemical reactions are assumed extinguished (*frozen*). This approach provides a quite good approximation of the hot gases expansion throughout a de Laval nozzle, as well as a more realistic estimation of the propulsion performance. The complete analysis of Bray approximation can be found in [162, 163]. As similarly done for butadiene correction, the ϕ_{corr}^{bray} database table was built by comparing the ideal performance with equilibrium expansion and, in this case, the performance obtained considering frozen condition from the throat to the exit section.

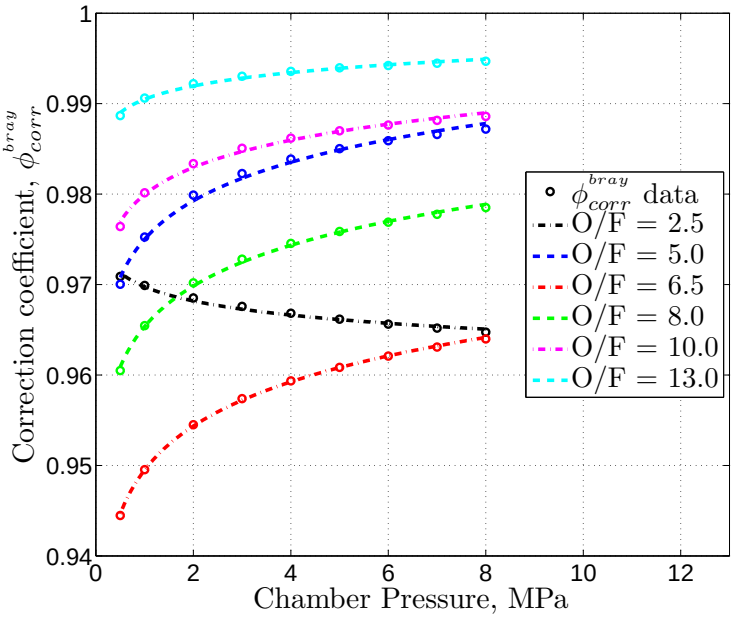

Figure 61.: Bray approx correction factor ϕ_{corr}^{bray} vs. chamber pressure. Power law approximations are considered for several O/F values (only few O/F values are shown for explanatory purpose) [HTPB + H_2O_2].

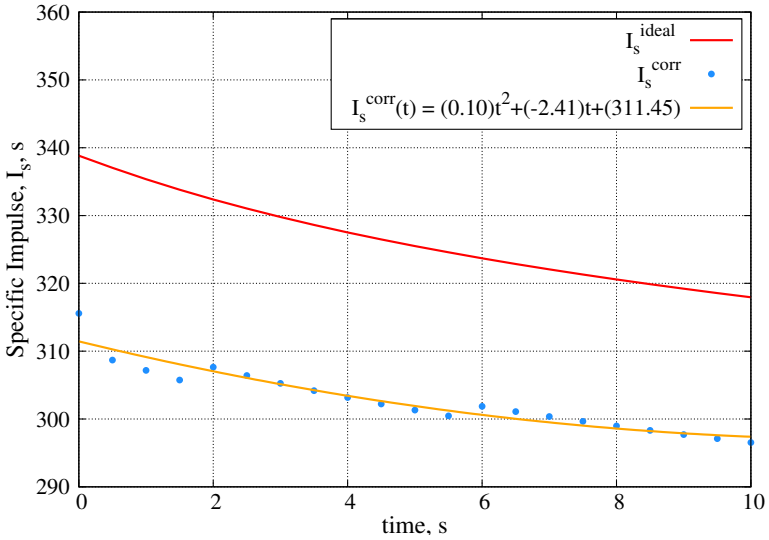

Figure 62.: Ideal vs. corrected specific impulse, vacuum conditions, with the application of multidimensional losses, ϕ_{corr}^{buta} and ϕ_{corr}^{bray} [HTPB + H_2O_2].

A significant factor variation was observed both with respect to oxidizer-to-fuel ratio and to chamber pressure. In Figure 61, the power law approximation curves used to fit the ϕ_{corr}^{bray} as a function of p_c are shown. These data are referred to pure hydrogen peroxide case. A maximum performance decrease of about 6% is achieved at $O/F = 6.5$ (stoichiometric O/F for $HTPB + H_2O_2$) and low p_c while for larger pressures and O/F the decrease becomes less than 1% (see Figure 61). In Figure 62, the comparison between the ideal specific impulse I_s^{ideal}, calculated in vacuum condition with HRE Code, and the corrected one I_s^{real}, obtained by the application of multidimensional losses and both ϕ_{corr}^{buta} and ϕ_{corr}^{bray} corrections, is presented. The ideal performance are referred to the couple $C_4H_6 + H_2O_2$. From Figures 60 and 61, it is easy to gather that performance correction by means of ϕ factors, collected in database tables, produces no smooth curves. At each t^n the corrections are applied and visible jumps between consecutive time steps can be obtained. Because of this, the corrected performance data are fitted with an interpolation function by means of least mean squares method (see Figure 62). The total reduction observed for I_s is between 8.2% ($t = 0.0$ s) and 6.2% ($t = 10.0$ s); this difference tends to decrease with time.

7.2 HTP WITH DIFFERENT CONCENTRATIONS

In real applications, the hydrogen peroxide is diluted in water at high concentration levels and also called High Tested Peroxide (HTP). Typical HTP concentrations are between 85% and 98%. As discussed in section 6.38, the HRE Code is designed for combustion simulations between HTPB and pure H_2O_2, therefore the achievable performance are higher than HTP in real applications. By following the same approach described in section 7.1.2, the ideal performance are decreased by a correction factor ϕ_{corr}, which depends on the desired hydrogen peroxide concentration. A database table, which collects the correction coefficients as a function of oxidizer-to-fuel ratio and chamber pressure, was built for each HTP concentration level. The O/F and p_c ranges are the same considered for butadiene and Bray corrections. In this study, two hydrogen peroxide percentages are considered: $H_2O_2(98\%)$ and $H_2O_2(90\%)$. In both cases, no significant variations was observed in the pressure range, hence an average value with respect to pressure was evaluated for each O/F value. In Figures 63 and 64, one can see, respectively, the trend of $\phi_{corr}^{98\%}$ and $\phi_{corr}^{90\%}$ by varying the oxidizer-to-fuel ratio. In both cases, the correction factor data are characterized by two different trends in the O/F intervals between 2.0-6.5 and 7.0-15.0. For an easy application into the HRE Code, the collected data are fitted with power law approximations. In the case of $H_2O_2(98\%)$, the performance decrease is very small, below 1.3% (see Figure 63), due to the small concentration difference from the pure hydrogen peroxide. As it is reasonable to suppose, in the case of $H_2O_2(90\%)$ a decrease larger than 2% is observed and, for low O/F values, the performance reduction is up to 7% (see Figure 64). In Figure 65, the corrected specific impulses I_s^{corr}, calculated in vacuum condition with HRE Code, for three different HTP concentrations are compared. The

multidimensional losses, ϕ_{corr}^{buta} and the respective ϕ_{corr}^{bray} corrections are applied as the following sequence:

$$I_s^{ideal} \rightarrow \phi_{corr}^{buta} \rightarrow (\phi_{corr}^{98\%} \quad or \quad \phi_{corr}^{90\%}) \rightarrow (\phi_{corr}^{bray98\%} \quad or \quad \phi_{corr}^{bray90\%}) \rightarrow I_s^{real} . \qquad (7.13)$$

where I_s^{real} includes the combustion efficiency parameter η_c; however, in Figure 65, ideal combustion efficiency is assumed ($\eta_c = 1$).

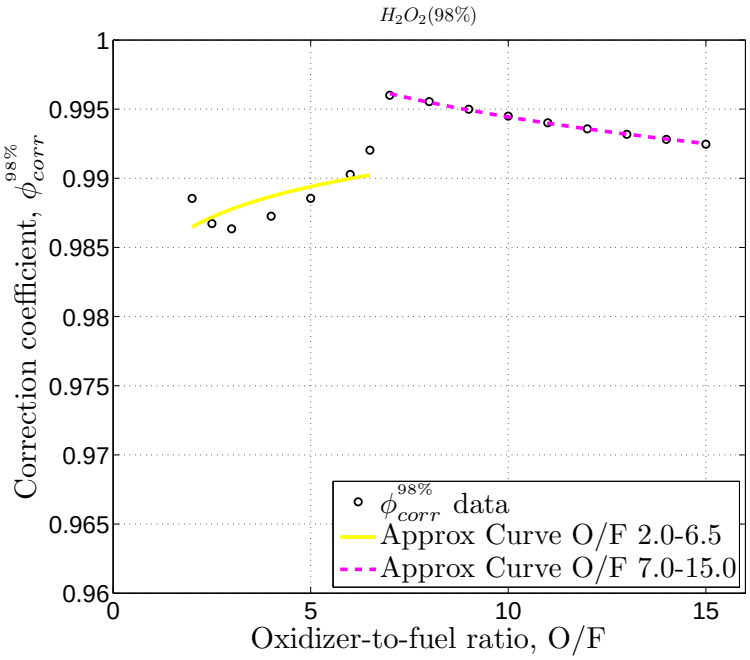

Figure 63.: HTP(98%): correction factor $\phi_{corr}^{98\%}$ vs. oxidizer-to-fuel ratio. Two power law approximations are considered for two O/F ranges.

Note that the bray factor is evaluated for both HTP concentrations, $\phi_{corr}^{bray98\%}$ and $\phi_{corr}^{bray90\%}$, and applied after the percentage correction. In the case of $H_2O_2(98\%)$ the average performance reduction with respect to the pure hydrogen peroxide is very small, around 0.64%, while for $H_2O_2(90\%)$ this difference results about an average value of 2.5%, according with the O/F trend during the test, see Figure 56.

Because of the correction factor ϕ application, collected in database table, the corrected performance values are approximated with interpolation functions by means of least mean square method. The polynomial functions obtained by data fitting in Figure 65 are:

- HTP(98%) $\rightarrow I_s^{corr}(t) = 0.08t^2 - 2.17t + 309.95$
- HTP(90%) $\rightarrow I_s^{corr}(t) = 0.06t^2 - 1.99t + 304.23$

while the function of pure H_2O_2 case is shown in Figure 62.

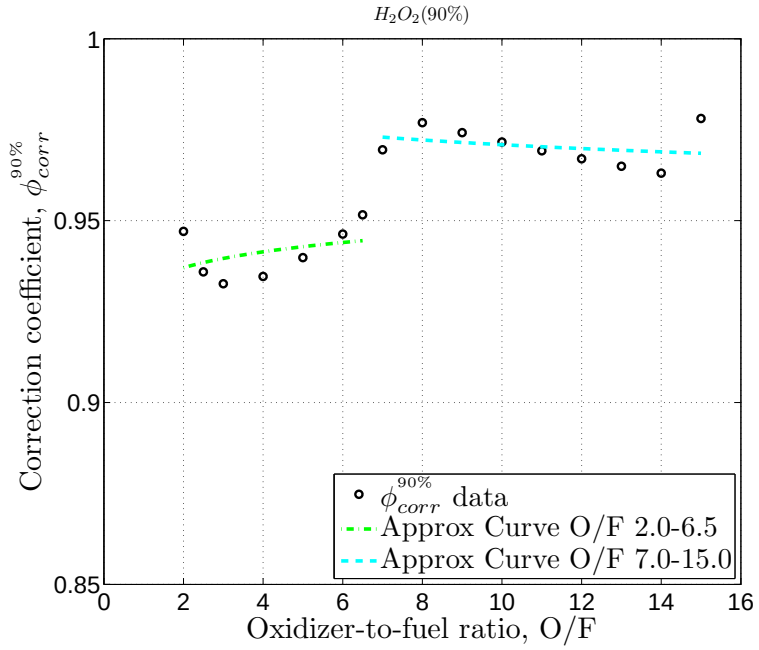

Figure 64.: HTP(90%): correction factor $\phi_{corr}^{90\%}$ vs. oxidizer-to-fuel ratio. Two power law approximations are considered for two O/F ranges.

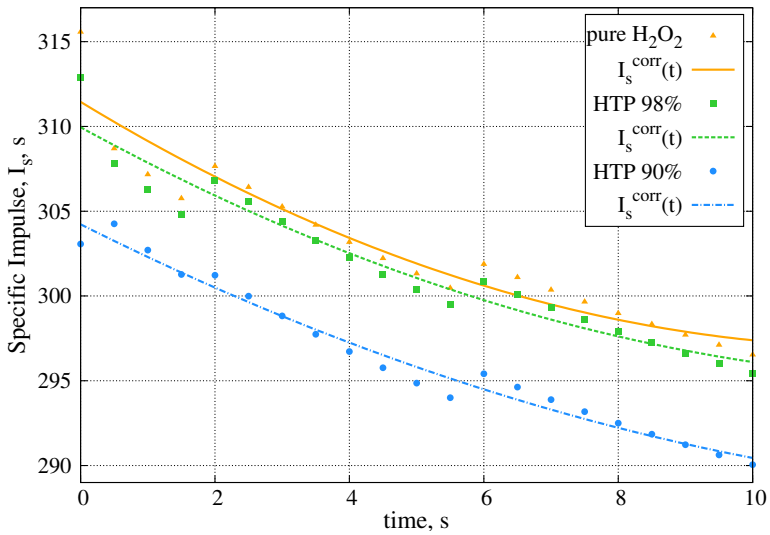

Figure 65.: Corrected specific impulse comparison, in vacuum conditions, between pure H_2O_2, HTP(98%) and HTP(90%). All corrections applied (ideal combustion efficiency).

7.3 THROAT EROSION

The combustion in a hybrid rocket is characterized by oxygen-rich environment, which significantly affects the nozzle material behavior. In fact, the throat erosion observed is larger than for solid rockets [48, 178]. A nozzle made by graphite material, typically used in Solid Rocket Motors (SRMs), results very weak if applied to a Hybrid Rocket Engine (HRE) and its performance will be reduced by the increase of throat diameter. Bianchi and Nasuti [178] developed a computational code, based on a full Navier-Stokes flow solver coupled with a thermochemical ablation model, to estimate the erosion rate $\dot{s}_t$ of a graphite nozzle during the combustion of HTPB with several oxidizers, such as GOX, N_2O_4, N_2O and H_2O_2. In the frame of this study, the main interest is about the throat erosion data obtained for oxygen and hydrogen peroxide. The water vapor was observed to be the dominant oxidizing species, because of its high reaction rate at high temperatures, as well as its great amount in the exhaust gases. In fact, the contribution of H_2O to the total erosion rate is about 50% for GOX and up to 68% for hydrogen peroxide [178], whose combustion with HTPB is characterized by a larger excess amount of water vapor. Nevertheless, a higher throat erosion rate was evaluated for the couple HTPB + GOX [178], which reaches significant higher temperatures during combustion (see Figures 120 and 121), hence higher wall temperatures. Also the hydroxyl radical provides a strong contribute to the erosion ($\sim$ 20%) [178], but its amount in exhaust gases is generally very small. The throat erosion depends on several aspects, such as chamber pressure, oxidizer-to-fuel ratio, wall radiation and combustion efficiency. The increase of combustion pressure involves larger convective heat transfer, producing a linear growth of erosion rate, as evaluated by Bianchi and Nasuti [178]. Also the O/F value has an important role, causing higher $\dot{s}_t$ for oxidizer-rich mixture than the fuel-rich one. The erosion rates estimated in [178] for HTPB + GOX and HTPB + H_2O_2 as a function of the equivalence ratio Φ, at 1.0 MPa of chamber pressure, are resumed in Table 23. The equivalence ratio is evaluated as

$$\Phi = \frac{F/O}{F/O_{st}} \tag{7.14}$$

which is the fuel-to-oxidizer ratio normalized with respect to the stoichiometric value. The wall radiation can significantly affect the erosion rate, due its important contribute in the surface energy balance, because of the high wall temperatures as well as the high emissivity of the material [178]. The wall radiation promotes the decrease of wall temperature and, as consequence, a lowering of the erosion rate, which results stronger in the case of HTPB with hydrogen peroxide (kinetic-limited oxidizing reactions). The combustion efficiency even produces reduction of $\dot{s}_t$, because its typically values, between 90% and 95% in hybrid rockets, imply lower flame temperature and nozzle wall temperature, therefore a reduced throat erosion rate. The combustion with H_2O_2 results more sensitive to combustion efficiency than with GOX [178]. For the purpose of a HPM preliminary design, an estimation of the throat erosion would allow for a better evaluation of rocket performance, hence the definition of a more

realistic mission profile. Thus, the erosion rate data obtained by Bianchi and Nasuti in [178] are used in the HRE Code to simulate a quasi-static throat diameter change, during the combustion.

$\dot{s}_t$ [mm/s]	$\Phi = 0.5$	$\Phi = 1.0$	$\Phi = 1.5$	$\Phi = 2.0$
O_2	0.100	0.105	0.080	0.042
H_2O_2	0.065	0.073	0.057	0.037

Table 23.: Throat erosion rate at $p_c = 1.0$ MPa as a function of equivalence ration (four Φ value considered) [178]. Oxidizer-rich between $0.5 < \Phi < 1.0$ and fuel-rich between $1.0 < \Phi < 2.0$.

At the time step t^n, once the convergent solution is achieved, the erosion rate $\dot{s}_t$ is selected among the data available from [178], as a function of chamber pressure p_c and equivalence ration Φ. The throat diameter is updated, accordingly to the nozzle geometry, and the HRE Code proceeds the calculation of the next time step. The erosion rate change with pressure is defined by assuming a linear approximation of data obtained for the couple $HTPB + N_2O_4$, at $\Phi = 1.0$, in [178] [Figure 15, pp. 21]. In a first approximation, the same curve slope is considered even for the couples $HTPB + O_2$ and $HTPB + H_2O_2$. The linear approximation, shown in Figure 126 in the Appendix F,

$$\dot{s}_t(p_c) = (8.337 \cdot 10^{-7})p_c + 0.166 \tag{7.15}$$

is normalized with respect to the reference erosion rate value $\dot{s}_{t,ref}^{N_2O_4}$ ($p_c = 1.0$ MPa and $\Phi = 1.0$) in order to be applied to the other propellant couples. Therefore, for GOX and H_2O_2 the erosion rate value $\dot{s}_t(\Phi)$ ($p_c = 1.0$ MPa) is selected from Table 23 and multiplied for the pressure factor ψ_{p_c}, obtained by the linear function. Then, as similarly done for the performance correction in section 7.1.2, two factors, one for combustion efficiency ψ_{eta_c} and one for wall radiation effect ψ_{wrad}, see Table 24, are evaluated, by using the Eqs. 7.8 and 7.9.

	ψ_{η_c}		ψ_{wrad}
	$\eta_c = 97\%$	$\eta_c = 93\%$	
O_2	0.980	0.925	0.919
H_2O_2	0.868	0.710	0.718

Table 24.: Combustion efficiency factor and wall radiation factor evaluated from Bianchi and Nasuti data [178], for two propellant couples: $HTPB + O_2$ and $HTPB + H_2O_2$.

The estimation of erosion rate at the time step t^n is described by the following sequence:

$$\dot{s}_t(\Phi) \cdot \psi_{p_c} \rightarrow \dot{s}_t(\Phi, p_c) \rightarrow \psi_{wrad} \rightarrow \psi_{\eta_c} \rightarrow \dot{s}_t^{HRE} \tag{7.16}$$

and $\dot{s}_t^{HRE}$ is used in HRE Code.

In Figure 66, one can see the throat diameter change over time in HRE Code simulation and the consecutive chamber pressure drop is shown in Figure 127, see Appendix

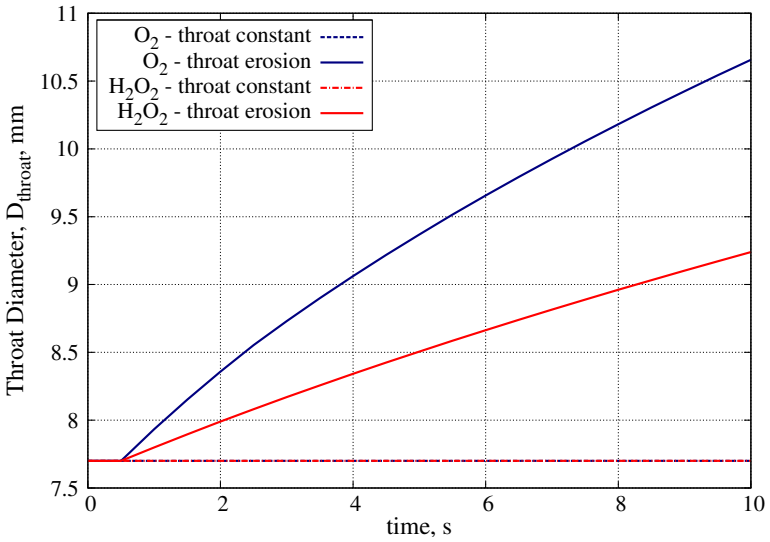

Figure 66.: Throat diameter variation due to erosion rate application from $t = 0.5$ s. Comparison between ideal performance.

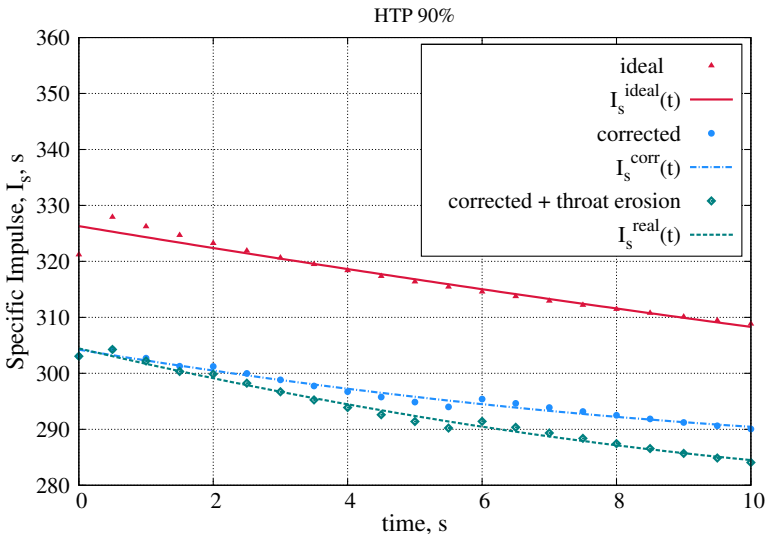

Figure 67.: Specific impulse for HTPB + HTP(90%); comparison between *ideal*, *corrected* and *corrected+erosion* cases (ideal combustion efficiency).

F. The erosion rate is applied from time step $t = 0.5$ s. Because of the higher erosion rate, the pressure drop for the GOX case is more pronounced, causing a pressure reduction of about 1.6 MPa in ten seconds of combustion. In Figure 67, the ideal and corrected specific impulses are compared with the throat erosion case. The throat diameter growth produces a further performance reduction, which increases with time. After 10 s of combustion a specific impulse decrease of about 1.7% is observed for the case HTP(90%). Despite the so relevant reduction of chamber pressure, the effects of throat erosion on the final performance are quite small. In fact, the regression rate seems characterized by small sensitivity to the pressure [55, 124]. However, the pressure drop involves a small reduction of flame temperature and, consequently, a little decrease of fuel regression rate. The latter with pressure drop causes a little performance decrease. The data provided in [178] are referred to a single engine scale case and the erosion rate can reasonable vary with different engine sizes and geometries. In the HRE Code the erosion rate, thus applied, is used to obtain a more conservative rocket design and performance estimate.

7.4 QUASI-STATIC THROTTLING

One of the most interesting advantages that characterize hybrid propulsion technology is throttleability. This feature is very important for the rendezvous with non-cooperating objects, especially in the close range phase. Furthermore, the disposal strategy can be optimized for a specific target: large abandoned spacecraft are made by complex structures, consisting of antennas, instruments and large solar panels. These appendages, once the target is connected to the propulsion unit, could not sustain the thrust impulse generated by the engine ignition. Therefore, the possibility of a gradual thrust generation, with a low thrust at the beginning, may avoid the generation of new debris due to the break up of some of these structures. Hybrid propulsion is characterized by O/F shifting (due to port area growth over time [48, 160, 55]) and pressure lowering during the combustion; therefore also the thrust generated decreases. The oxidizer mass flow rate can be throttled during the disposal flight in order to limit the thrust reduction, at the expense of a certain increase in oxidizer consumption. The HRE Code is suitable for a quasi-static throttling simulation, which consists in the possibility to change the oxidizer mass flow rate before each time step t^n. The new value can be defined as a fixed increment or by providing a function defined on the base of mission profile optimization. This approach does not consider any transient effect connected to the mass flow rate variation. However, from the point of view of preliminary rocket design and mission analysis, the quasi-static method allows for performance and propellant mass budget estimate. In Figure 68, the comparison between the thrust profile calculated with constant oxidizer mass flow rate $\dot{m}_{ox}$ and with quasi-static throttling for 10 s of combustion, for the couple HTPB + HTP(90%), is shown. The throttling, in this case, is performed by adding the 5% of the initial $\dot{m}_{ox}$ at each time step. This simulation allows to significantly reduce the thrust decrease observed for the constant $\dot{m}_{ox}$ case.

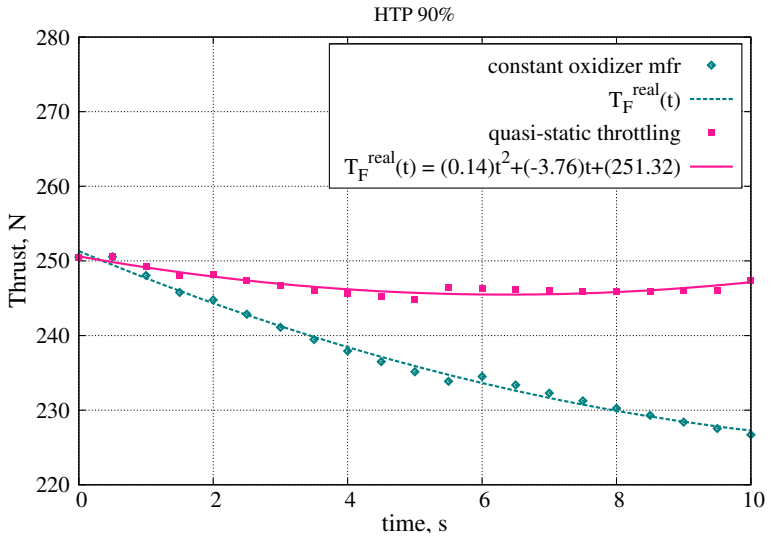

Figure 68.: Thrust for HTPB + HTP(90%) *corrected* + *erosion* case; comparison between constant oxidizer mass flow rate and quasi-static throttling cases (ideal combustion efficiency).

Nevertheless, the up-throttling involves a greater oxidizer consumption and a steeper O/F growth trend, see Figure 128 and 129, respectively, in the Appendix F. Depending of the mission profile, the increase or the reduction of oxidizer mass flow rate can be conveniently managed to limit the thrust decrease.

8 PRELIMINARY DESIGN

8.1 SIZING AND MASS BUDGET

8.1.1 Hybrid Propulsion Module

Once estimated the propellant mass consumed for a specific ADR mission, it is possible to proceed with the preliminary design of all major parts of the HPM. In this section, the design of the main components is described.

Combustion Chamber

The combustion chamber of a hybrid rocket is, generally, cylindrical, based on the fuel grain geometry. The initial conditions in HRE Code include the grain size, defined by the port diameter D_p and length L_f. The fuel diameter D_f is obtained at the end of combustion simulation, allowing to calculate the mass M_f. Since the regression rate r_f is not constant along the x-location, the fuel diameter is characterized by the same shape variation, hence D_f is assumed to be the average diameter along the port length.

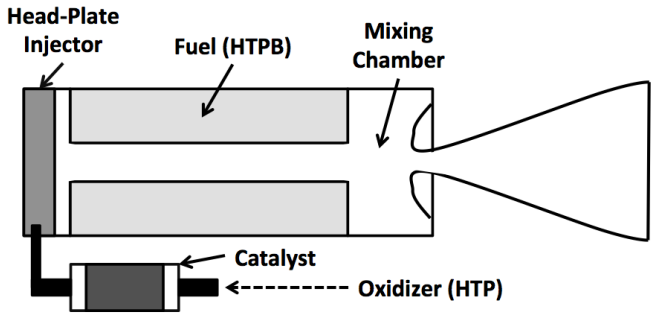

Figure 69.: Hybrid rocket engine conceptual scheme.

To maximize the achievable performance from the selected propellant couple, the completion of combustion processes before enter in the nozzle is generally favored by a post-mixing chamber. The latter promotes gas recirculation and recombination reactions and it is built by adding a certain length, L_{mix}/D_f between 0.5 and 1.0 [48], to the combustion chamber after the fuel grain. The total combustion chamber length is obtained by the sum of L_f and L_{mix}. For this configuration a submerged nozzle is

assumed (see Figure 69). The wall thickness is estimated by the theory of thin-walled pressure vessels, valid for a cylindrical case [48]:

$$t_c = \frac{p_b D_f}{2F_{tu}} \tag{8.1}$$

where p_b is the burst pressure calculated by multiplying the maximum chamber pressure p_c for a safety factor f_{safe}, which is generally assumed 1.25 for unmanned and 1.4 for manned systems, while 2.0 for small pressurization bottles or gas generators. For the preliminary sizing of the hybrid rocket engine, a f_{safe} of 2.0 is considered, due to the relative small size of the rocket and to be conservative. In Eq. 8.1, F_{tu} is the ultimate tensile strength of the specific material. A list of commonly used materials is presented in Table 25. For the hybrid motor chamber titanium or aluminum alloy can be considered. Once estimated the wall thickness, the combustion chamber mass M_c can be geometrically calculated.

Material	**ρ kg/m^3**	**F_{tu} MPa**
2219 - Aluminum	2800	414
6061-T6 Aluminum	2800	300
Titanium 11	4540	1040
AISI-316 Steel	7800	550
D6aC Steel	7830	1520

Table 25.: Properties of the typical used material for rocket propulsion and aerospace systems [48, 179]. ρ and F_{tu} are, respectively and the density, the ultimate tensile strength.

The internal walls of the aft mixing chamber would require an insulation layer for their protection from high temperature environment in the combustion chamber. Typical insulation material are Ethylene Propylene Dimethyl Monomer (EPDM) (with density 1000-2000 kg/m^3) or butadiene rubber, both loaded with fibrous material, such as silica [48, 180]. The estimation of the insulation thickness, as well as the insulation mass is quite difficult, since it is influenced by many factors. In this preliminary investigation, a certain thickness of EPDM is supposed applied to the internal surface of the aft mixing chamber. The rest of the case is covered by the HTPB solid fuel, which is itself a thermal insulation. Moreover, the diffusive flame is less aggressive than premixed one (typical of SRMs) and as much as the combustion proceeds the fuel regression rate decreases, due to the enlargement of the port diameter as well as the reduction of convective heat transfer; thus the chamber pressure and temperature decrease. Therefore, when the flame reaches the near-wall region the combustion is almost over, with no significant damage risks for the case wall.

Injection System

The hot gases generated by hydrogen peroxide decomposition are used for ignition of HTPB. The chemical decomposition is performed by a catalyst system, typically made

by several metal wires thin disks joined to create a cylindrical bed. The diameter of catalytic bed D_{cata} is evaluated considering the HTP mass flow rate as

$$D_{cata} = \sqrt{\frac{4\dot{m}_{cata}}{\pi G_{cata}}} \tag{8.2}$$

by choosing mass flux value G_{cata} between 140 and 211 $kg/(m^2 \cdot s)$, reasonable values for catalytic beds designed for HTP(90%) [56]. The length L_{cata}, in a first approximation, is obtained by a L_{cata}/D_{cata} ratio based on real cases, generally lengths between 5 and 15 cm [54, 56]. For the preliminary mass budget the catalytic bed is assumed made by silver ($\rho = 10490\ kg/m^3$) the most used and tested material for hydrogen peroxide decomposition and, being made by wire thin disks, a 50% of a full silver cylinder mass is assumed M_{cbed}. The thickness of the catalyst chamber is calculated with Eq. 8.1 by considering typical pressure values (0.7-7.0 MPa [56]). Since the temperatures involved are relatively low (below 1000 K) the chamber and the injection pipes can be made by stainless steel (see Table 25) [90, 96, 56]. The mass of a single catalyst system M_{cata} is the sum of the mass of catalytic bed and catalyst chamber. Each catalyst introduces a pressure drop which must be considered in the pressurization system sizing. The total pressure drop produced by the injection system is

$$\Delta p_{inj} = z_{cata} \cdot \Delta p_{cata} + 0.1 \cdot p_c \tag{8.3}$$

where z_{cata} is the number of the injection catalysts and the second term, 10% of the combustion chamber pressure, accounts for oxidizer throttling [48]. The suggested operative ranges are referred to the use of HTP with 90% of concentration. The fore section of the combustion chamber is closed by a head-plate, in which the injection ducts from the catalyst are dug. They are tangentially oriented to generate a swirling flow inside the main pipe aligned with the fuel perforation (see Figure 16). The enhanced heat exchange, promoted by swirl, could theoretically favor an easier HTPB reignition. For the preliminary sizing four injection ducts inside the head-plate are considered and four or two catalysts can be assembled. The head-plate is subjected to decomposed gas temperatures for all the burn duration, therefore, since the density of steel is too large, titanium is preferred for this component, due to its lower density and higher thermal resistance (see Table 25).

Nozzle

In the HRE Code a conical nozzle is considered. The divergent length can be calculated as

$$L_{div} = \frac{D_e - D_t}{2tg\alpha_{div}} \tag{8.4}$$

where D_e and D_t are respectively the diameter of exit and throat sections. The semi-aperture angle α_{div} is generally assumed of 15°. In the frame of this research, the solid fuel is not loaded with metal additives, hence, the absence of a large amount

of unburned metal agglomerates would allow for the use of a bell shape nozzle. The latter, providing a better exhaust gas expansion with lower losses (~ 2%), produces higher performance with restrained length of the divergent part. The final length L_{noz}^{bell} of the bell nozzle can be evaluated first by calculating the performance with a conical nozzle L_{noz}^{coni} ($\alpha_{div} = 15°$), then, by using the design charts provided by Humble [Chap. 5, pp. 225] [48], the correction factor for nozzle length $\phi_{L,noz}$ can be estimated. For expansion area-ratio ϵ_{noz} values greater than 40 and nozzle efficiency of 98%, a $\phi_{L,noz}$ of 0.675 is obtained. The nozzle mass M_{noz} is calculated by an empirical formula, based on a large number of real nozzle data, still provided by Humble and valid for phenolic-based materials [48]

$$M_{noz} = 125 \left(\frac{M_p}{5400}\right)^{2/3} \left(\frac{\epsilon_{noz}}{10}\right)^{1/4} \tag{8.5}$$

where M_p is the total mass of propellant. A phenolic-based material is preferred ($\rho = 2200$ kg/m^3 [48]), since the commonly used graphite has a lower resistance against oxygen-rich hot exhaust gases.

Oxidizer Tanks and Pressurization System

Spherical tanks, made by aluminum, are considered in the preliminary design. The aluminum material helps to reduce the natural chemical decomposition of hydrogen peroxide [96], favoring a more safe oxidizer storability. The total volume $V_{z,tank}$ of each tank is defined as

$$V_{z,tank} = \frac{V_{ox}}{z_{tank}} + V_{ull} + V_{dec} + V_{feed} \qquad z_{tank} = 1,..,4 \tag{8.6}$$

where V_{ull} is the ullage volume (about 1-3% of the tank volume), unfilled volume which accounts for oxidizer expansion or tank structure contraction [48], V_{dec} is empty volume for natural H_2O_2 decomposition (assumed about 2-4% of the tank volume) while V_{feed} is the volume of unusable oxidizer remained in the feed line (assumed about 4% of the tank volume). The oxidizer volume include the hydrogen peroxide both used for primary and secondary propulsion. For a spherical shape tank, the wall thickness is estimated by

$$t_{tank} = \frac{p_b r_{tank}}{2F_{tu}} \tag{8.7}$$

where r_{tank} is the tank radius calculated with the sphere volume formula and p_b is the burst pressure referred to the maximum operating tank pressure p_{ox} enhanced by a safety factor (as described for combustion chamber) [48]. The oxidizer pressure is evaluated as

$$p_{ox} = p_{c,max} \cdot f_{safe} + \Delta p_{dyn} + \Delta p_{feed} + \Delta p_{inj} + \Delta p_{RCS} \tag{8.8}$$

where Δp_{dyn} is the dynamic pressure (Bernoulli's equation), which increases with the static pressure drop when the oxidizer leaves the tank with velocity v [48], while

Δp_{feed} and Δp_{RCS} are, respectively, the pressure drop of the feed system (typically between 35-50 kPa [48]) and of the RCS systems. The max pressure $p_{c,max}$ reached during the combustion is used for p_{ox} evaluation. Got the tank radius and wall thickness, the tank mass M_{tank} is easily calculated. The mass of feed pipes M_{pipes} is assumed as the 15% of the combustion chamber mass [48].

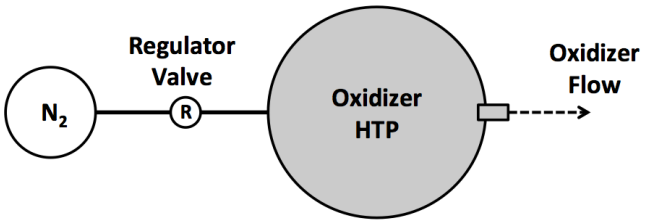

Figure 70.: Pressure-regulated system for oxidizer pressurization.

A pressure-regulated system is considered for the tank pressurization, see Figure 70. This kind of system is able to maintain the tank pressure meanwhile the oxidizer level decreases. The selected pressurant gas is nitrogen N_2, due to its properties and low cost. Generally, in real applications the pressurization system has a pressure of about 21.0 MPa [48]. The pressurant gas mass p_{pres} is calculated, in case of long thrust duration, by assuming an isentropic change in temperature

$$T_f = T_i \left(\frac{p_f}{p_i}\right)^{\frac{\gamma-1}{\gamma}} \tag{8.9}$$

where T_f and T_i are, respectively, the final and initial temperatures of the pressurant gas; its initial pressure is $p_i = p_{pres}$, while the final one is usually equal to the tank pressure p_{ox} [48]. Then the pressurant mass amount can be calculated by the perfect gas law

$$m_{pres} = \frac{V_{pres} p_f}{(R^\circ/w) T_f} \tag{8.10}$$

where V_{pres} is the pressurant volume and w the molecular weight of the gas. Since the final pressurant volume is the sum of tank volume and pressurant tank volume $V_{tank,pres}$, which is not known, an iterative process is required, by initially setting $V_{tank,pres} = 0$. Once obtained the convergent M_{pres} value, the mass of the pressurant tank is evaluated by the empirical formula

$$M_{tank,pres} = \frac{p_i V_{tank,pres}}{g_0 \cdot 6350} \tag{8.11}$$

valid for titanium material [48].

HPM Mass Budget

Once noted the mass of each single component, the inert mass results

$$M_{inert} = M_c + M_{noz} + M_{tank} \cdot z_{tank} + M_{tank,pres} + M_{cata} \cdot z_{cata} + M_{pipe} + M_{hp} \tag{8.12}$$

where M_{hp} is the mass of the injection head-plate. Additional mass contributes must be considered: the mass of structural connections M_{str}, such as bosses, beams, etc., which typically corresponds to a 10% of the inert mass M_{inert} [48] and the mass of the external covering case M_{case} (made by aluminum plates), assumed as the 20% of the inert mass. Finally, the hybrid propulsion module wet mass M_{HPM}^{wet} is obtained as

$$M_{HPM}^{wet} = M_{inert} + M_{str} + M_{case} + M_{fuel} + M_{ox} + M_{ox,RCS} + M_{pres} \tag{8.13}$$

and it is possible to define propellant-to-engine mass ratio

$$K_p \equiv \frac{M_p}{M_{HPM}^{wet}} \quad . \tag{8.14}$$

8.1.2 DeoKit Components

The De-orbiting Kit is equipped with a HPM, that is its primary propulsion system, and all the other components involved in the active removal mission: the avionics for trajectory control and positioning, the instrumentation for close-range operations with the target and communication with the Earth base, the thermal system for the temperature control of instrument and oxidizer, batteries for power supply, the docking systems for target capture and mating as well as a Reaction Control System (RCS) for the attitude control. Except the latter, all these components are collected in the *ADR platform*, whose total mass represents a further payload for the HPM, besides the target to remove. The ADR platform mass is estimated considering typical components mass values found in the literature survey [8]. Concerning the docking phase, for the soft docking it is assumed to load an electro-adhesive system proposed in [50, 51, 16, 17, 3] moved by a robotic arm, for a total estimated mass of about 60 kg, while for the hard docking, since a specific system is not yet defined, different mass budgets are accounted depending on the target size; at a first approximation, about 50 kg are assumed. Hybrid rockets with single perforation grains are characterized by high L_f/D_p ratios, resulting in long and thin engine bodies. This aspect can be exploited for the volume organization of the DeoKit as presented in Figure 71. In this configuration four spherical tanks are placed in the aft region of the rocket body, in correspondence of the nozzle; they define the maximum width of the DeoKit and the fore volume between them and the rocket, centrally located, is available for the components of the ADR platform. Because of this, the length and the width of the HPM correspond to the DeoKit dimensions.

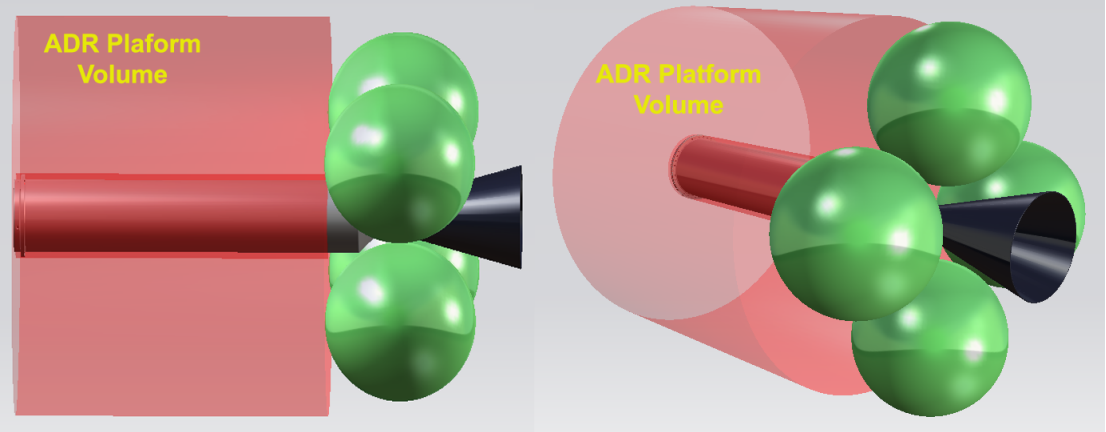

Figure 71.: DeoKit configuration: the red volume around the HPM is available for the components of the ADR platform.

Reaction Control Systems

Another great advantage of the hydrogen peroxide is the exploiting of its catalytic decomposition for a RCS system. For the preliminary sizing a certain amount of HTP $M_{ox,RCS}$ is stored in the oxidizer tanks, to be used for attitude control, and the mass of the RCS components are estimated. The DeoKit is equipped with two different RCS systems:

1. a Low-thrust-RCS for close-range rendezvous operations. It is composed by twelve nozzles (two directions for each of six degree of freedoms);
2. a High-thrust-RCS for far-range rendezvous operations and attitude control during the disposal maneuver. It is composed by six nozzles (four for pitch and flight direction, two for roll, spin).

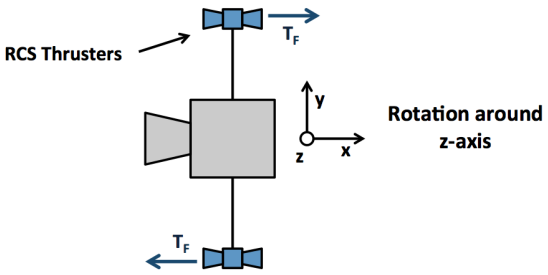

Figure 72.: RCS schematic for the rotation around z-axis. The same configuration is used even for x- and y-axis. A total of twelve nozzles are required for a complete attitude control (six degrees of freedom).

For the catalysts sizing, the nozzles expansion area-ratio, the thrust magnitude, the catalyst pressure and the number of impulses are defined. Then, by means of NASA CEA software [91, 92], with Bray approximation (see section 7.1.2), the performance

in vacuum expansion conditions are evaluated. Noted the specific impulse, by Eq. 7.2 one can calculate the required HTP(90%) mass flow rate. Then, by supposing the thrust after 1 s of burn, the hydrogen peroxide mass is achieved. The selected thrust value represents the max thrust obtainable with a burn of 1 s. For example, a range of 2500-5000 one-second-burns, with thrust values of 1 N, involves an oxidizer mass addition of about 1.5-3.0 kg. This oxidizer amount can be managed to generate impulses with thrust up to 1 N, in the considered example. Once noted the required HTP(90%) mass flow rate it is possible to evaluate the catalytic bed diameter with Eq. 8.2, by assuming a G_{cata} value [56], following the same approach described for injection catalyst system (catalytic beds made of silver). The pressure drop produced is estimated with respect to the selected G_{cata}, considering the ranges provided in [56]. The wall thickness of catalyst chamber is obtained by the equation

$$t_{c,cata} = R_{cbed}\left[\sqrt{\frac{F_{tu,amm}}{F_{tu,amm} - 2p_b}} - 1\right] \tag{8.15}$$

where $F_{tu,amm}$ is the admissible tensile strength of the material, while R_{cbed} and p_b are, respectively, the catalytic bed diameter and the burst pressure [181]. The catalyst chamber is assumed made by stainless steel (see Table 25). To take into account of the pressure-regulation and mass flow rate valves a certain addition of mass is supposed for both RCS systems. The throat area A_t of the nozzles is calculated with Eq. 7.6 noted the c^* value from performance calculation [160, 48]. By means of the expansion area-ratio, one can evaluate the exit area and then, the mass of a single nozzle with

$$M_{noz}^{RCS} = \pi\rho_{steel} t_{noz}^{RCS} L_{noz}^{RCS}\left(R_e^{RCS} + R_t^{RCS}\right) \tag{8.16}$$

where R_e^{RCS} and R_t^{RCS} are the exit and throat radius of a RCS nozzle.

8.2 SPACE DESIGN ANALYSIS

The HRE Code can simulate the combustion process, as well as the thrust generated by a hybrid rocket and the most important required inputs are the solid fuel grain length L_f and the oxidizer mass flow rate $\dot{m}_{ox}$. In order to allow for the best selection of these parameters, for the propulsion system sizing with regards to a specific ADR mission, a design space is evaluated by relating the HPM mass with the velocity increment required and other propulsion parameters. For this purpose a target mass of 1400 kg (Cosmos-3M 2nd stage) on a circular orbit at a mean altitude of about 770 km is assumed. In this case, the controlled reentry performed by means of a single boost maneuver able to lower the perigee below 60 km with a FPA $< -1.5°$ at an interface of 120 km, requires a ΔV of about 200 m/s. The mass supposed for the ADR platform is of 270 kg, thus obtaining a total payload for the HPM of 1670 kg. To the latter, the dry mass of the RCS systems must be added: a low-thrust system which provides 2000 impulses up to 3 N and a high-thrust system with 200 impulses

up to 50 N (~ 8 kg of dry mass for such configuration). As oxidizer HTP(90%) is considered while HTPB as solid fuel. Ideal efficiency (~ 1 with adiabatic conditions) of the catalyst injection system is assumed and the final performance are corrected as described in Sections 7.1.2 and 7.2. The erosion of nozzle throat is evaluated every 1.0 s of combustion.

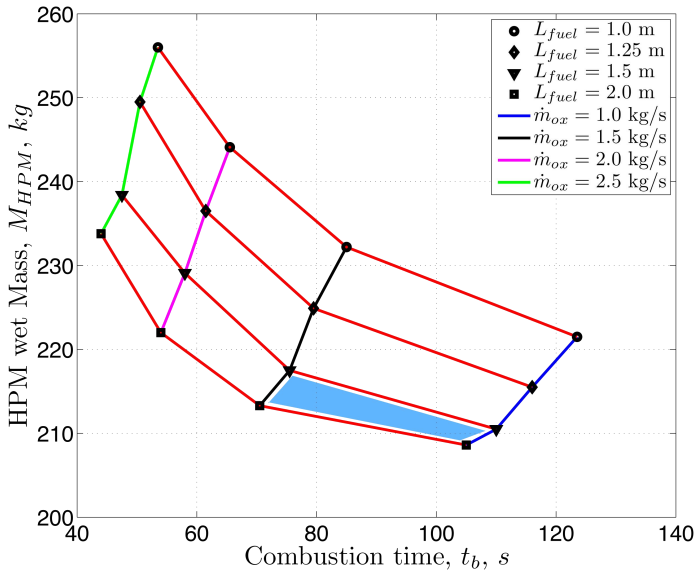

Figure 73.: HPM space design net: HPM wet mass vs. burn time. L_f between 1.0 and 2.0 m, $\dot{m}_{ox}$ between 1.0 and 2.5 kg/s. Target mass 1400 kg and ADR platform mass 270 kg.

In Figure 73, one can see the space design net used to identify the best combination of grain length and oxidizer mass flow rate that provide the greatest performance and smallest engine size. Each intersection point corresponds to a HPM able to sustain the required velocity increment. Once calculated the thrust profile for a fixed burn time, the achievable ΔV is evaluated, in first approximation, by applying the linear accelerated motion, having a small variation between the acceleration produced at each time step and assuming equilibrium between centripetal and centrifugal forces (the atmospheric drag is not considered). Four different solid grain lengths are selected, with values between 1.0 and 2.0 m, while the $\dot{m}_{ox}$ is varied from 1.0 to 2.5 kg/s. The latter is kept constant during the combustion time, simulated with a Δt of 0.5 s. The central fuel port diameter is defined assuming an initial maximum G_{ox} of 600 kg/(m$^2 \cdot$ s) for the gaseous oxidizer [48], while the throat diameter of the nozzle is sized to provide a mean initial chamber pressure of about 3.5 MPa. The HPM wet mass becomes smaller with the increase of the grain length and the decrease of oxidizer mass flow rate. In fact, for the considered L_f values, to lower $\dot{m}_{ox}$ corresponds smaller average oxidizer-to-fuel ratios, see Figure 74. From the latter one can see that the grain length of 2.0 m is characterized by an average O/F very close to the optimum one for the couple HTPB + HTP(90%). For this grain size, the lightest HPM is obtained with a $\dot{m}_{ox}$ of 1.0 kg/s, while the highest average vacuum specific impulse is got

with $\dot{m}_{ox} = 1.5$ kg/s, see Figure 82 in the Appendix A. Low oxidizer mass flow rates involve lower thrust levels, see Figure 83 in Appendix A, hence larger burn time to satisfy the disposal requirements. The combustion time represents an important constraint for the HPM, whose nozzle is not cooled. In order to avoid the need of an expensive and complex cooling system, the boost phase must be limited.

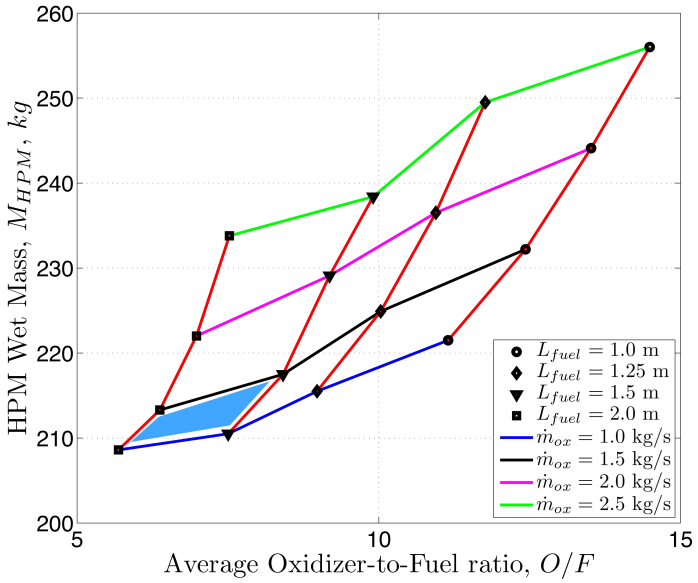

Figure 74.: HPM space design net: HPM wet mass vs. O/F. L_f between 1.0 and 2.0 m, $\dot{m}_{ox}$ between 1.0 and 2.5 kg/s. Target mass 1400 kg and ADR platform mass 270 kg.

Real applications, such as SpaceShipOne and Two, worked with combustion times of the orders of 90 s, for a single burn [55, 61, 66]. However, low thrust is preferred for the disposal of an abandoned S/C, since high thrust levels might provoke the break up of satellite appendages, such as solar panels, antennas etc. In fact, after the end of the mission, a spacecraft typically remains in its operative configuration. Therefore, for a fixed grain length, the oxidizer mass flow rate must be selected in order to generate enough thrust to keep the combustion time below 100 s and imparting low g acceleration levels to the system DeoKit-Debris. For the removal of a Cosmos-3M 2nd stage by means of a single burn, the best configuration considers a L_f between 1.5 and 2.0 m and a $\dot{m}_{ox}$ smaller than 1.5 kg/s but higher than 1.0 kg/s, see the blue area in space design figures. In this region of the space design net, the average thrust results between 3.5 and 5.0 kN, with average g accelerations of about 0.25g. The latter can be easily sustained by a R/B, that is Cosmos-3M, if the DeoKit is attached to its gas dynamic nozzle or to the payload castle structure. If the same target is on a higher orbit altitude, the required velocity increment for the disposal grows. In Figure 75, the HPM wet mass is shown as a function of burn time for different ΔV, considering three grain lengths and $\dot{m}_{ox} = 1.5$ kg/s. At this conditions, solid grains with length between 1.5 and 2.0 m are able to provide velocity increments up to 250 m/s with a single boost phase below 100 s. For higher ΔV or objects at higher altitudes, a multi-

boost disposal is necessary because the significantly increase of combustion time for the single burn would be possible only with a cooled nozzle. To keep the one-burn disposal also for higher ΔV, it would be possible to increase the oxidizer mass flow rate, generating higher thrust levels, as well as strong accelerations on the system.

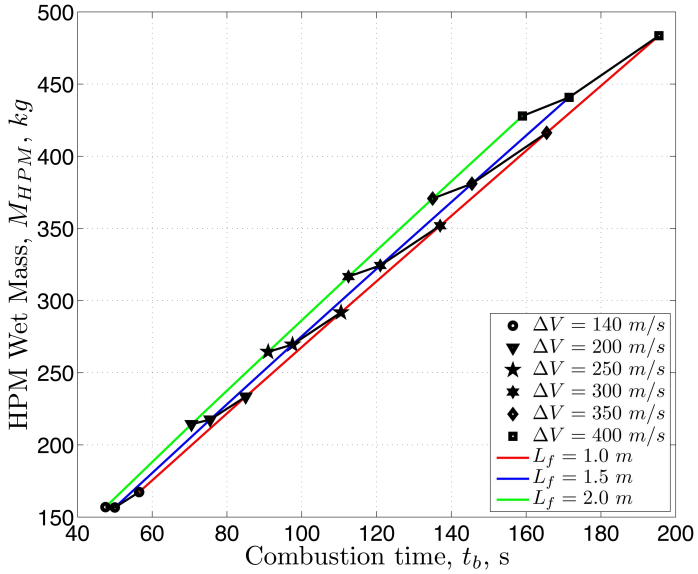

Figure 75.: HPM space design net: HPM wet mass vs. time, for different DV requirements. L_f between 1.0 and 2.0 m, $\dot{m}_{ox} = 1.5$ kg/s. Target mass 1400 kg and ADR platform mass 270 kg.

Moreover, in order to get high specific impulses, hence O/F close to the optimum, the fuel grain should be longer, thus designing a larger HPM in terms of overall mass and size. The multi boost disposal, for such cases, seems the best solution, allowing for small and lighter engines and promising low accelerations to the target during the disposal. The DeoKit is carried on orbit by a space launcher and this means that the HPM must be sufficiently compact to be embarked in the payload fairing, especially in case of multi-removal scenario. Thus the grain length, which defines the final HPM size, is an important constraint. The use of a single central perforation in the solid fuel produces long and thin grains ($8 < L_f/D_p < 20$ [48]); if high thrust levels are required a multiple port grain configuration could be considered in order to reduce the grain length and the overall HPM size.

8.3 PRELIMINARY SIZING FOR ADR

8.3.1 HPM for Cosmos-3M

Following the design analysis performed in the previous section, a Hybrid Propulsion Module has been designed for the removal of a Cosmos-3M 2nd stage. The mission requirements and the engine characteristics are the same just described in Section 8.2

and Table 2. However, a safety increase of 10% on the disposal ΔV is applied, plus an addition of 20 m/s [8], to account for the far-mid rendezvous that the DeoKit must perform to reach the target, once it has been released on the same orbital plane by the space launcher upper stage. The HPM is design to supply for a total velocity increment of 240 m/s. A heavier ADR platform is assumed, 300 kg of mass. In Figure 77, one can see the vacuum specific impulse of the HPM during a single burn of 83 s, enough to provide a ΔV of 220 m/s for the disposal maneuver. The average I_s is 298.5 s while the O/F about 7.2, see Figure 84 in Appendix B. The thrust generated, see Figure 85 (Appendix B), results between 5.5 and 4.5 kN, imposing an average acceleration to the system of about 0.27g. One can see the plot of the other performance parameters in Appendix B. The HPM has a grain length of 1.8 m and a constant $\dot{m}_{ox}$ of 1.5 kg/s. In Table 26, the HPM mass budget is reported.

Cosmos-3M	M_{HPM}^{wet}	M_{HPM}^{dry}	M_{ox}	M_f	M_{ox}^{RCS}	M_{pres}	K_p
HPM [kg]	258.31	83.26	135.75	20.03	9.83	9.44	0.64

Table 26.: HPM preliminary sizing mass budget. Target of 1400 kg, ADR platform of 300 kg.

The total mass of HPM is 258.3 kg and the DeoKit results of 566.83 kg, of which about 8.5 kg is the dry mass of the RCS systems. The HPM, hence the DeoKit (see Figure 71), has a total length of 2.143 m and a width of 0.90 m. The resulted DeoKit mass corresponds to the 40.5% of the removed mass (i.e. 1400 kg).

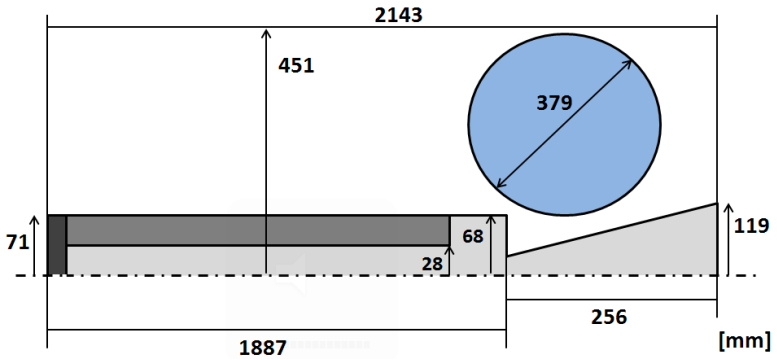

Figure 76.: HPM for Cosmos-3M 2nd stage removal: dimensions sketch.

In Figure 76, one can see the HPM dimensions, expressed in millimeters. The nozzle has a bell shape with an expansion-area ratio ϵ of 50. Concerning the available launchers for ADR mission, see Section 3.2, a multi-removal mission might be performed with Vega, which can carry up two DeoKits, for a total mass of 1135 kg, while the upper stage of Soyuz, Fregat, able to provide up to 22 controlled burns, could carry up to 6 DeoKits, i.e. 3402 kg, preserving about 1000 kg of payload. The Deokits could be clustered by putting in line three pairs of module into the Fregat payload firing. In Figure 78, one can see the disposal trajectory analysis performed by U. Tancredi for the system DeoKit-Debris (6.15 m^2 frontal surface area), starting from the thrust profile generated by the HPM. The trajectory code, Simulink® based, is the same developed for the preliminary ADR calculations presented in [17, 166].

The code assumes a single boost maneuver to lower the perigee below 60 km with a FPA $< -1.5°$ at an interface of 120 km. Future code upgrades will allow for multi-burn disposal analysis.

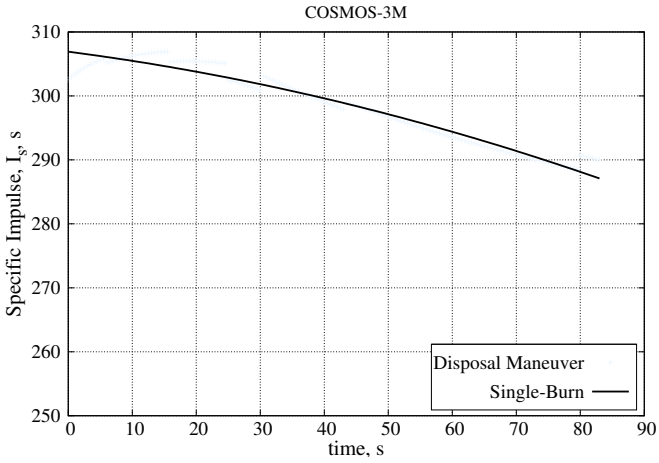

Figure 77.: Vacuum specific impulse generated by HPM for active removal of a Cosmos-3M 2nd stage from an altitude of 767 km by means of a single boost.

Concerning the designed HPM, the trajectory requirements are largely satisfied, obtaining a very steep FPA of about $-2.5°$, reducing the orbit transfer perigee 15 km below the Earth surface. With a so steep flight path the system DeoKit-Debris would be largely exposed during the atmospheric phase, going to an easy fragmentation, but with a limited ground impact area [17]. The obtained results suggest an overestimation of the HPM, since the disposal constraints are lower.

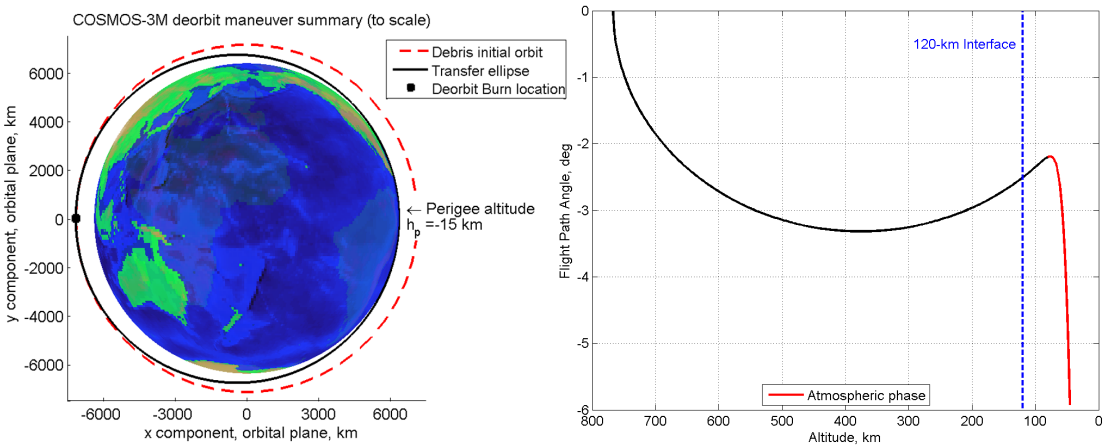

Figure 78.: Disposal maneuver summary: transfer ellipse trajectory (left) and FPA vs. altitude (right).

Therefore, the ΔV estimation by means of the basic approach of linear accelerated motion provides a larger thrust than required. However, from the point of view of engine design and mass budget, this means that the HPM is able to transfer a higher

mass value, hence a heavier ADR platform or capture systems or, alternatively, the overall HPM mass and size could be reduced, making more compact and small DeoKits, being an advantage for multi-removal scenario. In Appendix D, further charts about the disposal are available. More optimized results in term of HPM preliminary sizing can be achieved by combining the HRE code and the disposal code into an optimization algorithm, considering a specific disposal maneuver, thus an ad hoc evaluation of the obtainable ΔV as well as of the trajectory constraints.

8.3.2 HPM for Envisat

Envisat, with a mass of about 7800 kg, is orbiting at a mean altitude of about 767 km. The preliminary sizing is evaluated for two disposal approaches:

1. *single-burn* to lower the perigee below 60 km with a FPA $< -1.5°$ at an interface of 120 km. ΔV of about 200 m/s;
2. *multi-burn* to lower the perigee by means of two consecutive elliptical transfer orbits, the second burn starts in correspondence of the first transfer orbit perigee. Total ΔV of about 200 m/s.

The mass supposed for the ADR platform is of 500 kg, thus obtaining a total payload for the HPM of 8300 kg. To the latter, the dry mass of the RCS systems must be added: a low-thrust system which provides 2000 impulses up to 15 N and a high-thrust system with 600 impulses up to 150 N ($\sim$ 10 kg of dry mass for such configuration). As oxidizer HTP(90%) is considered while HTPB as solid fuel. Ideal efficiency ($\sim$ 1 with adiabatic conditions) of the catalyst injection system is assumed and the final performance are corrected as described in Sections 7.1.2 and 7.2. The erosion of nozzle throat is evaluated every 1.0 s of combustion. As assumed for Cosmos-3M case, a safety increase of 10% on the disposal ΔV is applied, plus 20 m/s for the far-mid rendezvous, obtaining a total ΔV of 240 m/s. In Figure 79, the thrust generated during the disposal maneuvers are compared: the two boost phases of the multi-burn maneuver are plotted consecutively for comparison purpose, despite during the disposal the second one starts only when the perigee of the first transfer orbit is reached. The single-burn HPM satisfy the ΔV requirement with a 91 s of combustion, but generating a quite high thrust level, imparting to the system a maximum acceleration of 0.25g. For the single-burn maneuver the reentry trajectory profile was evaluated with the code of Tancredi [17]. Also for the system DeoKit-Envisat (70 m^2 of frontal section surface area) the thrust generated by the HPM resulted largely enough, able to lower the perigee of the transfer orbit about 60 km below the Earth surface, with a steeper FPA of $-2.9°$, see Figures 109 and 111 in Appendix E. These results suggest the possibility to little reduce the thrust generated, obtaining a smaller HPM. However, a more significant analysis could be done when the trajectory code will allow for multi-burn disposals. The multi-burn HPM provides 110 m/s in 99 s of combustion, enough to reduce the target altitude little below 400 km (see Figure 11), then, by means of a second boost of 77 s (i.e. further 110 m/s), the perigee of the elliptical transfer orbit is

reduced below 60 km. In this case, the level of thrust is significantly smaller, average values of 10.5 kN (1st burn) and 12.8 kN (2nd burn) against the an average thrust of 22.3 kN for the single-burn HPM.

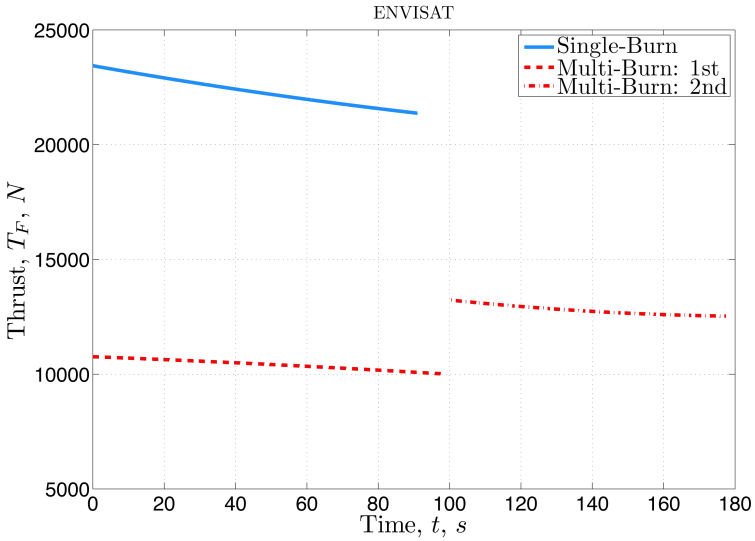

Figure 79.: Thrust generated by HPM for active removal of Envisat from an altitude of 767 km. Comparison between single- and multi-burns maneuvers.

During both burns the acceleration to the system remains below 0.143g, with average values of 0.11g (1st burn) and 0.13g (2nd burn). The single-burn HPM provides an average vacuum specific impulse of about 302 s, while the multi-burn HPM an overall average $I_{s,vac}$ 296 s (1st: 302 s, 2nd: 290 s). In Appendix C, one can see further plots with the performance comparison between the single- and multi-burn HPM.

Envisat	L_f[m]	$D_{p,i}$[m]	$D_{t,i}$[m]	$\dot{m}^{(1)}_{ox,i}$[kg/s]	$\dot{m}^{(2)}_{ox,i}$[kg/s]
Single-burn HPM	4.00	0.118	0.069	6.6	—
Multi-burn HPM	3.25	0.080	0.048	3.0	4.0

Table 27.: HPM initial geometry and mass flow rate for preliminary sizing. Target of 7800 kg, ADR platform of 500 kg.

Concerning the grain geometry, the central port diameter is defined assuming an initial maximum G_{ox} of 600 kg/($m^2 \cdot s$), while for the multi-burn HPM the second oxidizer mass flux required a greater $\dot{m}_{ox}$, due to the larger port diameter, to obtain an acceptable regression rate.

Envisat	M^{wet}_{HPM}	M^{dry}_{HPM}	M_{ox}	M_f	M^{RCS}_{ox}	M_{pres}	K_p
Single-burn HPM [kg]	1319.31	440.23	656.70	98.92	73.72	49.55	0.63
Multi-burn HPM [kg]	1260.21	369.68	665.00	101.16	73.72	50.66	0.67

Table 28.: HPM preliminary sizing mass budget. Target of 7800 kg, ADR platform of 500 kg.

The throat diameter of the nozzle is sized to provide a mean initial chamber pressure of about 3.5 MPa for both cases. In Table 27, the initial geometry configuration and mass flow rates used for the preliminary sizing are shown, while in Table 28, one can see the HPMs mass budget. The multi-burn HPM is about 4.7% lighter than the single-burn one. The DeoKit results:

1. *single-burn HPM*: 1830 kg with a length of 4.68 m and a width of 1.54 m;
2. *multi-burn HPM*: 1771 kg with a length of 3.76 m and a width of 1.55 m.

No large difference is observed on the DeoKits width, while the multi-burn module is about 19.7% shorter. A more compact system is preferred in order to favor a better clustering of the DeoKit with others of the same type (multi-removal scenario) or with new satellites for usual commercial or governmental activities. As one can gather, a multi-burn strategy involves lower structural stress to the target, reducing the break up risk of its appendages, and a more compact and lighter DeoKit module. A further way to lower the module length is the use of multi-perforated fuel grain configuration, which, despite a lower volumetric efficiency, allows for higher thrust levels with shorter solid fuel cylinders. In Figure 80, one can see the dimension details of the multi-burn HPM. The nozzle has a bell shape with an expansion-area ratio ϵ of 50.

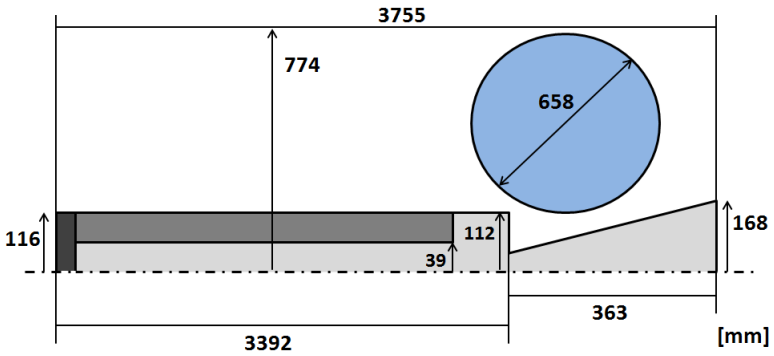

Figure 80.: Multi-burn HPM for Envisat removal: dimensions sketch.

The preliminary sizing of a HPM for the removal of an Envisat-like object highlights the need of a heavier space launcher than Vega. The upper stage of Soyuz, in this case, would be able to carry two multi-burn DeoKits, for a total mass of 3542 kg, preserving about 1000 kg of payload. The mass of one module corresponds to the 23% of the removed mass (i.e. 7800 kg).

9 CONCLUSIONS AND FUTURE DEVELOPMENTS

Hybrid propulsion is a promising technology for space missions in near-Earth region. A very attractive application is the active removal of large abandoned objects in LEO, each one representing a dangerous source of new space debris in case of catastrophic collision. Actually, the active debris removal is largely discussed within the international space community and, besides the technological challenge, significant obstacles are put by the economic impact and, in a more complex manner, the political issues related to the implementation of such kind of missions. In this work, the possibility to use a Hybrid Propulsion Module for ADR mission has been evaluated. Hybrid motors provide several advantages with respect to solid and liquid propulsion systems and, if compared with the latter, significant lower overall costs. This, in the frame of the international discussion, might favor the development of ADR missions, even because one of the most effective removal approaches is the controlled reentry by means of chemical propulsion systems, especially for large massive objects, such as Envisat or Russian and Chinese large abandoned R/Bs.

Preliminary HPM Design

The HRE code, developed for ballistics analysis and preliminary HPM design, provides reasonable results in term of performance and engine mass budget. Two different missions has been considered: the removal of a Cosmos-3M 2nd stage, as possible demonstrative mission for ADR technology, and the removal of an Envisat-like object. The Cosmos-3M can be removed by an DeoKit 566.8 kg, powered by a HPM of 258 kg, with a total length of 2.14 m and a width 90 cm (4 spherical tanks around the HPM rocket body). The disposal maneuver consists of a single boost used to lower the perigee below 60 km with a FPA $< -1.5°$ at an interface of 120 km. An excess of propellant is considered as safety factor and for a mid-range rendezvous performed once the DeoKit is released on the same orbit of the selected target. The DeoKit, besides the primary propulsion hybrid engine, consists of an ADR platform (e.g. avionics, instrumentation, supporting system, docking and capture systems) and two RCS systems, one for close-proximity operations and one for attitude control. Two disposal approaches have been considered for Envisat, a single boost and a multi boost strategy; the latter provided the best results in term of performance and mass budget, according to the defined constraints. An Envisat-like object can be removed by a DeoKit of 1771 kg, powered by a HPM of 1260 kg, with a length of 3.76 m and a width 1.55 m. In spite of these results, concerning the Cosmos-3M, Vega can load 2 DeoKits, while Soyuz up to 6 allowing for multi-removal scenario. On the other hands, the heavier DeoKit required for Envisat removal can be transferred only by a heavy launcher such as Soyuz, which can load up a couple of DeoKits. These final considerations are quite

in agreement with the early studies, performed with a simpler calculation approach, about ADR by means of hybrid propulsion [16, 17, 165, 166]. Trajectory simulations have been performed by the *University of Naples "Parthenope"*, by means of a dedicated developed code. The results achieved highlight a certain overestimation in the HPM performance with respect to the single boost maneuver, suggesting the possibility to reduce the HPM size and mass or to carry a heavier target or ADR platform, keeping the same thrust profile.

Ballistics Investigation for Regression Rate Enhancement

A ballistics combustion analysis for the regression rate enhancement for HTPB-based fuel formulation was performed by means of a 2D-Radial hybrid micro burner. A swirl oxidizer injection flow was used together an innovative micro-sized energetic additive. The data reduction was carried out by an optical time-resolved technique. The two considered techniques were, initially, applied separately. Under the tested conditions, with a swirl intensity of $\sim$ 3.2, a percent r_f enhancement of 28% at $G_{ox} = 350\ kg/(m^2 \cdot s)$ was achieved for pure HTPB fuel with respect to standard flow injection. This performance positive contribute decreases as combustion proceeds, nearly disappearing around $G_{ox} = 100\ kg/(m^2 \cdot s)$. The HTPB was loaded with micron-sized A-Al1 and burned with standard oxidizer flow. Under the investigating conditions, a regression rate enhancement of 19% at $G_{ox} = 300\ kg/(m^2 \cdot s)$ with respect to not loaded HTPB was observed. Then, the combustion of HTPB + A-Al1 with swirling injection provided percent increases quite similar to those achieved by the same formulation but with standard flow, although the presence of swirl provides better performance as the G_{ox} decreases. It was observed that for $G_{ox} < 150\ kg/(m^2 \cdot s)$ the swirl limits the convective heat transfer reduction allowing for a combustion less sensitive to G_{ox} changes. Certainly further analysis are required, but this results suggest the possibility of limiting the performance shift of combustion hybrid systems by means of swirling injection. The performance on HTPB + A-Al1, under the investigated conditions, highlighted the effectiveness of powder activation process to enhance the reactivity of micron-sized additives. However, the use of metal additives produces large amounts of agglomerates ejected throughout the nozzle exhaust. Because of this, their use for space missions, such as ADR, may cause the generation of micron-sized debris that, even though they do not represent a high hazard for operative S/C, would be better to avoid. On the contrary, metal additives may be considered for special flat pancake hybrid motors, like VFP [54], in which the chamber geometry together with vortex combustion may significantly reduce the agglomerates expulsion.

HTPB Simulate Aging

The HTPB R45 is one of the most used materials in the space propulsion field, in particular as solid fuel in hybrid propulsion. The need to store the cured HTPB sometimes for a long time in ground facilities or loaded on operative motors for satellites PMD operations, requires a good comprehension of its material properties change

over time. The study was performed by thermal accelerated aging treatment. The test campaign was defined considering the Arrhenius equation and the relative empirical *van't Hoff rule*. Four aging temperatures was assumed to simulate a total aging of 10 years. The samples thermal treatment was carried out with completely dry conditions, excluding the effects due to humidity. For each temperature value 12 HTPB samples were prepared and by means of DMA the Storage modulus E', Loss modulus E'' and $\tan\delta$ were measured after 2, 4, 7 and 10 years of simulated aging. Under the investigated conditions, the Storage modulus decreases with the simulated aging time, from the baseline value, measured for not aged samples. In particular, two different fashions were observed, one for low temperatures 60°C and 70°C and the other for high temperatures 80°C and 90°C. At low temperatures one can see an initial increase of E', which then decreases after 4 simulated years. At high temperatures the opposite behavior was observed, a significant decrease from the baseline followed by a little increase after 7 simulated years. These two different behaviors can be associated with the activation of further chemical and thermal reactions for the treatments above 80°C. Such reactions should not be present in the typical storage conditions, making the treatments at 60°C and 70°C reasonably better for the analysis of HTPB in-service conditions. By comparing the Storage modulus trend with the thermal treatment temperature, a quasi-linear decrease from 60°C to 90°C was achieved. The Flory-Huggins test was applied to the samples, demonstrating that the E' decrease for aged HTPB is due to the break of polymer cross-links, which produces a softening of the material. However, the aging behavior seems to disagree with the aging showed in literature, in which it is commonly to observe a material hardening over the simulated aging time. Probably, these differences can be caused by the presence, in the furnished HTPB R45 batch, of an unknown antioxidant inserted by AVIO to preserve the material properties of the polyurethane resin. In addition, a strange distribution of tridimensional hotspots was observed within the thickness of rectangular samples. They appear as darkener regions in which the aging is more advanced. This pigmentation could be associated with the reaction of extinguished tin, activated by the thermal treatment or by the light. In fact, no hotspots were found on baseline samples, stored in low humidity conditions without light exposition. However, for real applications the addition of TIN is not required.

Suggestions for Future Developments

Concerning future works and activities about the HPM preliminary sizing:

- The HRE code and the trajectory disposal code (Tancredi) could be combined within an algorithm for the HPM design optimization.
- Different regression rate models could be analyzed and compared. In order to achieve a better matching between numerical solution and experimental measures the contribute the radiant heat flux, due to soot particles, should be considered.

- Different propellant combinations could be simulated. The list of chemical species implemented in the chemical equilibrium algorithm can be modified in order to consider the nitrous oxide (N_2O) as oxidizer and, as solid fuel, thermoplastic polymers like PMM, PP, PE and paraffin wax materials; the latter suitable in the case of single boost disposal maneuvers.
- Actually, within HRE code a single central circular port geometry is assumed; multi-port grain configuration could be implemented in order to increase the preliminary design analysis. Depending on the imposed constraints, in some cases, despite the lower fuel volumetric efficiency, a multi-port grain would allow for a higher or the required thrust level, keeping smaller and compact engine sizes.

With regard to experimental activities:

- The replacement of the injection system actually used by the 2D-Radial micro burner with the new swirl injector would allow for a better and more complete combustion ballistics analysis based on swirling oxidizer. Several swirl intensities could be tested both with loaded and not loaded solid fuels. Moreover, the combination of a swirling oxidizer with a metallized fuel could be better investigated, also by testing different additives sizes, such as nAl powders.
- Concerning the aging study of HTPB, the implementation of an ad-hoc law to relate the simulated aging of a selected mechanical property with the real aging time (as described by Layton model) would be necessary. Then, in order to make a comparison with the Arrhenius behavior it would be interesting the evaluation of the aging rate constant. Furthermore, with the aim to verify the importance of the antioxidant, a new accelerated aging campaign with pure HTPB R45, without any antioxidant substance, could be performed.

BIBLIOGRAPHY

[1] J.-C. Liou. Engineering and Technology Challange for Active Debris Removal. *Progress in Propulsion Physics*, 4:735–748, 2013.

[2] J.-C. Liou. Orbital Debris Modeling and Future Orbital Debris Environment. Orbital debris lecture (ASEN 6519), NASA Orbital Debris Program Office, Johnson Space Center, Huston, Texas, University of Colorado Boulder, September 18 2012.

[3] L.T. DeLuca, F. Bernelli, F. Maggi, P. Tadini, C. Pardini, L. Anselmo, M. Grassi, D. Pavarin, A. Francesconi, F. Branz, S. Chiesa, N. Viola, C. Bonnal, V. Trushlyakov, and I. Belokonov. Active Space Debris Removal by a Hybrid Propulsion Module. *Acta Astronautica*, 91:20–33, 2013.

[4] J.-C. Liou. A Parametric Study on Using Active Debris Removal for LEO Environment Remediation. In 61*st International Astronautical Congress (IAC)*, Prague, Czech Republic, September 27-October 1 2010.

[5] D.J. Kessler and G. Cour-Palais. Collision Frequency of Artificial Satellites: The Creation of a Debris Belt. *Journal of Geophysiscal Research*, 83(A6):2637–2646, June 1 1978.

[6] M. Emanuelli, T. Chow, D. Prasad, G. Federico, and J. Loughman. Conceptualizing an Economical, Legally and Politically Viable Active Debris Removal Option. In 64*th International Astronautical Congress (IAC* 2013*)*, Beijing, China, 2013.

[7] C. Wiedemann et al. Cost Estimation of Active Debris Removal. In 63*rd International Astronautical Congress (IAC* 2012*)*, Naples, Italy, 2012.

[8] Th. Martin, E. Pérot, M.-Ch. Desjean, and L. Bitetti. Active Debris Removal Mission Design in Low Earth Orbit. *Progress in Propulsion Physics*, 4:763–788, 2013.

[9] M.M. Castronuovo. Active Space Debris Removal - A Preliminary Mission Analysis and Design. *Acta Astronautica*, 69:848–859, 2011.

[10] L.T. DeLuca. Active Space Debris Removal by Hybrid Propulsion Module. Prin 2012, Research project proposal to the italian Ministry of Education, University and Research (MIUR), 2013.

[11] Y. Funami and T. Shimada. Validation with Experiments on Simplified Numerical Prediction of Hybrid Rocket Internal Ballistics. *AIP Conf. Proc.*, 1493:395–400, 2012.

[12] Y. Funami and T. Shimada. On Assessment of Numerical Methods for Diffusion-Combustion Flow with Fast Chemistry. *AIP Conf. Proc.*, 1493(401), 2012.

[13] D.J. Kessler, N.L. Johnson, J.-C. Liou, and M. Matney. The Kessler Syndrome: Implications to Future Space Operations. In *33rd Annual AAS Guidance and Control Conference*, Febraury 10 2010.

[14] L. Anselmo. A Short Introduction to the Space Debris Problem. Lecture at Politecnico di Milano (Bovisa Campus), January 11 2013.

[15] SpaceFlight101. Russian blits satellite hit by space debris.

[16] L.T. DeLuca, M. Lavagna, F. Maggi, P. Tadini, C. Pardini, L. Anselmo, M. Grassi, U. Tancredi, A. Francesconi, F. Branz, S. Chiesa, N. Viola, and V. Trushlyakov. Active Removal of Large Massive Objects by Hybrid Propulsion Module. In *5th European Conference for Aeronautics and Space Sciences (EUCASS)*, Munich, Germany, July 1-5 2013.

[17] P. Tadini, U. Tancredi, M. Grassi, L. Anselmo, C. Pardini, F. Branz, A. Francesconi, F. Maggi, M. Lavagna, L.T. DeLuca, N. Viola, S. Chiesa, V. Trushlyakov, and T. Shimada. Active Debris Removal Space Mission Concepts based on Hybrid Propulsion. In *64th International Astronautical Congress (IAC 2013)*, Beijing, China, September 23-27 2013.

[18] D.J. Kessler. Collisional Cascading: The Limits of Population Growth in Low Earth Orbit. *Advance in Space Research*, 11(12):63–66, 1991.

[19] S.-Y. Su. On Runaway Conditions of Orbital Debris Environment. *Advance in Space Research*, 13(8):221–224, August 1993.

[20] L. Anselmo, A. Rossi, and C. Pardini. Updated Results on the Long-Term Evolution of the Space Debris Environment. *Advance in Space Research*, 23(1):201–211, 1999.

[21] S.-Y. Su and D.J. Kessler. A Rapid Method of Estimating the Collision Frequencies between the Earth and the Earth-Crossing Bodies. *Advance in Space Research*, 11(6):623–627, 1991.

[22] A. Rossi, A. Cordelli, P. Farinella, and L. Anselmo. Collisional Evolution of the Earth's Orbital Debris Cloud. *Journal of Geophysical Research: Planets (1991-2012)*, 99(E11):23195–23210, November 25 1994.

[23] L. Anselmo, A. Cordelli, P. Farinella, C. Pardini, and A. Rossi. Modelling the Evolution of the Space Debris Population: Recent Research Work in Pisa. In *Second European Conference on Space Debris*, Darmstadt, Germany, March 17-19 1997. ESA.

[24] D.J. Kessler and P.D. Anz-Meador. Critical Number of Spacecraft in Low Earth Orbit: Using Satellite Fragmentation Data to Evaluate the Stability of the Orbital Debris Environment. In *3rd European Conference on Space Debris*, pages 265–272, Darmstadt, Germany, March 19-21 2001. ESA.

[25] P.H. Krisko. Evolve 4.0 orbital debris mitigation studies. *Advance in Space Research*, 28(9):1385–1390, 2001.

[26] J.-C. Liou et al. LEGEND – A Three-dimensional LEO-to-GEO Debris Evolutionary Model. *Advance in Space Research*, 34(5):981–986, 2004.

[27] J.-C. Liou. Collision Activities in the Future Orbital Debris Environment. *Advance in Space Research*, 38(9):2102–2106, 2006.

[28] N.L. Johnson, P.H. Krisko, J.-C. Liou, and P.D. Anz-Meador. NASA's New Breakup Model of Evolve 4.0. *Advance in Space Research*, 28(9):1377–1384, 2001.

[29] Anonymous. Process for Limiting Orbital Debris. NASA Technical Standard 8719.14A with Change 1, National Aeronautics and Space Administration (NASA), Washington, DC, 2012.

[30] IADC Steering Group & Working. Space Debris Mitigation Guidelines. Technical Report IADC-02-01, Inter-Agency Space Debris Coordination Committe (IADC), 2002.

[31] EDMSWG. European Code of Conduction for Space Debris Mitigation. issue 1.0, European Debris Mitigation Standards Working Group (EDMSWG), 2004.

[32] UNCOPUOS. Space Debris Mitigation Guidelines of the United Nations Committe on the Peaceful Uses of Outer Space, Endorsed by the General Assembly Resolution A/RES/62/217. Technical Report a/62/20 (2007), United Nations, New York, USA, 2008.

[33] G. S. Haag, M. N. Sweeting, and G. Richardson. Low cost propulsion development for small satellites at the surrey space centre. *Paper SSC99-XII-5*, August 1999.

[34] Institute of Aerospace Systems. Meteoroid and Space Debris Terrestrial Environment Reference Model (master-2009). Technical Report Version 7.0.2, European Space Agency (ESA), TU Braunschweig, October 5 2012.

[35] ESA Earth Online ESA Webpage. Envisat.

[36] D.S Mcknight. Collision and Breakup Models: pedigree, regimes, and validation/verification. In *National Research Council Committee on Space Debris Workshop*, Irvine, CA, November 18 1993.

[37] M. Loesch et al. Economic Approach for Active Space Debris Removal Services. In *i-SAIRAS* 2010, Sapporo, Japan, August 29 - September 1 2010.

[38] K. Wormnes et al. ESA Technologies for Space Debris Remediation. Technical report, European Space Agency (ESA), 2013.

[39] C. Pardini, T. Hanada, and P.H. Krisko. "Benefits and Risks of using Electrodynamic Tethers to De-orbit Spacecraft. In 57*th International Astronautical Congress (IAC)*, 2006.

[40] R.A.C. Schonemborg and H.F.R Schyer. Solid Propellant De-orbiting and Reorbiting. In 5*th European Conference on Space Debris*, March 2009.

[41] E. Ahedo, M. Merino, C. Bombardelli, H. Urrutxua, J. Pelaez, and L. Summerer. Space Debris Removal with an Ion Beam Shepherd Satellite. In 47*th AIAA/ASME/SAE/ASEE Joint Propulsion Conference and Exhibit*, San Diego, CA, July 31 - August 3 2011.

[42] R. Benvenuto and M. Lavagna. Flexible Capture Device for Medium to Large Debris Active Removal: Simulation Results to Drive the Experiments. In *Astra* 2013, 2013.

[43] M. Emanuelli, S. Ali Nasseri, S. Raval, and A. Turconi. Active space debris removal using Modified Launch Vehicle Upper Stages Equipped with Electrodynamic Tethers. In *6th IAASS Conference*, 2013.

[44] V. Aslanov and V. Yudintsev. Dynamics of Large Space Debris Removal using Tethered Space Tug. *Acta Astronautica*, 91:149–156, October-November 2013.

[45] C. Bombardelli and J. Pelaez. Ion Beam Shepherd for Contactless Space Debris Removal. *Journal of Guidance, Control and Dynamics*, 34(3):916–920, June 2011.

[46] H. Burkhardt et al. Evaluation of Propulsion Systems for Satellite End-of-Life De-orbiting. In 38*th AIAA/ASME/SAE/ASEE Joint Propulsion Conference and Exhibit*, AIAA No. 2002-4208, Indianapolis, IN, July 7-10 2002.

[47] M. Lavagna, R. Benvenuto, L.T. DeLuca, F. Maggi, P. Tadini, and M. Graziano. Contact-less Active Debris Removal: the Hybrid Propulsion Alternative. In 5*th European Conference for Aeronautics and Space Sciences (EUCASS)*, Munich, Germany, July 1-5 2013.

[48] R. Humble, G. Henry, and W. Larson. *Space Propulsion Analysis and Design*. McGraw-Hill, 1995.

[49] A. Ruggiero, P. Pergola, and M. Andrenucci. S Small Electric Propulsion Platform for Active Space Debris Removal. In 33*rd International Electric Propulsion Conference*, Washington, DC (USA), October 6-10 2013.

[50] F. Branz and A. Francesconi. Innovative Technologies for Non-Cooperative Targets Close Inspection and Grasping. In 63*rd International Astronautical Congress (IAC* 2012*) ISSN* 1995-6258, 2012.

[51] F. Branz and A. Francesconi. Soft Docking System for Capture of Irregularly Shaped, Uncontrolled Space Objects. In *6th European Conference on Space Debris*, 2013.

[52] C. Bonnal. Active Debris Removal: Current Status of Activities in CNES. In *IAF Workshop on Space Debris Removal*, Vienna, Febraury 11 2013.

[53] R. Benvenuto, S. Salvi, and M. Lavagna. Dynamic Analysis and GNC Design of Flexible Systems for Space Debris Active Removal. In *IAA-AAS-DyCoSS*2-14-09-02, 2013.

[54] D.M. Gibbon and G.S. Haag. Investigation of an Alternative Geometry Hybrid Rocket for Small Spacecraft Orbit Transfer. Technical report, Surrey Satellite Technology LTD, Final Report 0704-0188, Guilford, Surrey, UK, July 27 2001.

[55] M.J. Chiaverini and K.K. Kenneth. *Fundamentals of Hybrid Rocket Combustion and Propulsion*, volume 218 of *Progress in Astronautics and Aeronautics*. American Institute of Aeronautics and Astronautics, Inc., 2007.

[56] M. Ventura and E. Wernimont. Advancements in High Concentration Hydrogen Peroxide Catalyst Beds. In *37th AIAA/ASME/SAE/ASEE Joint Propulsion Conference and Exhibit*, AIAA No. 01-34049, Salt Lake City, Utah, July 8-11 2001.

[57] S. Yuasa, O. Shimada, T. Imamura, T. Tamura, and K. Yamamoto. A Technique for Improving the Performance of Hybrid Rocket Engines. In *35th AIAA/ASME/SAE/ASEE Joint Propulsion Conference and Exhibit*, AIAA No. 99-2322, Los Angeles, CA, June 20-24 1999.

[58] P. Czysz and C. Bruno. *Future Spacecraft Propulsion System*. Springer Praxis, 2006.

[59] M.M. Micci and A.D. Ketsdever. *Micropropulsion for Small Spacecraft*, volume 187 of *AIAA*. Progress in Astronautics and Aeronautics, 2000.

[60] D.M. Gibbon et al. Energetic Green Propulsion for Small Spacecraft. In *37th AIAA/ASME/SAE/ASEE Joint Propulsion Conference*, AIAA No. 2001-3247, Salt Lake City, Utah, July 8-11 2001.

[61] L.T. DeLuca. *Problemi Energetici in Propulsione Aerospaziale*. Politecnico di Milano, 1998.

[62] G.A. Marxman and M. Gilbert. Turbulent Boundary Layer Combustion in the Hybrid Rocket. In *Ninth International Symposium on Combustion*, pages 371–383. Academic Press, 1963.

[63] G.A. Marxman, C.E. Woodrige, and R.J. Muzzy. Fundamentals of Hybrid Boundary Layer combustion. In *Heterogeneous Combustion*, AIAA No. 63-505, Palm Beach, Florida, December 11-13 1963.

[64] G.A. Marxman. Combustion in the Turbulent Boundary Layer on a Vaporizing Surface. In *Tehth Symposium (International) on Combustion*, pages 1337–1349. Combustion Inst., 1965.

[65] G.A. Marxman. Boundary-Layer Combustion in Propulsion. In *Eleventh Symposium (International) on Combustion*, pages 269–289. Combustion Inst., 1966.

[66] Virgin Galactic Homepage - http://www.virgingalactic.com, 2013.

[67] MarsScientific - http://marsscientific.com/, September 5 2013.

[68] ORPHEE Project - http://www.orphee–fp7–space.eu.

[69] SPARTAN Project - http://www.spartanproject.eu.

[70] S. Yuasa, K. Yamamoto, H. Hachiya, K. Kitagawa, and Y. Oowada. Development of a Small Sounding Rocket with a Swirling-Oxidizer-Type Engine. In 37*th AIAA/ASME/SAE/ASEE Joint Propulsion Conference and Exhibit*, AIAA No. 2001-3537, Salt Lake City, Utah, July 8-11 2001.

[71] K. Kitagawa, T. Mitsutani, T. Ro, and S. Yuasa. Effects of Swirling Liquid Oxygen Flow on Combustion of a Hybrid Rocket Engine. In 40*th AIAA/ASME/SAE/ASEE Joint Propulsion Conference and Exhibit*, Fort Lauderdale, Florida, July 11-14 2004.

[72] M. Motoe and T. Shimada. Large Eddy Simulation of Swirling Combustion Flow in a Modeled Hybrid Rocket with Wall Fuel Blowing. In 49*th AIAA/ASME/SAE/ASEE Joint Propulsion Conference and Exhibit*, AIAA No. 2013-3644, San Jose, CA, July 14-17 2013.

[73] C. Carmicino and A. Russo Sorge. Role of Injection in Hybrid Rocket Regression Rate Behavior. *Journal of Propulsion and Power*, 21(4):606–612, July-August 2005.

[74] C. Carmicino and A. Russo Sorge. Influence of a Conical Axial Injector on Hybrid Rocket Performance. *Journal of Propulsion and Power*, 22(5):984–995, September-October 2006.

[75] C. Carmicino. Acoustics, Vortex Shedding, and Low-Frequency Dynamics Interaction in an Unstable Hybrid Rocket. *Journal of Propulsion and Power*, 25(6):1322–1335, November-December 2009.

[76] M. Lazzarin, M. Faenza, F. Barato, N. Bellomo, A. Bettella, D. Pavarin, and M. Grosse. CFD Simulation of a Hybrid Rocket Motor with Liquid Injection. In 47*th AIAA/ASME/SAE/ASEE Joint Propulsion Conference and Exhibit*, AIAA No. 2011-5537, San Diego, CA, July 31 - August 3 2011.

[77] F. Barato, N. Bellomo, M. Faenza, M. Lazzarin, A. Bettella, and D. Pavarin. A Numerical Model to Analyze the Transient Behavior and Instabilities on Hybrid Rocket Motors. In 47*th AIAA/ASME/SAE/ASEE Joint Propulsion Conference and Exhibit*, AIAA No. 2011-5538, San Diego, CA, July 31 - August 3 2011.

[78] L. Casalino and D. Pastrone. Oxidizer Control and Optimal Design of Hybrid Rockets for Small Satellites. *Journal of Propulsion and Power*, 21(2):230–238, 2005.

[79] L. Casalino and D. Pastrone. Optimal Design and Control of Hybrid Rockets for Access to Space. In 41*st AIAA/ASME/SAE/ASEE Joint Propulsion Conference and Exhibit*, AIAA No. 2005-3547, Tucson, Arizona, July 11-13 2005.

[80] D. Pastrone, L. Casalino, M.R. Sentinella, and C. Carmicino. Acoustic Analysis of Hybrid Rocket Combustion Chambers. In 43*rd AIAA/ASME/SAE/ASEE Joint Propulsion Conference and Exhibit*, AIAA No. 2007-5368, Cincinnati, Ohio, July 8-11 2007.

[81] L.T. DeLuca, L. Galfetti, F. Maggi, G. Colombo, C. Paravan, A. Reina, P. Tadini, A. Sossi, and E. Duranti. Optical Time-Resolved Technique of Solid Fuels Burning for Hybrid Rocket Propulsion. In 47*th AIAA/ASME/SAE/ASEE Joint Propulsion Conference and Exhibit*, AIAA No. 2011-5753, San Diego, CA, July 31 - August 3 2011.

[82] C. Paravan, M. Viscardi, L.T. DeLuca, and A. Kazakov. Regression Rates and Anisotropy Effects in Hybrid Rockets Microburner. In 3*rd European Conference for Aeronautics and Space Sciences (EUCASS)*, Versailles, France, July 4-7 2009.

[83] P. Tadini, C. Paravan, F. Maggi, M. Boiocchi, G. Colombo, and L.T. DeLuca. Regression Rate Measurements in Lab-Scale Hybrid Burners. In 5*th European Conference for Aeronautics and Space Sciences (EUCASS)*, Munich, Germany, July 1-5 2013.

[84] F. Bosisio, H. Raina, A. Colombo, G. Colombo, L. Galfetti, and L.T. DeLuca. Setting up an Hybrid Microcombustor. In 3*rd AAAF On Board Energetic Equipment Conference*, Avignon, France, June 26-28 2006.

[85] L. Galfetti, L.T. DeLuca, P. Grassi, C. Paravan, V. Luoni, A. Bandera, G. Colombo, L. DeCillia, R. Sempio, and H. Raina. Combustion Behavior Investigation of Solid Fuels using a Micro-sized Hybrid Rocket Motor. Advancements in Energetic Material and Chemical Propulsion, edited by K.K. Kuo and K. Hori, Begel House, pp. 199-213, 2008.

[86] C. Paravan, M. Viscardi, L.T. DeLuca, and L. Prada Lopez. Anisotropy Effects in Hybrid Fuels Burning in a Micro-burner. In *XX AIDAA Congress*, Milan, Italy, June 29 - July 3 2009.

[87] L. Galfetti, L.T. DeLuca, C. Paravan, L. Merotto, and M. Boiocchi. Regression Rate and CCPs Measurement of Metallized Solid Fuels. In 8*th International Symposium on Chemical Propulsion (ISICP)*, Cape Town, South Africa, 2009.

[88] L.T. DeLuca, L. Galfetti, F. Maggi, G. Colombo, A. Reina, S. Dossi, D. Consonni, and M. Brambilla. Innovative Metallized Formulations for Solid or Hybrid Rocket Propulsion. In *International Autumn Seminar on Propellants, Explosives and Pyrotechnics (IASPEP)*, Nanchino, China, September 20-23 2011.

[89] HTPB R45M - http://www.rocketsrus.com/research-chemicals.html.

[90] M. Ventura and P. Mullens. The use of Hydrogen Peroxide for Propulsion and Power. In 35*th AIAA/ASME/SAE/ASEE Joint Propulsion Conference and Exhibit*, AIAA No. 99-2880, Los Angeles, CA, June 20-24 1999.

[91] S. Gordon and B.J. McBride. Computer Program for Calculation of Complex Chemical Equilibrium Composition and Applications I. Analysis. Reference Publication 1311, NASA, 1994.

[92] B.J. McBride and S. Gordon. Computer Program for Calculation of Complex Chemical Equilibrium Composition and Applications II. Users Manual and Program Description. Reference Publication 1311, NASA, 1996.

[93] M. Ventura and S. Yuan. Commercial Production and Use of Hydrogen Peroxide. In *American Institute of Aeronautics & Astronautics*, AIAA No. 00-36740, 2000.

[94] Encyclopedia Astronautica. N2O4/MMH - Propellant Combinations Database, http://www.astronautix.com/props/n204mmh.htm.

[95] Encyclopedia Astronautica. H2O2/UDMH - Propellant Combinations Database, http://www.astronautix.com/props/h202udmh.htm.

[96] M. Ventura, E. Wernimont, S. Heister, and S. Yuan. Rocket Grade Hydrogen Peroxide (RGHP) for use in Propulsion and Power Devices - Historical Discussion of Hazards. In 43*rd AIAA/ASME/SAE/ASEE Joint Propulsion Conference and Exhibit*, AIAA No. 2007-5468, Cincinnati, OH, July 8-11 2007.

[97] M. Ventura. Long Term Storability of Hydrogen Peroxide. In 41*st AIAA/ASME/SAE/ASEE Joint Propulsion Conference and Exhibit*, AIAA 2005-4551, Tucson, Arizona, July 10-13 2005.

[98] E. Perez. Vega. User's Manual Issue 3, Revision 0, Arianespace, March 2006.

[99] E. Perez. SOYUZ from the Guiana Space Centre. User's Manual Issue 1, Revision 0, Arianespace, June 2006.

[100] E. Perez. Ariane 5. User's Manual Issue 5, Revision 0, Arianespace, July 2008.

[101] P.N. Estey, D. Altman, and J.S. McFarlane. An Evaluation of Scaling Effects for Hybrid Rocket Motors. In *AIAA/SAE/ASME 27th Joint Propulsion Conference*, AIAA No. 91-2517, Sacramento, CA, June 24-26 1991.

[102] L.D. Strand, M.D. Jones, R.L. Ray, and N.S. Cohen. Characterization of Hybrid Rocket Internal Heat Flux and HTPB Fuel Pyrolisis. In *AIAA/SAE/ASME/ASEE 30th Joint Propulsion Conference and Exhibit*, AIAA No. 94-2876, Indianapolis, IN, June 27-29 1994.

[103] M.J. Chiaverini, N. Seryn, D.K. Johnson, Y.-C. Lu, K.K. Kuo, and G.A. Risha. Regression Rate Behavior of Hybrid Rocket Solid Fuel. *Journal of Propulsion and Power*, 16(1):125–132, 2000.

[104] M.J. Chiaverini, K.K. Kuo, A. Peretz, and G.C. Harting. Regression Rate and Heat Transfer Correlations for Hybrid Combustion. *Journal of Propulsion and Power*, 18(3), 2001.

[105] G.A. Risha, G.C. Harting, K.K. Kuo, A. Peretz, and D.E. Koch. Pyrolysis and Combustion of Solid Fuels in Various Oxidizing Enviroments. In 34*th AIAA/ASME/SAE/ASEE Joint Propulsion Conference and Exhibit*, Cleveland, OH, July 13-15 1998.

[106] P. George, S. Krishnan, M. Varkey, M. Ravindran, and L. Ramachandran. Fuel Regression Rate Enhancement Studies in HTPB/GOX Hybrid Rocket Motors. In 34*th AIAA/ASME/SAE/ASEE Joint Propulsion Conference and Exhibit*, AIAA No. 98-3188, Cleveland, OH, July 13-15 1998.

[107] L.D. Smoot and C.F. Price. Regression Rates of Nonmetalized Hybrid Fuel Systems. *AIAA Journal*, 3(8):1408–1413, 1965.

[108] L.D. Smoot and C.F. Price. Regression Rates of Metalized Hybrid Fuel Systems. *AIAA Journal*, 4(5):910–915, 1965.

[109] L.D. Smoot and C.F. Price. Pressure Dependence of Hybrid Fuel Regression Rates. *AIAA Journal*, 5(1):102–106, 1967.

[110] K.H. Shin, C. Lee, S.Y. Chang, and J.Y. Koo. The Enhancement of Regression Rate of Hybrid Rocket Fuel by Various Methods. In 43*rd AIAA Aerospace Science Meeting and Exhibit*, AIAA No. 2005-0359, Reno, NV, January 10-13 2005.

[111] F. Chang and V.K. Dhir. Turbulent Flow Field in Tangentially Injected Swirl Flows in Tubes. *International Journal of Heat and Fluid Flow*, 15:346–356, 1994.

[112] F. Chang and V.K. Dhir. Mechanisms of Heat Transfer Enhancement and Slow Decay of Swirl in Tubes using Tangential Injection. *International Journal of Heat and Fluid Flow*, 16:78–87, 1995.

[113] H. Ando et al. Development of a 5 kN-thrust Swirling-Oxidizer-Flow-Type Hybrid Rocket Engine. In *Tenth International Conference on Flow Dynamics (ICFD)*, Sendai, Japan, November 25-27 2013.

[114] S. Aso et al. Enhancement of Higher Regression Rate and Combustion Efficiency of Hybrid Rocket Engines by Multi-Section Swirl Injection Method. In *Tenth International Conference on Flow Dynamics (ICFD)*, Sendai, Japan, November 25-27 2013.

[115] C. Lee, Y. Na, and G. Lee. The Enhancement of Regression Rate of Hybrid Rocket Fuel by Helical Grain Configuration and Swirl Flow. In 41*st AIAA/ASME/SAE/ASEE Joint Propulsion Conference and Exhibit*, AIAA No. 2005-3906, Tucson, Arizona, July 10-13 2005.

[116] A. Karabeyoglu. Evaluation of Fuel Additives for Hybrid Rockets and SFRJ Systems. In *New Energetic Materials and Propulsion Techniques for Space Exploration*, pages 442–480, Milan, Italy, June 9 2014. Politecnico di Milano.

[117] H.R. Lips. Metal Combustion in High Performance Hybrid Rocket Propulsion Systems. In 12*th AIAA/SAE Propulsion Conference*, AIAA No. 76-640, Palo Alto, CA, July 26-29 1976.

[118] L.D. Strand, R.L. Ray, F.A. Anderson, and N.S. Cohen. Hybrid Rocket Fuel Combustion and Regression Rate Study. In 28*th AIAA/ASME/SAE/ASEE Joint Propulsion Conference and Exhibit*, AIAA No. 92-3302, Nashville, TN, July 6-8 1992.

[119] B. Natan and Gany. A. Ignition and Combustion of Boron in the Flowfiled of a Solid Fuel Ramjet. *Journal of Propulsion*, 7(1):37–43, 1991.

[120] Gany. A. Comprehensive Consideration of Boron Combustion in Airbreathing Propulsion. In 42*nd AIAA/ASME/SAE/ASEE Joint Propulsion Conference and Exhibit*, AIAA No. 2006-4567, Sacramento, CA, July 9-12 2006.

[121] P.A. Storozhenko, S.L. Guseinov, and S.I. Malashin. Nanodispersed Powders: Synthesis Methods and Practical Applications. *Nanotechnology in Russia*, 4(05-06):262–274, 2009.

[122] A.P. Ilyin, A.A. Gromov, and G.V. Yablunovski. Reactivity of Aluminum Powders. *Combustion Explosion and ShockWaves*, 37(4):418–422, 2001.

[123] G.A. Risha, A. Ulas, E. Boyer, S. Kumar, and K.K. Kuo. Combustion of HTPB-based Solid Fuels Containing Nano-sized Energetic Powder in a Hybrid Rocket Motor. In 37*th AIAA/ASME/SAE/ASEE Joint Propulsion Conference and Exhibit*, Salt Lake City, Utah, July 8-11 2001.

[124] C. Paravan. *Ballistic of Innovative Solid Fuel Formulations for Hybrid Rocket Engines*. PhD thesis, Politecnico di Milano, Milano, 2012.

[125] B.D. Larson, E. Boyer, T. Wachs, K.K. Kuo, J.D. DeSain, T.J. Curtiss, and B. Brady. Characterization of the Performance of Paraffin/$LiAlH_4$ Solid Fuels in a Hybrid Rocket System. In 47*th AIAA/ASME/SAE/ASEE Joint Propulsion Conference and Exhibit*, AIAA No. 2011-5822, San Diego, CA, July 31 - August 3 2011.

[126] J.D. DeSain, T.J. Curtiss, K. Metzler, and B. Brady. Testing Hypergolic Ignition of Paraffin Wax/$LiAlH_4$ Mixtures. In 47*th AIAA/ASME/SAE/ASEE Joint Propulsion Conference and Exhibit*, AIAA No. 2011-6636, San Diego, CA, July 31 - August 3 2011.

[127] R. Humble. Fuel Performance Enhancements for Hybrid Rockets. In *36th AIAA/ASME/SAE/ASEE Joint Propulsion Conference and Exhibit7*, AIAA No. 2000-3437, Huntsville, Alabama, July 16-19 2000.

[128] M. Calabro, L.T. DeLuca, L. Galfetti, and C. Perut. Advanced Hybrid Solid Fuels. In 58*th International Astronautical Congress*, number IAC-07-C4.2.09, Hyderabad, India, 2007.

[129] F. Maggi, G. Gariani, L. Galfetti, and L.T. DeLuca. Theoretical Analysis of Hydrides in Solid and Hybrid Rocket Propulsion. *Journal of Hydrogen Energy*, 37:1760–1769, 2012.

[130] A. Karabeyoglu, D. Altman, and B.J. Cantwell. Combustion of Liquefying Hybrid Propellants: Part 1, General Theory. *Journal of Propulsion and Power*, 18(3), 2002.

[131] A. Karabeyoglu and D. Altman. Combustion of Liquefying Hybrid Propellants: Part 2, Stability of Liquid Films. *Journal of Propulsion and Power*, 18(3), 2002.

[132] A. Karabeyoglu. Homologous Series of N-Alkanes as Hybrid Rocket Fuels. In *Tenth International Conference on Flow Dynamics (ICFD)*, Sendai, Japan, November 25-27 2013.

[133] M. Kobald and S. Schlechtriem. Investigation of Different Hybrid Rocket Fuels in a 2D Slab Burner with Optical Techniques. In *Tenth International Conference on Flow Dynamics (ICFD)*, Sendai, Japan, November 25-27 2013.

[134] Y. Wada, K. Seki, N. Kato, and K. Hori. Study on Mechanical Property of Low Melting Temperature Thermoplastic Fuel. In *Tenth International Conference on Flow Dynamics (ICFD)*, Sendai, Japan, November 25-27 2013.

[135] C. Paravan et al. Time-Resolved Regression Rate of Innovative Hybrid Solid Fuel Formulations. In *Progress in Propulsion Physics*, volume 4, pages 75–96, Moscow, Russia, 2013. Torus Press.

[136] A. Hahma, Gany. A., and K. Palovuori. Combustion of Activated Aluminum. *Combustion Flame*, 145(3):464–480, 2006.

[137] G.A. Risha, B. Evans, E. Boyer, R.B. Wehrman, and K.K. Kuo. Nano-sized Aluminum, and Boron-based Solid Fuel Characterization in a Hybrid Rocket Engine. In 39*th AIAA/ASME/SAE/ASEE Joint Propulsion Conference and Exhibit*, AIAA No. 2003-4593, Huntsville, Alabama, July 20-23 2003.

[138] Q.S.M. Kwok, R.C. Fouchard, A. Turcotte, P.D. Lightfoot, R. Bowes, and D.E.G. Jones. Characterization of Aluminum Nanopowder Compositions. *Propellants, Explosives, Pyrotechnics*, 27(4):229–240, 2002.

[139] A. Sossi, E. Duranti, M. Manzoni, C. Paravan, L.T. DeLuca, A.B. Vorozhtsov, M.I. Lerner, N.G. Rodkevich, A.A. Gromov, and N. Savin. Combustio of HTPB-based Solid Fuels Loaded with Coated Nanoaluminum. *Combustion Science and Technology*, 185(1):17–36, 2013.

[140] C. Paravan, A. Reina, A. Frosi, and L.T. DeLuca. Nano-sized Aluminum for Solid Fuel Regression Rate Enhancement. In 5*th European Conference for Aeronautics and Space Sciences (EUCASS)*, Munich, Germany, July 1-5 2013.

[141] S. Cerri, M.A. Bohn, K. Menke, and L. Galfetti. Ageing Characteristics of HTPB-based Rocket Propellant Formulations. *Cent. Eur. J. Energ. Mater.*, 6(2):149–165, 2009.

[142] L.T. DeLuca, L. Galfetti, F. Bosisio, H. Raina, F. Maggi, and G. Colombo. An Hybrid Micro–combustor for Regression Rate Measurements. In 57*th International Astronautical Congress (IAC)*, Valencia, Spain, October 2-6 2006.

[143] M. Manzoni. Experimental Investigation and Modeling of Solid Fuel Regression Rate for Hybrid Propulsion. Master's thesis, Dept. of Science and Aerospace Technologies, Politecnico di Milano, 2012.

[144] C. Paravan, M. Manzoni, G. Rambaldi, and L.T. DeLuca. Quasi-Steady and Transient Burning of Hybrid Fuels in a Lab-scale Burner by an Optical Technique. *International Journal of Energetic Materials and Chemical Propulsion*, 12(5):385–410, 2013.

[145] L. Fanton, C. Paravan, and L.T. DeLuca. Testing and Modeling Fuel Regression Rate in a Miniature Hybrid Burner. *International Journal of Aerospace Engineering*, 2012:15, ID 673838 2012.

[146] J. Carissimi, G. Gerhardinger, P. Tadini, and L.T. DeLuca. Indagine Preliminare sulle Prestazioni Balistiche ottenibili tramite l'Iniezione di Flusso di Ossidante Swirl in un Combustore Ibrido. Technical report, Dept. of Science and Aerospace Technologies, SPLab, Politecnico di Milano, 2011.

[147] T. Tamura, S. Yuasa, and K. Yamamoto. Effects of Swirling Oxidizer Flow on Fuel Regression Rate of Hybrid Rocket. In 35*th AIAA/ASME/SAE/ASEE Joint Propulsion Conference and Exhibit*, AIAA No. 99-2323, Los Angeles, CA, June 20-24 1999.

[148] R. Wilkinson, K. Hart, and R. Day. Proof-of-Concept Testing of a Sustained Vortex-Flow Configuration for Hybrid Rocket Motors. In 46*th AIAA/ASME/SAE/ASEE Joint Propulsion Conference and Exhibit*, AIAA No. 2010-6782, Nashville, TN, July 25-28 2010.

[149] A.K. Gupta, D.G. Lilley, and N. Syred. *Swirl Flows*. Abacus Press, Tunbridge Wells (Kent), 1984.

[150] M. Masugi, T. Ide, S. Yuasa, T. Sakurai, N. Shiraishi, and T. Shimada. Visualization of Flames in Combustion Chamber of Swirling-Oxidizer-Flow-Type Hybrid Rocket Engines. In 46*th AIAA/ASME/SAE/ASEE Joint Propulsion Conference and Exhibit*, AIAA No. 2010-6546, Nashville, TN, July 25-28 2010.

[151] F. Maggi et al. Activated Aluminum Powders for Space Propulsion. *Submitted for publication to Powder Technology*, 2013.

[152] P. Tadini, C. Paravan, and L.T. DeLuca. Ballistic Characterization of Metallized HTPB-based Fuels with Swirling Oxidizer in Lab-Scale Hybrid Burner. In *9th High Energy Materials (HEMS)*, Sagamihara, Japan, October 7-9 2013.

[153] J.L. de la Fuente and O. Rodriguez. Dynamic Mechanical Study on the Thermal Aging of a Hydroxyl-terminated Polybutadiene-base Energetic Composite. *Journal of Applied Polymer Science*, 87(2397-2405), 2003.

[154] F. Maggi. Preparazione e caratterizzazione meccanica di un polimero a base di HTPB caricato con $caco_3$. Technical report, Dept. of Science and Aerospace Technologies, Politecnico di Milano, 2005.

[155] W.F. Smith. *Scienza e Tecnologia dei Materiali*. McGraw Hill Italia, italian edition of "foundation of materials science and engineering 2/e", ISBN 88-386-0709-5 edition, April 1995.

[156] S. Cerri, A. Bohn, K. Menke, and L. Galfetti. Ageing Behavior of HTPB Based Rocket Propellant Formulations. *Central European Journal of Energetic Materials*, 6(2):149–165, 2009.

[157] M.A. Bohn. Prediction of In-Service Time Period of Three Differently Stabilized Single Base Propellants. *Wiley InterScience, Propellants Explos. Pyrotech*, 34:252–266, 2009.

[158] L.D. Villar, T. Cicaglioni, M.F. Diniz, F.K. Takahashi, and L.C. Rezend. Thermal Aging of HTPB/IPDI-Based Polyurethane as a Function of NCO/OH Ratio. *Material Research*, 14(3):372–375, 2011.

[159] P. Tadini. Hydroxyl-Terminated Polybutadiene Characterization aftet Thermal Accelerated Aging. Technical report, Dept. of Science and Aerospace Technologies, Politecnico di Milano, 2012.

[160] G.P. Sutton. *Rocket Propulsion Elements*. John Wiley and Sons, Inc., New York, 6th edition, 1992.

[161] T. Stevens and H.M. Hobart. *Steam Turbine Engineering*. MacMillan Company, 1st edition, 1906.

[162] K.N.C. Bray. Simplified Sudden-freezing Analysis for Nonequilibrium Nozzle Flows. *ARS Journal*, 31:831–834, 1961.

[163] K.N.C. Bray. Chemical Reactions in Supersonic Nozzle Flows. *International Symposium on Combustion*, 9(1):770–784, 1963.

[164] L.T. DeLuca, M. Lavagna, F. Maggi, P. Tadini, C. Pardini, L. Anselmo, M. Grassi, D. Pavarin, A. Francesconi, F. Branz, S. Chiesa, N. Viola, U. Tancredi, and C. Bonnal. Large Debris Removal in LEO based on Hybrid Propulsion. In *XXII Italian Association of Aeronautics and Astronautics (AIDAA)*, Naples, Italy, September 9-12 2013.

[165] P. Tadini, F. Maggi, M. Lavagna, L.T. DeLuca, M. Grassi, C. Pardini, L. Anselmo, A. Francesconi, N. Viola, and U. Tancredi. Large-Debris Active Removal Challenge: the Hybrid Propulsion Approach. In 57*th Symposium on Space Science and Technology*, Yonago, Japan, October 9-11 2013.

[166] P. Tadini, U. Tancredi, M. Grassi, L. Anselmo, C. Pardini, F. Branz, A. Francesconi, F. Maggi, M. Lavagna, L.T. DeLuca, N. Viola, S. Chiesa, V. Trushlyakov, and T. Shimada. Multi-Active Removal of Large Abandoned Rocket Bodies by Hybrid Propulsion Module. In *Tenth International Conference on Flow Dynamics (ICFD)*, Sendai, Japan, November 25-27 2013.

[167] J.D. Jr. Anderson. *Fundamentals of Aerodynamics*. Aeronautical and Aerospace Engineering. McGraw-Hill, 4th edition, 2005.

[168] T. Shimada. Hybrid Rocket Engine Internal Flow Simulation - Quasi 1D Modeling. Consideration on elements number conservation, 2012.

[169] T. Shimada, M. Hanzawa, T. Morita, T. Kate, T. Yoshikawa, and Y. Wada. Stability Analysis of Solid Rocket Motor Combustion by Computational Fluid Dynamics. *AIAA Journal*, 46(4):947–957, April 2008.

[170] G. Lengellé, B. Fourest, J.C. Godon, and C. Guin. Condensed Phase Behavior and Ablation Rate of Fuels for Hybrid Propulsion. In *AIAA/SAE/ASME/ASEE 29th Joint Propulsion Conference and Exhibit*, Monterey, CA, June 28-30 1993.

[171] D.R. Greatrix. Regression Rate Estimation for Standard-flow Hybrid Rocket Engines. *Aerospace Science and Technology*, 13:358–363, 2009.

[172] R.B. Shanks and M.K. Hudson. The Design and Control of a Labscale Hybrid Rocket Facility for Spectroscopy Studies. In *AIAA/SAE/ASME/ASEE 30th Joint Propulsion Conference and Exhibit*, AIAA No. 94-3016, Indianapolis, IN, June 27-29 1994.

[173] R.B. Bird, W.E. Stewart, and E.N. Lightfoot. *Transport Phenomena*. Jonh Wiley & Sons, 2nd edition, 2002.

[174] K.E. Atkinson. *An Introdution to Numerical Analysis*. John Wiley & Sons, Inc., New York, 2nd edition, 1989.

[175] E. Farbar, J. Louwers, and T. Kaya. Investigation of Metallized and Nonmetallized Hydroxyl Terminated Polybutadiene/Hydrogen Peroxide Hybrid Rockets. *Journal of Propulsion and Power*, 23(2):476–486, 2007.

[176] X. Fang, Y. Xu, and Z. Zhou. New Correlations of Single-Phase Friction Factor for Turbulent Pipe Flow and Evaluation of Existing Single-Phase Friction Factor Correlations. *Nuclear Engineering and Design*, 241:897–902, 2011.

[177] D. Brkíc. New Explicit Correlations for Turbulent Flow Friction Factor. *Nuclear Engineering and Design*, 241:4055–4059, 2011.

[178] D. Bianchi and F. Nasuti. Numerical Analysis of Nozzle Material Thermochemical Erosion in Hybrid Rocket Engines. In *AIAA/SAE/ASME/ASEE* 48*th Joint Propulsion Conference and Exhibit*, AIAA No. 2012-3809, Atlanta, Georgia, July 30 - August 1 2012.

[179] Wikipedia. Ultimate tensile strength, April 2014.

[180] A.K. Bhowmick. *Current Topics in Elastomers Research*. CRC Press, 2008.

[181] E. Maasa. *Costruzioni di Macchine*, volume 2. Masn Ittalia Editori, Milano, 1985.

[182] T. Shimada. Numerical Analysis of Non-Linear Scalar Equations. Numerical Tutorial: High Order Accuracy MUSCL scheme, 2012.

[183] C. Berthone. Stability of the MUSCL Schemes for the Euler Equations. *Comm. Math. Sci.*, 3(2):133–157, 2005.

[184] Y. Wada and M.-S. Liou. A Flux Splitting Scheme with High-Resolution and Robustness for Discontinuities. In 32*nd Aerospace Sciences Meeting* & *Exhibit*, AIAA No. 94-0083, Reno, NV, January 10-13 1994.

[185] E. Süli and D. Mayers. *An Introduction to Numerical Analysis*. Cambridge University Press, 2003.

[186] P.L. Roe. Approximate Riemann Solvers, Parameter Vectors, and Difference Schemes. *Journal of Computational Physics*, 43:357–372, 1981.

[187] F.A. Warren. *Solid Propellant Technology*. AIAA Selected Reprint Series, New York, NY, USA, 1970.

[188] S.S. Penner and J. Ducarme. *The Chemistry of Propellants*. AGARD Combustion and Propulsion Panel, Pergamon Press, 1960.

Part i.

Appendix

A HPM DESIGN ANALYSIS

In this chapter further space design net graphs are presented (with reference to Section 8.2). A target mass of 1400 kg (Cosmos-3M 2nd stage) on a circular orbit at a mean altitude of about 767 km is assumed. The controlled reentry is performed by means of a single boost maneuver able to lower the perigee below 60 km with a FPA <?1.5° at an interface of 120 km, requiring a velocity increment of 200 m/s. The mass supposed for the ADR platform is of 270 kg, thus obtaining a total payload for the HPM of 1670 kg. To the latter, the dry mass of the RCS systems must be added: a low-thrust system which provides 2000 impulses up to 3 N and a high-thrust system with 200 impulses up to 50 N (~ 8 kg of dry mass for such configuration). As oxidizer HTP(90%) is considered while HTPB as solid fuel. Ideal efficiency (~ 1 with adiabatic conditions) of the catalyst injection system is assumed and the final performance are corrected as described in Sections 7.1.2 and 7.2. The erosion of nozzle throat is evaluated every 1.0 s of combustion.

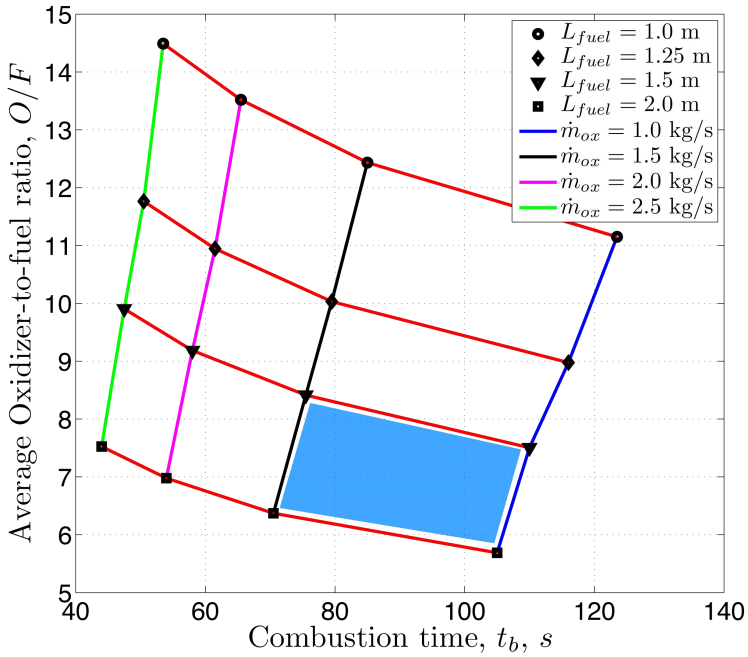

Figure 81.: HPM space design net: O/F vs. burn time. L_f between 1.0 and 2.0 m, $\dot{m}_{ox}$ between 1.0 and 2.5 kg/s.

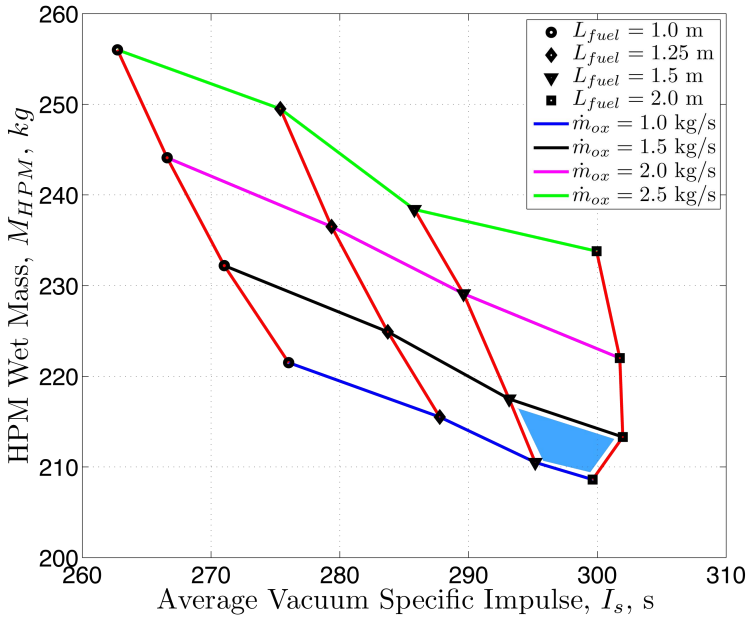

Figure 82.: HPM space design net: HPM wet mass vs. average vacuum specific impulse. L_f between 1.0 and 2.0 m, $\dot{m}_{ox}$ between 1.0 and 2.5 kg/s.

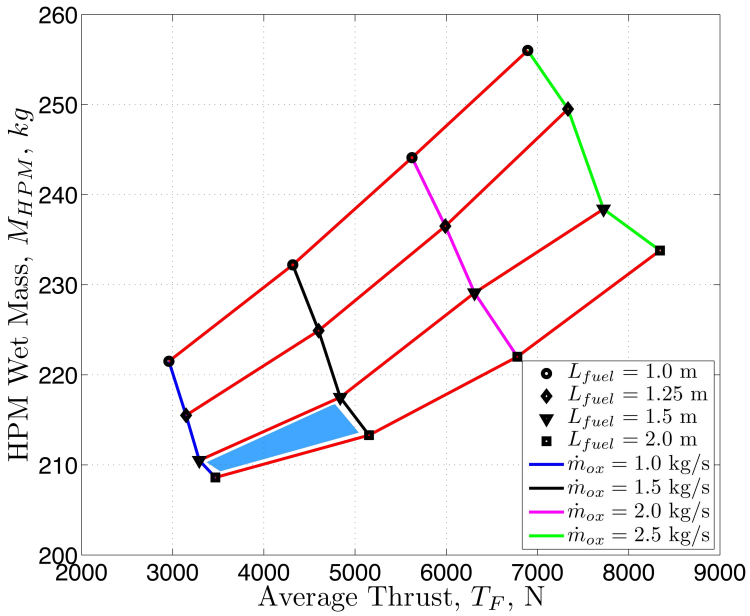

Figure 83.: HPM space design net: HPM wet mass vs. average thrust. L_f between 1.0 and 2.0 m, $\dot{m}_{ox}$ between 1.0 and 2.5 kg/s.

B HPM - COSMOS-3M 2ND STAGE

The performance evaluated by HRE code for Cosmos-3M 2nd stage removal are presented (with reference to Section 8.3.1). The disposal assumes a velocity increment of about 220 m/s (200 + 10% m/s) necessary for a single boost maneuver to lower the perigee below 60 km with a FPA $< -1.5°$ at an interface of 120 km.

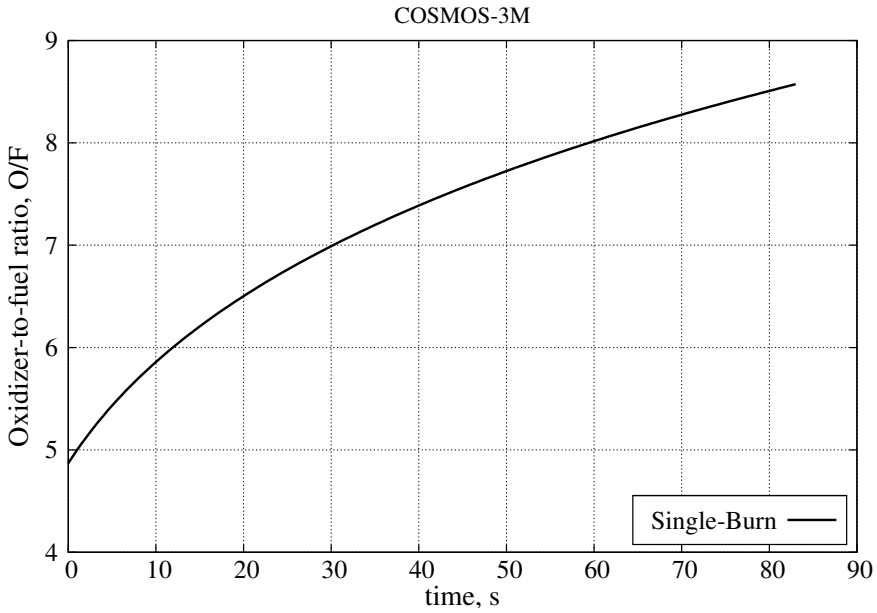

Figure 84.: HPM for active removal of Cosmos-3M 2nd stage. Single-burn disposal maneuver: oxidizer-to-fuel ratio.

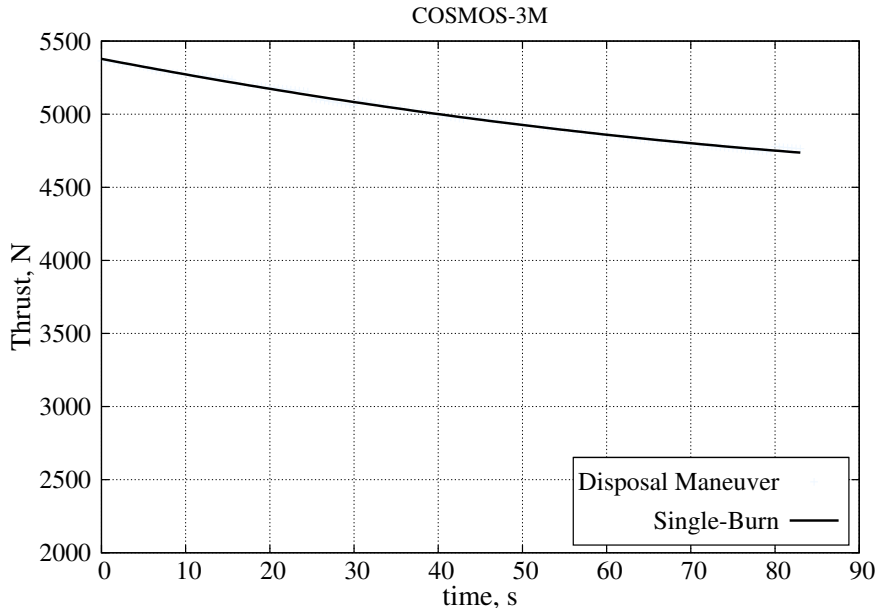

Figure 85.: HPM for active removal of Cosmos-3M 2nd stage. Single-burn disposal maneuver: thrust.

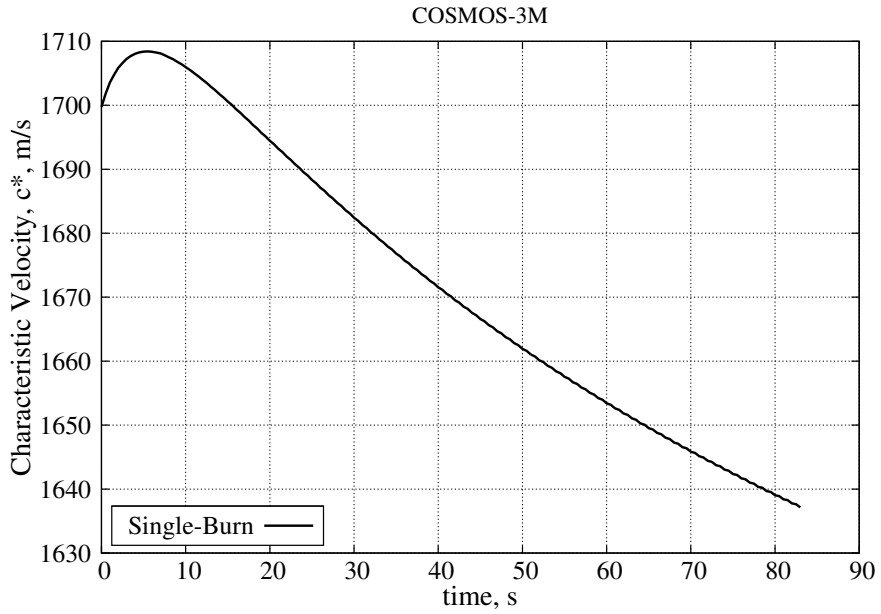

Figure 86.: HPM for active removal of Cosmos-3M 2nd stage. Single-burn disposal maneuver: characteristic velocity.

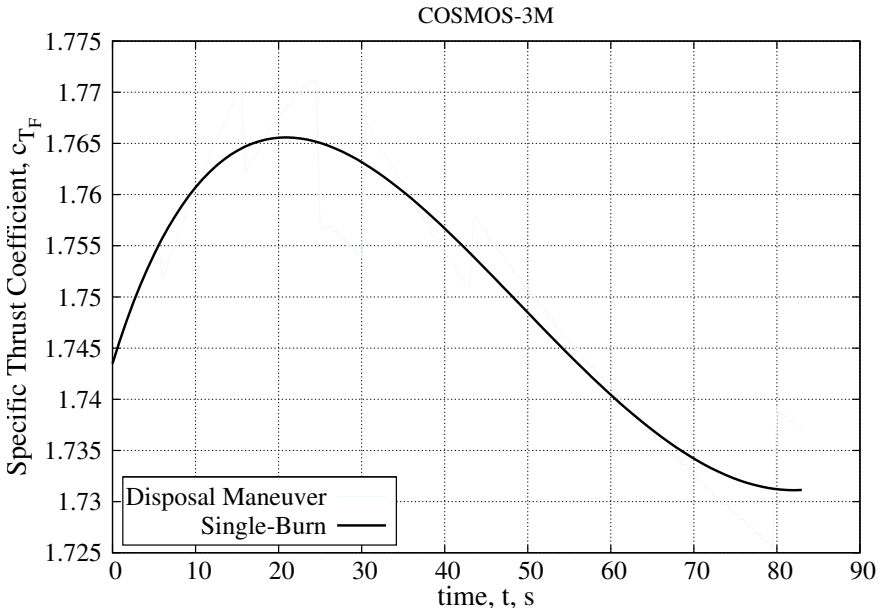

Figure 87.: HPM for active removal of Cosmos-3M 2nd stage. Single-burn disposal maneuver: thrust coefficient.

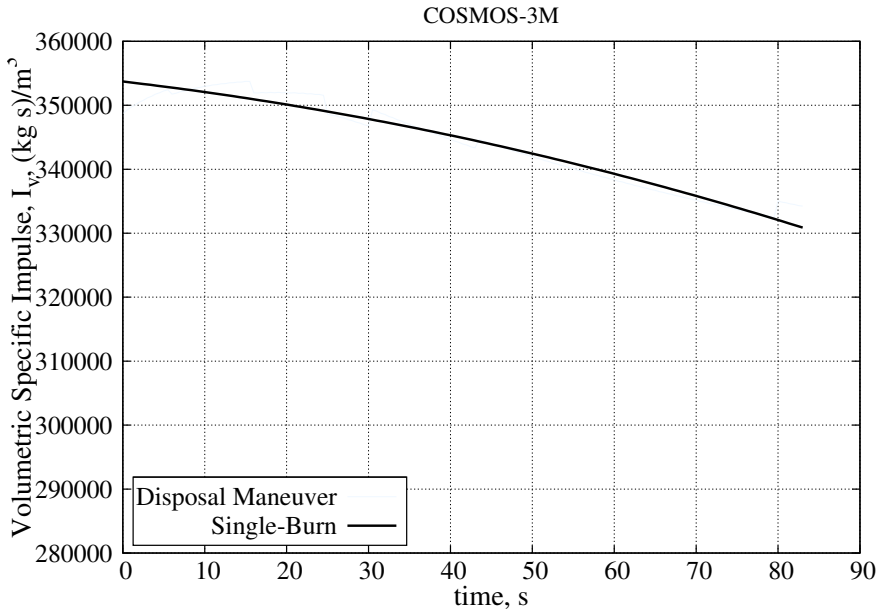

Figure 88.: HPM for active removal of Cosmos-3M 2nd stage. Single-burn disposal maneuver: volumetric specific impulse.

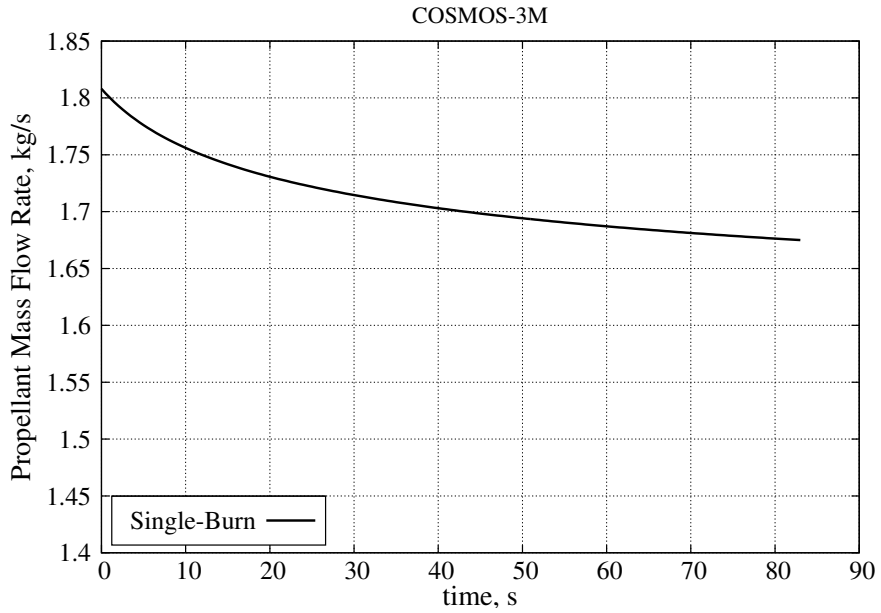

Figure 89.: HPM for active removal of Cosmos-3M 2nd stage. Single-burn disposal maneuver: propellant mass flow rate.

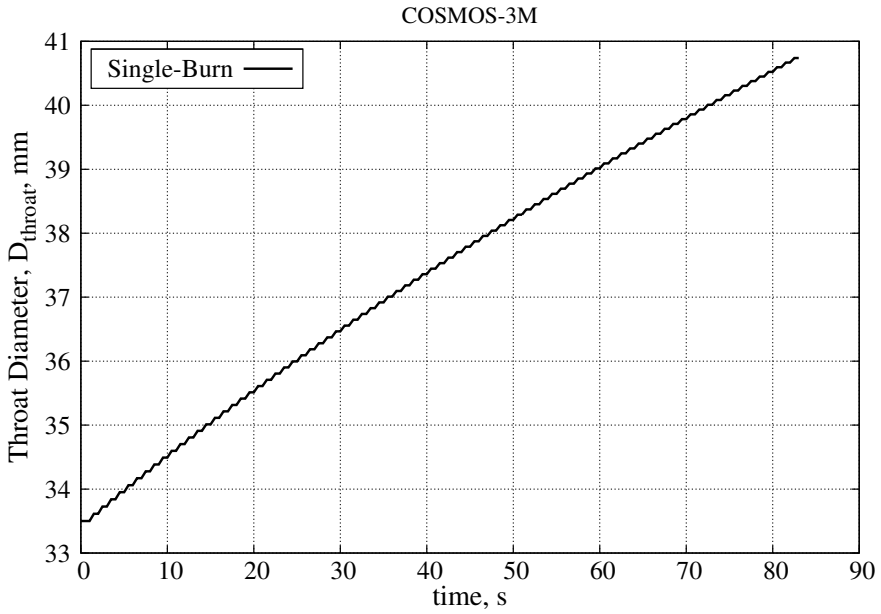

Figure 90.: HPM for active removal of Cosmos-3M 2nd stage. Single-burn disposal maneuver: throat diameter.

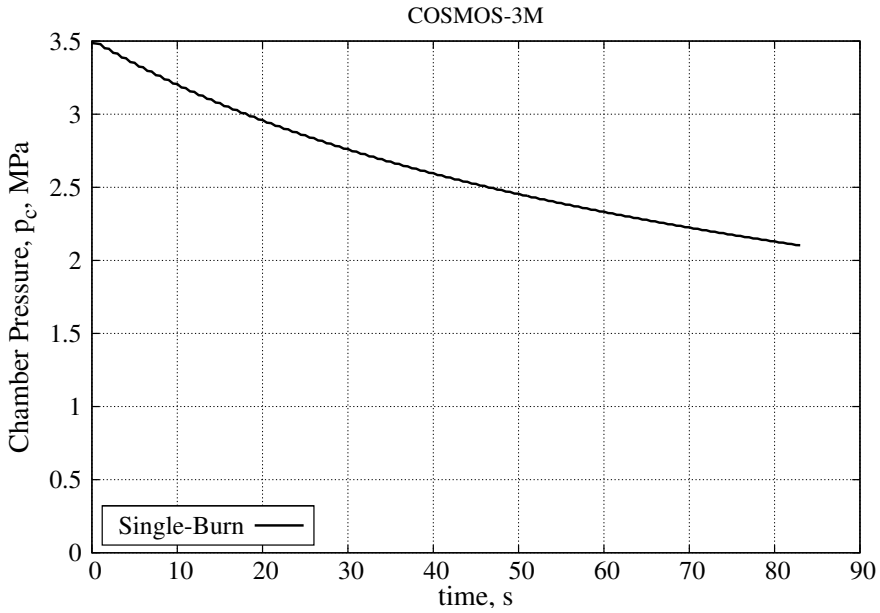

Figure 91.: HPM for active removal of Cosmos-3M 2nd stage. Single-burn disposal maneuver: chamber pressure.

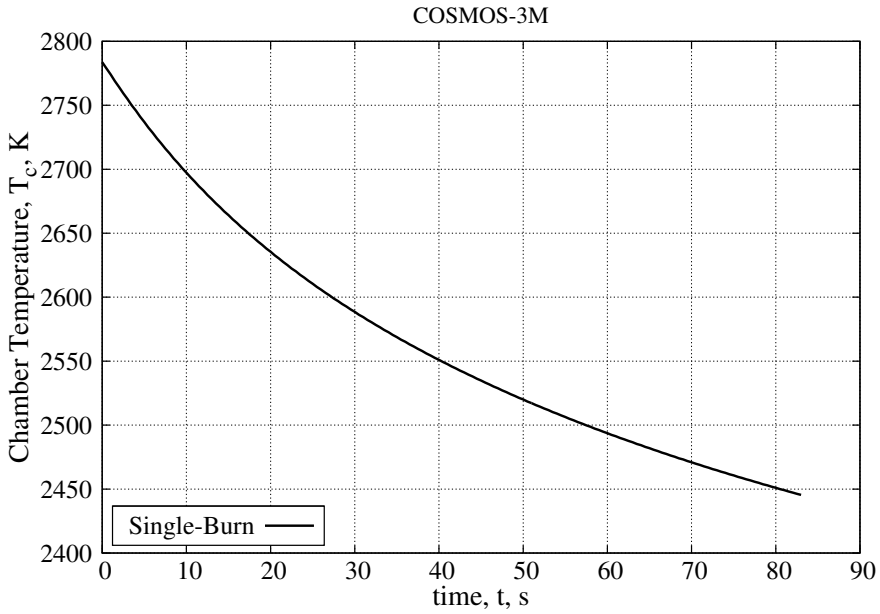

Figure 92.: HPM for active removal of Cosmos-3M 2nd stage. Single-burn disposal maneuver: chamber mean temperature.

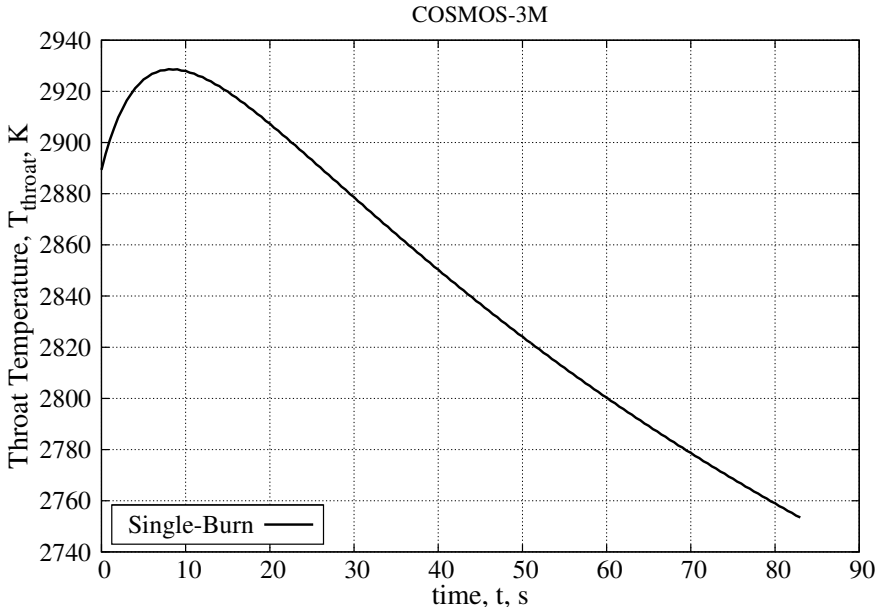

Figure 93.: HPM for active removal of Cosmos-3M 2nd stage. Single-burn disposal maneuver: throat temperature.

C | HPM - ENVISAT

The performance evaluated by HRE code for Envisat removal are presented for two mission approaches:

1. *single-burn* to lower the perigee below 60 km with a FPA<-1.5° at an interface of 120 km. ΔV of about 200 m/s;
2. *multi-burn* to lower the perigee by means of two consecutive elliptical transfer orbits, the second burn starts in correspondence of the first transfer orbit perigee. Total ΔV of about 200 m/s.

The results achieved are following compared (with reference to Section 8.3.2).

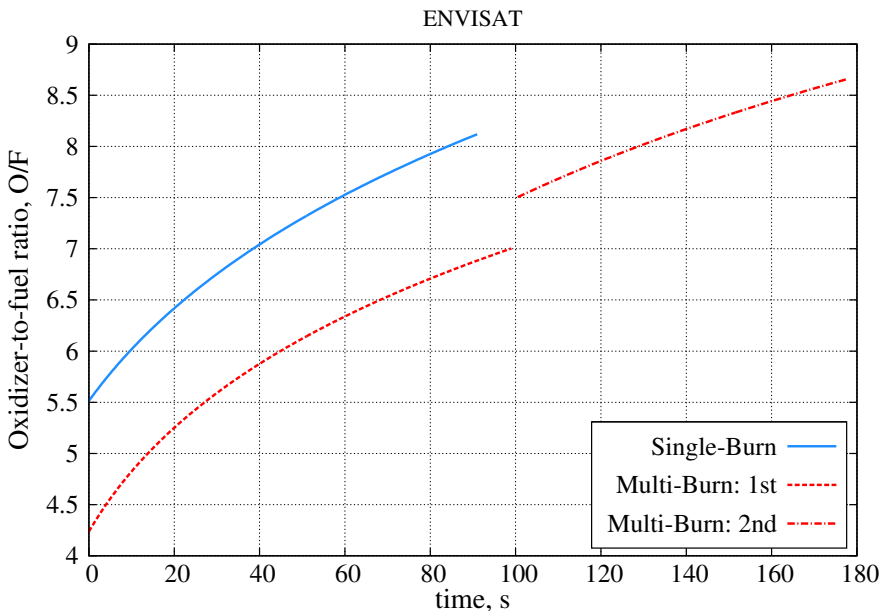

Figure 94.: HPM for active removal of Envisat. Single-burn vs. Multi-burns disposal maneuvers: oxidizer-to-fuel ratio.

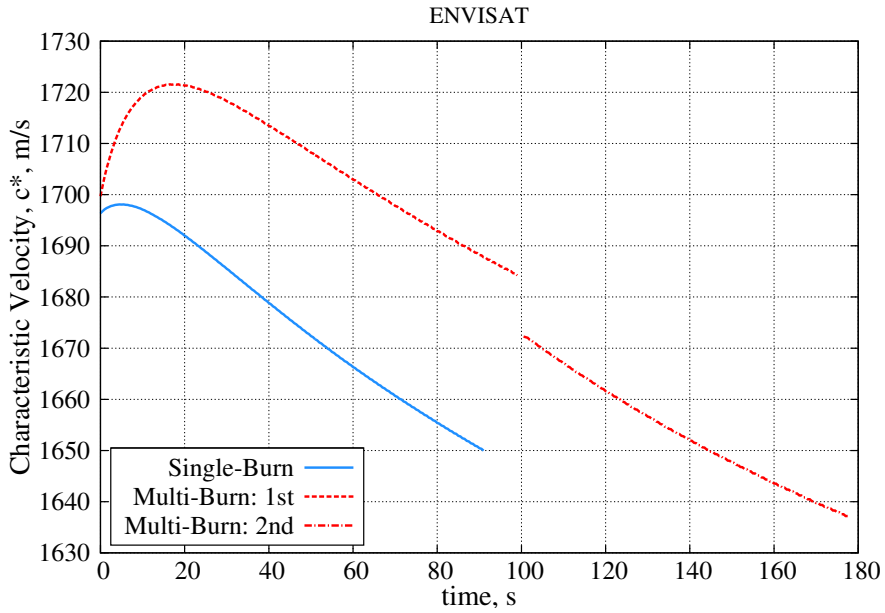

Figure 95.: HPM for active removal of Envisat. Single-burn vs. Multi-burns disposal maneuvers: characteristic velocity.

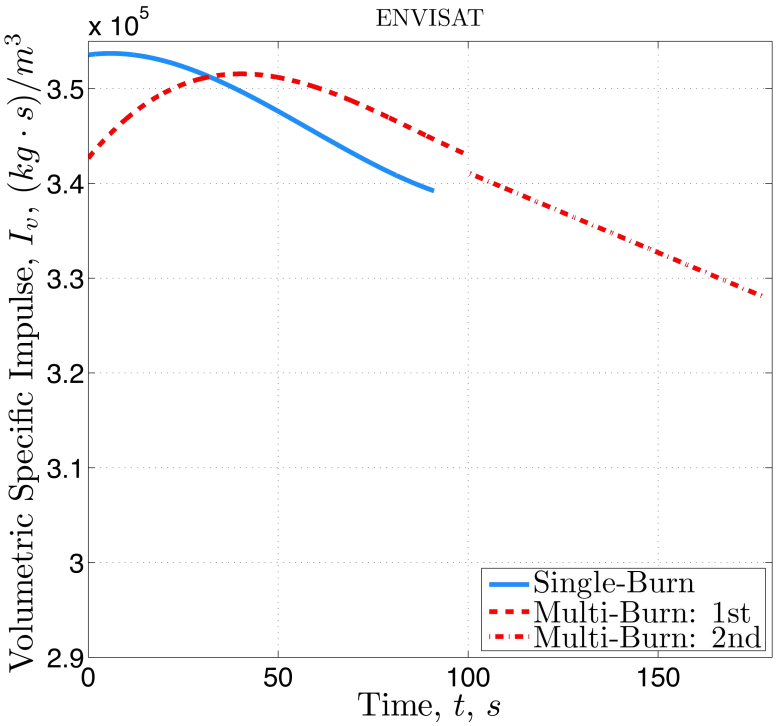

Figure 96.: HPM for active removal of Envisat. Single-burn vs. Multi-burns disposal maneuvers: thrust coefficient.

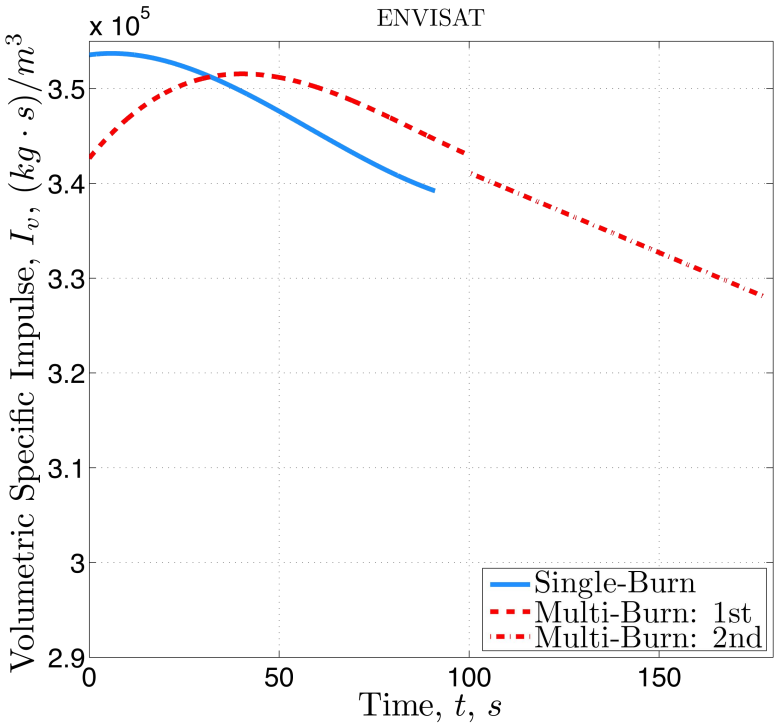

Figure 97.: HPM for active removal of Envisat. Single-burn vs. Multi-burns disposal maneuvers: volumetric specific impulse.

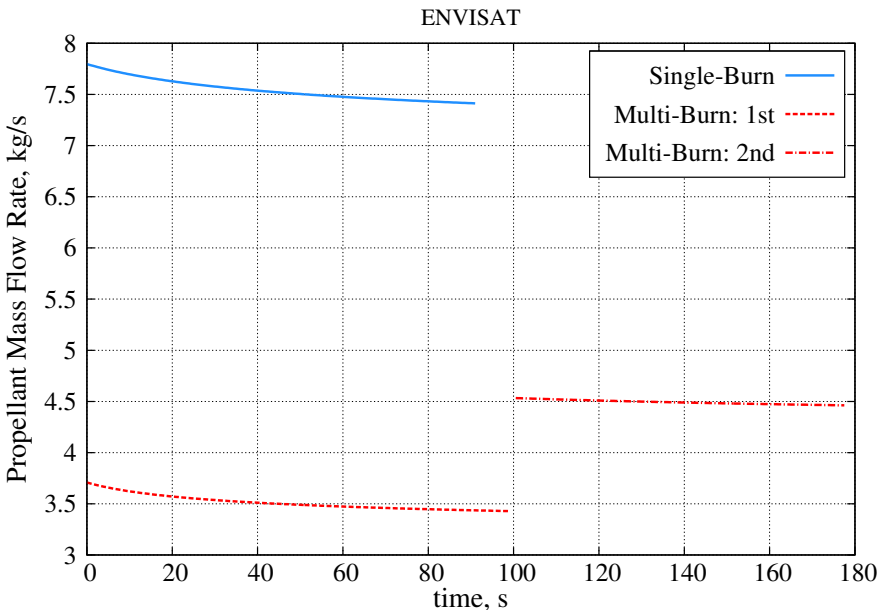

Figure 98.: HPM for active removal of Envisat. Single-burn vs. Multi-burns disposal maneuvers: propellant mass flow rate.

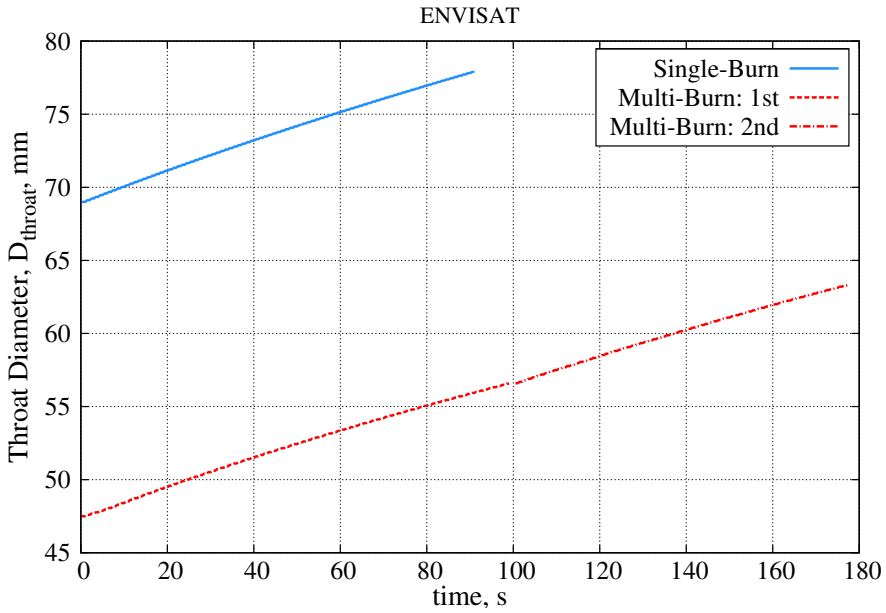

Figure 99.: HPM for active removal of Envisat. Single-burn vs. Multi-burns disposal maneuvers: throat diameter.

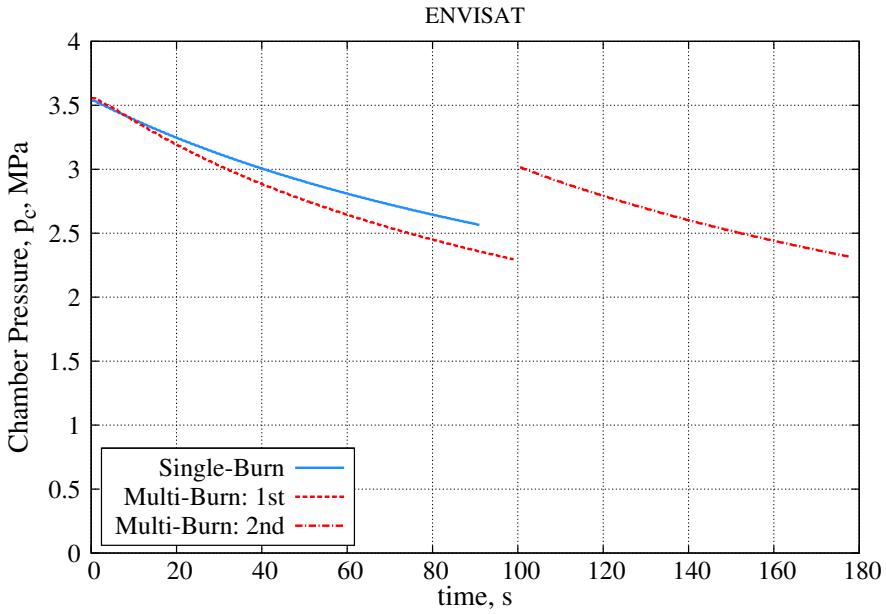

Figure 100.: HPM for active removal of Envisat. Single-burn vs. Multi-burns disposal maneuvers: chamber pressure.

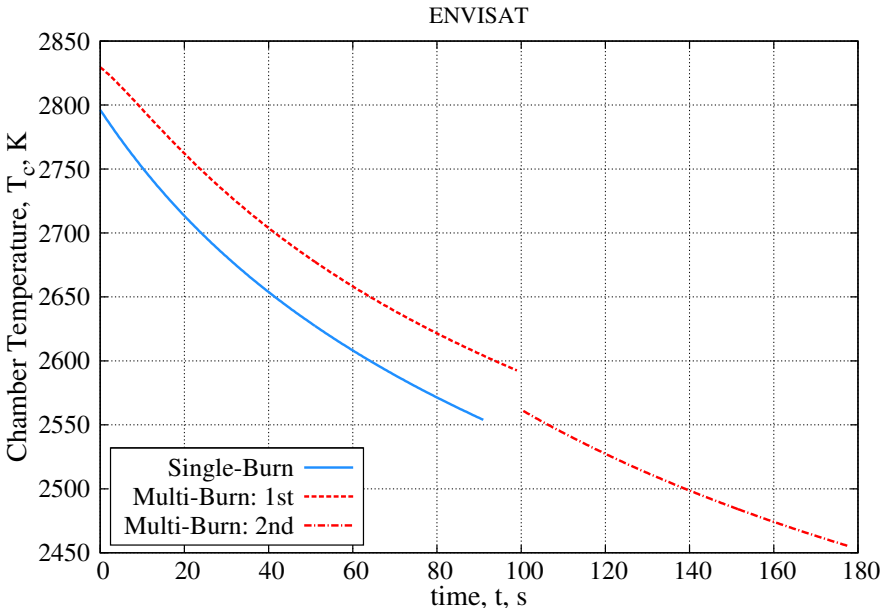

Figure 101.: HPM for active removal of Envisat. Single-burn vs. Multi-burns disposal maneuvers: chamber mean temperature.

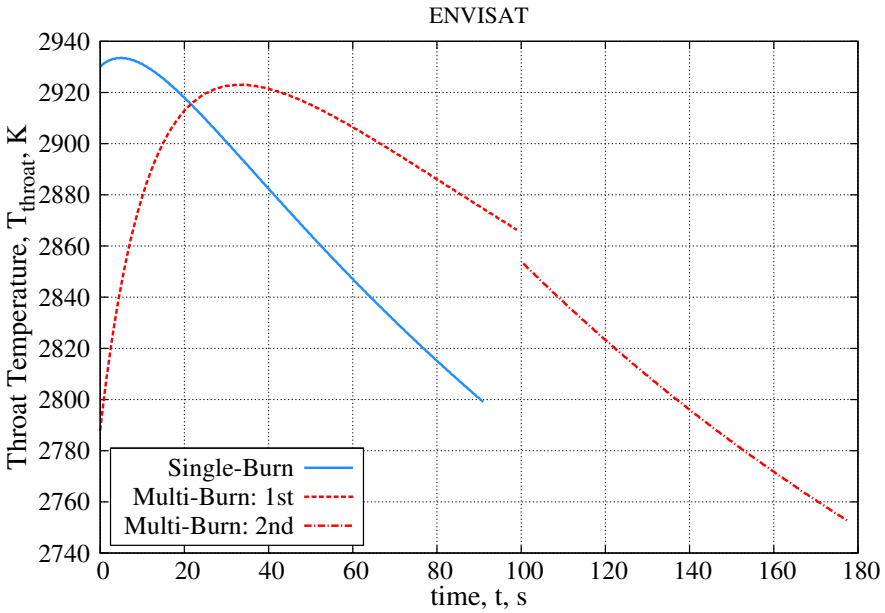

Figure 102.: HPM for active removal of Envisat. Single-burn vs. Multi-burns disposal maneuvers: throat temperature.

D | COSMOS-3M - DISPOSAL TRAJECTORY

In this chapter, the trajectory analysis results achieved for the disposal of the system DeoKit-Cosmos-3M are presented (with reference to Section 8.3.1). The simulation code, based on Simulink®, was developed by U. Tancredi, in the frame of the collaboration project on the ADR missions by Hybrid Propulsion Modules [17, 166].

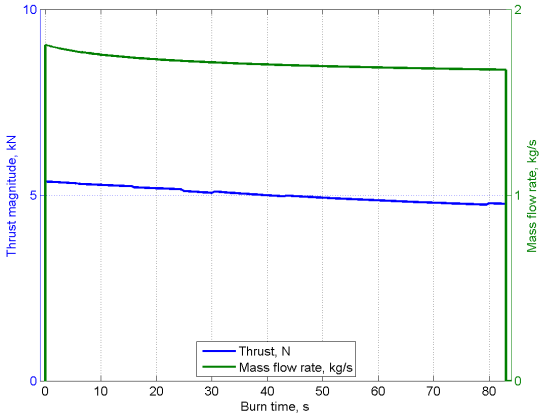

Figure 103.: Cosmos-3M 2nd stage trajectory reentry: thrust and propellant mass flow rate vs. burn time.

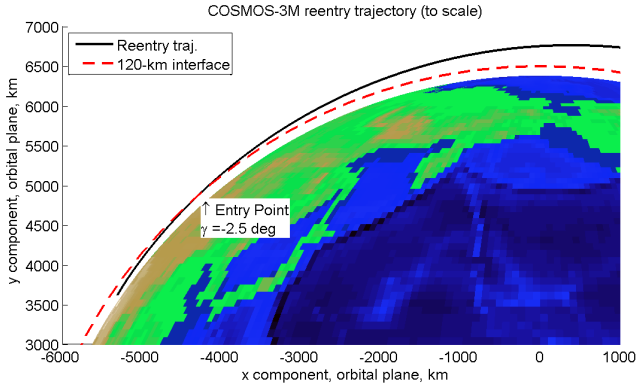

Figure 104.: Cosmos-3M 2nd stage trajectory reentry: entry point and FPA at 120 km.

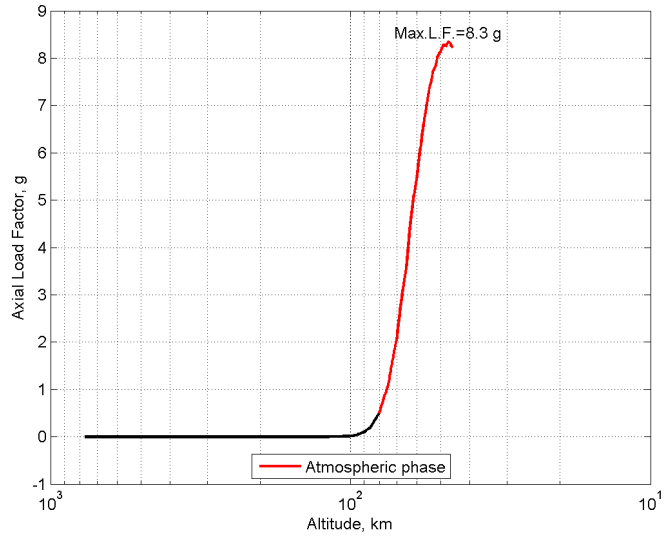

Figure 105.: Cosmos-3M 2nd stage trajectory reentry: axial load factor vs. altitude.

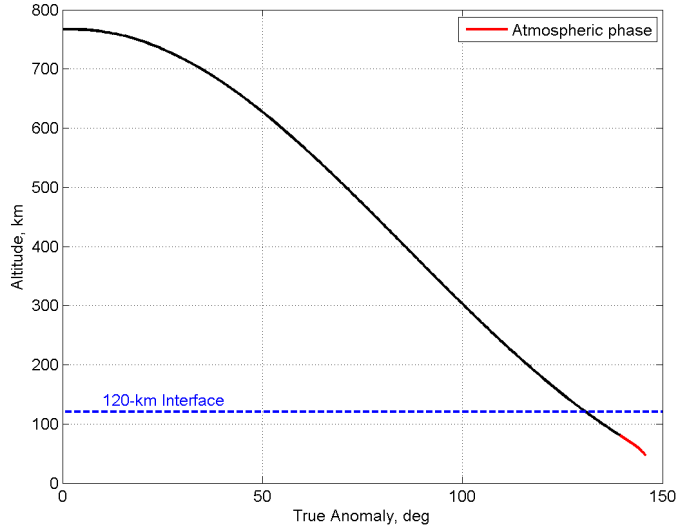

Figure 106.: Cosmos-3M 2nd stage trajectory reentry: altitude vs. true anomaly.

E ENVISAT - DISPOSAL TRAJECTORY

In this chapter, the trajectory analysis results obtained for the disposal of the system DeoKit-Envisat are presented (with reference to Section 8.3.2). The simulation code, based on Simulink®, was developed by U. Tancredi, in the frame of the collaboration project on the ADR missions by Hybrid Propulsion Modules [17, 166].

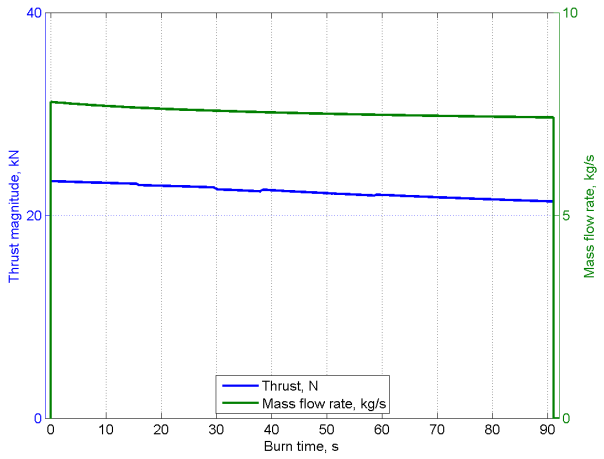

Figure 107.: Envisat trajectory reentry: thrust and propellant mass flow rate vs. burn time.

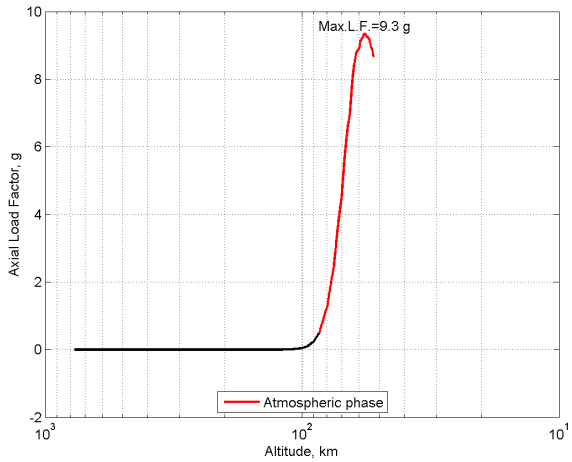

Figure 108.: Envisat trajectory reentry: axial load factor vs. altitude.

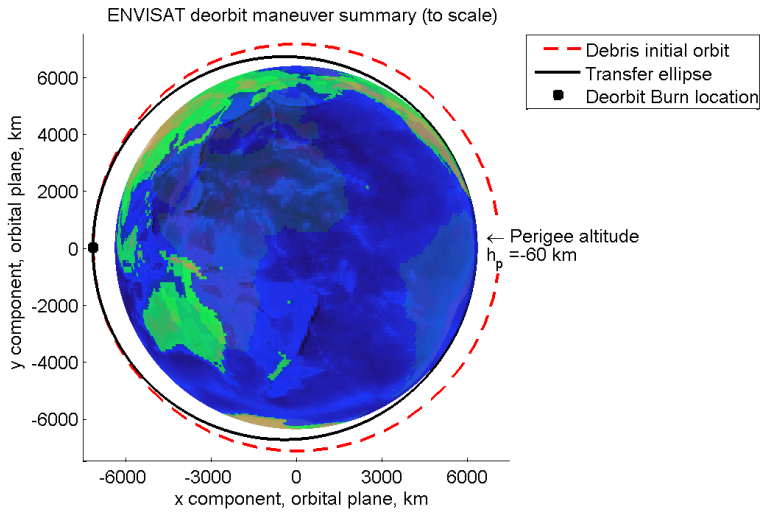

Figure 109.: Envisat trajectory reentry: maneuver summary and perigee of elliptical transfer orbit.

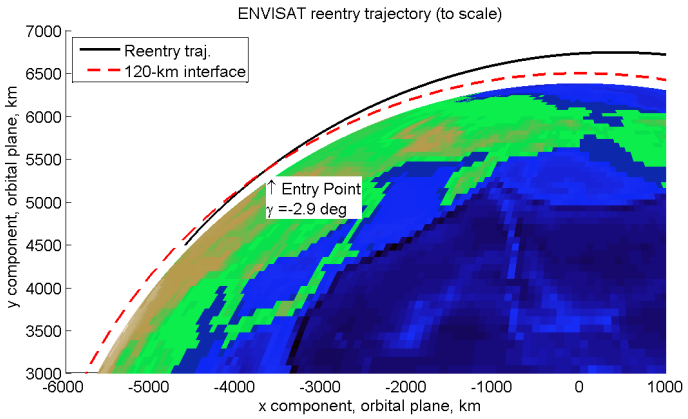

Figure 110.: Envisat trajectory reentry: entry point and FPA at 120 km.

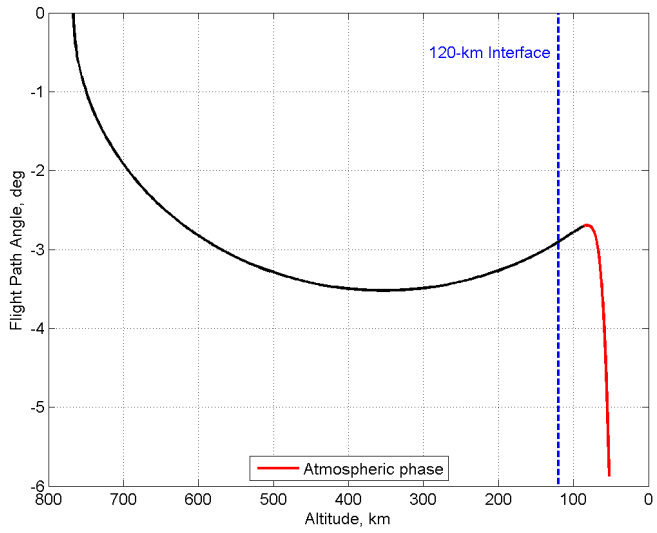

Figure 111.: Envisat trajectory reentry: Flight Path Angle vs altitude.

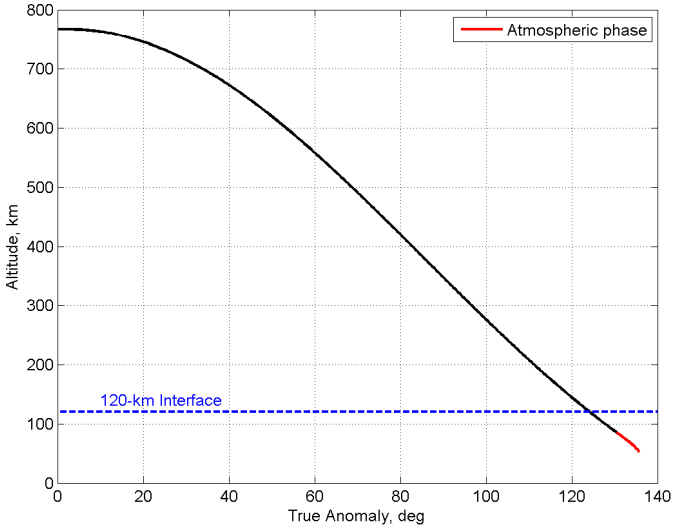

Figure 112.: Envisat trajectory reentry: altitude vs. true anomaly.

F HRE CODE

F.1 NUMERICAL SCHEMES

The Q1D compressible Euler equations (Eqs. 6.5) are discretized with finite volumes method and, to achieve a high order accuracy on space solution, a second order MUSCL scheme [182, 183] is applied. For numerical flux calculation the AUSMDV scheme [184] is used while the time integration is performed by a two-stages Runge-Kutta method. The selected schemes are characterized by quite simple algorithms and by a certain computational efficiency, making them suitable for fast rocket ballistics analysis, rocket performance estimation and preliminary sizing. The HRE Code is written in *Fortran 90* and compiled with Intel® Fortran Compiler, provided in free license for Linux users, on OS Ubuntu 12.04 LTS. The pc-station consists of an Intel® Core™ i7-4770K processor, an ASUS z87-Pro motherboard and 16Gb memory ram.

F.1.1 Discretization

The computational domain, made by the combustion chamber and de Laval nozzle, is discretized with one-dimensional finite elements. The domain has been divided in three regions with different cell distributions. In Figure 113, one can see the finite elements distribution over all considered regions: combustion chamber, nozzle convergent and nozzle divergent.

The nozzle convergent has been discretized equally with elements of the same size, while for the combustion chamber and for nozzle divergent, in order to obtain a good solution in correspondence of regions boundary and to use a not too large number of finite elements, the following function has been considered

$$\Delta x + \Delta x(1+\epsilon_x) + \Delta(1+\epsilon_x)^2 + ... + \Delta x(1+\epsilon_x)^{N_x-2} = L \tag{F.1}$$

where Δx is the smallest cell size defined, L is the length of the region to be discretized, ϵ_x is the parameter of the cell size function, achieved by applying the Newton method. In this work, the minimum Δx is that of nozzle convergent discretization. In Figure 114, the detail of the finite elements distribution on the nozzle divergent region is presented; the elements size increases going toward the nozzle exit.

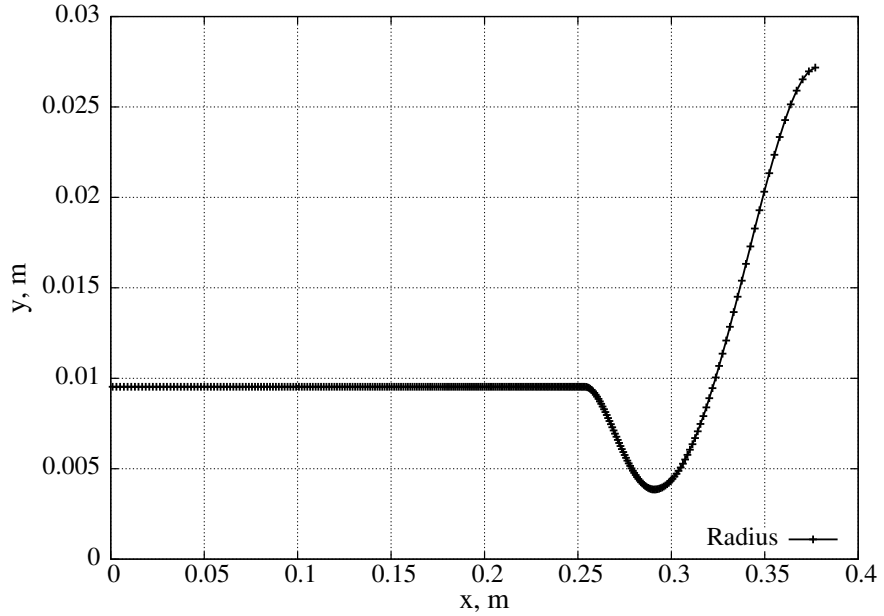

Figure 113.: Finite volumes discretization in the combustion chamber and nozzle.

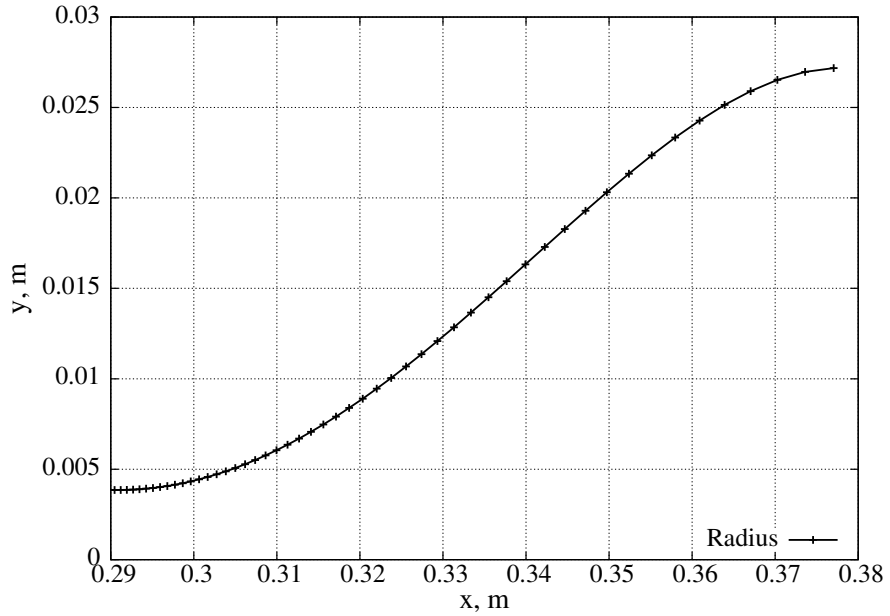

Figure 114.: Finite volumes discretization: nozzle divergent detail, 50 assumed as expansion area ratio.

F.1.2 Governing Equations Integration

The Q1D compressible Euler equations [167], discretized with finite elements method, are integrated on each single cell

$$\int_{x_{i-1/2}}^{x_{i+1/2}} \left(\frac{\partial A\mathbf{Q}}{\partial t} + \frac{\partial A\mathbf{F}}{\partial x} \right) dx = \int_{x_{i-1/2}}^{x_{i+1/2}} \left(\mathbf{S}_{Q1D} + \mathbf{S}_{Mass} \right) dx \tag{F.2}$$

the mean area on the *ith* cell is defined as

$$\overline{A}_i \equiv \frac{\int_{x_{i-1/2}}^{x_{i+1/2}} A dx}{\Delta x_i} \tag{F.3}$$

where $\Delta x_i \equiv x_{i+1/2} - x_{i-1/2}$. The area-mean physical quantities on the *ith* cell are defined as

$$\overline{\mathbf{Q}}_i \equiv \frac{\int_{x_{i-1/2}}^{x_{i+1/2}} \mathbf{Q} dx}{\int_{x_{i-1/2}}^{x_{i+1/2}} A dx} \tag{F.4}$$

and the general area-mean source $\mathbf{S} = \mathbf{S}_{Q1D} + \mathbf{S}_{Mass}$ terms is

$$\overline{\mathbf{S}}_i \equiv \frac{\int_{x_{i-1/2}}^{x_{i+1/2}} \mathbf{S} dx}{\int_{x_{i-1/2}}^{x_{i+1/2}} A dx} \tag{F.5}$$

By substituting the area-mean quantities in Eq. F.2, one can obtain

$$\frac{d\overline{\mathbf{Q}}_i}{dt} + \frac{(FA)_{i+1/2} - (FA)_{i-1/2}}{\Delta x_i \overline{A}_i} = \overline{\mathbf{S}}_{Q1D,i} + \overline{\mathbf{S}}_{Mass,i} \tag{F.6}$$

and it is possible to proceed with time integration between t_n and t_{n+1} ($n = 1, .., N_t$)

$$\int_{t_n}^{t_{n+1}} \left[\frac{d\overline{\mathbf{Q}}_i}{dt} + \frac{(FA)_{i+1/2} - (FA)_{i-1/2}}{\Delta x_i \overline{A}_i} \right] dt = \int_{t_n}^{t_{n+1}} \left[\overline{\mathbf{S}}_{Q1D,i} + \overline{\mathbf{S}}_{Mass,i} \right] dt \tag{F.7}$$

which can be solved by the Explicit Euler method [174, 185]

$$\overline{\mathbf{Q}}_i^{n+1} = \overline{\mathbf{Q}}_i^n - \frac{\Delta t^n}{Vol_i} \left(\mathbf{F}_{i+1/2}^n A_{i+1/2} - \mathbf{F}_{i-1/2}^n A_{i-1/2} \right) + \overline{\mathbf{S}}_i \Delta t^n \tag{F.8}$$

where $Vol_i \equiv \Delta x_i \overline{A}_i$. For simplicity, one can define

$$L_i(\overline{\mathbf{Q}}_i^n) = \frac{1}{Vol_i} \left(\mathbf{F}_{i-1/2}^n A_{i-1/2} - \mathbf{F}_{i+1/2}^n A_{i+1/2} \right) + \overline{\mathbf{S}}_i \tag{F.9}$$

and rewrite the Explicit Euler method as

$$\overline{\mathbf{Q}}_i^{n+1} = \overline{\mathbf{Q}}_i^n + \Delta t^n L_i(\overline{\mathbf{Q}}_i^n) \tag{F.10}$$

which represents the simplest form of Runge-Kutta family methods [174, 185, 169]: first order accuracy. Runge-Kutta methods allows to achieve high accuracy in the solution calculation, giving Euler's method efficiency up by re-calculating the term $L_i(\overline{\mathbf{Q}}_i)$ at an intermediate point between t_n and t_{n+1}. In this study, a second-order explicit Runge-Kutta methods (or two-stages Runge-Kutta) [185, 11, 169] is considered

$$\begin{cases} \overline{\mathbf{Q}}_i^{(1)} = \overline{\mathbf{Q}}_i^n + \Delta t^n L_i(\overline{\mathbf{Q}}_i^n) & 1^{st} step \\ \overline{\mathbf{Q}}_i^{n+1} = \frac{1}{2}\left[\overline{\mathbf{Q}}_i^n + \overline{\mathbf{Q}}_i^{(1)} + \Delta t^n L_i(\overline{\mathbf{Q}}_i^{(1)})\right] & 2^{nd} step \end{cases} \tag{F.11}$$

In order to provide a complete description of all calculation components, the area-mean source terms components, $\overline{S}_{Q1D,i}^{(2),n}$, $\overline{S}_{Mass,i}^{(1),n}$, $\overline{S}_{Mass,i}^{(3),n}$ and $\overline{S}_{Mass,i}^{(4),n}$ are obtained as follow

$$\overline{S}_{Q1D,i}^{(2),n} = \frac{\int_{x_{i-1/2}}^{x_{i+1/2}} p \frac{dA}{dx} dx}{\int_{x_{i-1/2}}^{x_{i+1/2}} A dx} \approx \frac{\overline{p}_i (A_{i+1/2} - A_{i-1/2})}{Vol_i} \tag{F.12}$$

$$\overline{S}_{Mass,i}^{(1),n} = \frac{\int_{x_{i-1/2}}^{x_{i+1/2}} \dot{m}_f l_p dx}{\int_{x_{i-1/2}}^{x_{i+1/2}} A dx} \approx \frac{\overline{l}_{p,i}}{\overline{A}_i} \overline{\dot{m}}_{f,i} = \overline{S}_{Mass,i}^{(4),n} \tag{F.13}$$

$$\overline{S}_{Mass,i}^{(3),n} = \frac{\int_{x_{i-1/2}}^{x_{i+1/2}} l_p \dot{m}_f h_w dx}{\int_{x_{i-1/2}}^{x_{i+1/2}} A dx} \approx \frac{\overline{l}_{p,i}}{\overline{A}_i} \overline{\dot{m}}_{f,i} \overline{h}_{w,i} \tag{F.14}$$

F.1.3 Numerical Flux Scheme

The numerical fluxes across the cell interfaces are calculated with the AUSMDV scheme, based on Advection Upwind Splitting Method (AUSM), developed by Liou and Steffen [184] for generalized non-equilibrium flow equations. The AUSMDV consists in a *mixture* of AUSMD and AUSMV schemes, that are, respectively, an AUSM with a flux difference splitting scheme and a flux vector splitting scheme. This method is characterized by interesting properties such as numerical efficiency, applicability to chemically reacting flows, high resolution for contact discontinuities, enthalpy conservation for steady flows, as well as high robustness and algorithm simplicity. The general numerical flux definition for this scheme [184] is

$$\mathbf{F}_{1/2} = \frac{1}{2}\left[(\rho u)_{1/2}(\boldsymbol{\Psi}_L + \boldsymbol{\Psi}_R) - |(\rho u)_{1/2}|(\boldsymbol{\Psi}_R - \boldsymbol{\Psi}_L)\right] + \mathbf{p}_{1/2} \tag{F.15}$$

with

$$\boldsymbol{\Psi} = [1, u, H, \xi]^T \quad and \quad \mathbf{p}_{1/2} = \left[0, p_{1/2}, 0, 0\right]^T \tag{F.16}$$

where H is the total enthalpy $H = e_t + p/\rho$, the subscript $1/2$ is referred to the cell interface boundary, while the subscripts L and R respectively correspond to the left

side and right side of the cell interface. By applying the AUSMDV flux scheme to the Q1D compressible Euler equations one can write

$$\begin{cases} F_{1/2}^{(1)} = \frac{1}{2}\left[(\rho u)_{1/2}(1+1) - |(\rho u)_{1/2}|(1-1)\right] \\ F_{1/2}^{(2)} = \left[\left(\frac{1}{2} + f_{spl}\right)(\rho u^2)_{AUSMV} + \left(\frac{1}{2} - f_{spl}\right)(\rho u^2)_{AUSMD}\right] + p_{1/2} \\ F_{1/2}^{(3)} = \frac{1}{2}\left[(\rho u)_{1/2}(H_L + H_R) - |(\rho u)_{1/2}|(H_R - H_L)\right] \\ F_{1/2}^{(4)} = \frac{1}{2}\left[(\rho u)_{1/2}(\xi_L + \xi_R) - |(\rho u)_{1/2}|(\xi_R - \xi_L)\right] \end{cases} \tag{F.17}$$

where $(\rho u)_{1/2}$ is the muss flux term, defined as

$$(\rho u)_{1/2} = u_L^+ \rho_L + u_R^- \rho_R \tag{F.18}$$

and the velocity splitting u_L^+, u_R^- is given by

$$u_L^+ = \begin{cases} \beta_L \left[\frac{(u_L + a_{s,m})^2}{4a_{s,m}} - \frac{u_L + |u_L|}{2}\right] + \frac{u_L + |u_L|}{2}, & \text{if} \frac{|u_L|}{a_{s,m}} \leqslant 1 \\ \frac{u_L + |u_L|}{2}, & \text{otherwise} \end{cases} \tag{F.19}$$

$$u_R^- = \begin{cases} \beta_R \left[-\frac{(u_R - a_{s,m})^2}{4a_{s,m}} - \frac{u_R - |u_R|}{2}\right] + \frac{u_R - |u_R|}{2}, & \text{if} \frac{|u_R|}{a_{s,m}} \leqslant 1 \\ \frac{u_R - |u_R|}{2}, & \text{otherwise} \end{cases} \tag{F.20}$$

where $a_{s,m} = max(a_{s,L}, a_{s,R})$ is the maximum sound velocity value across the interface, while β_L and β_R depend on pressure and density across the interface and are calculated as

$$\beta_L = \frac{2p_L/\rho_L}{p_L/\rho_L + p_R/\rho_R}, \tag{F.21}$$

$$\beta_R = \frac{2p_R/\rho_R}{p_L/\rho_L + p_R/\rho_R}. \tag{F.22}$$

Then, the pressure flux $p_{1/2}$ is given by

$$p_{1/2} = p_L^+ + p_R^- \tag{F.23}$$

where the pressure splitting is defined as

$$p_{L/R}^{\pm} = \begin{cases} p_{L/R}\left(\frac{u_{L/R}}{a_{s,m}} \pm 1\right)^2 \left(2 \mp \frac{u_{L/R}}{a_{s,m}}\right)/4 & , \text{if} \frac{|u_{L/R}|}{a_{s,m}} \leqslant 1 \\ p_{L/R}\frac{u_{L/R} \pm |u_{L/R}|}{2u_{L/R}}, & \text{otherwise.} \end{cases} \tag{F.24}$$

Finally, the term $F_{1/2}^{(2)}$ is the mixed momentum flux [184] between AUSMV and AUSMD and f_{spl} is a switching function of the pressure gradient

$$f_{spl} = \frac{1}{2} min\left(1, K\frac{|p_R - p_L|}{min(p_L, p_R)}\right) \tag{F.25}$$

where K is a constant parameter (assumed equal to 10 [184]). The AUSMV momentum flux is obtained as

$$(\rho u^2)_{AUSMV} = u_L^+(\rho_L u_L) + u_R^-(\rho_R u_R) \tag{F.26}$$

while the AUSMD momentum flux is

$$(\rho u^2)_{AUSMD} = \frac{1}{2}\left[(\rho u)_{1/2}(u_L + u_R) - |(\rho u)_{1/2}|(u_R - u_L)\right]. \tag{F.27}$$

In [184], one can find a more detailed description of the AUSMDV scheme, including its comparison with Roe's scheme in different test cases.

F.1.4 High Order Accuracy Scheme

The numerical flux calculation requires the solving of Riemann problem [186] at both sides of the cell interface. To perform this procedure it is necessary to know the value of the cell variable in correspondence of cell boundaries, $\mathbf{W}_i^L, \mathbf{W}_i^R$, see the scheme in Figure F.29 and primitive vector 6.6. The most simple approach consists in the assuming of a constant piece-wise distribution of the value $\mathbf{W}_i$ all over the cell.

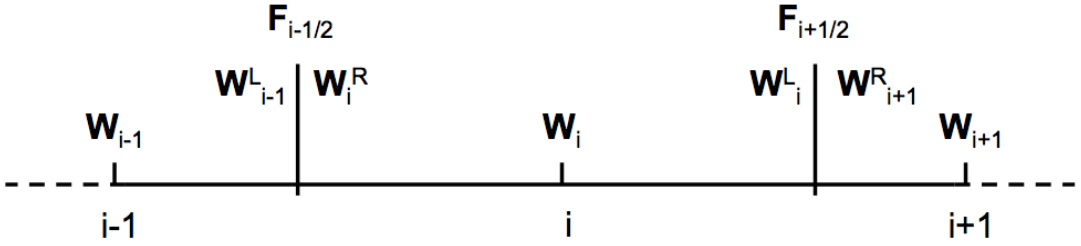

Figure 115.: Numerical fluxes at cell interfaces.

However, in order to achieve an higher accuracy level in space solution, a second-order MUSCL (Monotone Upstream-centered Schemes for Conservation Laws) method can be applied [182, 12, 183]. This scheme allows for *reconstruction*, that is the evaluation of piece-wise linear or parabolic distributions from the piece-wise constant data of each cell. First of all, the general MUSCL scheme [182] without limiter function is

$$\begin{cases} \mathbf{W}_{i-1/2}^R = \mathbf{W}_i - \frac{1}{2}\delta\mathbf{W}^R \\ \mathbf{W}_{i+1/2}^L = \mathbf{W}_i - \frac{1}{2}\delta\mathbf{W}^L \end{cases} \tag{F.28}$$

where

$$\begin{cases} \delta \mathbf{W}^{R} = \frac{1}{2}\left[(1+\kappa)\nabla \mathbf{W}_{i} + (1-\kappa)\Delta \mathbf{W}_{i})\right] \\ \delta \mathbf{W}^{L} = \frac{1}{2}\left[(1-\kappa)\nabla \mathbf{W}_{i} + (1+\kappa)\Delta \mathbf{W}_{i})\right] \end{cases} \tag{F.29}$$

The parameter κ is used for accuracy level selection, as described in Table 29. The terms $\Delta \mathbf{W}_{i}$ and $\nabla \mathbf{W}_{i}$ are, respectively, the backward difference $\Delta \mathbf{W}_{i} = \mathbf{W}_{i} - \mathbf{W}_{i-1}$ and the forward difference $\nabla \mathbf{W}_{i} = \mathbf{W}_{i+1} - \mathbf{W}_{i}$.

κ	-1	0	$1/3$	$+1$
Accuracy	2^{nd} order	2^{nd} order	3^{rd} order	2^{nd} order
Characteristic	1^{st} order Upwind	1^{st} order Symmetry Method	2^{nd} order Polynomial Function	Central Difference Scheme

Table 29.: Accuracy level selection for MUSCL scheme [182].

Since the use of high order methods can destroy the monotonicity and precision of the solution, a slope limiter is required for monotonicity preservation. There are different types of limiter functions, in this work the limiter $R(\theta)$ is applied [182]. Considering the limiter, the physical values at the left and right side of the *ith* cells are

$$\begin{cases} \mathbf{W}^{R,lim}_{i-1/2} = \mathbf{W}_{i} - \frac{1}{2}\delta \mathbf{W}_{lim} \\ \mathbf{W}^{L,lim}_{i+1/2} = \mathbf{W}_{i} - \frac{1}{2}\delta \mathbf{W}_{lim} \end{cases} \tag{F.30}$$

where

$$\delta \mathbf{W}_{lim} = \frac{1}{2}\left[sign(\mathbf{W}^{R}_{lim}) + sign(\mathbf{W}^{L}_{lim})\right] \cdot min\left[|\mathbf{W}^{R}_{lim}|, |\mathbf{W}^{L}_{lim}|\right] \tag{F.31}$$

The terms $\mathbf{W}^{R}_{lim}$ and $\mathbf{W}^{L}_{lim}$ are defined as

$$\begin{cases} \mathbf{W}^{R}_{lim} \equiv R^{R}(\theta)\delta \mathbf{W}^{R} \\ \mathbf{W}^{L}_{lim} \equiv R^{L}(\theta)\delta \mathbf{W}^{L} \end{cases} \tag{F.32}$$

and θ is the ratio between the forward difference and the backward difference $\theta \equiv \Delta \mathbf{W}_{i}/\nabla \mathbf{W}_{i}$. The limiter functions $R^{R}(\theta)$ and $R^{L}(\theta)$ satisfy the following conditions:

A. if $\mathbf{W}_{i-1}, \mathbf{W}_{i}, \mathbf{W}_{i+1}$ do not increase monotonically (i.e. $\theta < 0$) then $R^{R}(\theta) = R^{L}(\theta) = 0$ (i.e. first order accuracy);

B. if $\mathbf{W}_{i-1}, \mathbf{W}_{i}, \mathbf{W}_{i+1}$ increase monotonically (i.e. $\mathbf{W}_{i-1} < \mathbf{W}_{i} < \mathbf{W}_{i+1}$) then

$$\begin{cases} \mathbf{W}_{i-1} \leqslant \mathbf{W}_{i} - \frac{1}{2}\delta \mathbf{W}^{R}_{lim} \leqslant \mathbf{W}_{i} \\ \\ \mathbf{W}_{i} \leqslant \mathbf{W}_{i} + \frac{1}{2}\delta \mathbf{W}^{L}_{lim} \leqslant \mathbf{W}_{i+1} \end{cases} \tag{F.33}$$

and, by developing the Eqs. F.33, one can obtain the next condition;

c. if $\mathbf{W}_{i-1}, \mathbf{W}_i, \mathbf{W}_{i+1}$ decrease monotonically (i.e. $\mathbf{W}_{i-1} > \mathbf{W}_i > \mathbf{W}_{i+1}$) the following relations must be satisfied

$$\begin{cases} \frac{4}{1+\kappa+(1-\kappa)\theta} \geqslant R^R(\theta) \geqslant 0 \\ 0 \leqslant R^L(\theta) \leqslant \frac{4\theta}{1-\kappa+(1+\kappa)\theta} \end{cases} \tag{F.34}$$

d. if $\nabla\mathbf{W}_i = 0$ and $\Delta\mathbf{W}_i \neq 0$ (i.e. $\theta \to \infty$) then

$$\begin{cases} R^R(\theta) = 0 \\ 0 \leqslant R^L(\theta) \leqslant \frac{4}{1+\kappa} \end{cases} \tag{F.35}$$

e. if $\nabla\mathbf{W}_i \neq 0$ and $\Delta\mathbf{W}_i = 0$ (i.e. $\theta = 0$) then the condition F.34 is applied.

Therefore, the limiter functions $R^R(\theta)$ and $R^L(\theta)$ can be equal of less than 1:

$$0 \leqslant R^R(\theta) \leqslant \min\left[\frac{4}{1+\kappa+(1-\kappa)\theta}, 1\right] \tag{F.36a}$$

$$0 \leqslant R^L(\theta) \leqslant \min\left[\frac{4\theta}{1-\kappa+(1+\kappa)\theta}, 1\right]. \tag{F.36b}$$

F.2 FURTHER PLOT RESULTS AND COMPARISONS

With reference to Section 6.3.6, further graphs about the results comparison between HTPB + GOX and HTPB + H_2O_2, simulated with HRE code, are presented:

Figures 116, 117, 118, 119, 120 and 121.

With reference to Sections 7.3 and 7.4, further graphs about performance analysis and comparison are presented:

Figures 122, 123, 124, 125, 126, 127, 128 and 129.

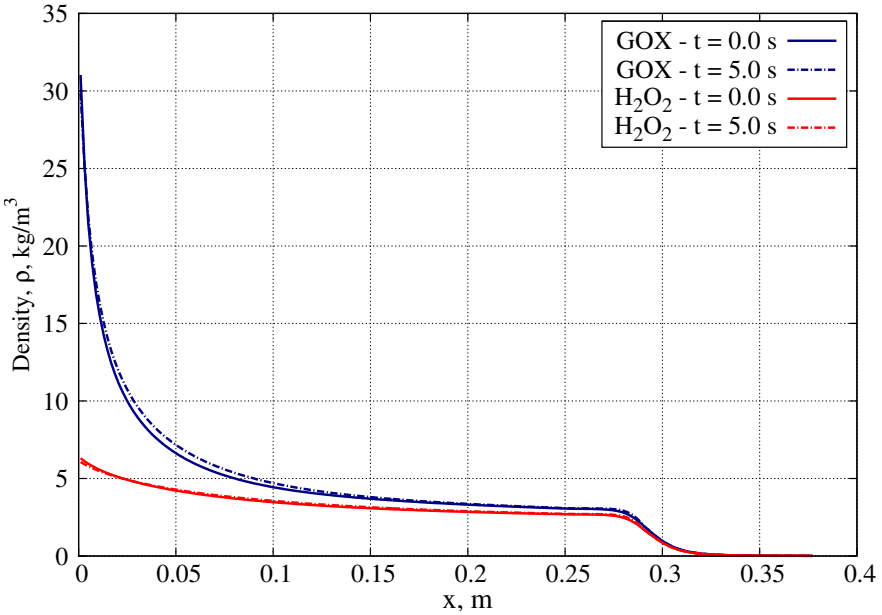

Figure 116.: Density profile along x-location in the combustion chamber and de Laval nozzle. Comparison between two different propellant couples: HTPB + GOX (blue) and HTPB + H_2O_2 (red) at t = 0.0 s and t = 5.0 s.

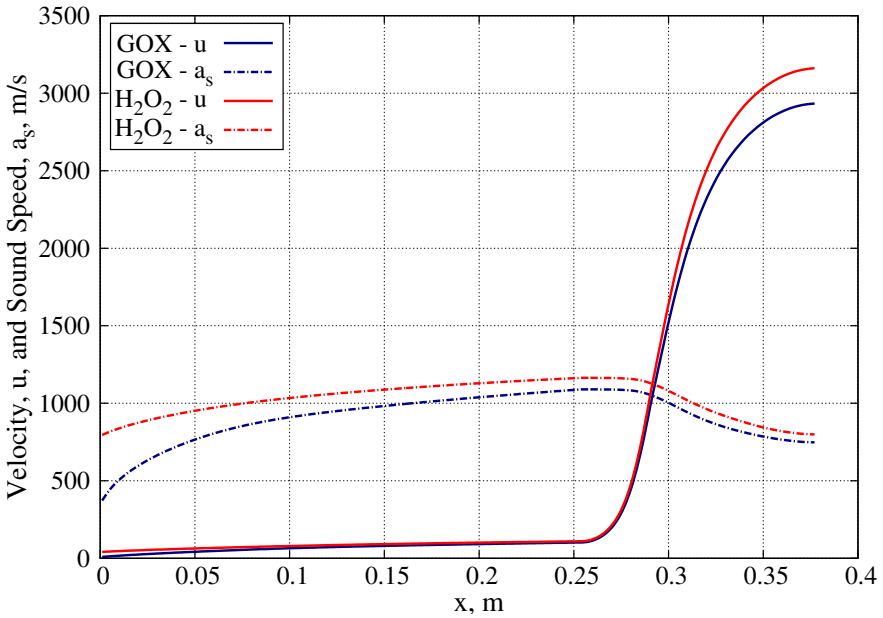

Figure 117.: Velocity and sound speed profiles along x-location in the combustion chamber and de Laval nozzle. Comparison between two different propellant couples: HTPB + GOX (blue) and HTPB + H_2O_2 (red) at t = 0.0 s.

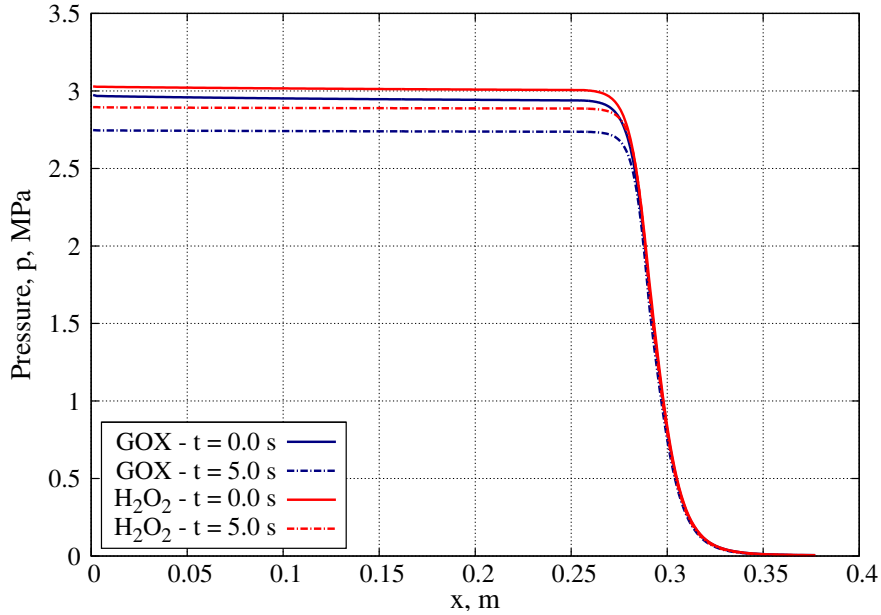

Figure 118.: Pressure profile along x-location in the combustion chamber and de Laval nozzle. Comparison between two different propellant couples: HTPB + GOX (blue) and HTPB + H_2O_2 (red) at t = 0.0 s and t = 5.0 s.

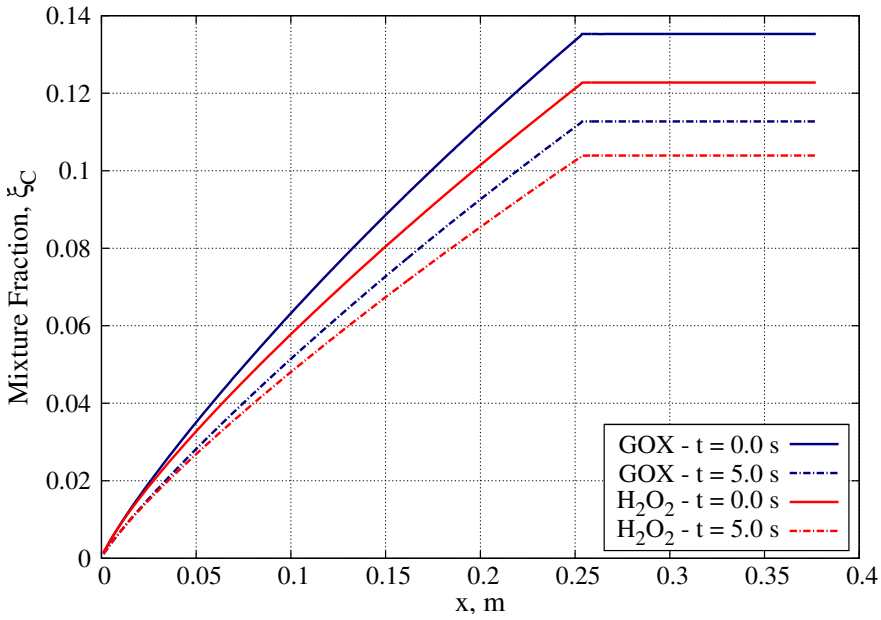

Figure 119.: Mixture fraction profile along x-location in the combustion chamber and de Laval nozzle. Comparison between two different propellant couples: HTPB + GOX (blue) and HTPB + H_2O_2 (red) at t = 0.0 s and t = 5.0 s.

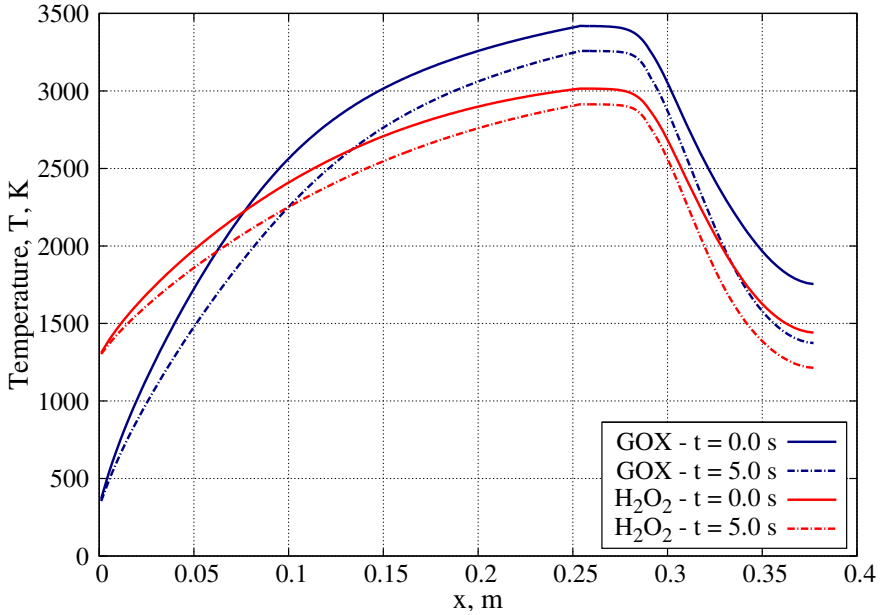

Figure 120.: Average temperature profile along x-location in the combustion chamber and de Laval nozzle. Comparison between two different propellant couples: HTPB + GOX (blue) and HTPB + H_2O_2 (red) at t = 0.0 s and t = 5.0 s.

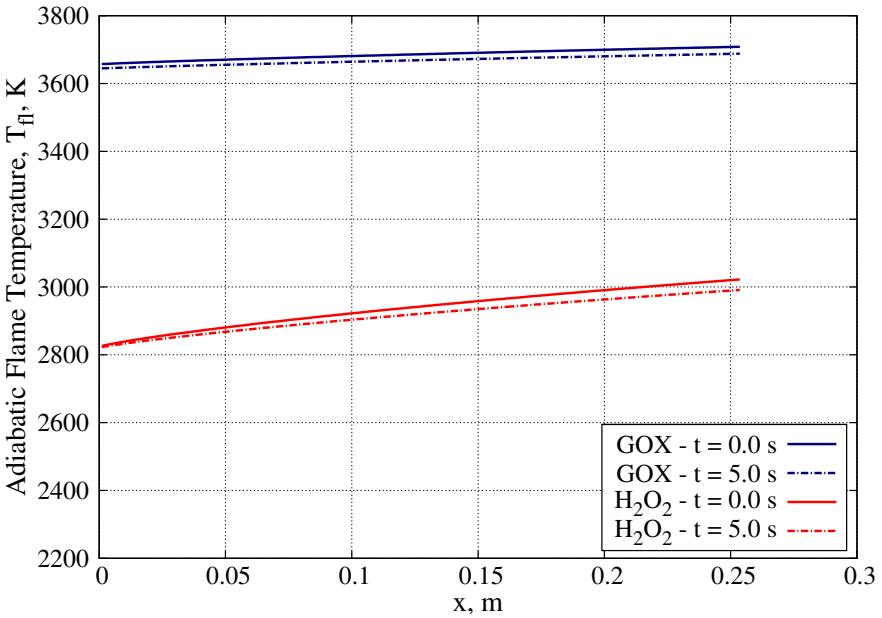

Figure 121.: Flame temperature profile along x-location in the combustion chamber and de Laval nozzle. Comparison between two different propellant couples: HTPB + GOX (blue) and HTPB + H_2O_2 (red) at t = 0.0 s and t = 5.0 s.

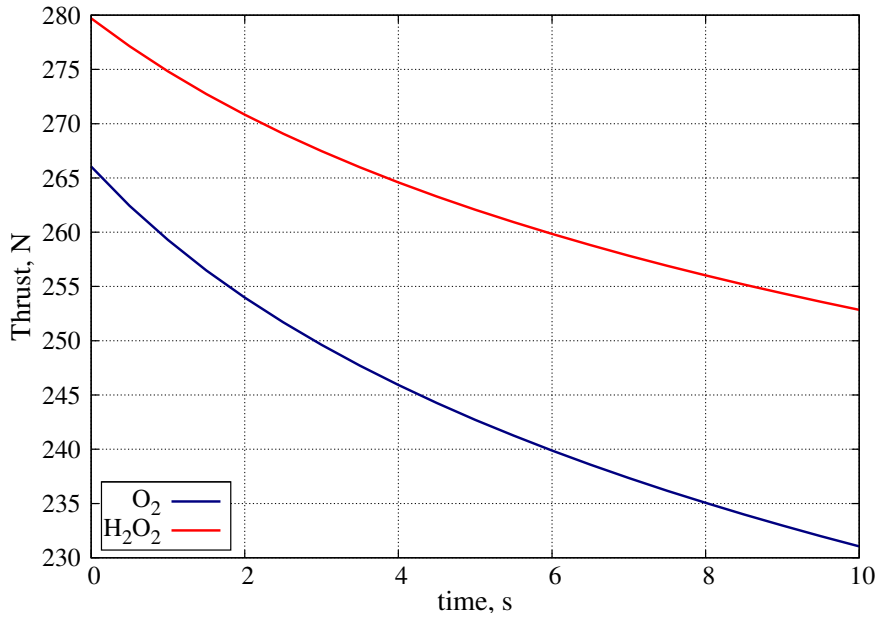

Figure 122.: Ideal thrust comparison between two different propellant couples: HTPB + GOX (blue) and HTPB + H_2O_2 (red); 10 seconds combustion time.

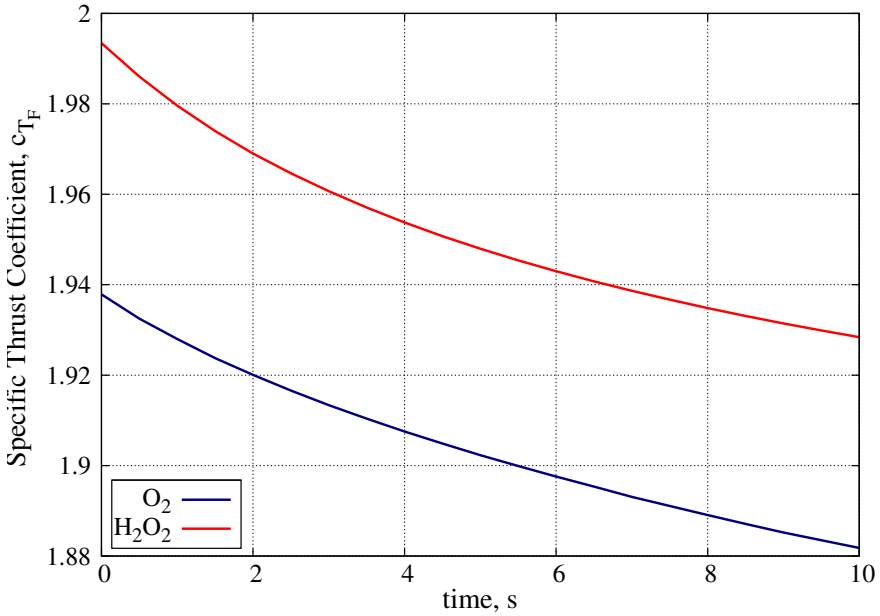

Figure 123.: Ideal thrust coefficient comparison between two different propellant couples: HTPB + GOX (blue) and HTPB + H_2O_2 (red); 10 seconds combustion time.

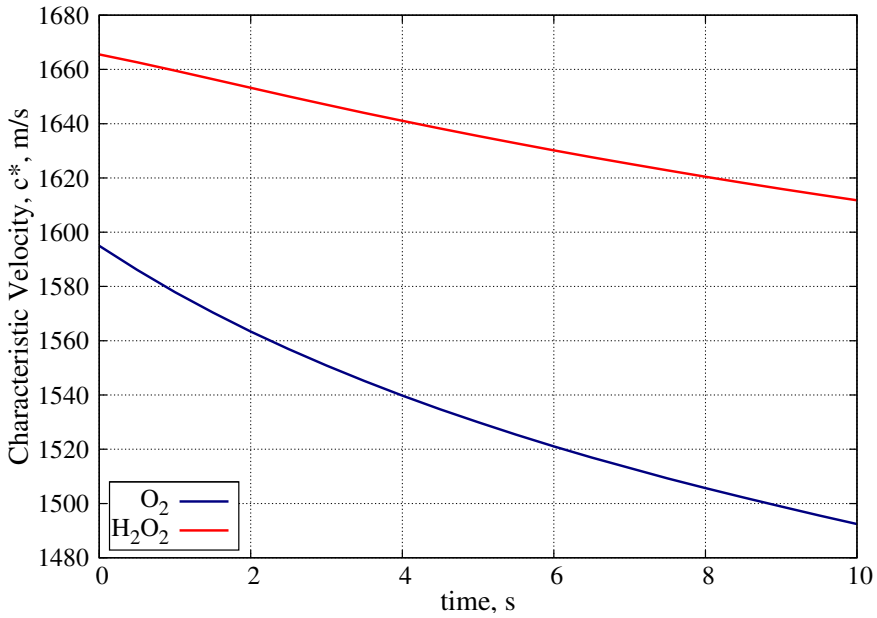

Figure 124.: Ideal characteristic velocity comparison between two different propellant couples: HTPB + GOX (blue) and HTPB + H_2O_2 (red); 10 seconds combustion time.

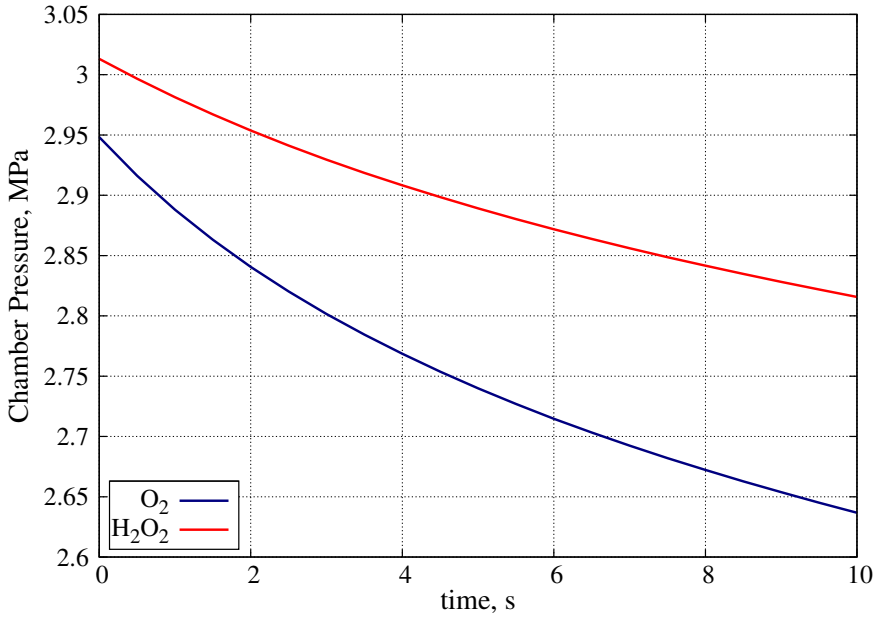

Figure 125.: Chamber pressure comparison between two different propellant couples: HTPB + GOX (blue) and HTPB + H_2O_2 (red); 10 seconds combustion time.

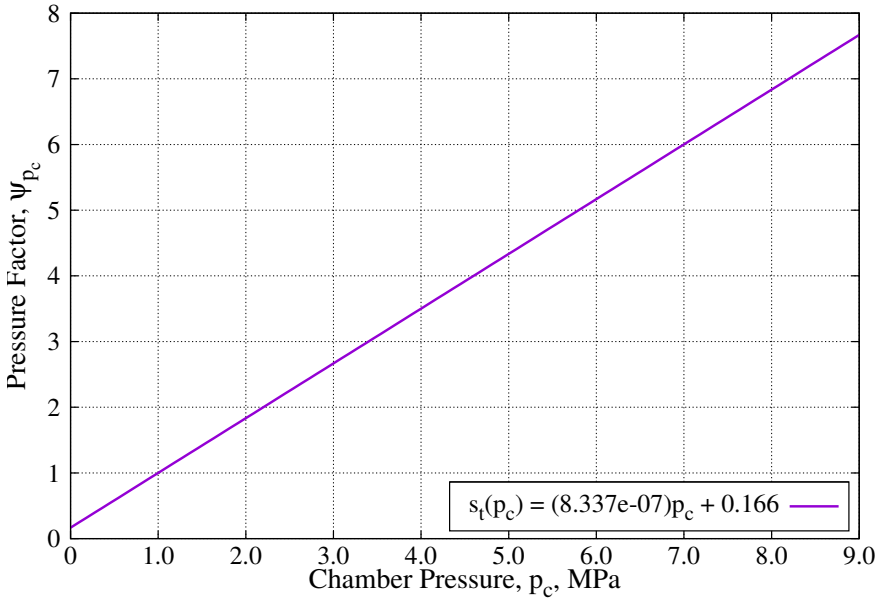

Figure 126.: Linear approximation of throat erosion rate data as function of pressure. Values referred to N_2O_4 oxidizer [178].

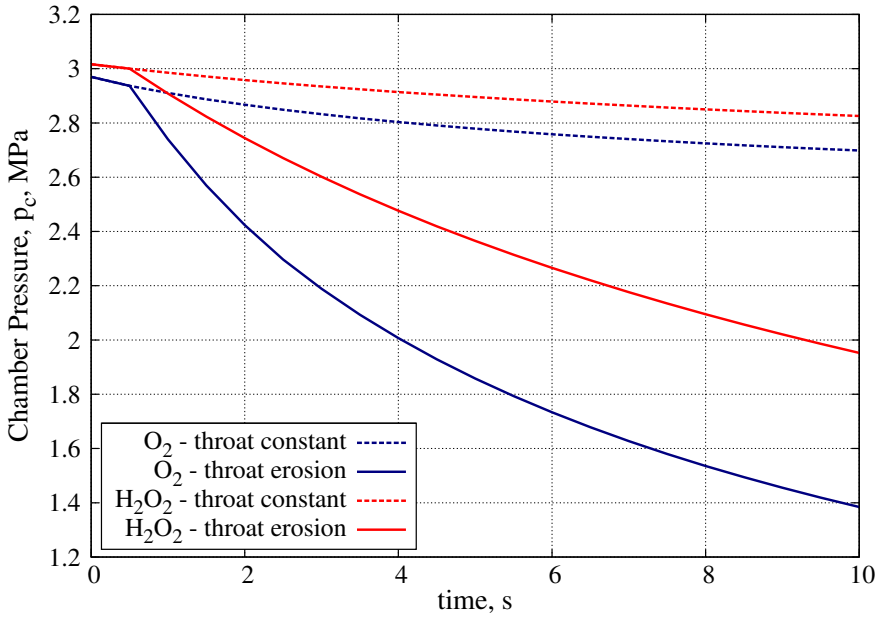

Figure 127.: Chamber pressure drop due to erosion rate application from $t = 0.5$ s. Comparison between ideal performance.

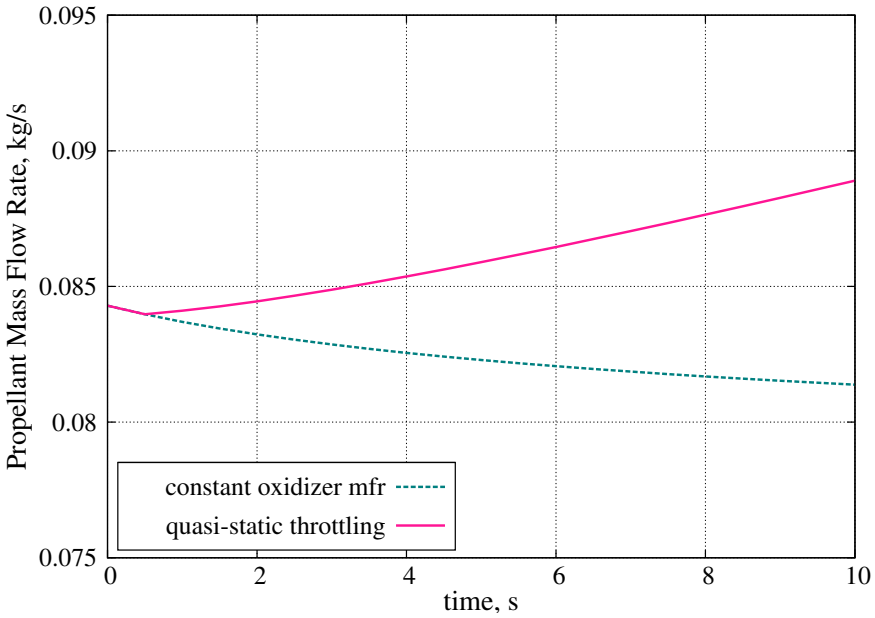

Figure 128.: Propellant mass flow rate change over combustion time; comparison between constant oxidizer mass flow rate and quasi-static throttling cases.

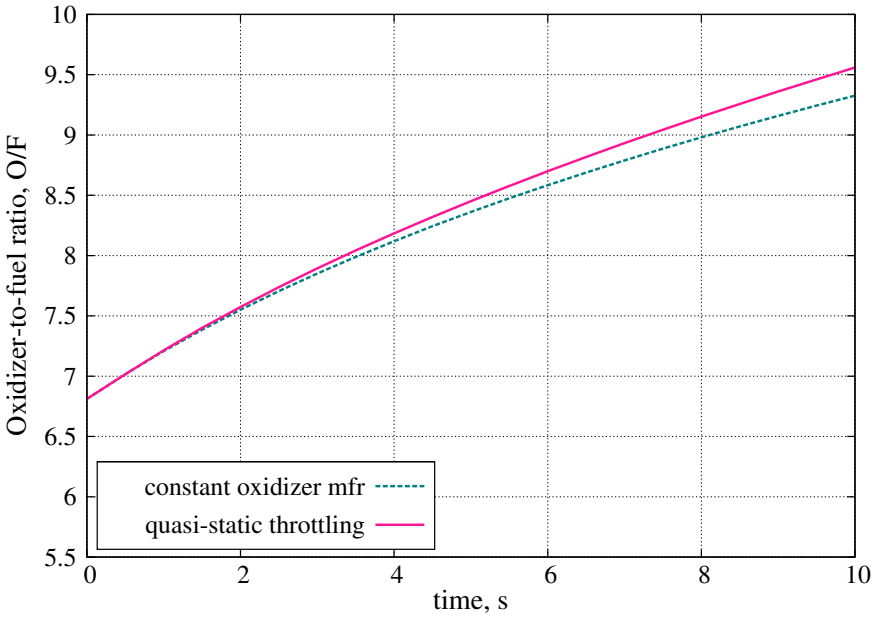

Figure 129.: Oxidizer-to-fuel ratio change over combustion time; comparison between constant oxidizer mass flow rate and quasi-static throttling cases.

G HYDROXYL-TERMINATED POLYBUTADIENE

Hydroxyl-terminated polybutadiene (HTPB) is a polymer of butadiene terminated at each end with a hydroxyl functional group. It reacts with diisocyanate to form polyurethane, a stable and easily stored synthetic material. HTPB is a translucent liquid with a very similar color to wax paper; it is highly viscous. The properties cannot be precisely stated, because HTPB is manufactured in various grades to meet specific requirements. HTPB is thus a generic name for a class of compounds. It consists of many butadiene molecules linked together into a polymer forming polybutadiene [155]. Both ends of the chain are terminated with a hydroxide ion $OH-$, thus giving it the name Hydroxyl-Terminated Polybutadiene. It is insoluble in water making it a good sealant. Although it is used as rocket fuel it does not ignite easily, requiring temperatures above 773 K to combust. As curing agent an isonate or isocyanate compound is usually selected. Common solid polymer propellants are viscoelastic materials and show a nonlinear viscoelastic behavior. This means that the maximum stress and maximum elongation, or strain, diminish every time a significant load is applied. The material becomes weaker and suffers some damages with each loading cycle or thermal stress application. The physical properties also change with the time rate of applying loads. The HTPB gives a good elongation and a stronger propellant than other polymers used with the same percentage of binder. Therefore, it is the preferred binder today. The physical properties are also affected by the manufacturing process. For example, tensile specimens cut from the same conventionally cast grain of composite propellant can show 20 to 40% variation in the strength properties between samples of different orientations relative to the local casting slurry flow direction [187, 188]. Viscoelastic material properties change as a function of prior loading and damage history. They have the capability to re-heal and recover partially after a damage. Chemical deterioration will degrade the properties of the solid fuel over time, making difficult to characterize the material and predict its behavior in operative conditions. HTPB fuel grains should be strong enough, having an elongation capability sufficient to meet the high stress concentrations present during shrinkage at low temperature and also under the dynamic load conditions of ignition and motor operations.

G.1 MANUFACTURE PROCEDURE

The hydroxyl-terminated polybutadiene appears as a viscous amber-colored fluid, at standard conditions of pressure and temperature. It is obtained from the monomeric

butadiene C_4H_6, which is an *alkene polieno*, characterized by a chemical structure with double bonds between adjacent carbon atoms, Figure 130.

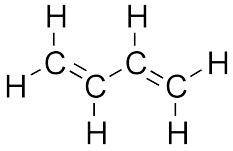

Figure 130.: Butadiene Atomic Structure

The polymerization process of Ziegler-Natta, Figure 131, allows to create the *oligomer polybutadiene*, a *dienic polymer* which preserves the double bonds between carbons in the main chemical chain [155].

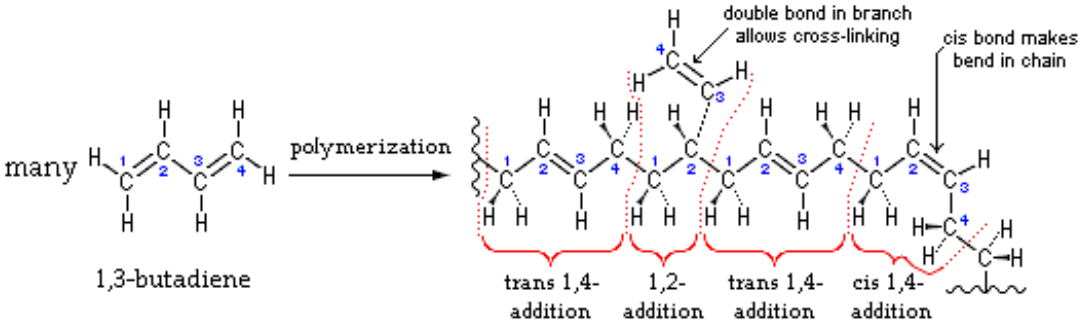

Figure 131.: Polybutadiene polymerization

The last step consists in the hydroxylation process, that is the insertion of hydroxyl groups at the double ends of the polymeric molecule. The final compound is the hydroxyl-terminated polybutadiene and its molecular weight depends on the number of monomers that constitute the chain.

G.1.1 Crosslinking

For propulsion purpose HTPB at standard conditions is not usable, hence the curing of the material is necessary. The curing process creates a permanent tridimensional network between the polymeric molecules, thanks to crosslinking mechanism. This procedure transforms the HTPB in a stable and elastic polyurethane resin.

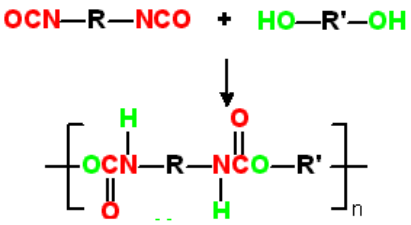

Figure 132.: Polyurethane Synthesis

This process consists in the addition of *isocyanate* compounds, in particular *di-isocyanate*, characterized by two isocyanate groups ($OCN-R-NCO$), Figure 132. The isocyanate group $-N=C=O$ reacts easily with compounds that contain active hydrogen, such as the hydroxyl groups $-OH$ at the ends of the polybutadiene chain [155]. The addition reaction of the active hydrogen involves the nitrogen atom, while the remainder molecule becomes attached to the carbon atom. This is an exothermic reaction with $\Delta H \approx 150\ kJ/mol$ and an activation energy of $42\ kJ/mol$. For the curing of HTPB it was chosen the *isophorone di-isocyanate* or IPDI, $C_{12}H_{18}N_2O_2$, Figure 133. It has a lower reactivity than other di-isocyanate compounds.

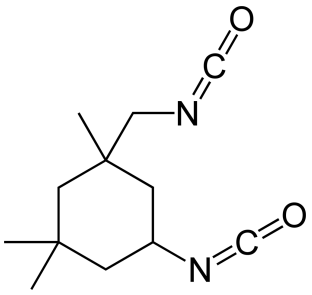

Figure 133.: IPDI chemical structure

G.1.2 Catalyst

The crosslinking reaction occurs spontaneously when HTPB and IPDI get in contact during the mixing. It requires about one week to end completely, a too long timeframe to perform an experimental campaign consisting in mechanical and combustion tests. In order to accelerate the crosslinking process the addition of a catalyst is required. *Dibutyltin Diacetate*, Figure 134, is able to lower the threshold bonds activation between hydroxyl and isocyanate groups, promoted by tin. This catalyst consists in a solution made by dibutyltin diacetate and anhydrous ethyl acetate.

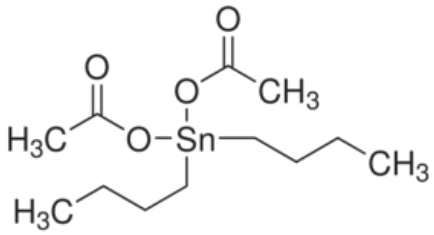

Figure 134.: Dibutyltin Diacetate chemical structure

G.1.3 Plasticizer

In order to make the final product soft and flexible, increasing its mechanical properties, a plasticizer compound is introduced, which creeps into the space between polymer crosslinks, providing a better relative sliding of the material. The plasticizer used for HTPB is the *Dioctyl Adipate* or DOA, a diester of adipic acid and two equivalents of *n-octanol*, $C_{22}H_{42}O_4$, Figure 135.

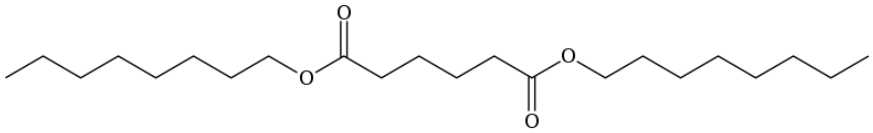

Figure 135.: Dioctyl Adipate chemical structure

G.2 DMA SAMPLES

The procedure described was performed using a Resodyn® Acoustic Mixer. This system is able to transfer acoustic energy into the loaded substance, by an oscillating mechanical driver. Only the mix load absorbs the energy, apart some negligible losses. It provides an high mixing efficiency thanks to the direct mechanical energy transfer into the mixing materials.

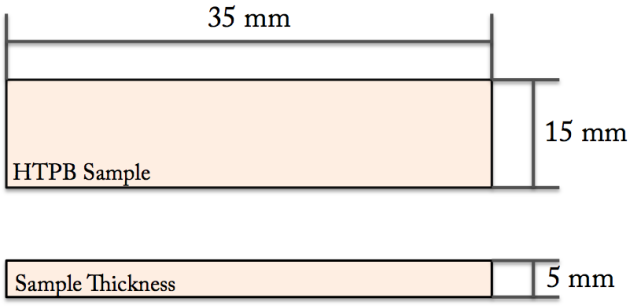

Figure 136.: HTPB sample size, required for DMA grip.

The samples produced for the aging test campaign have an hexagonal shape with an average size of 35x15x5 mm, Figure 136, suitable for the grip of DMA. The thickness and the width can change a little bit for each casting, due to microscopic mold irregularities, different level of compression during the curing or cutting procedure of the final polyurethane. The samples prepared for this research project are made of HTPB R45, where 45 is the number of monomers, supplied by AVIO Space. In Table 30 one can see all the components of the polyurethane resin and their mass percentages, defined during several investigations performed during last years at SPLab.

	Percentages by Mass
HTPB R45	78.86%
Isophorone Di-isocyanate (IPDI)	7.67%
Dibutyltin Diacetate (TIN)	0.43%
Dioctyl Adipate (DOA)	13.04%

Table 30.: Percentages by mass for sample casting

The acoustic mixer allows a very fast preparation of the final polyurethane samples. Before the mixing phase, HTPB is subject to vacuum conditions in order to extract air bubbles trapped in the polymer. Then, the first step, consists in the mixing of the right quantities of HTPB with IPDI and DOA, for about 3 minutes. After a second shift in vacuum conditions, the last mixing is performed with the addition of TIN, with a duration of only 45 seconds, because this catalyst starts to react around a temperature of 36°C easily reached during the mixing, due to friction between polymer chains. The effect of the catalyst is very quick and the curing of HTPB begins during casting in the mold. To have the final polyurethane resin 23 hours of stand at 36°C are necessary.

G.2.1 The Unknown Antioxidant

The HTPB R45 provided by AVIO Space contains an *unknown antioxidant*, which is added to the HTPB when it is still in the viscous liquid condition, lending the light pink color that characterizes the final polyurethane resin. The effect of this substance is significant, making the in-service life of the final polyurethane resin longer. The HTPB without the unknown antioxidant usually degrades faster, with a large increase of hardness and, consequently, high fragility.

G.3 CYLINDRICAL SAMPLES – 2D-RADIAL MICRO BURNER

The 2D-Radial micro burner allows the combustion of cylindrical samples with an initial port diameter of 4.0 mm, a web thickness of 7 mm and a fuel length of 30 mm, see Figure 21. Different fuel formulations can be tested with or without energetic additives. For this work, the manufacturing process for HTPB-based fuel is described. This procedure has been developed and refined at SPLab during the years. The fuel preparation occurs in a controlled environment, a dedicated chemical room, and consists of the following steps:

1. The required amount of HTPB is poured into a Teflon beaker (after check of static electric charge absence). Teflon beaker is then placed in a furnace with a constant temperature of 60°C for 30 minutes. This procedure reduces the HTPB viscosity, allowing for a better air extraction during the vacuum phase (next step);

2. the Teflon beaker is extracted from the furnace and placed in a vacuum bell until its temperature reach the ambient value;
3. DOA and dibutyltin diacetate catalyst are poured into the beaker (after check of static electric charge absence);
4. the beaker containing HTPB, DOA and catalyst is closed and connected to mixing impeller and vacuum pump. The components mixing proceeds for 30 minutes;
5. the metal additive is prepared in the proper amount into a Pyrex beaker (to lessen static electric charge problems);
6. the vacuum pump is turned off and the impeller is extracted from the beaker. The latter is then placed in vacuum bell for 15 minutes (or till the end of apparent bubbling from the beaker);
7. the metal powder is added to HTPB, DOA, and catalyst mixture. To properly disperse the additive, no vacuum-cycle is performed on the compound for the first 5 minutes of mixing. Then the vacuum pump is activated and the formulation is mixed for 10 minutes;
8. in the meantime, IPDI is added to the compound during impeller mixing;
9. at least 10 minutes of mixing are required to grant the proper dispersion of IPDI;
10. the compound can be poured into cylindrical stainless steel moulds;
11. moulds are closed (by teflon taps and with a central stick for the fuel port) and placed in a 36°C furnace for 23 hours.

The same procedure can be used even for the manufacture of pure HTPB, just avoiding the addition of metal powders. Pure HTPB fuel can also be prepared by means of Resodyn® Acoustic Mixer, which allows for a better molecular mixing and lower manufacturing time. The percentages of HTPB R45, IPDI, DOA and TIN are the same of the Table 30.